DE-FG36-07GO17006
3M Company

Final Report

Project Title: Membranes and MEA's for Dry, Hot Operating Conditions

Project Period: April 1, 2007 to March 31, 2011
Date of Report: June 30, 2011

Recipient: 3M Company
Award Number: DE-FG36-07GO17006

Working Partners: Case Western Reserve University, Colorado School of Mines, University of Detroit Mercy, University of Tennessee - Knoxville.
Cost-Sharing Partners: Case Western Reserve University, Colorado School of Mines, University of Tennessee - Knoxville.

Contact: Technical: Steven Hamrock, 651-733-4254, sjhamrock@mmm.com
Contract Administrator: Steven Kays, 651-737-0853, slkays@mmm.com

DOE Managers: DOE Technology Development Manager: Kathi Epping Martin
DOE Project Officer: David Peterson

Project Objective:
The objectives of the project are:

a) Develop an understanding of factors affecting the conductivity and durability of the membrane in a fuel cell operating under the dry, hot conditions required for automotive applications.
b) Develop new membrane(s) with improved performance and durability under hot, dry operating conditions (temperatures up to 120ºC, %RH ≤ 40%)
c) Characterize these new membranes in fuel cells.

Protected Rights Notice: These protected data were produced under Agreement No. DE-FG36-07GO17006 with the U.S. Department of Energy and may not be published, disseminated, or disclosed to others outside the Government until five (5) years from the date they were generated, unless express written authorization is obtained from the recipient. Upon expiration of the period of protection set forth in this Notice, the Government shall have unlimited rights to this data. This Notice shall be marked on any reproduction of this data, in whole or in part.

Contents

1. Summary

Proton exchange membrane fuel cells (PEMFC’s) represent a promising energy technology for transportation and other applications. While many breakthroughs have been made over the last few years in the development of PEMFC’s, technical and economic barriers for their commercialization still exist. Key areas where improvements are still needed are in expanding the temperature range and lowering the humidification requirements of the stack. This is particularly true for automotive fuel cell applications. Requirements of system size, efficiency, performance, start-up and cooling mean that automotive fuel cells must be able to run robustly and exhibit adequate durability under a wide variety of operating temperatures, including temperatures up to 120ºC. They must also be able to do this with little or no external gas humidification (i.e., “dry”). The temperature and humidification range under which a fuel cell system can operate is defined by the operating range of the Membrane Electrode Assembly (MEA), and, while the Proton Exchange Membrane (PEM) is not the only factor that influences the MEA operating range, it is very often the most critical. Hence, new membranes are the key to meeting automotive fuel cell requirements.

The focus of this program was to develop a new Proton Exchange Membrane (PEM) which can operate under hotter, dryer conditions than the state of the art membranes today and integrate it into a Membrane Electrode Assembly (MEA). These MEA's should meet the performance and durability requirements outlined in the solicitation, operating under low humidification conditions and at temperatures ranging from -20ºC to 120ºC, to meet 2010 DOE technical targets for membranes. This membrane should operate under low humidification conditions and at temperatures ranging from -20ºC to 120ºC in order to meet DOE HFCIT 2010 commercialization targets for automotive fuel cells. Membranes developed in this program may also have improved durability and performance characteristics making them useful in stationary fuel cell applications. The new membranes, and the MEA’s comprising them, should be manufacturable at high volumes and at costs which can meet industry and DOE targets. This work included:

A) Studies to better understand factors controlling proton transport within the electrolyte membrane, mechanisms of polymer degradation (*in situ* and *ex situ*) and membrane durability in an MEA;
B) Development of new polymers with increased proton conductivity over the range of temperatures from -20ºC to 120ºC and at lower levels of humidification and with improved chemical and mechanical stability;
C) Development of new membrane additives for increased durability and conductivity under these dry conditions;
D) Integration of these new materials into membranes and membranes into MEA’s, including catalyst and gas diffusion layer selection and integration;
E) Verification that these materials can be made using processes which are scalable to commercial volumes using cost effective methods;
F) MEA testing in single cells using realistic automotive testing protocols.

This project addresses technical barriers A (Durability) and C (Performance) from the Fuel Cells section of the 2005 Hydrogen, Fuel Cells and Infrastructure Technologies Program Multi-Year R&D Plan. In the course of this four-year program we developed a new PEM with improved proton conductivity, chemical stability and mechanical stability. We incorporated this new membrane into MEAs and evaluated performance and durability.

The development of this new membrane involved synthesizing and evaluating new ion containing polymers, new stabilizing additives and polymer nanofibers for mechanical stabilization. Process development work included developing and/or optimizing methods of making stable dispersions with ionomers and additives as well as coating and post processing nanofiber stabilized membranes. MEA constructions were optimized to allow effective evaluation of the membranes performance and durability in a fuel cell. The membrane selected for the final evaluation and testing is a 625 Equivalent Weight (EW) Perfluoro Imide Acid (PFIA) ionomer membrane, which we described in our presentation at the 2010 DOE Hydrogen Program Annual Merit Review & Peer Evaluations (AMR). The structure of this ionomer is shown in Figure 1. This membrane is reinforced with polymer nanofibers (Figure 2). The membrane also comprised our stabilizing additive package described in previous quarterly reports. The durability improvements that this additive package provides, including providing MEAs which lasted up to 18,000 hours in our accelerated durability test have been presented.[1] Durability test results for the additive package are shown in Figure 3.

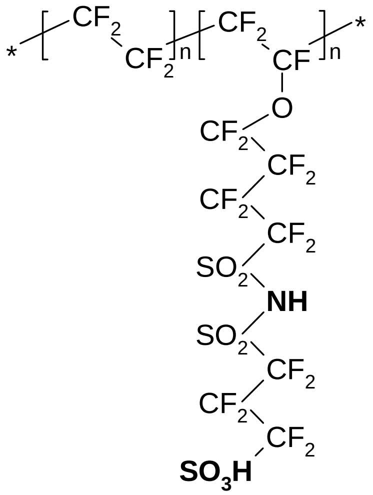

Figure 1. Structure of the Perfluoro Imide Acid (PFIA) polymer.

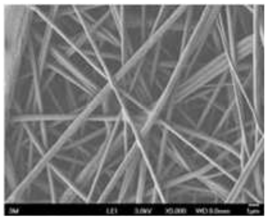

SEM Image of Nanofiber Support

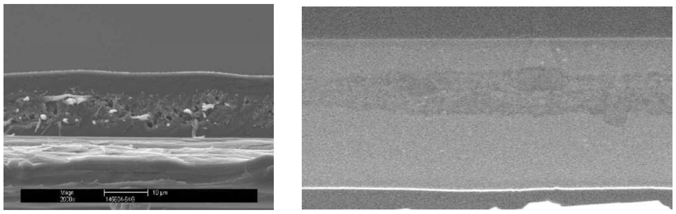

Freeze Fracture Focused Ion Beam

Figure 2. Scanning Electrode Micrographs (SEMs) of the nanofibers and cross sections showing similar membranes with nanofiber support. Samples were prepared while still on carrier liner (bottom layer in images).

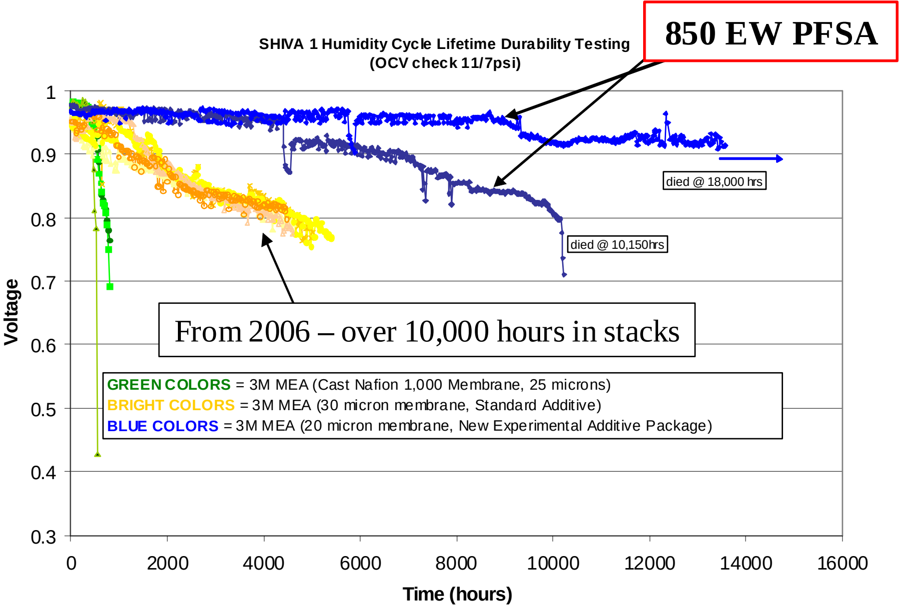

Figure 3. Single cell durability test results from 2010 AMR. Blue curves show additive package selected to be used with our nanofiber reinforced PFIA membrane. Yellow curves show data presented at the 2006 AMR for an older stabilizing additive package. Green curves show data for an unstabilized Nafion™ membrane.

A summary of performance and durability data collected, including data from the FreedomCAR & Fuel Partnership Fuel Cell Tech Team Cell Component Accelerated Stress Test Protocols for PEM Fuel Cell Membranes, are shown in Table 1.[2]

Table 1. Results of testing on 625 Equivalent Weight (EW) PFIA membrane.

All membranes are 15 micron supported or 20 micron unsupported 625 EW PFIA		3M 2011 Status	2015 target	
ASR at 120º C (H_2O pp 40-80 kPa)	Ohm cm^2	.023 (40 kPa) 0.012 (80kPa)	<0.02	✓
Cond. at 120º C	S/cm	0.087 (25% RH) 0.167 (40% RH)		
ASR at 80º C (H_2O pp 25-45 kPa)	Ohm cm^2	0.013 (25 kPa) 0.006 (44 kPa)	<0.02	✓
Cond. at 80º C	S/cm	0.154 (50% RH) 0.3 (95% RH)		
ASR at 30º C (H_2O pp 4 kPa)	Ohm cm^2	0.02 (3.8 kPa)	<0.03	✓
Cond. at 30º C	S/cm	0.09 (90% RH)		
ASR at -20º C	Ohm cm^2	0.10	<0.2	✓
Cond. at -20º C	S/cm	0.02		
O_2 cross-over	mA/cm^2	=1.0	<2	✓
H_2 cross-over	mA/cm^2	=1.8	<2	✓
Durability Mechanical (%RH Cycle)	Cycles	>20,000	>20,000	✓
Chemical (OCV)	Hours	>900+	>500	✓

Remaining gap

2. Polymer Development

Perfluorinated sulfonic acid containing polymers (PFSA's) are the most common membrane polymers used in fuel cells today. Membranes made from these ionomers provide the benefits of highly acidic pendant acid groups for high proton conductivity, good mechanical properties, excellent chemical stability, and fairly low cost. The first PFSA used in PEMFCs was DuPont's Nafion™ ionomer, originally developed in the 1960's for brine electrolysis to produce chlorine[3]. Since then several other PFSA membranes have been developed and introduced for use in fuel cells[4]. All of these are copolymers of tetrafluoroethylene (TFE) and a sulfonic acid containing monomer. The chemical structures of some of these polymers are shown in Figure 4.

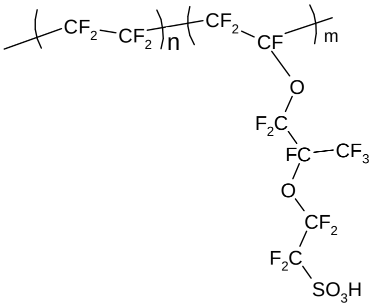

1

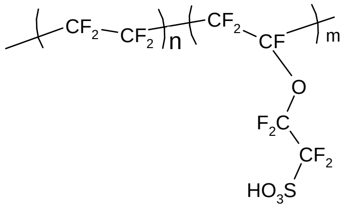

2

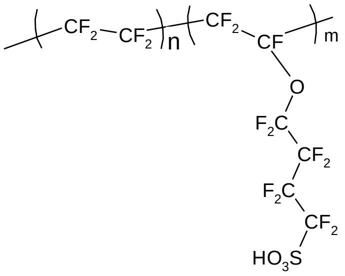

3

Figure 4. Structures of some PFSA's. Polymer 1 is available from DuPont (as Nafion™), Asahi Glass (as Flemion™) and others, Polymer 2 is the short-side chain ionomer developed at Dow, currently available from Solvacore (as Aquavion™) and Polymer 3 is the ionomer available from 3M Company.

When enough acid groups are present in the ionomer, the very hydrophilic sulfonic acid aggregates will absorb water. These hydrated acid groups can provide a continuous, acid rich, hydrated pathway through the polymer. For PFSAs, in addition to the ionic regions, the TFE segments in the backbone provide another structural feature of the polymer. If the ratio of TFE units to acid containing monomers is high enough to provide TFE runs of sufficient length (about 4 or more TFE monomer units) these can crystallize, much like the highly crystalline polymer, polytetrafluoroethylene. These crystallites in the hydrophobic region of the polymer provide significant mechanical stabilization to the membrane. The amount of acid contained in the membrane is typically expressed as *equivalent weight* (EW), the number of grams of polymer required to provide one mole of acidic protons. For traditional PFSA's such as the Nafion™ ionomer, this value is in the range of 1,000 – 1,100. This gives a ratio of TFE to acidic monomers of about 5.5 to 6.5, enough to provide some stabilizing backbone crystallinity. Such polymers have a good combination of proton conductivity and mechanical properties when fully hydrated. Much work has been done over the years to provide a detailed understanding of the structure of PFSA's, and this is still an active area of research. A comprehensive review on the subject has been written by Mauritz and Moore[5]. A generalized representation of a hydrated PFSA structure is shown in Figure 5.

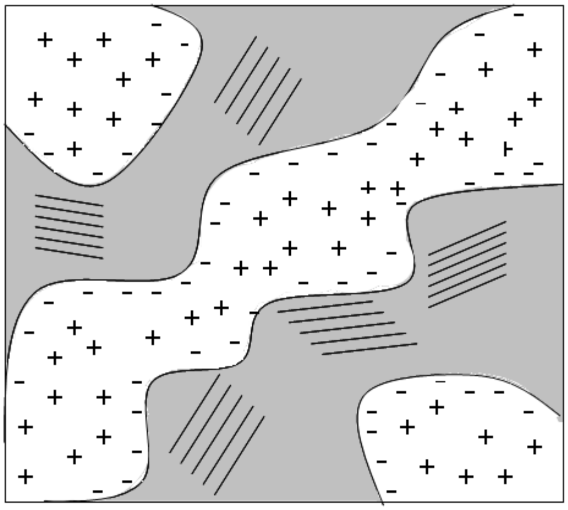

Figure 5. A general representation of the morphology of a hydrated PFSA. The + represents the hydrated protons and the – represents the sulfonate groups at the edges of the hydrated region. These hydrated regions are thought to have the dimensions of 2-3 nm. The parallel lines represent the crystallites formed from the TFE groups of the backbone.

The amount of water present in the hydrated channels of the membrane is a function of the number of sulfonic acid groups present in the membrane and the humidity of the reactant gasses[6]. In a typical PFSA membrane, at a given relative humidity the ratio of water molecules to sulfonic acid groups (referred to as lambda, λ) is fixed. At low %RH, there are a few tightly bound water molecules. As the %RH is increased more water is absorbed and these additional water molecules are less tightly bound and more mobile. It is thought that the less tightly bound, more mobile water molecules that are farther from the sulfonic acid groups are more able to contribute to proton transport[7]. When the temperature is increased, or humidity levels in the reactant gasses are decreased, the membrane will dry out and the conductivity drops. This represents an increase in the resistance of the cell and causes a loss in efficiency and performance.

It is well know that PFSA ionomers with lower EW (higher acid content) have higher ionic conductivity. This can have a significant effect on fuel cell performance, particularly under dry operating conditions.[11] It is also know that the degree of crystallization of the polymer backbone of PFSAs is related to membrane mechanical properties and to the degree of swelling of the membranes caused by changes in hydration during fuel cell operation.[8,9] Membrane swelling induced stresses are a contributing cause of membrane and cell failure during fuel cell operation.[10] The relative crystallinity as a function of EW for the 3M Ionomer is shown by the Wide Angle X-Ray Scattering (WAXS) spectra in Figure 6. Note that the WAXS shows little crystallinity below about 700 EW. We have observed polymers with crystallinity maintain that crystallinity when hydrated, as shown in Figure 7.

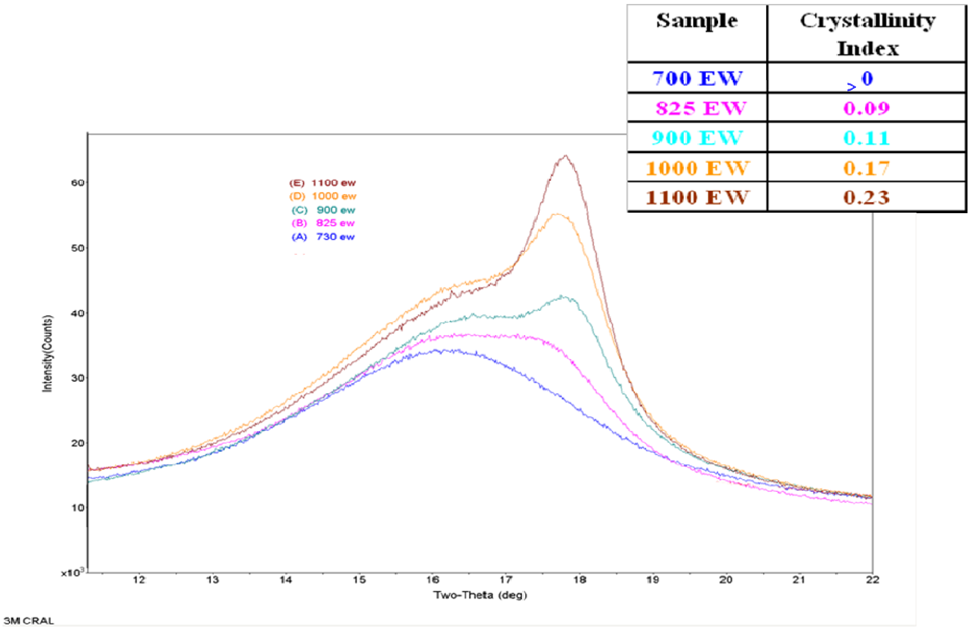

Sample	Crystallinity Index
700 EW	> 0
825 EW	0.09
900 EW	0.11
1000 EW	0.17
1100 EW	0.23

Figure 6. WAXS spectra for a range of different EW 3M Ionomers.

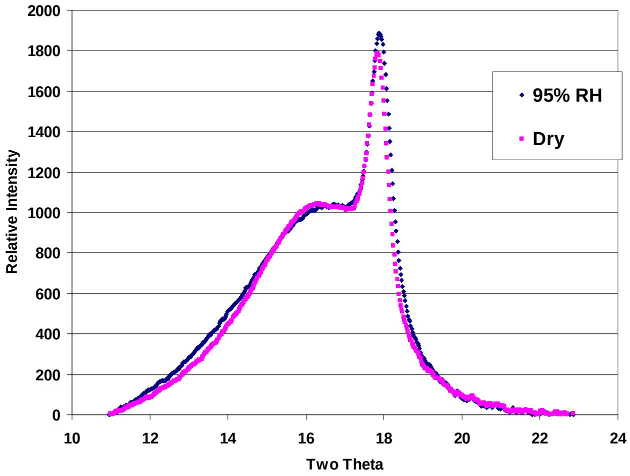

Figure 7. WAXS spectra showing no decrease in peak intensity due to backbone crystallinity upon hydration for 1100 EW 3M Ionomer.

The focus of this program was to try to create ultra low EW PEMs with excellent mechanical and chemical stability.

2.1 Low EW PFSAs and Ionomer Blends

By exploring the lower practical EW limits, it was felt we could enhance conductivity and performance of the new PEMs, particularly under conditions of higher temperature and lower humidity. PFSAs having EW's as low as 580EW were polymerized and lab processed. The conductivity of some of these polymers is shown in Figure 8.

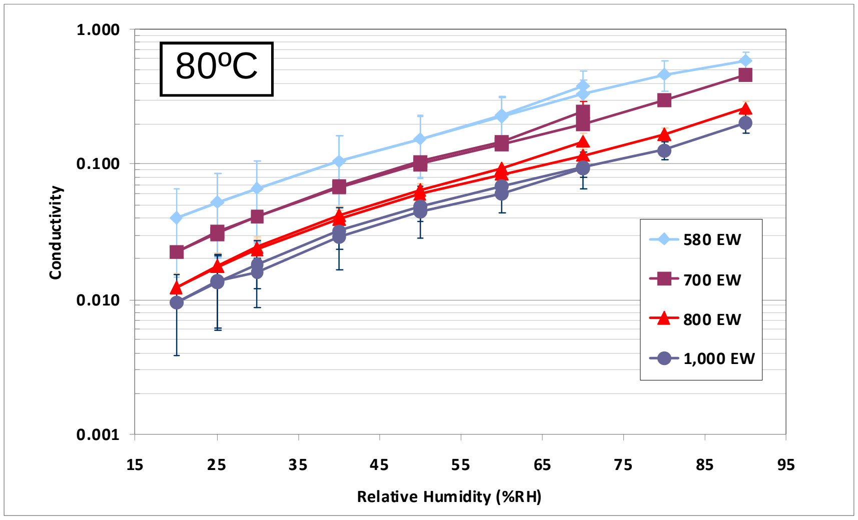

Figure 8. Conductivity vs. relative humidity for several different 3M Ionomers measured by AC impedance spectroscopy at 80ºC.

While low EW polymers performed very well under conditions of lower RH the reduced backbone crystallinity of these polymers provides poorer mechanical properties (Table 2) and they also suffered from higher water solubility at elevated temperature.

Table 2. Physical Property Comparisons for 3M PFSA

	800EW	636EW
Caliper	0.76"	0.78"
Puncture Resitance	40.2 gf	24.6 gf
Stress @ Break	3927 psi	2017 psi
Strain @ Break	134.6 psi	124.6 psi
Initial Modulus	45,268 psi	32,515 psi
Modulus after yield	1816 psi	764 psi

Table 3. Swelling of PFSAs and blends after 100 hours of boiling.

sample	EW	Dry area	area after boiling	% Increase
3M 644EW	644	6.45	13.69	112%
Blended 851EW	851	6.45	8.04	25%
Blended 795EW	795	6.45	9.36	45%

Blended 749EW	749	6.45	11.39	77%
3M 800EW	800	6.45	7.87	22%
3M 1000EW	1000	6.45	7.56	17%
Nafion™ 112	1100	6.3	7.65	22%

851EW blend with a composition of 33/67 644EW/ 1010EW
795 EW blend with a composition of 33/67 644EW/ 900EW
749 EW blend with a composition of 70/30 644EW/1206EW

We also evaluated blending different EW 3M PFSAs, attempting to incorporating the attributes of the individual polymers with high and low EWs. We hoped to produce a PEM with the organized structure of ion conducting regions containing the low EW polymer and the constrained to reduce the water swell/leaching with a matrix of higher EW PFSA. Selected EW polymers were polymerized and worked up to blended solutions and coated. Table 3 shows the area of these membranes, along with a few different EW controls. The plot of % area increase vs. EW for the blends and 3M ionomer controls shown in Figure 9 does not show any advantage to this approach. The in-plane swelling of the ionomer blends is equivalent to the single EW control film series.

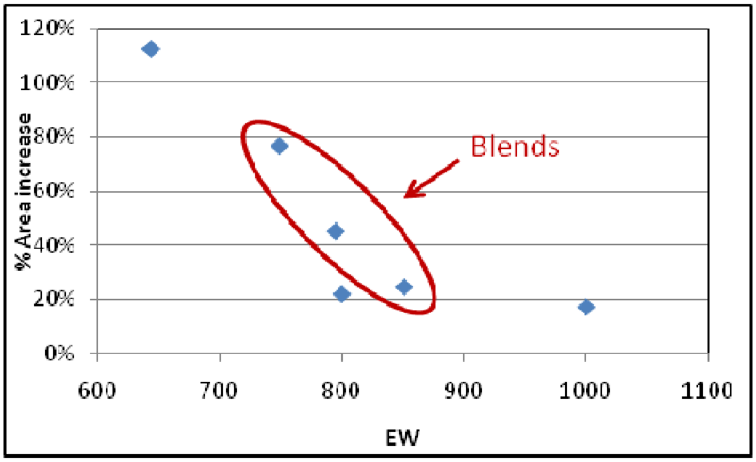

Figure 9. Percent in-plane area increase vs. EW for the blends and 3M ionomer controls boiled for 100 hours (data from Table 3)

Over the course of the contract a number of polymer blends where made in an attempt to provide better PEM performance and durability. These included blending different EWs of the same PFSA and blending PFSAs with inert polymers like PVDF, PES, and PBI). For most of these studies the conductivity, mechanical properties, dimensional stability, were at best the weighted average of the constituents.

In another set of studies we were able to make multilayer cast films of different ionomers and/or different equivalent weights of the same ionomer. The layers were stable and an optical microscopy technique was developed to that showed the different equivalent weight layers. Again, the performance, dimensional stability, and mechanical properties were just the weighted average of the effective equivalent weight. Furthermore, no advantage was observed in having lower or higher equivalent weights as the layer closest to the anode or cathode.

2.2 Multi Acid Side-Chain Ionomers

A major thrust of our research was to synthesize new ionomers with Multi Acid Side Chains (MASC ionomers) based on the 3M Ionomer structure.[11] The synthetic route we used gave us a great deal of flexibility in modifying our polymer by changing the structure of the proton conducting group, adding hydrocarbon or fluorine content, adding acid groups or cross linking the system. The initial step in this process involves the reaction of ammonia with the ionomer precursor (the SO_2F form of the polymer) to create a sulfonamide functional side chain. A second reaction involving the newly created sulfonamide and available residual sulfonyl fluoride groups can lead to formation of a bissulfonyl imide crosslink. This may be desirable or undesirable depending on your intentions, but in general we avoided cross linking the ionomer at this stage. Small but significant concentrations of these bissulfonyl imide groups can lead to lower polymer solubility and swelling, reduced chain mobility and changes in polymer physical properties. The formation of the sulfonamide functionality in a clean, processable way has been critical to this project as the first step toward modification of the polymer side chains.

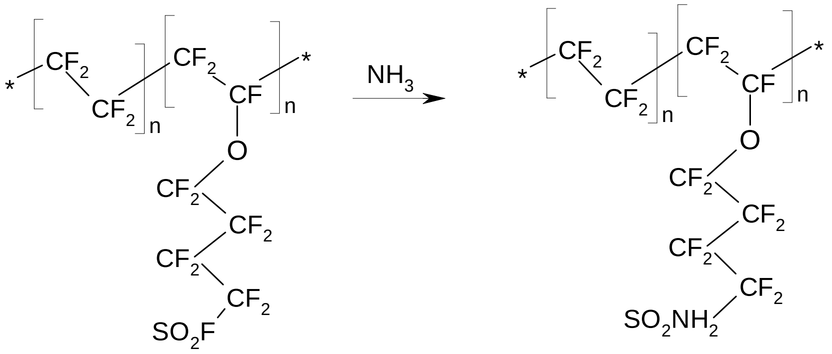

Figure 10. Synthesis of a sulfonamide

The reaction scheme in
Figure 10 shows the idealized case. In actuality, any available water can create multiple polymer products containing a range of sulfonic acid and sulfonamide functional side chains. By controlling the amount of water and ammonia added, we have been able to reproducibly prepare a variety of these terpolymers having sulfonamide content ranging from ~5% - ~98%.

The sulfonamide synthesis is followed by the reaction of the sulfonamide groups with a sulfonyl halide or other reactive group to generate bissulfonyl imide containing polymers. Examples of these new polymers include side-chains based on aromatic sulfonic acids (Ortho Bis Acid) as well as completely perfluorinated side-chains (perfluoro imide acids, or PFIAs). A schematic detailing these attachment reactions is shown in Figure 11.

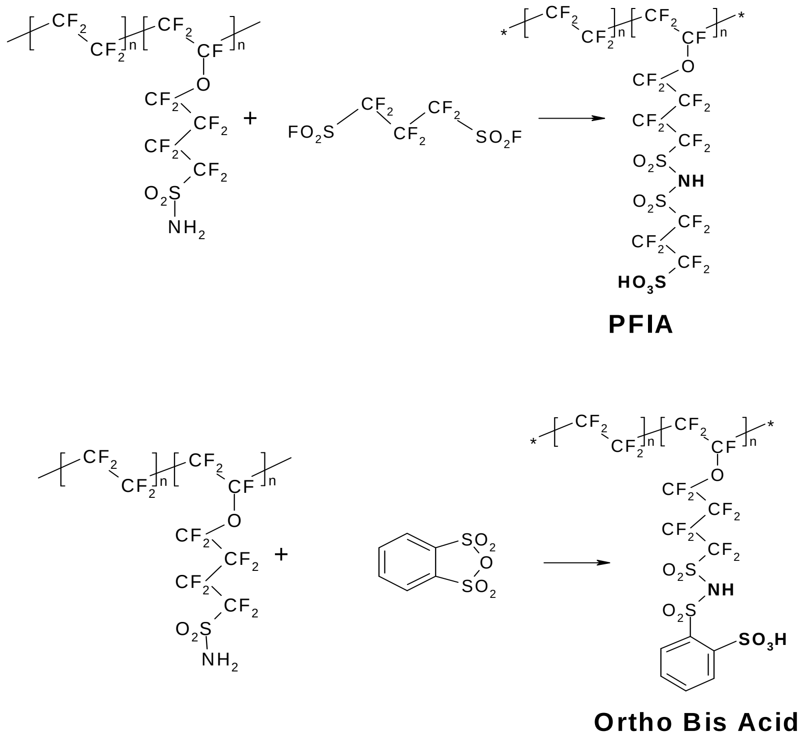

Figure 11. Synthesis of multi acid side chain ionomers.

By choosing the small molecule carefully one can select for hydrophilicity /hydrophobicity, chemical stability, aromaticity, fluorine content and additional acid groups leads to the creation of MASC's(multi acid side chains). Figure 12 shows some of the molecules we have reacted with and attached to a sulfonamide containing polymer.

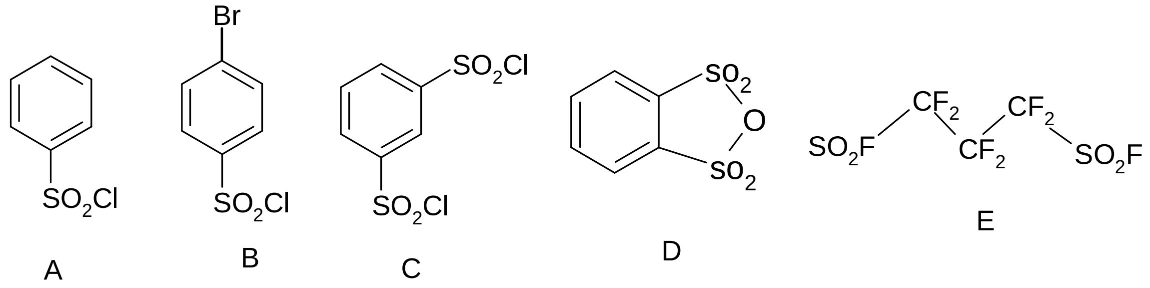

Figure 12. Examples of reactive molecules attached to sulfonamide polymers as part of this program.

A critical piece in the successful synthesis of polymers from difunctional molecules such as Figure 12c, without undesired cross linking reactions is the substantial difference in reactivity between the reaction of the first and second SO_2F group. This is best illustrated with a separate hydrolysis experiment, in which stoichiometric amounts of water and triethyl amine were carefully added to Perfluoropropane Disulfonyl Fluoride (PPDSF). The ^{19}F NMR of the resulting products is shown in Figure 13. A single SO_2F group could be hydrolyzed, showing a remarkable selectivity.

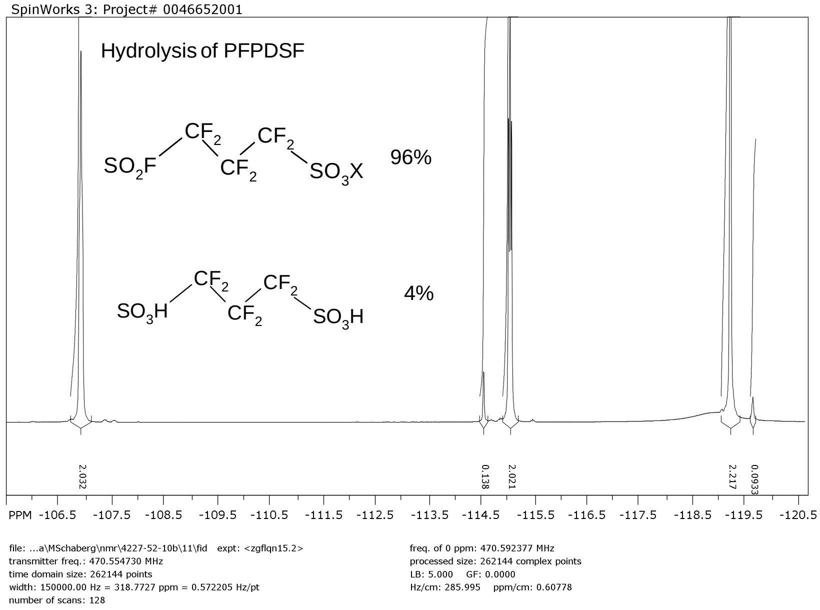

```
file: ...a\MSchaberg\nmr\4227-52-10b\11\fid   expt: <zgflqn15.2>
transmitter freq.: 470.554730 MHz
time domain size: 262144 points
width: 150000.00 Hz = 318.7727 ppm = 0.572205 Hz/pt
number of scans: 128
```

```
freq. of 0 ppm: 470.592377 MHz
processed size: 262144 complex points
LB: 5.000    GF: 0.0000
Hz/cm: 285.995    ppm/cm: 0.60778
```

Figure 13. Hydrolysis Product of PPDSF

Having analytical techniques available to understand what is happening with the chemistry is critical to any project. ^{19}F NMR has proven to be the best method to help our understanding. Figure 14 shows the 19F NMR spectrum of the 3M Ionomer. The signal at about -115 ppm has proved to be quite sensitive to chemical changes of the protogenic group. Figure 15 shows the ^{19}F NMR spectrum of a phenyl substituted bissulfonyl imide (derived from the 3M ionomer SO_2F precursor and Compound A from Figure 12) in the region of the CF_2 group bonded to the sulfur. In this spectrum, in addition to the bissulfonyl imide, a small amount of unreacted intermediate sulfonamide groups can be seen at about -115 ppm. On can also see a signal from a small amount of a sulfonic acid group at about -115.8 ppm, presumable generated from a small amount of water present during the sulfonamide synthesis.

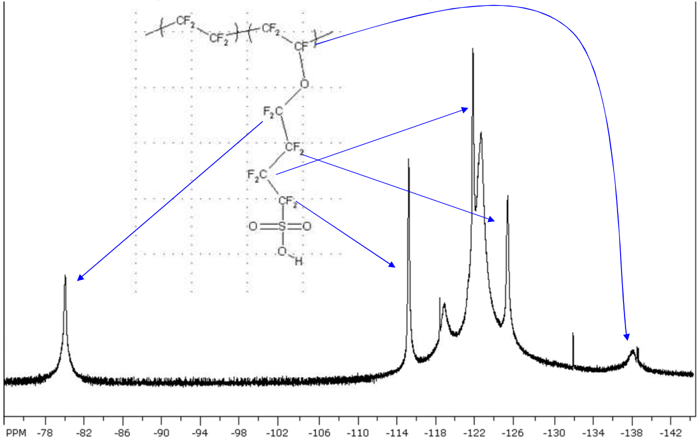

Figure 14. 19F NMR spectrum of the 3M PFSA.

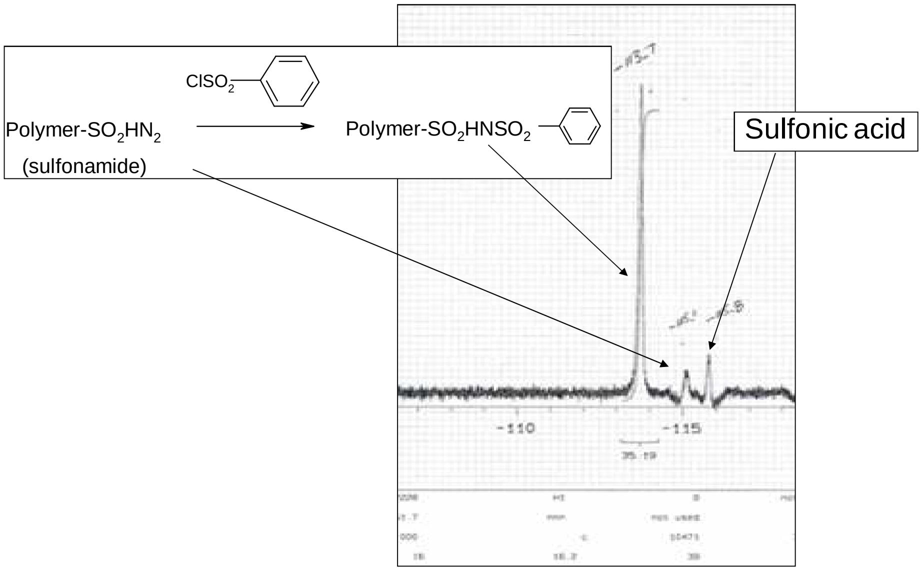

Figure 15. ^{19}F NMR Spectrum of a phenyl substituted bissulfonyl imide derived from the 3M ionomer precursor.

Bis sulfonyl imide acids are known to be highly stable, very strong Bronsted acids, and perfluorinated imide acids have been shown to be much stronger than the corresponding sulfonic acids.[12] This is a beautiful thing to have in a proton exchange membrane. By using the imide functional groups as both a linking group and a protogenic group, we can prepare polymers with multiple acidic hydrogens on a single side-chain. While bis sulfonyl imide containing fluoropolymers have been prepared before, mixed imide/acid MASC ionomers allowing very low EW have not been evaluated in fuel cells.[13]

The motivation for preparing these compounds is to generate low equivalent weight (EW = grams polymer/moles acidic hydrogen[14]) ionomers having enough TFE units in the backbone to provide a higher degree of crystallinity than that of PFSAs with the same acid content. Figure 16 shows the calculated ratio of TFE monomer units to sulfonic acid monomer units as a function of EW for several ionomers. It is generally thought that more than 3 TFE units per acid containing monomer are required for significant backbone crystallinity. Three PFSA ionomers, Nafion™ ionomer, 3M Ionomer and SSC ionomer, show the same relationship (same slope) between EW and monomer ratio, with the EW value at a given monomer ratio being a function of the MW of the side-chain (Nafion™ ionomer > 3M Ionomer > SSC ionomer). It can be seen that the MASC polymers provide a much more favorable combination of low EW and higher TFE to acid monomer ratio than the PFSAs with a single protogenic group on each side-chain.

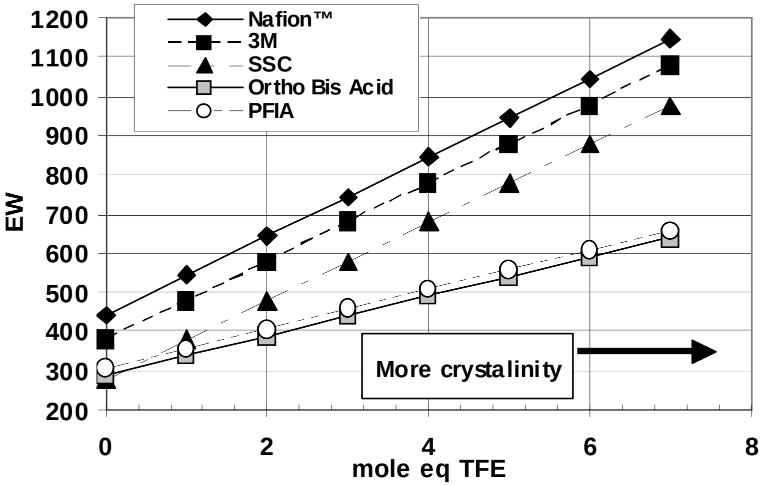

Figure 16. Plot of EW vs. the number of TFE units in the backbone of three PFSA ionomers (Nafion™, 3M and SSC) and two MASC ionomers

Mechanical properties and ionic conductivity of membranes prepared from these new ionomers have been characterized. DMA experiments on a membrane made from the PFIA polymer showed a significantly higher Tα than PFSA's of the same EW (Figure 17). This transition has been described as the thermally activated destabilization of the electrostatic network formed from the ionic groups.[15] It is reasonable to believe that a higher temperature for this transition in the membrane ionomer would be advantageous for higher temperature fuel cell operation. WAXS shows that the crystallinity of the starting SO_2F polymer is maintained in the MASC polymers. An example of this is shown in Figure 18.

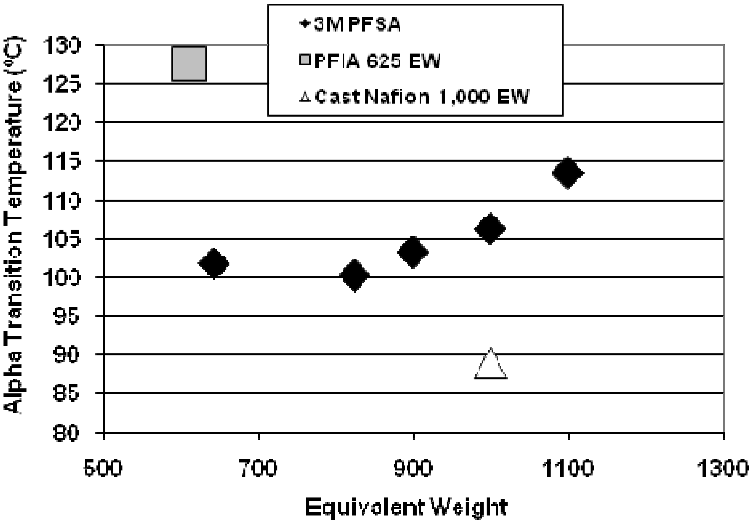

Figure 17. Dynamic Mechanical Analysis (DMA) of selected PFSAs and PFIA (structure shown in Figure 2, 625 EW).

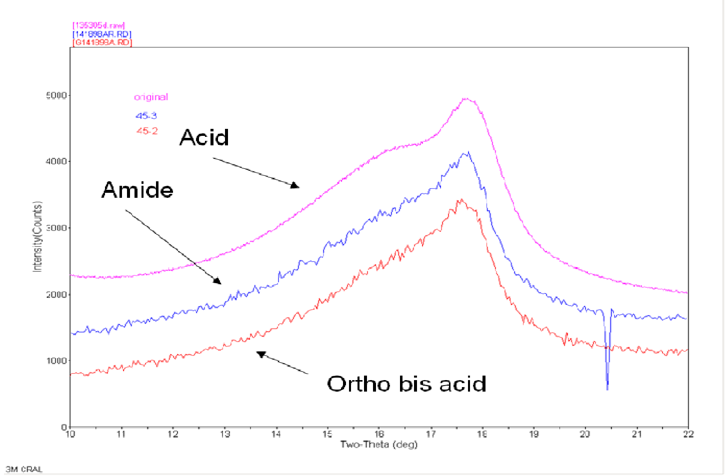

Figure 18. WAXS spectra of an Ortho Bis Acid made from 1,000 EW SO_2F polymer with the sulfonamide precursor and a PFSA made from the same starting SO_2F polymer. The Ortho Bis Acid has an EW of about 700. The backbone crystallinity does not seem to be affected by larger side chain.

These new multi acid ionomers show higher conductivity than the PFSA's made from the same ionomer precursors. Conductivity data for these, with some PFSA controls of different EW's is shown in Figure 19.

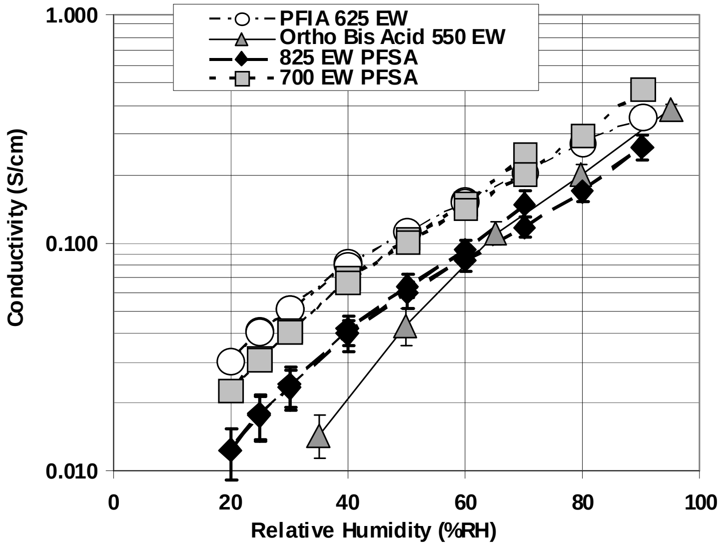

Figure 19. Conductivity of two different EW PFSAs and the two MASC polymers shown in Figure 2. Both MASC polymers were prepared from ca. 850 EW PFSA precursors at conversions of between 80 to 100%. Conductivity was measured in-plane at 80ºC using a 4-piont conductivity probe.[11]

Both of these new MASC polymers have very high conductivity at high %RH. As the humidity is lowered, the conductivity of the Ortho Bis Acid decreases to a greater extent than the PFSA polymers. This effect is similar to what one sees for aromatic sulfonic acid ionomers, and may be due the lower acidity of the aromatic sulfonic acid groups compared to the fluorocarbon sulfonic acids of PFSA's.[4] Conversely, the perfluorinated PFIA ionomer provides higher ionic conductivity compared to a PFSA made from the same EW ionomer precursor polymer at all relative humidities.

Figure 20 shows the water uptake values, after 3 hours in boiling water, for the 3M PFSA as a function of EW and for the PFIA and the Ortho Bis Imide. The data is shown in terms of lambda, or the number of water molecules pre number of acid groups absorbed. The PFSAs absorb about 20 water molecules per sulfonic acid group at EW values below about 750 to 800. Below this EW, the ionomers no longer have significant backbone crystallinity and they swell excessively. Below an EW of about 650 to 700, the PFSAs become soluble in boiling water and this test can no longer be performed.

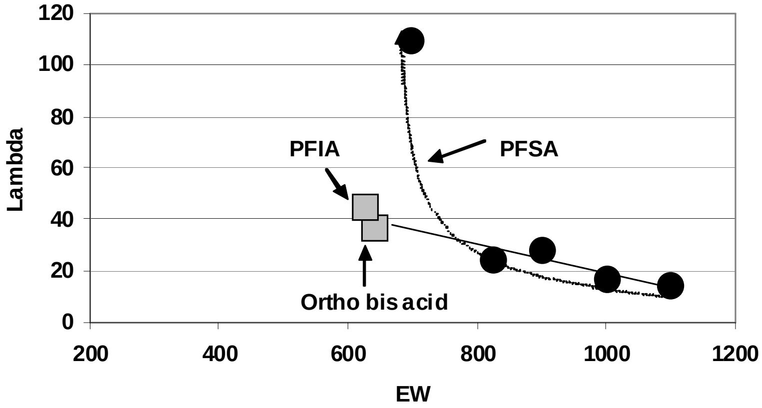

Figure 20. Water uptake for selected PFSAs and PFIA (structure shown in Figure 2, 625 EW) and the Ortho Bis Acid (structure shown in Figure 2, 650 EW).

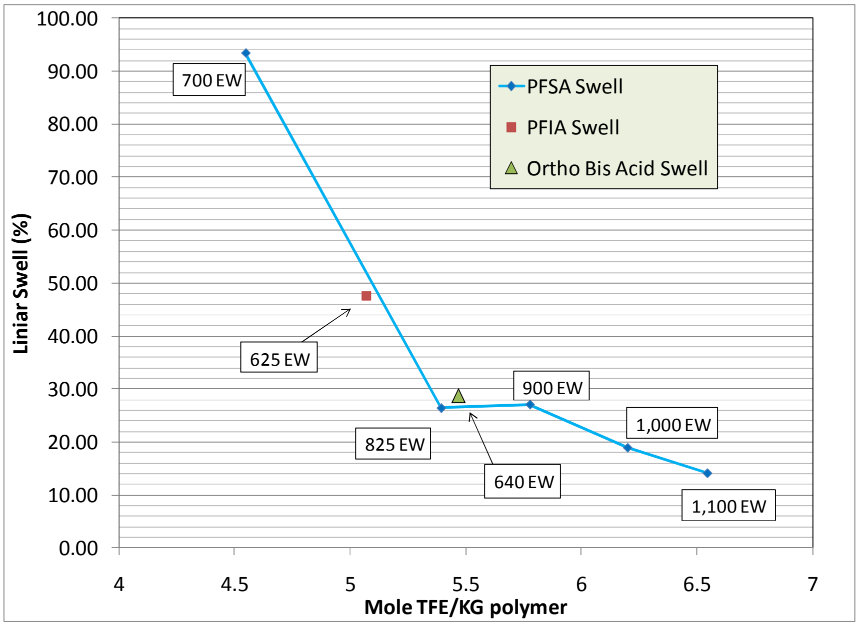

Figure 21. In-Plane swelling in boiling water as a function of TFE content.

While the swelling and water uptake for these MASC polymers are slightly higher than for PFSA's with similar crystallinity content, they are significantly more stable than PFSA's of the same EW. Figure 21 shows the in-plane linear swelling membranes after the same 3 hours in boiling water test, as a function of the mole % of TFE in the polymer. This data suggests this swelling is strong function of the amount of backbone crystallinity.

2.3 Additional Polymer Modifications

Several approaches have been studied to prepare ionomers for a high temperature proton exchange membrane (PEM) fuel cell. The goal is for these ionomers to be very low equivalent weight (EW), chemically stable, solvent resistant and highly conductive. The synthetic approaches included grafting, multiblock and hybrid formation and cross-linking. The approaches described here are:

a) Tethering perfluorosulfonic side-chain into polyarylene backbone.
b) Hybrid materials from PFSA and polyarylenes
c) Cross-linking of low EW PFSA

These are described in Appendix 1.

2.4 Polymer Down-selection

The polymer down-selected to be a component of the membrane used in the final MEA testing in this program was 625 EW PFIA. It offered the best combination of conductivity, chemical stability and mechanical properties.

3. Additive Development

3.1 Zirconium Based Additives for Enhanced Conductivity

The layered *α*-zirconium phosphate is the most interesting in terms of its proton conductivity because it has a pendant –OH group which extends into the interlayer region and forms a hydrogen bonded network with water. The transport mechanism in *α*-ZrP at room temperature is dominated by surface transport four orders of magnitude greater than the bulk transport; however, the crystallinity also plays an important role.[16] In addition, conductivity in *α*-ZrP is highly dependent on the hydration, varying by two orders of magnitude as the relative humidity is increased from 5 to 90%.[17] Recent research has confirmed the dominance of the surface transport and demonstrated enhancements that can be made through modification of the P–OH groups.[18] Based on this understanding of *α*-ZrP, attempts to enhance the proton conductivity have been made. This approach was not used in the final membrane and is described in Appendix 2.

3.2 Composites with Mn Substituted Heteropoly Acids

The free radical attack and decomposition of ionomers during fuel cell operation is a severe problem. To mitigate against free radical attack cations, such as Mn or Ce can be added to the ionomer. While these cations decompose the free radicals before they can attack the ionomer and dramatically increase membrane electrode assembly lifetime they take up ion exchange capacity and so increase area specific resistance of the MEA. To improve on this approach we investigated the use of Mn substituted heteropoly acids (HPAs) which are proton conductors. The issue with this approach is that the HPA are water soluble. We show dramatic improvements in fuel cell performance with the Mn substituted HPAs but we were unsuccessful in discovering an immobilization strategy for these useful additives. Details of this work are shown in Appendix 3.

3.3 Additive Down-Selection

In the course of this program we have studied non-polymeric membrane additive packages for both enhanced conductivity as well as increased stability. The package down-selected for the final testing is a proprietary blend of chemically stabilizing additives. We did not identify a performance enhancing additive for down-selection, but several promising materials were evaluated. Examples of the additives we studied are described in the sections and appendices indicated. Membranes and MEAs comprising the down-selected additive package are described in the sections on membrane and fuel cell testing.

4. Nanofiber Stabilized Membranes

Reinforcing fibers can be an effective strategy for increasing membrane durability in fuel cells run in accelerated tests[19]. Generally, the fibers need to increase the strength of the membrane as well as be hydrolytically and oxidatively stable. The structures in Figure 22 represent two categories of polymers that may be suitable for use as reinforcing fibers.

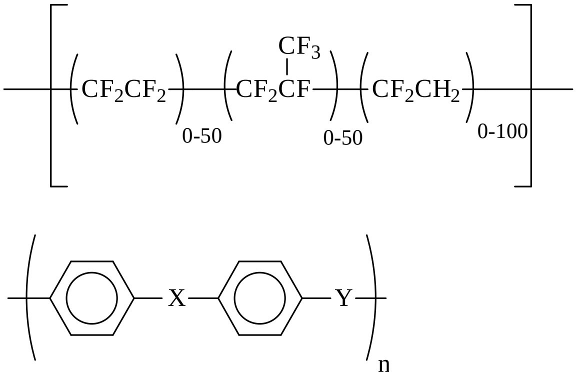

Figure 22. Generalized Structures for fluorinated (top) and hydrocarbon (bottom) polymer candidates for reinforcing fibers. A variety of copolymer ratios are

possible in the fluoropolymer case as indicated by the subscripts. In the hydrocarbon case, X and Y represent linking groups such as CO, SO2, S, O, etc.

Many different polymers may be chosen from the generalized structures in Figure 22 are soluble in common organic solvents and are candidates for solvent spinning into light weight, nanofiber, nonwoven mats. An example electron microscope image of this type of nonwoven material is shown in Figure 2.
In this project we evaluated several nonwoven materials made with differing polymer candidates, polymer blends, fiber diameters, and basis weights. Membranes were made in both the lab and on pilot scale equipment. Evaluations were made based on mechanical properties and durability in accelerated fuel cell testing. In addition, experiments were conducted on our pilot scale equipment to determine viable production methods.

In general, the fabrication of the reinforced membrane consisted of introducing the nonwoven mat onto a liner followed by coating with an ionomer solution. The solution is then dried in zone controlled ovens to make the final composite membrane. Methods were explored to control the thickness of the ionomer layers on top and bottom of the support layer. Figure 23 shows two representative experimental membranes where the ionomer filled support layer has unsupported ionomer on just one side (a) or both sides of the support (b).

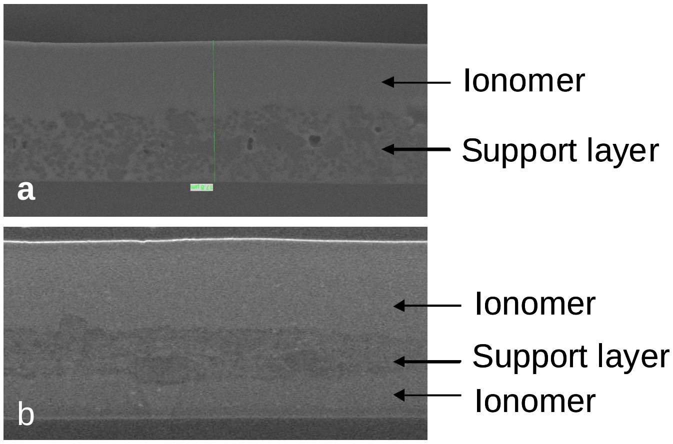

Figure 23. Electron microscope cross section images of reinforced membrane samples. The support layer is biased to one side (a) or more centered (b) depending on process methods.

Once a coating method was established a large number of samples could be generated for further evaluations.

One main objective of this project was to determine the required fiber content in order to restrict membrane swell to less than 5% when soaked in hot water. Figure 24 shoes several samples with differing fiber content (basis weight) as well as a variety of fiber compositions (symbol type).

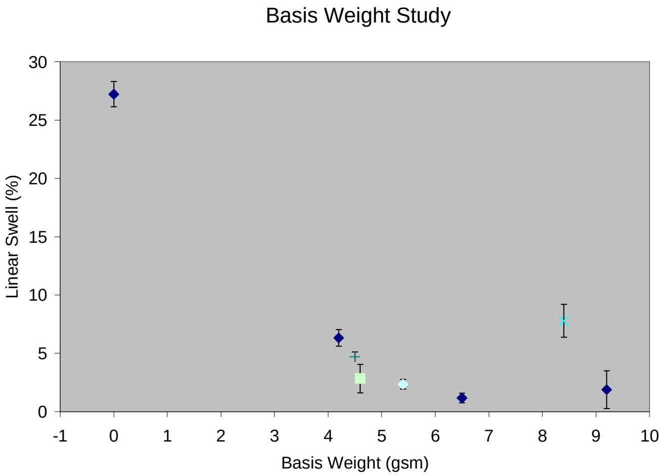

Figure 24. Linear swell (%) in hot water as a function of nanofiber support basis weight. Each symbol type represents a different fiber composition.

Based on this data, it was determined that a minimum nanofiber basis weight of about 4.0 grams/m^2 is required to reduce the swell below 5%. Interestingly, the fiber type was not as critical over the range investigated. The one point at about 8.2 was the exception, where a more flexible polymer was used in the composite allowing for the greater swell.

In addition to the swell behavior, the mechanical properties were evaluated. Room temperature tensile properties were measured for many of the experimental films. A typical comparison is shown in Figure 25 where the supported membrane 3M-S (343-15) has significantly higher modulus, yield stress and break stress.

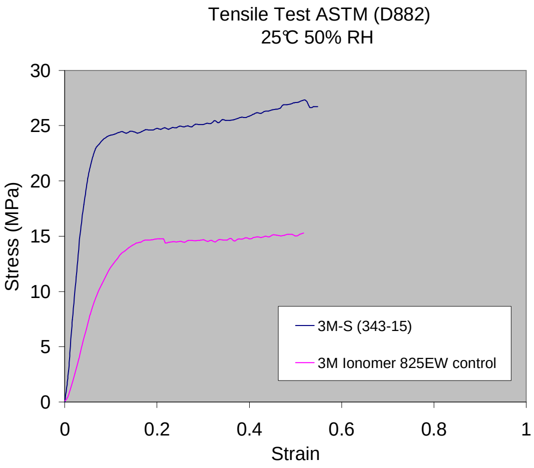

Figure 25. Tensile test ASTM D882 data comparing 3M reinforced membrane (top) to a control, membrane with no reinforcement (bottom)

The modulus was also measured over a wide range of temperatures using a dynamic mechanical analysis (DMA) method. The data in Figure 26 shows the modulus for the supported membrane (top squares) as compared to a control.

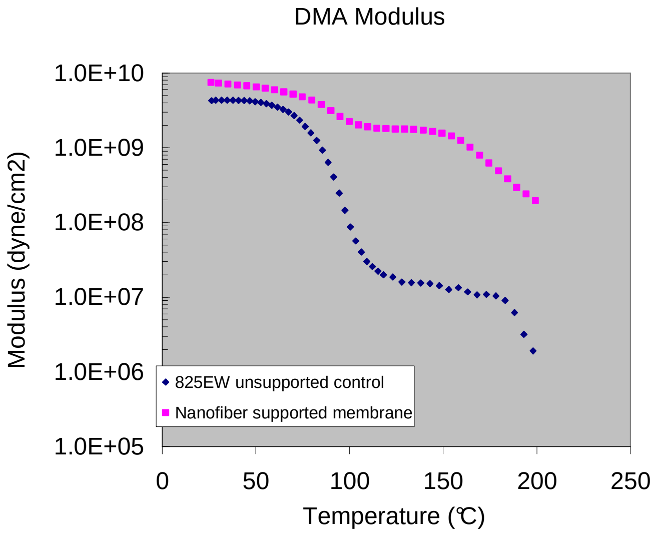

Figure 26. Dynamic Mechanical Analysis (DMA) comparing the storage modulus of a reinforced membrane (top squares) to a non-reinforced control (bottom diamonds).

While the alpha transition is still evident at about 100℃ in both samples, the reinforced membrane maintained a modulus that was almost two orders of magnitude higher than the unreinforced control.

Selected candidates were then further tested in a fuel cell under accelerated durability conditions. The details of these tests can be found in Section
6.3 Accelerated Durability Testing. Briefly, two DOE specified tests (OCV hold and RH cycle) and two 3M internal load cycle tests were used to assess the potential for these new supported membranes to meet the program objectives. From our data is appears that the nanofiber reinforcement is increasing the membrane lifetime by a factor of about 3-6 in the OCV test, depending on the MEA and additive package. Similar improvements were observed in the RH cycle test. The data in Figure 71 shows the nanofiber reinforced sample passes the test (>20,000 cycles) where the similar control died at about 15,000 cycles. Finally, Figure 27 shows the results from one of the accelerated load cycle tests (Section
6.3 Accelerated Durability Testing). Several samples of reinforced membranes were compared to historical controls without reinforcement. An increase in lifetime from an average of 180 hours to over 1,000 hours was observed in this test.

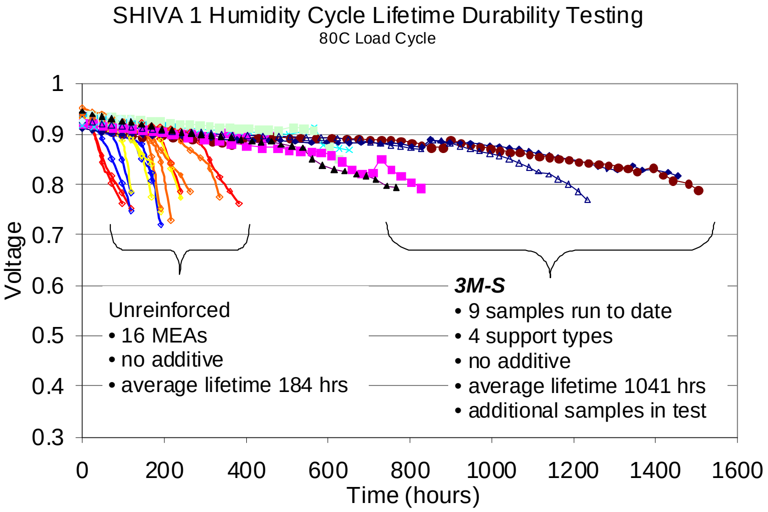

Figure 27. Accelerated load cycle test comparing unreinforced control membranes (grouping on left) to new reinforced membranes (grouping on right).

Post mortem analysis of MEAs that failed in these tests had similar characteristics. Unreinforced membranes most often had large tears or holes near the cell outlet while the reinforced membrane did not fail via tears and typically had several smaller holes (see Section 6.3 Accelerated Durability Testing). The implication of this observation is that the reinforcing fibers retard the growth of a hole or tear that would otherwise propagate quickly through and unreinforced membrane.

After feasibility of the nanofiber support was established with the 825 EW ionomer, samples were made with the new PFIA ionomer. Membranes were made in both the lab and on pilot scale equipment. The performance and durability of this membrane was further characterized and is detailed in Section 6.

5. Ex Situ Material and Membrane Studies

Critical materials characterization methods used and/or developed during this program include conductivity as a function of RH and temperature, lambda measurements, dimensional stability as measured by swell. In addition water and methanol solubility, WAX, SAX, TGA, DMA and Fenton's testing gleaned important insights into PEM properties key to performance and durability. Many of these are highlighted in other sections of the report. Optical microscopy, IR imaging, SEM, FESEM and EDAX were critical to post mortem analysis, electrode development and support development.

5.1 Membrane Physical Property Testing

The workhorse of our membrane screening efforts was conductivity as a function of RH and temperature as measured in a humidity oven at ambient pressure (Figure 8). We worked with Bekktech LLC over the course of the contract to improve the reproducibility of results at both institutions. We have further confidence in our conductivity measurements as a predictive tool of impedance and performance in a fuel cell based on our correlation of fuel cell HFR, corrected for electrode loss, and conductivity agreement, Figure 28.

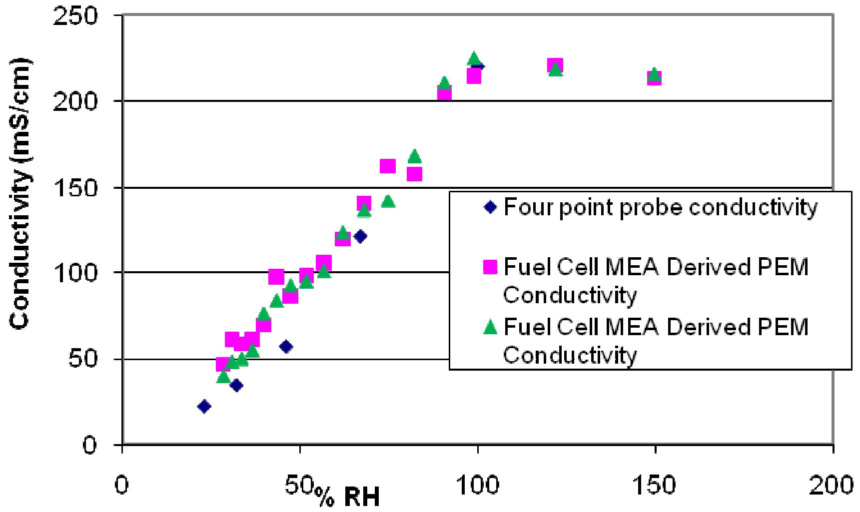

Figure 28. Agreement between conductivity measurements ex-situ vs. conductivity determined from HFR measurements in a fuel cell subtracting the electrode contribution.

In addition, a test for assessing dimensional stability of PEMs upon hydration was developed. Early swell measurements began with room temperature water swell but these proved very unreliable. We found that swell values of fuel cell tested PEMs best matched those obtained by boiling the PEM for three hours. Linear swell at room temperature after boiling for three hours became our metric for dimensional stability. We looked for anisotropies in xy plane of swelling of cast unsupported PEMs but never observed any, however extruded and supported films may have differences down web vs. cross web. All our reported swell values are in the least stable direction. In doing the swell measurements we also did water uptake. These values were consistently higher in this method then our measurements taken at 100% RH in our environmental chamber. This difference is consistent with the Schrödinger paradox where water uptake is higher for a PEM exposed to liquid water compared to one that is exposed to a vapor at near 100%. Our measurement system for determining lambda as a function of dewpoint and temperature uses a 10g load cell where a large area sample is suspended from its arm within the humidity chamber. This system was instrumental in understanding differences in conductivity with RH and for correlating water uptake and conductivity.

Many different process variables were tested for their effect on dimensional stability. The first set of data looked at dimensional stability and equivalent weight (Figure 30). The next set of variables centered about the process variables of casting solvent and process conditions for roll goods. The use of different casting solvents in general showed only small but consistent differences in dimensional stability, tensile properties, SAX spectra and fuel cell performance. Most striking in that set was the decrease in fuel cell performance seen with water only dispersion castings. The loss was not associated with any IR losses and it is postulated that the loss in performance was related to poor water permeability which could be consistent with the SAX data.

During this contract we had no technique that we felt comfortable with for directly measuring the z-axis swell of our PEMs. However we found that by combing the linear swell and water uptake data we could make an inference of the z-axis swell. Plotting our water uptake values vs. the linear swell value would fall along a line except for thinner samples was the water uptake was greater than the linear swell. This is captured in
Figure 29. We later confirmed this result working in collaboration with Lou Madsen at Virginia Tech using his unique sample preparation for NMR measurements[20] and in SAX measurements with CSM. This potentially may have large implications for electrode development where it has been observed that for low loadings an additional mass transport factor is needed to model the performance. Other materials that showed this behavior included much of the supported PEM work where the water uptake most often matched that of the unsupported PEM but the xy swell was highly constricted.

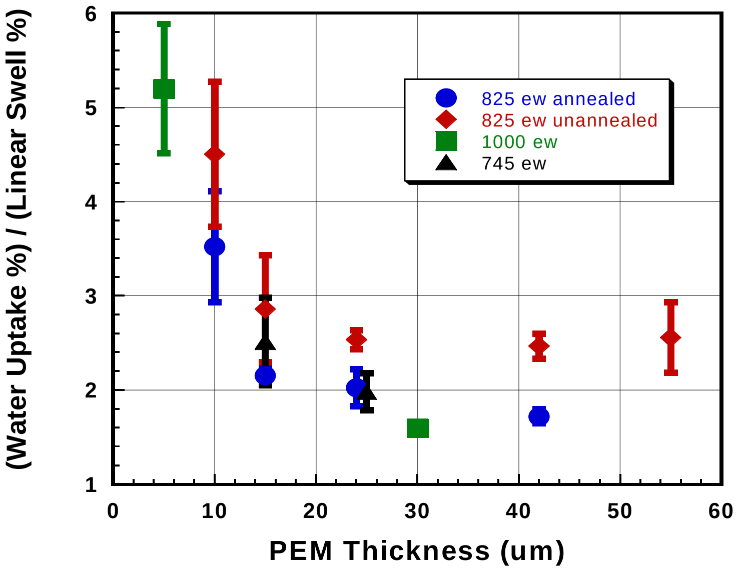

Figure 29. Implication of increased z-axis swell with decreasing PEM thickness as observed by the change of the ratio of water uptake to linear swell.

Swell and water uptake testing was a workhorse for dimensional stability performance in optimizing different support types. In addition, it was used extensively for understanding process variables associated with filling the support and post processing for optimal polymer stability. The importance of developing a support technology can be seen in Figure 31 where we are looking at just one support type and basis weight and three different low EW ionomers. This figure reinforces the use of the support and the gain in dimensional stability with the PFIA with negligible loss in conductivity to a 620 EW standard PFSA. Note, the 620 EW PFSA in this figure is also the one seen in Figure 30 and represents an optimized method in the synthesis of low EW. The data in Figure 30 shows not only a gain in dimensional stability but also in terms of water solubility which had been an issue in further lowering the EW of 3M polymers. Water and methanol solubility measurements were done for our equivalent weight series and other polymers and serve as good indicator of membrane chemical stability. Methanol solubility typically follows the trend line of the water solubility but is shifted to the higher EWs by about 100 EW.

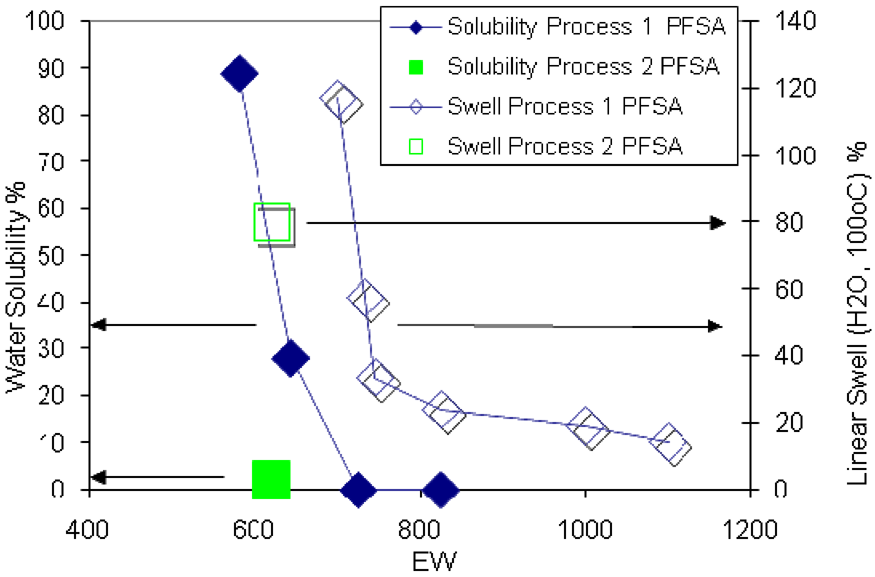

Figure 30. Water solubility and dimensional stability as a function of equivalent weight for two different polymerization processes.

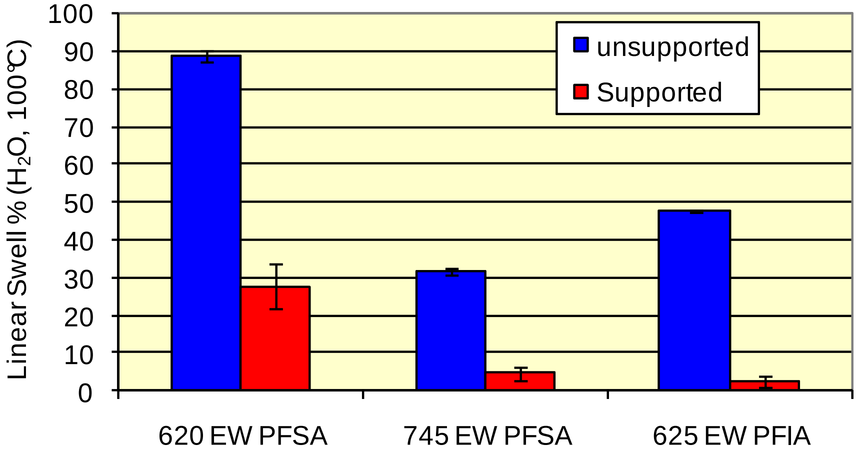

Figure 31. Dimensional stability both supported and unsupported with three different ionomers.

5.2 Studies of Water and Proton Transport and Related Physical Chemistry-Carried Out in Collaboration with the University Of Tennessee

Proton and water transport are among the defining characteristics of fuel cell membranes. The coupling between facile proton transport and water content of in membranes has presented a substantial challenge in light of efforts to decrease the operating RH of fuel cells. In this work, we explored the 3M-PFSA membranes as a function of equivalent weight (EW). At low EW, they show markedly higher conductivity, albeit at the expense of mechanical properties. To elucidate the underlying mechanisms associated with the apparently high conductivity, 3M-PFSA membranes with different ionic exchange capacity (IEC) were characterized with respect to water sorption, proton conductivity and water diffusion at two widely different time scales as functions of temperature and relative humidity. In addition, to further the analysis of the conductivity, a new method for determining the density of hydrated polymers was developed.

The effect of EW on the PFSA conductivity as a function of relative humidity (RH) is shown in Figure 32. At every RH value, the low EW polymers have higher conductivity, with the difference increasing dramatically below 700 g/eq and most pronouncedly at low RH. For lower EW polymers, the decrease of conductivity with decreasing RH is substantially less than typically observed for commonly used PFSAs of EW ~1000 or greater. For 580 EW, conductivity approaches that set by DOE for automotive fuel cells, which is 100 mS/cm.

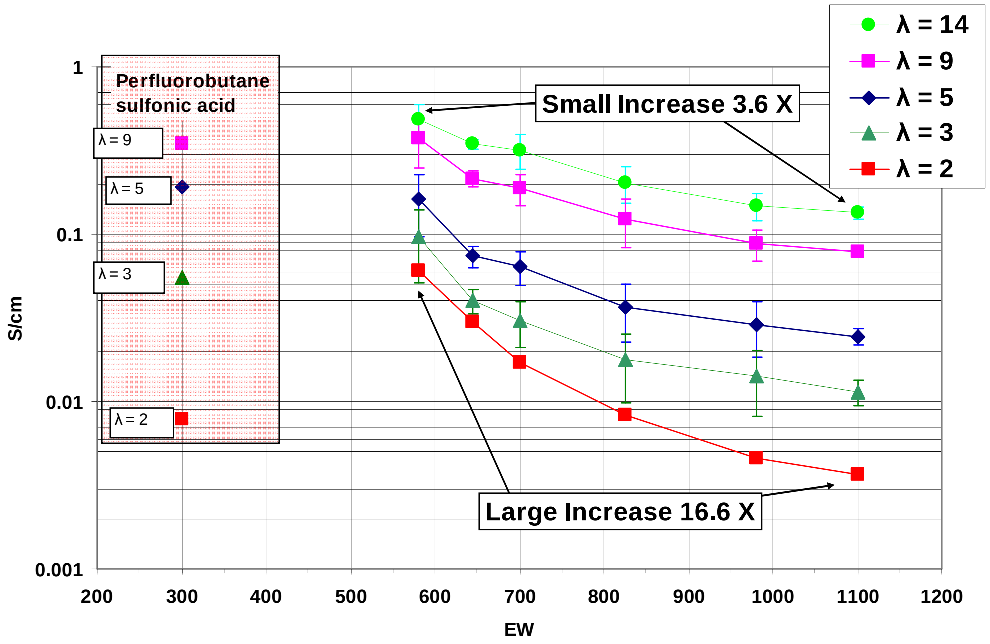

Figure 32. Conductivity of 3M-PFSA membranes as a function of EW at different RH.

At high water content, the conductivity increases 3.6X from the highest EW 1100 to the lowest 580 EW. Under this relative humidity conditions, protons are moving in a watery environment. However, for low water contents (lambda=2) the increase of conductivity with decreasing EW is very large. The conductivity for 580 EW is 16.6X higher than that of 1100 EW under these drier conditions. It is also noteworthy that the low EW ionomers at lower lambda values have higher conductivity than the perfluorobutane sulfonic acid, a small molecule with the same chemical structure at the ionomer side chain. Under these conditions, it is intriguing to understand the mechanism of proton conductivity and hence the factors controlling conductivity.

To develop a hypothesis explaining these results, we consider factors controlling conductivity in fixed-site proton conductors. In general, the conductivity of the polymer electrolyte will be a function of both concentration and mobility of H^+:

$$\sigma_{H^+} = z_{H^+}\mu_{H^+}C_{H^+}$$

The concentration of protons is determined by the EW of the polymer, its density and by the extent of dissociation of the acid group in the polymer. The extent of dissociation should be similar for this series of polymers. The extent of dissociation is controlled by the water content and the type of acid group. The perfluorinated sulfonic acid is likely to be completely dissociated even down to the lowest RH values used here. As a first level correction to the conductivity, we simply corrected by the polymer equivalent weight, which is inversely proportional to the concentration of protons. To do this rigorously, however, we need to correct for density and hydration effects on the overall weight. Thus, we calculate the proton concentration as:

$$C_{H^+} = \frac{\rho}{(EW + 18 \cdot \lambda)}$$

Correction of the conductivity by this factor then directly yields the proton mobility. The results are shown in Figure 33.

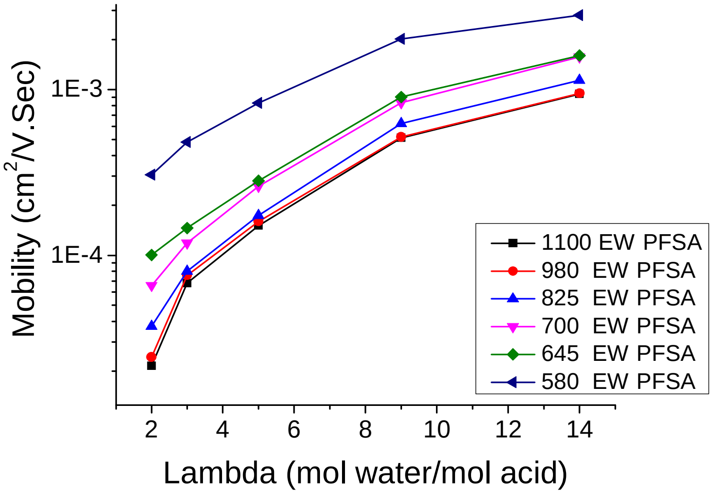

Figure 33. Electrical mobility (μ) of PFSA membranes of different EW as a function of λ at T=80℃.

As seen in the figure, the mobility is similar at all water contents for all EWs of 825 and above, increases slightly for EWs 700 and 645 and jumps markedly for the 580 EW polymer. Clearly, the origin of the high conductivity at low water content is in this exceptionally high mobility. Thus, we next consider factors that could influence the mobility of the proton. Of course, the most important factor is the water content of the polymer. As shown in Figure 34, the water uptake of the low EW polymers is very similar to that of the high EW polymers at all RH values. In higher EW 3M-ion, as in Nafion™ ionomer and other materials, the water content dependence of conductivity is derived from the change in the nature of the hydration environment around the proton. At high lambda (>6), with plentiful water, the proton essentially moves as if it is in an aqueous solution in the channels of the ionomer. It is well-shielded from the effects of the fixed sulfonate groups. As lambda drops below this value, the proton is now held with the solvation shell surrounding the sulfonate. At still lower values, the proton is reasonably localized on a hydronium ion and is likely to participate in a solvent-separated or contact ion pair with the sulfonate. Thus the proton ‘feels’ increasing ‘friction,’ i.e. hindrance to its motion, as the water content decreases. However, the results in Figure 33 are shown as a function of water content and, as noted, the low EW proton mobility is less sensitive to water content than is that at high EW.

This implies that some other factor(s) must play a role in the excess proton mobility observed. Two remaining possibilities are (i) changes in morphology as a function of EW, resulting in a more open proton conduction pathway and (ii) changes in the proton transport mechanism such that water molecules more readily ‘hop’ from one cluster of 2 or 3 water molecules plus a sulfonate anion (plus a proton) when the separation of the sulfonate groups is smaller (i.e. for the low EW case).

First, the morphology of the polymer most likely does change. Residual crystallinity in the polymer disappears below 825 EW, essentially the same point below which substantial increases in mobility are observed. Also, mobility differences *are* observed even at high water contents, though they are not as dramatic as for low lambda. Thus, the overall ‘tortuosity’ for transport is probably decreased. This may be a similar effect to that observed for highly sulfonated BPSH polymers by McGrath and co-workers.[21] To explain the low lambda results, we suggest that as the EW decreases, the spacing between one sulfonate anion plus water cluster to another decreases substantially, leading to better transport of protons due to vicinity of donors and acceptors as illustrated in Figure 34. The high conductivity in the 583 EW PFSA membranes can be attributed to the proximity of the side chains facilitating the formation of hydrogen bonds between the clusters of water molecules and sulfonic acid groups at the end of side chains. Since hydrogen conduction is believed to rely on hydrogen bond forming and breaking in a network of hydrogen bonds, the shorter the distance between side chains the easier the network formation will be. To this favorable spatial structure adds the proton continuous motion. It does not adopt one fixed position but rather oscillates back and forth continuously in a movement described as libration. In low EW samples at low lambda, the small amounts of water provide a bridge between adjacent sulfonate groups and the protons can readily cross this bridge from chain to chain. This effect is similar to, but distinct from, Paddison's 'continuity' condition for conduction.[22] In that case, Paddison is referring to a continuous network of connected clusters. Here, we are positing a more local continuity that is ***required*** by the high density of side-chains. Since the determining interaction moving protons is a pairwise interaction and all side-chains are spaced closely, no special polymer morphology is required. Rather, the primary structure of the low EW polymer determines the needed pairwise packing.

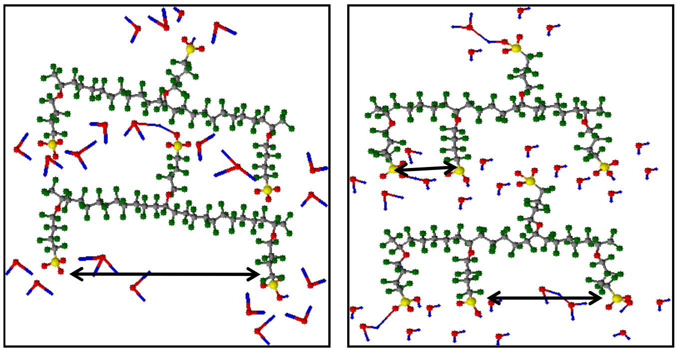
825 EW PFSA
λ=4

583 EW PFSA
λ=4

Figure 34. Comparison of side-group spacings between 825 and 583 EW PFSA membranes at lambda=4.

We pursued NMR diffusion measurements (a long range probe of motion) and NMR relaxation measurements (a molecular scale probe), to shed further insight into the nature of these pathways. ^{1}H diffusion coefficients were determined using the dependence of the signal attenuation on gradient strength according to the following relation:

$$\ln\left[\frac{S(g)}{S(0)}\right] = -\gamma^2 D g^2 \delta^2 \left(\Delta - \frac{\delta}{3}\right)$$

NMR diffusion coefficients as a function of water content at 30^{o}C for different EW polymer are shown in Figure 35. At low water content - lambda between 2 and 4 - we see that as the EW decreases, the water diffuses faster.

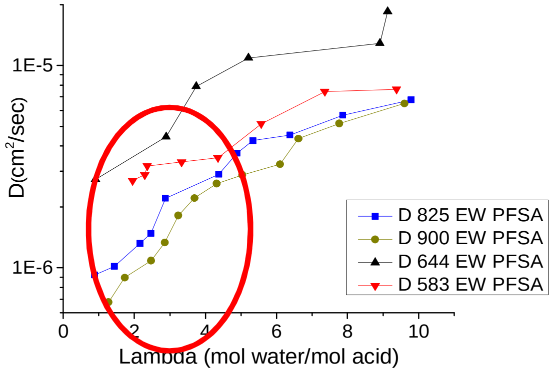

Figure 35. 1H Diffusion coefficients as a function of water content for different EW PFSA membranes.

These observations are further supported by the local diffusion data, shown in Figure 36, derived from ^{2}H relaxation measurements. These show that in 583 EW, the lowest EW studied, water molecules have high mobility at low water content.

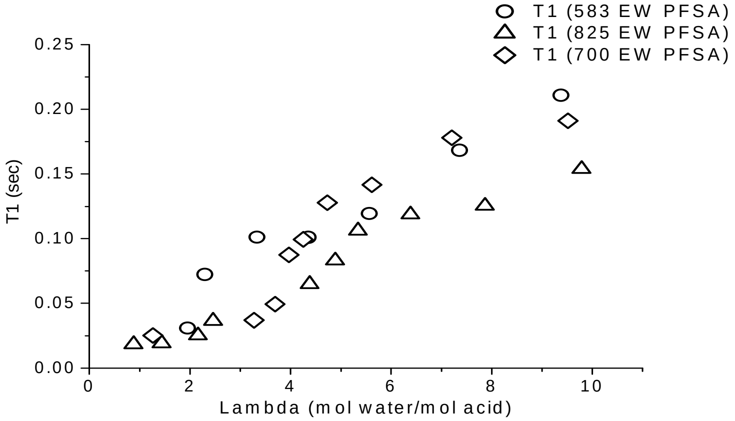

Figure 36. 2H relaxation times as a function of water content for different EW PFSA membranes.

By comparing the relaxation data, we see that T_1 values are similar at most different water contents, with an increase in that for EW = 583 in the range between 2 and 4. This conclusion is amplified in Figure 37, which shows the relaxation times recast as local diffusion coefficients.

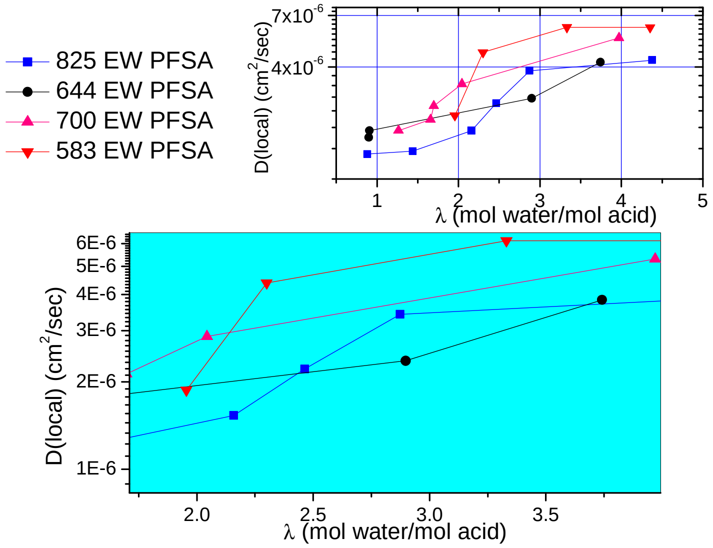

Figure 37. Local Diffusion of 2H at T = 30 ℃, derived from relaxation data, in different EW PFSA membranes

Therefore, any differences in micron scale diffusion among the samples with different EWs at certain water content must be due to an effect that is larger than few nanometers.

Taken together, these results refute the conclusion drawn by previous researchers that at low degrees of hydration, the long side chain architecture is more favorable for accommodating well-connected water structure even at low degrees of hydration.[23] Despite its short side chain, 583EW 3M-PFSA membrane retains high water mobility at low degrees of hydration. To consider the mobility of protons and water on a similar basis, we derive 'diffusion coefficients' from T_1 and conductivity measurements. Figure 38 compares the three types of diffusion coefficients for 800 EW, for example. We see that these diffusion coefficients are very similar, suggesting that protons are diffusing at the same rate as water. This in turn implies that a similar mechanism is operating to transport protons and water.

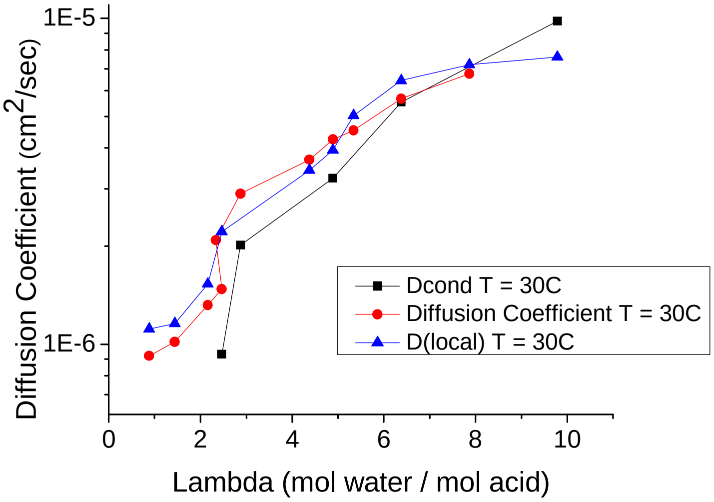

Figure 38. Diffusion Coefficients of 800 EW PFSA at 30℃.

5.3 ESR and IR Studies - Carried out in Collaboration with the University Of Detroit Mercy

During the four-year funding period we have focused on the following main topics, aiming to an understanding of the degradation and stabilization processes of proton exchange membranes (PEMs) used in fuel cells (FCs).

a) Ranking the Stability of Perfluorinated PEMs to Attack by Hydroxyl Radicals.
b) In Situ ESR Studies with MEAs Based on 3M Membranes.
c) Using β-cyclodextrin (β-CD) Encapsulation to Detect "Very Early Events" in the Fragmentation Process of Perfluorinated Membranes.
d) 2D Spectral-Spatial FTIR Imaging of Degraded Nafion™ Membranes.

Ranking the Stability of Perfluorinated PEMs to Attack by Hydroxyl Radicals.
The stability of the Nafion™, stabilized Nafion™ (StNafion™), 3M and Aquivion™ membranes to attack of the hydroxyl radical, $HO^\bullet$, was compared at 300 K. Detection of radicals: by spin trapping with DMPO in the aqueous dispersions of the membranes. The experiments consisted of measuring by ESR the concentration of the DMPO/OH

adduct in the presence of the membranes, which are considered as “competitors” that react with HO$^•$ radicals and thus compete with the spin trapping reaction HO$^•$ + DMPO → DMPO/OH. The competitive kinetics (CK) approach has been adapted for ranking the membrane stability and led to the determination of the reaction rate constant between hydroxyl radicals and the membranes.

<u>Method</u>: Competition Reactions for HO$^•$ in the Presence of DMPO as the Spin Trap.
HO$^•$ + DMPO → DMPO/OH
HO$^•$ + C → C$^•$ (C is membrane, C$^•$ is a membrane-derived fragment)
The formalism of “<u>parallel reactions</u>” leads to the expression:

$$\frac{V}{v}-1=\frac{k_c[C]}{k_{DMPO}[DMPO]}$$

V and *v* are reaction rates for the formation of the DMPO/OH adduct in the absence and in the presence of the competitor C (the membrane). A plot of [C]/[DMPO] vs k_c/k_{DMPO} gives the ratio *V/v* - 1and a measure of the ability of the competitor to be attacked by hydroxyl radicals. The results are shown in Figure 39 and Figure 40 and in Table 4.

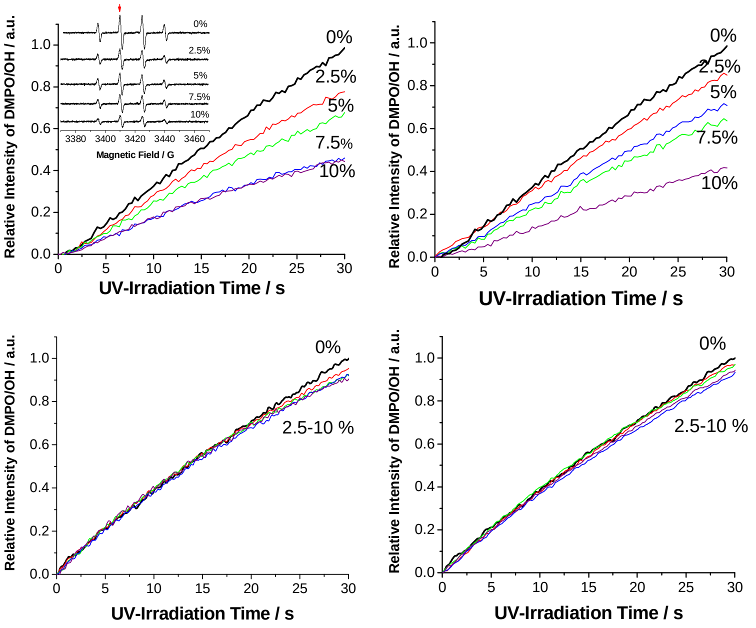

Figure 39. ESR spectra of the DMPO/OH adduct for the indicated Nafion™ ionomer concentrations in the range 0-10 wt % are shown in the inset of (A); the red arrow indicates the peak that was monitored in the time scans. The intensity of the ESR signal from the DMPO/OH adduct as a function of membrane concentration is shown in time scans: (A) Nafion™, (B) StNafion™, (C) 3M Membrane, (D) Aquivion™ membranes. The thicker black line in each case shows the results in the absence of membranes. Data were normalized to the intensity measured after 30 s of UV irradiation at 300 K in the absence of the membrane.

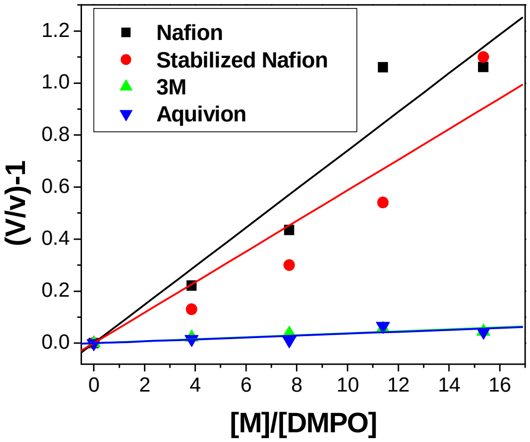

Figure 40. Plots of (V/v)-1 vs the concentration ratio [M]/[DMPO] for Nafion™ (■), stabilized Nafion™ (●), 3M (▲), and Aquivion™ membranes (▼), using the inhibition data of the DMPO/OH adduct shown in Figure 1. Note that the membrane concentration, [M], is expressed in terms of the number of backbone carbons. The data for the each membrane were fitted by assuming that the straight lines extrapolate to the origin.

Table 4. Reaction Rates of Fluorinated Membranes with Hydroxyl Radicals*

Membrane	k_M/k_{DMPO}	k_M **x**10^{-8} $M^{-1}s^{-1}$
Nafion™	0.0741	2.7
StNafion™	0.0588	2.1
3M	0.0038	0.137
Aquivion™	0.0037	0.133

*The k_M values are calculated for [M] expressed as the number of carbons in main chain.

The intensity of the DMPO/OH adduct as a function of irradiation time for the indicated membrane concentrations indicated a greater stability of the 3M and Aquivion™ membranes. The absence of the ether group and of the tertiary carbon in the side chain of 3M and Aquivion™ membranes may be responsible for their greater stability.[24]

In Situ ESR Studies with MEAs Based on 3M Membranes.

Experiments were performed at 300 K on MEAs based on the 3M Membrane (EW = 825 g/mol), in a FC inserted in the resonator of the ESR spectrometer. Radical detection was performed by spin trapping ESR with 5,5-dimethylpyrroline-N-oxide (DMPO) added at the anode or cathode sides. The hyperfine splitting and the relative intensities of the spin adducts were determined by fitting the spectra using the WinSim (NIEHS/NIH) simulation package. Major results are shown in Figure 41 (spin trap on the anode side) and Figure 42 (spin trap on the cathode side), for membranes of thickness 25 µm.

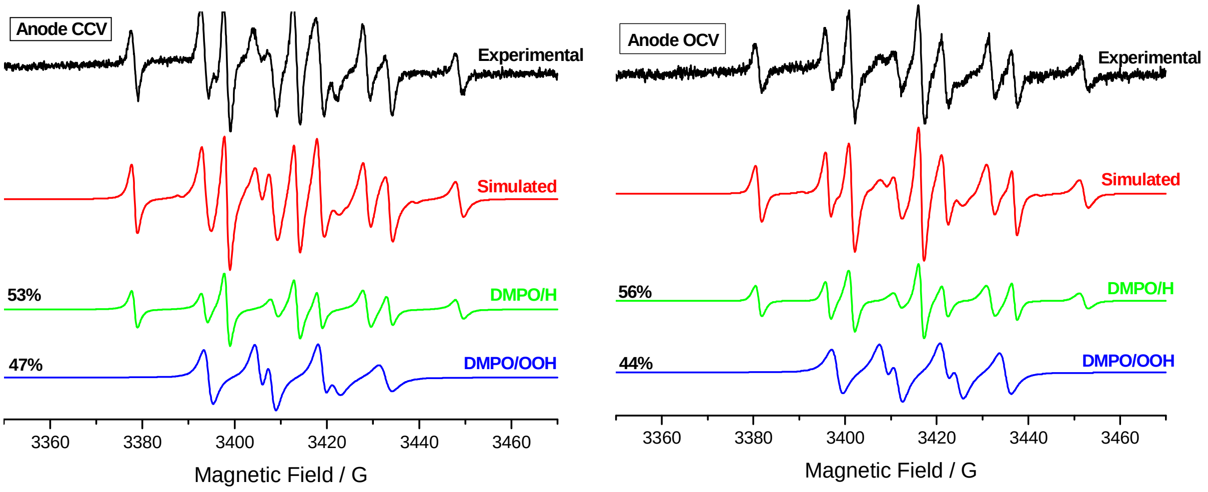

Figure 41. Experimental and simulated ESR spectra of adducts when the DMPO was added at the anode side before CCV operation (left) and OCV operation (right). The relative intensity of each adduct is shown on the left.

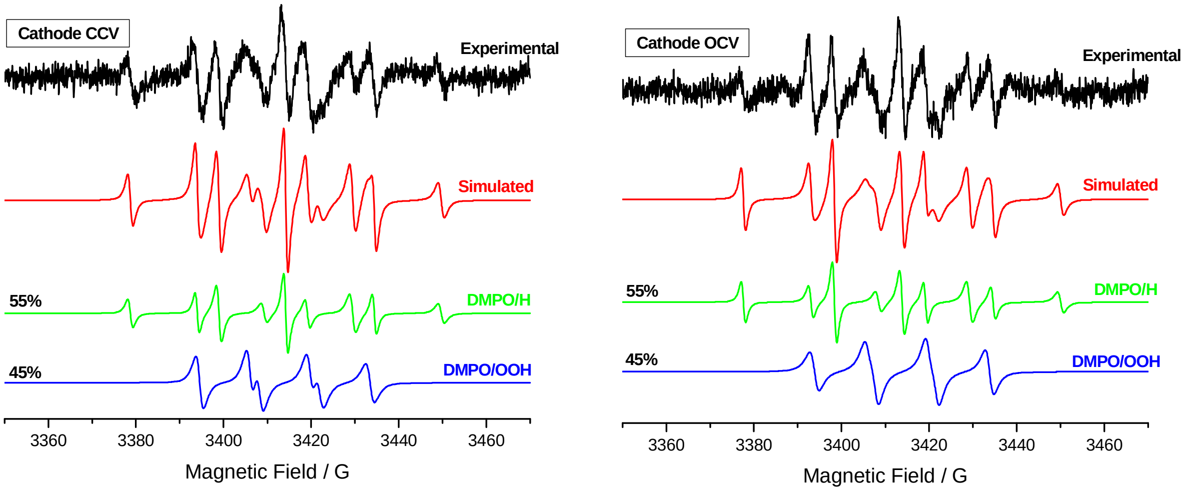

Figure 42. Experimental and simulated ESR spectra of adducts when the DMPO was added at the cathode side before CCV operation (left) and OCV operation (right). The relative intensity of each adduct is shown on the left.

Conclusions:

- DMPO/H and DMPO/OOH adducts were detected in all experiments (anode CCV and OCV, cathode CCV and OCV); no adducts of the hydroxyl radical, HO$^{\bullet}$, were detected.

  Crossover oxygen from the cathode to the anode is expected to react with hydrogen atoms generated at the anode catalyst and to form the detected DMPO/OOH adduct. Hydrogen atoms can also be formed on the cathode catalyst, leading to the DMPO/OOH adduct at the cathode.

- No carbon-centered radical (CCR) adducts were detected, suggesting that the 3M Membranes are more stable compared to Nafion™ membranes, where DMPO/CCR adducts were detected at the cathode, and at lower intensity also at the anode.
- The signals detected at the cathode and anode sides are similar, a result that may be explained by the high crossover through the thin membrane (thickness 25 µm). However, results suggest that oxygen crossover to the anode is lower than that of H_2 to the cathode, as the signals detected at the cathode side are weaker than those at the anode side.

- Experiments with thicker membranes have suggested that the membrane thickness is an important parameter, which determines the rate of gas crossover, and the generation of hydrogen atoms and oxygen radicals.

Using β-cyclodextrin (β-CD) Encapsulation to Detect "Very Early Events" in the Fragmentation Process of Perfluorinated Membranes.

Our study of membrane *dispersions* exposed to hydroxyl radicals has detected the presence of carbon-centered radical adducts, DMPO/CCR. Our previous studies have also demonstrated that using 2-methyl-2-nitrosopropane (MNP) as the spin trap allows the detection of both CCR and OCR (oxygen-centered radical) adducts.[25] In this and other studies we have detected "Early Events" in the fragmentation process, before the conversion of the radicals into stable species.

We have extended these studies by exposing Nafion™, Aquivion™ and the 3M membranes to hydroxyl radicals, using MNP as a spin trap. As described below, this work demonstrates that MNP as spin trap together with encapsulation in β-cyclodextrin (β-CD) allows the detection of "Very Early Events": fragments that are too short-lived to be detected in the absence of β-CD.

Figure 43 presents the results obtained for Nafion™ membrane in the *absence* of β-cyclodextrin (β-CD) and for the three membranes in the *presence* of β-CD. For all the three membranes (Nafion™, Aquivion™ and 3M) only one adduct was detected, with $a_N = 16.5$ G and $a_F = 11.1$ G (2F); the adduct was assigned to the MNP/OCF_2CF_2R adduct, suggesting the attack of hydroxyl radicals on the ether bonds of the membranes. The downward arrows in Figure 5 point to the signals from the MNP/OCF_2CF_2R adduct. The other signals are from di-*tert*-butyl nitroxide (DTBN).

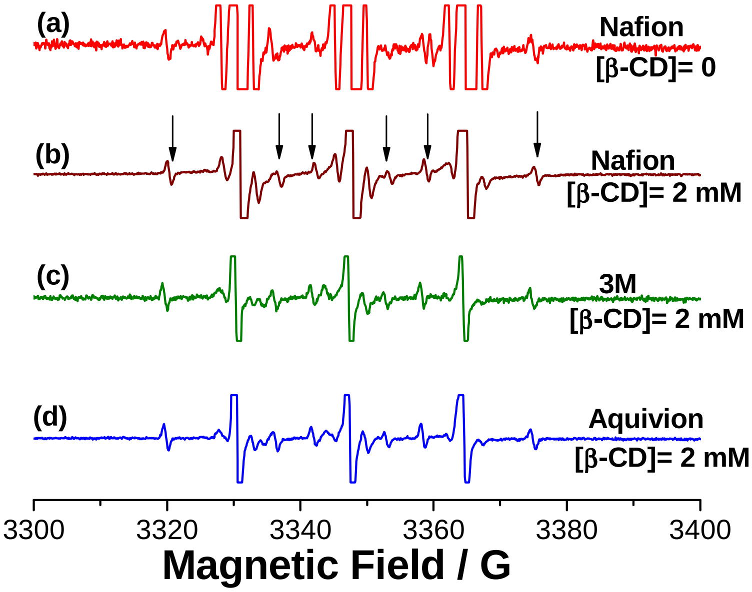

Figure 43. Experimental spectra of MNP/OCF2CF2R adducts generated in the absence (a) and in the presence of b-CD (b, c, d) for the indicated perfluorinated membranes (Nafion™ (a, b), 3M (c) and Aquivion™ (d)) in water solutions at 300 K and pH 7. Note that the signal in (a) was vertically enhanced compared to the other spectra. For the same vertical enhancement the height of the low field signal in (a) (red line) is lower compared to the corresponding signal in (b) by a factor of 4, within ±10 %. The same ratio was also detected for the 3M and Aquivion™ membranes.

No MNP/CCR adducts were detected even after four hours of UV irradiation. The relative intensity of the MNP adducts was very low in the absence of β-CD, see (a) above; however, the presence of β-CD led to a significant increase of the relative intensity of MNP adducts, as seen in Figure 43 (b), (c) and (d). The increase of the relative intensities of MNP adducts is probable due to the stabilization process of the oxygen-centered radicals (OCR) and their selective encapsulation in β-CD, especially in comparison with DTBN radicals, which are present in the “out of host” form (a_N = 17.1 G, compared to 16.6 G for the “in the host” form). The results can be explained by the initial generation of the OCR radicals with low stability and their rapid transformation into CCR radicals; *this process is interrupted by stabilization of the OCR radicals as they become encapsulated as adducts in β-CD.*[26]

2D Spectral-Spatial FTIR Imaging of Degraded Nafion™ Membranes.
Degraded Nafion™ MEAs were prepared in a multi-membrane cell described in section 6.3 Accelerated Durability Testing and in reference27. Before the FTIR measurements the membrane was immersed in deionized water and the catalyst layers were removed in an ultrasonic bath. Micro FTIR measurements were performed with the Spotlight 200

Micro ATR FTIR spectrometer. Line scans FTIR spectra were collected from the cathode side to the anode side, as indicated by the arrow in Figure 44.

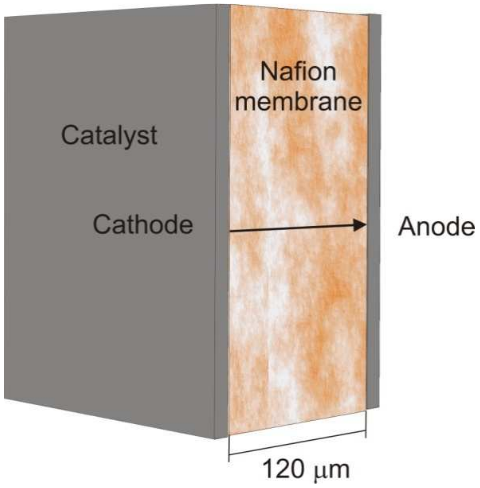

Figure 44. Schematic representation of the Nafion™ MEA. The data acquisition direction is indicated by the line scan arrow.

Figure 45 shows optical images of non-degraded and heavily degraded Nafion™ membranes after catalyst removal. As seen in Figure 7, the degradation process is not homogeneous.

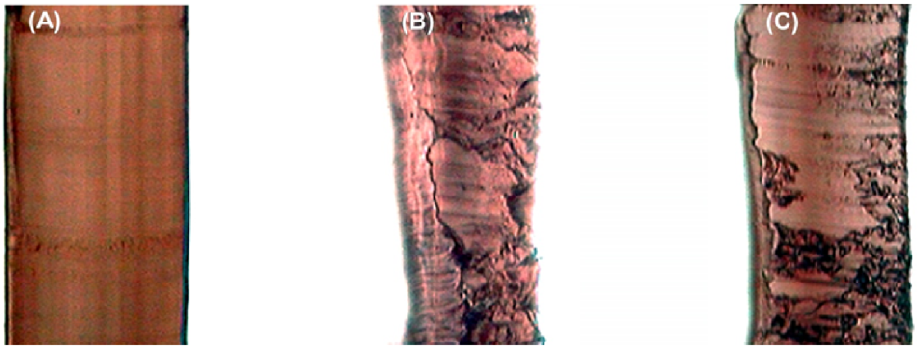

Figure 45. Optical images of cross-sections of non-degraded (A) and degraded (B and C) Nafion™ membranes. (A) and (B) are different sections of the same membrane after removal of the catalyst.

Figure 46 shows line scan spectra collected for non-degraded and degraded Nafion™ membranes in the 2000-750 cm^{-1} range. It is clearly visible that after degradation the bands intensities have changed. Bands at 1156, 1060, 982 and 969 cm^{-1} are losing intensity in the center of membrane, between 40 and 80 µm, and at the anode side. These bands are associated with vibrations of groups in the side chain, suggesting a *higher degradation rate of the side chain in the center of the membrane and at the anode side.*

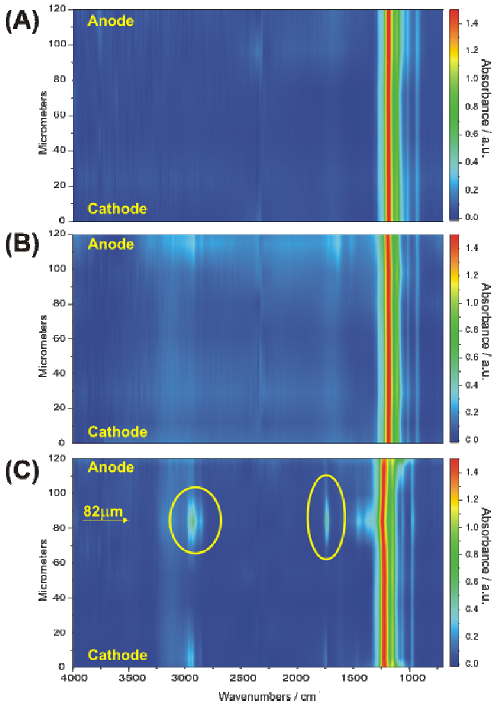

Figure 46. Line scan spectral maps of Nafion™ 115 membrane: non-degraded (A), and degraded during 52 h (B) and 180 h (C). Yellow ovals in (C) show the appearance of strong bands at 82 □m as a result of degradation.

Non-degraded Degraded 52 h Degraded 180 h

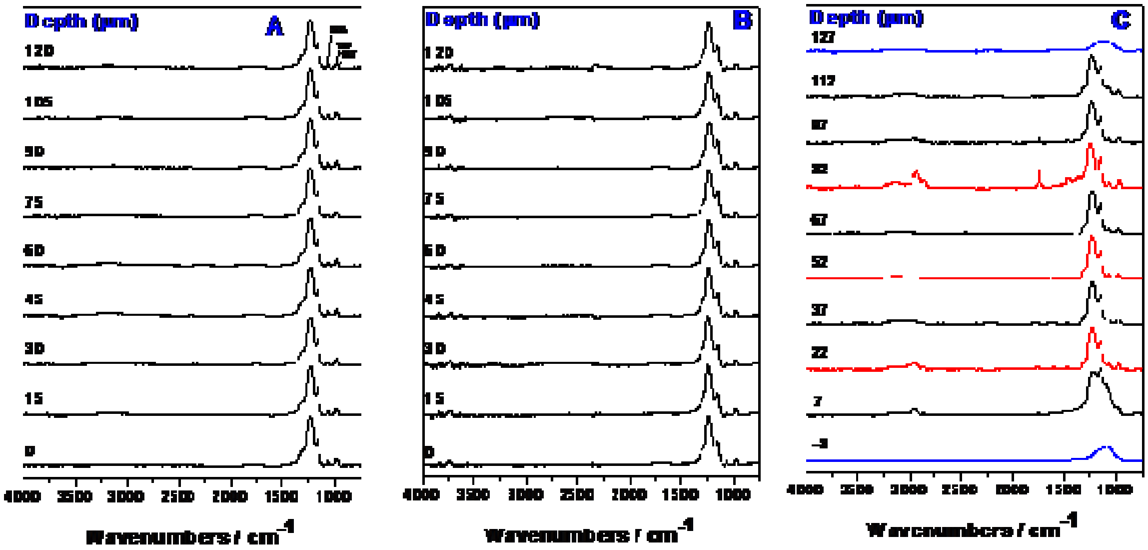

Figure 47. In-depth profiling: FTIR spectra of Nafion™ membranes as a function of depth: nondegraded membrane (A), degraded for 52h (B), and degraded for 180h (C) (in blue are spectra of sample holder, in red are spectra presented on the next slide and compared with spectrum of nondegraded membrane). All spectra

were recorded in reflectance mode with Perkin-Elmer Spotlight 200 microscope system.

From the spectral maps shown in Figure 46 it is possible to track the spatial variation of FTIR spectra in the interval cathode-to-anode, as shown in Figure 47. A blow-up of the FTIR spectra for the degraded membrane during 180 h at several distances from the cathode, and the comparison with the non-degraded membrane is shown in Figure 48.

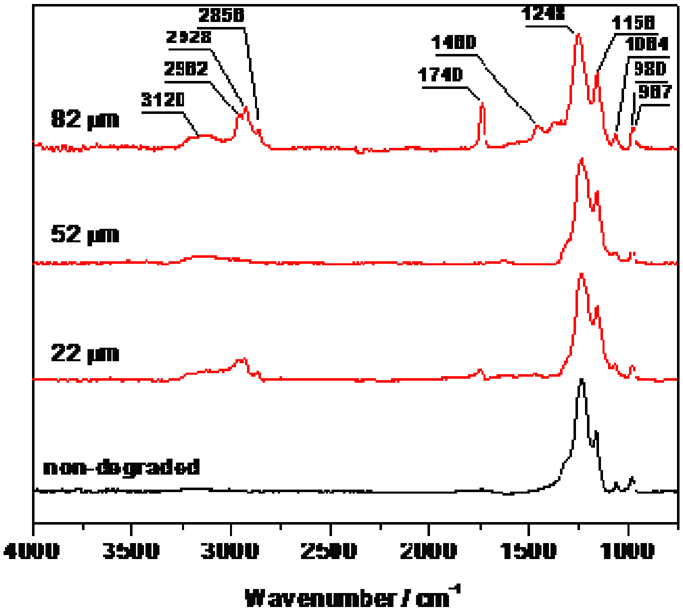

Figure 48. FTIR spectra of Nafion™ membranes: degraded for 180h at various depths from the cathode side (in red), and non-degraded (in black).

Assignment of bands shown in Figure 10 for depth=82 µm
3120 cm^{-1} C-H
2928 cm $^{-1}$ ν_{as}(C-H)
2962 cm $^{-1}$ ν_{as}(C-H)
2856 cm $^{-1}$ ν_{s}(C-H)
1740 cm $^{-1}$ ν_{s}(C=O)
1460 cm^{-1} sulfonic anhydrate
1248 cm $^{-1}$ $\nu_{s}(CF_2)$
1156 cm $^{-1}$ $\nu_{as}(CF_2)$
1064 cm $^{-1}$ $\nu_{s}(SO_3^-)$
980 cm $^{-1}$ ν_{s}(C-F) in CF_3
967 cm $^{-1}$ ν(C-S)

The detection of the C-H FTIR bands at 3120 cm^{-1}, 2928 cm $^{-1}$, 2962 cm $^{-1}$ and 2856 cm $^{-1}$ suggests attack of hydrogen atoms on the membrane, a process that is expected to start by abstraction of F atoms connected to a tertiary membrane carbon.

In summary: The micro FTIR technique can provide valuable information on the *spatial* dependence of the membrane degradation process. As seen from the line scans of Nafion™ MEAs, this technique allows the detection of the distribution of functional groups over a very small sampling area. As such, it can visualize the surface of the membrane and describe the degradation process as a function of depth. We call this approach 2D spectral-spatial FTIR imaging. [28]

Conclusions

Direct ESR and spin trapping ESR methods have detected unstable intermediates generated during in situ FC experiments; allowed the comparison of membranes stability to hydroxyl radicals; and suggested that hydrogen atoms are present in an operating FC and can contribute to membrane fragmentation.

2D spectral-spatial FTIR imaging is posed as a new method for the determination of the membrane degradation process as a function of depth. Experiments with membranes as a function of membrane thickness are planned, and are expected to provide guidance about the limiting membrane thickness that can be used in a FC, before appearance of defects and pinholes.

5.5 Morphological Studies- Carried out with the Colorado School of Mines

In order to obtain in-depth morphological information of PFSA membranes, small angle X-ray scattering should be one of the most important characterization techniques. For PFSA membranes, generally we get SAXS images and patterns like the ones shown on Figure 49 and Figure 50**,** due to the inhomogeneous of electron density between different structure levels e.g. hydrophilic ionomer clusters and hydrophobic crystalline matrix, a outer ring corresponds to ionomer peak, a inner ring is the so-called crystalline matrix knee, and the inner most light spot is the ultra-small angle x-ray scattering upturn, which is attribute to some long-range order of the polymer.

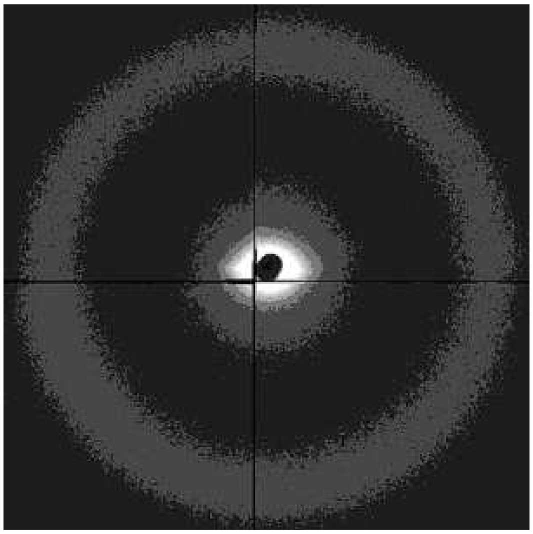

Figure 49. SAXS image of one of 3M PFSA films

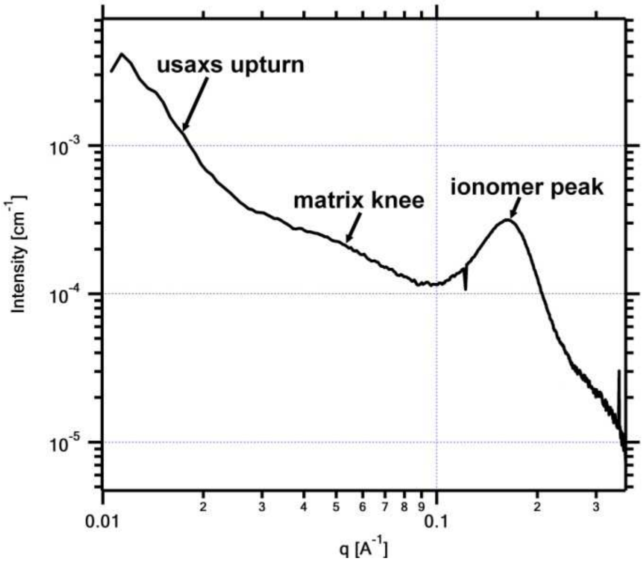

Figure 50. Typical SAXS pattern of 3M PFSA membranes

Water Sorption Study

We studied water uptake dynamically, and believe we captured the first fast water equilibrium values after several 10s of minutes, these are approximately half those reported for full equilibrium to be established, days. From the lambda against RH plot, Figure 51, we can see the increase as water is taken up is linear with RH; up to around 75% RH. The SAXS patterns shows the ionomer peak shift to lower q and higher intensity as relative humidity increases, indicating an increase of domain sizes and abundances by redistribution and recombination of ionomer clusters and formation of aggregates. We calculated the D-spacing which equals 2π/q, and from Figure 52, we see D-spacing increase linearly with amount of water taking up to lambda = 5, i.e, lambda, suggest that the scattering objects form a lamella structure in this hydration level. However above lambda = 5 we observe a shift point indicating a structural change of the membrane to possibly randomly distributed rod-like structures.

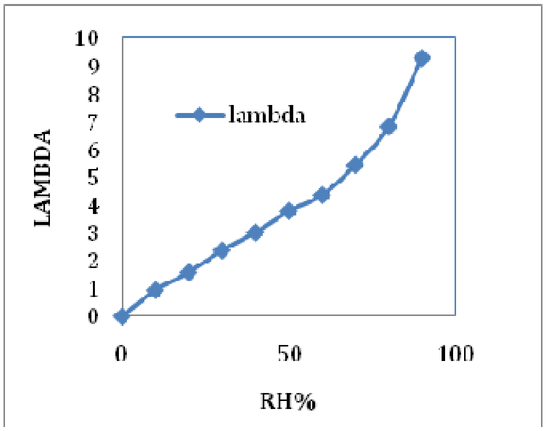

Figure 51 Calculated water contain against different RH of 3M825EW PFSA membrane.

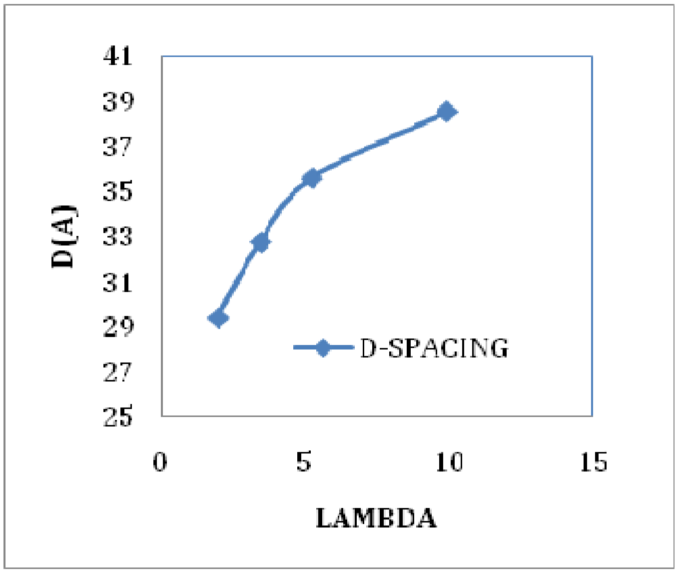

Figure 52. Calculated D-spacing at different water sorption of 3M825EW PFSA membrane.

Equivalent Weight Study

The SAXS patterns were analyzed using the unified model that allows a radius of gyration, R_g, to be calculated, Figure 53. In these phase separated materials typically two domains where identified, one corresponding to the hydrophobic backbone of the polymer and one to the hydrophilic ion conducting part of the material. As equivalent weight increases, sizes of second structural level, which is the crystalline structure formed by hydrophobic backbones, increase approximately linearly. This is attributed to that polymer of larger equivalent weight has higher portion of hydrophobic backbone, hence form larger crystalline structure. For the first level, i.e. the ionomer clusters, their sizes also increase with increasing of equivalent weight. This observation agrees with previous studies.

Annealing Study

We annealed the 825 EW 3M ionomer cast dispersion at different temperatures, we can see that generally sizes of both crystalline region and ionomer cluster region increases as anneal temperature increases from 180℃ to 190℃ , due to increase of energy make chains have lager mobility, especially after temperature exceeding glass transition point. However, membranes annealed at 200℃ seems to have a less increase or even have a decrease of size for ionomer level at certain relative humidities. This shows a optimum annealing temperature should exist for these membranes, further increase of annealing temperature will form larger crystalline region therefore make chains stiffer and less mobile, therefore form smaller hydrophilic ionomer clusters during the water taking process.

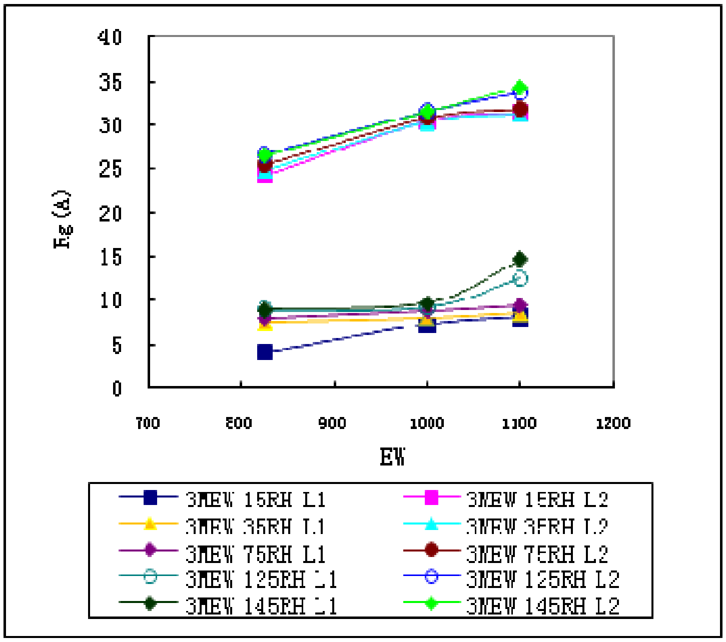

Figure 53. Unified fit results of 3M PFSA equivalent weight series

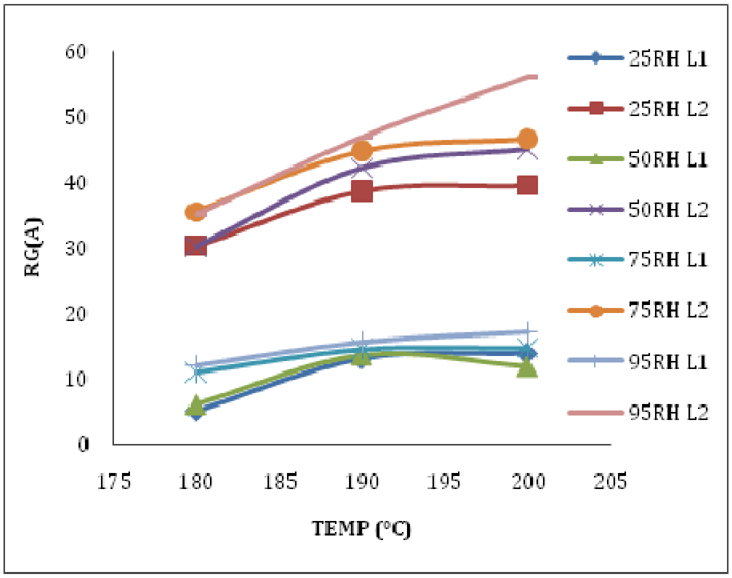

Figure 54. Unified fit results of 3M825EW PFSA membrane ex-situ annealing at different temperatures

In Figure 55 we show a complete cycle of the dynamic changes observed by dynamic SAXS from annealing a film under dry gasses and its first wet up to 100% RH. For this full dynamic experiment, we can see the morphological change during the annealing, cooling down, and water taking process: the first five minutes of annealing shows the similar result as other the dynamic annealing experiments with this material. During the cooling process, the crystalline region begins to form, which is for the well-know reason that more crystalline region will form with a slower cooling rate, and stay longer at its glass transition temperature. While if the sample is cooled very fast, most of the structure will remain amorphous, result in less crystalline after annealing. For this experiment, we see general results of higher crystallinity after annealing. The humidification immediately after cooling down shows continuing increase of crystalline structure and the development of ionomer peak.

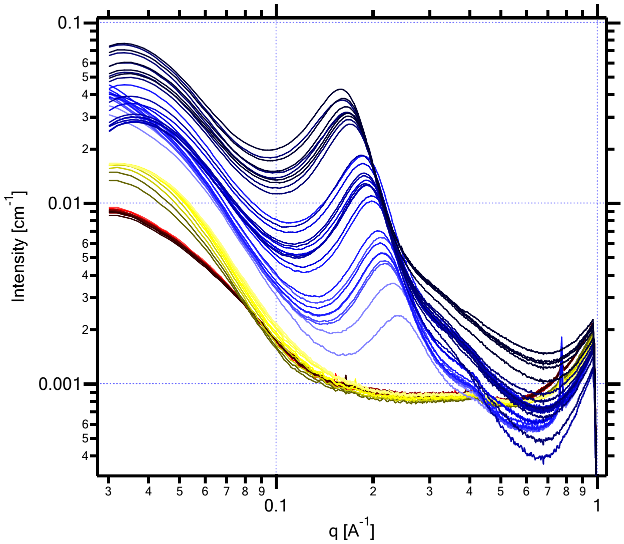

Figure 55. SAXS patterns of full dynamic experiment on 3M825EW PFSA membranes. Light red to dark red: anneal at 200C for 5 min. Dark yellow to light yellow: cooled from 200C to 80C. Light blue to dark blue humidified from 25%RH to 95%RH.

Water Equilibrating Study

From the SAXS patterns, we see a huge shift of q to the lower values after 33h and an increase of intensity between as cast film and water equilibrated films; this trend continues as the membrane was put in water for longer time and it cannot be assumed that equilibrium has necessarily been reached after 26 days, i.e. the film is constantly changing.

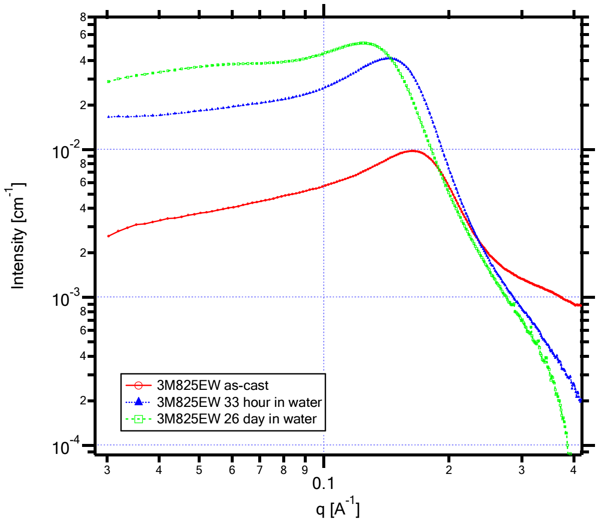

Figure 56. SAXS patterns of long-term water equilibrating experiment on 3M PFSA membranes.

Solvent Study

The solvent used to form the dispersion of the 3M ionomer has big effect on the properties of the as cast membrane, Figure 57. We can see that membranes cast from H_2O completely lost their crystalline region structure, while membranes casted from MeOH still maintain their crystalline structure, and have higher degree of phase separation of hydrophilic and hydrophobic domains. Also we observed that structures of membranes casted from MeOH depends more on relative humidity than those casted from H_2O. In other words, they intake more water during the humidification process.

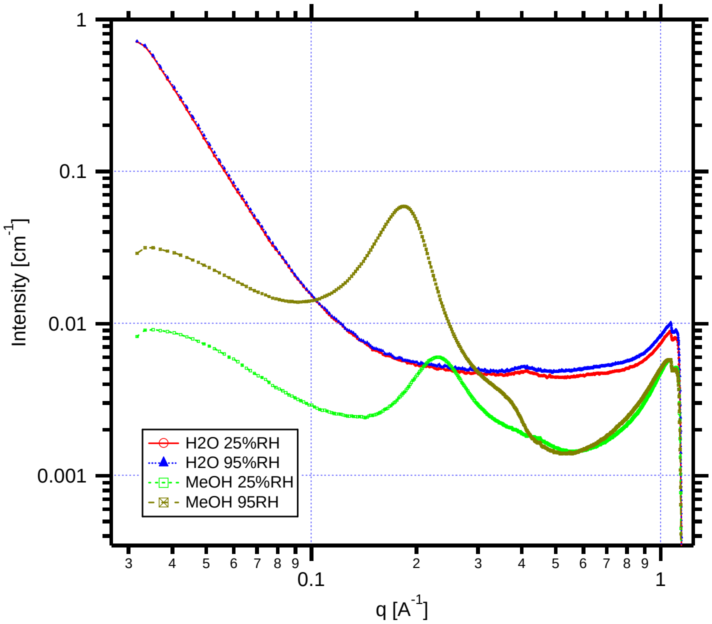

Figure 57. SAXS pattern of 3M PFSA membrane casted from different solvents.

5.4 Chemical Degradation Studies of Membranes

These mechanistic studies focused on understanding the degradation pathways in PEMs. They also looked at the effect of different mitigating additives, combinations thereof, their best use in the MEA, their migration, and their potential impact on performance.

In addition to the work carried out on model compounds stability (Appendix 4 - Chemical Degradation Studies of Model – Carried out in Collaboration with Case Western Reserve University), a series of Fenton experiments were carried out on neat polymer membranes, the bare nanofiber supports and membranes of polymers cast into the supports. In these experiments membranes were aged at 80^{o}C in a weak peroxide solution with Fe additive. Weight changes of the polymer were monitored with each change of the Fenton solution, and the solutions were tested for anion such as fluoride and sulfate by ion chromatography. Neat support structures with their high porosity and high surface area did not fare well in these tests, losing much of their mechanical integrity in the first solution and showing high concentrations of degradation products. For one of the support structures, high concentrations of sulfate where observed. a supported PEM prepared from this support was tested, it showed much higher stability and reduced sulfate concentrations. It is important to note that his same S-PEM tested in our most aggressive fuel cell membrane stability test showed no sulfate concentrations above the background despite high F^- concentrations.

We also applied this same Fenton's test to our new PFIA PEM as well as Nafion and the 3M PFSAs. In addition to doing ion chromotagraphy on these Fenton's solutions we also did LC-MS and NMR to determine the composition of any polymer fragments. For PFIA, as was previously observed for Nafion ionomer and the 3M Ionomer, the fragment most observed is the side chain.[29,30] It is important to note that there was no evidence that the imide acid bond was a weak link, quite the contrary. The observed mass spectrometer spectra for the Fenton test degraded PFIA polymer along with the NMR spectra of the same solution can be seen in Figure 58 and Figure 59. These results are again, consistent with PFSA polymers where the primary decomposition is the unzipping of the backbone.

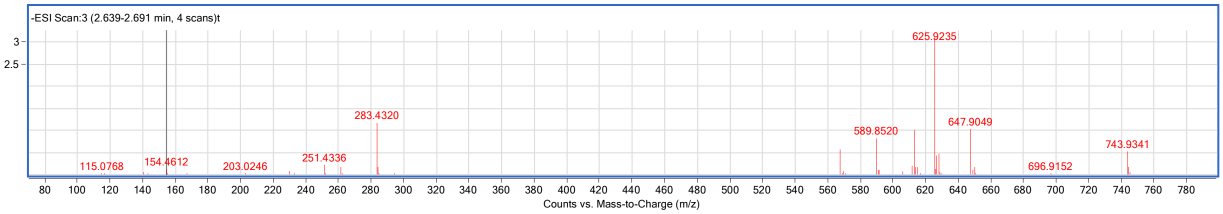

Figure 58. LC/MS spectra of the predominate PFIA polymer fragment from the Fenton solution.

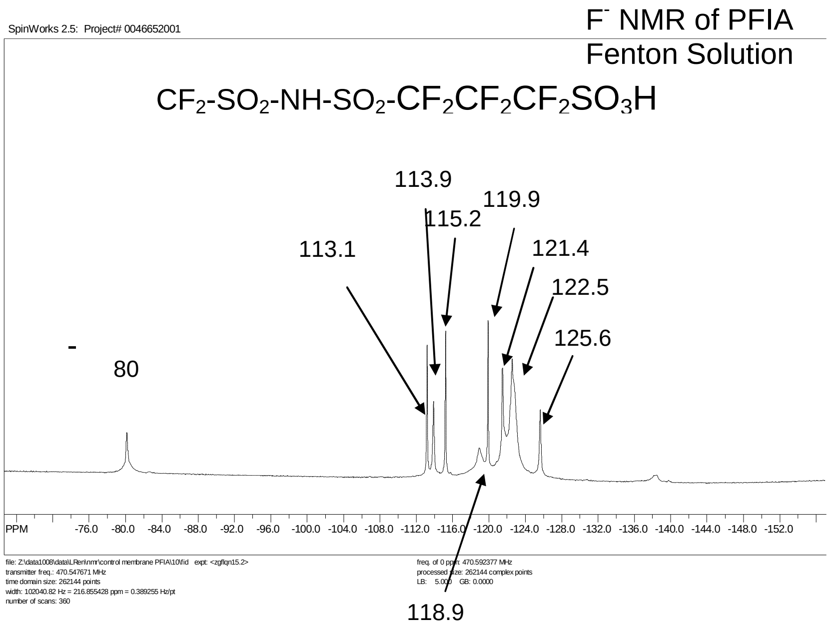

Figure 59. F^- NMR spectra of PFIA Fenton solution showing the side chain fragment.

5.6 Chemical Degradation Studies of Model Compounds

Aromatic, fluorinated and partially fluorinated model compounds (AMCs), representative of hydrocarbon fuel cell membranes were studied under accelerated fuel cell conditions to understand the degradation patterns. Liquid Chromatography-Mass Spectrometry (LC-MS) was used as the major analytical technique to identify degradation fragments. The degradation products observed under the conditions used were mostly due to hydroxylation of the aromatic ring.

6. Fuel Cell Testing

6.1 MEA Development

In the beginning of this project we developed an MEA construction for membrane screening under relevant conditions. We did parametric testing to understand how reproducible the results were with the test script using different cells, test stations, compression levels, etc. We did a number of studies to understand the role of overall cell resistance in our measurement of the membrane properties, and how well PEM conductivity results correlated with fuel cell performance. This was necessary to make sure our gains in PEM resistance were not limited or masked by our electrode. Further, to do this we would make a number of MEAs with different thicknesses of PEM. Plotting HFR vs. PEM thickness at each temperature, by the transmission line method of analysis fitting the linear portion of the plot, the slope would be proportional to the PEM resistance and the intercept would be the electrode resistance (Figure 60). We had excellent agreement between our conductivity measurement and PEM resistance as determined by the TLM analysis(Figure 28). Further, the values for electrode resistance matched those determined using impedance, dilute hydrogen pump and other methods. In the end, we and down selected an electrode and automotive gas diffusion layer for our development work.

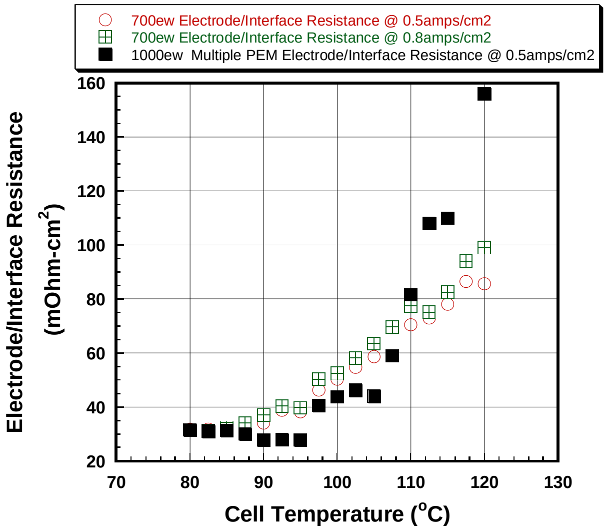

Figure 60. Determination of electrode contribution to cell resistance via TLM.

Later in the contract it was recognized that our ability to measure gains in PEM performance might be hindered by lack of commensurate gains in the electrodes. Specific studies were carried out over a wide range of electrode ionomer EWs, new ionomers, I/C ratios, catalyst types, catalyst structures, additives, and processes. The same GDL was use for this work.

One clear performance gain we did see was with a particular catalyst type. To a first approximation performance is proportional to the geometric surface area of a catalyst over a variety of catalysts. Poor electrode construction will bring the performance lower than the line of proportionality. We found that by applying proprietary treatments to the catalyst we could greatly increase that catalysts activity. A plot of performance vs. geometric surface area in Figure 61 shows the gains realized with this catalyst. Other catalysts treated in this way would either not change in performance or most likely have a reduction in performance. The activation process was done in-situ but we did develop methods that could potentially do the activation ex-situ but at the time of our down select we had not reduced this to practice. This catalyst was chosen for our final MEA cathode for its high activity and stability.

In addition, Figure 61 highlights the differences in performance with PEM types. The new catalyst structure tested with the lower equivalent weight PEM did not perform well highlighting the need to match electrode to PEM for optimal performance. The addition of low EW ionomers in the electrode ink did not surprisingly change the performance at the dry condition for this high performing PEM as seen in Figure 62. In this figure three different equivalent weights with two different ionomer types show only small changes in performance. Unfortunately, electrodes are a multidimensional issue where I/C, ionomer form, dispersion solvent, support type, mixing process and drying process can all be dependent variables.

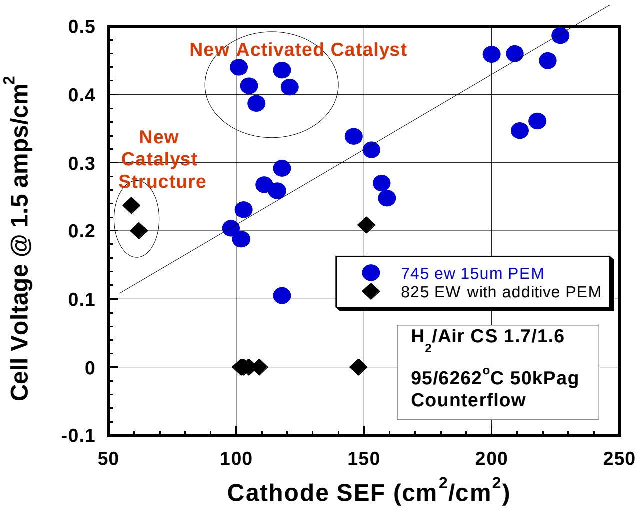

Figure 61. Performance as a function of catalyst geometric surface area under dry polarization scans.

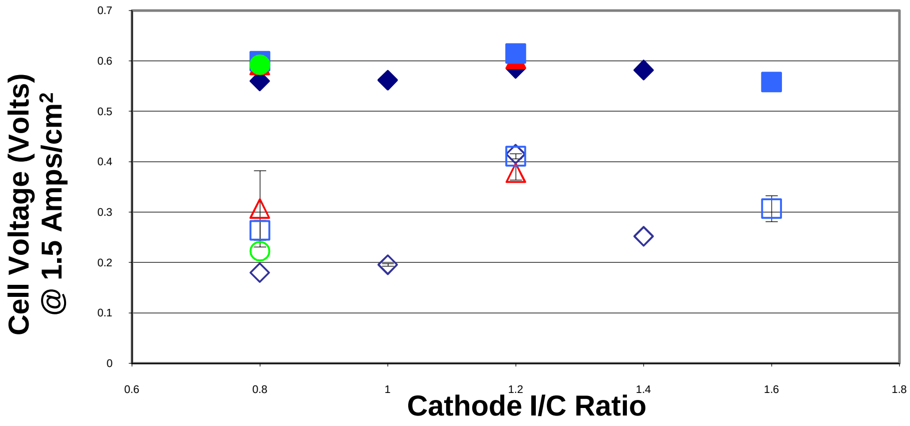

Figure 62. Performance at 1.5 A/cm2 under wet (closed symbols) and dry (open symbols) conditions vs. I/C ratio for ionomers ranging from 745 EW to 1000 EW.

Accomplishments of the our efforts in MEA development –

- An MEA construction was selected for the final membrane testing in this program.
- Development of an activated non-alloy stable catalyst that led to the same performance at nearly half the cathode loading.
- Development of a process method that can lead to a 10-15% gain in geometric surface area for the same loading having a commensurate gain in performance.
- Successful implementation of a peroxide mitigating additive to the anode catalyst layer with little or no loss in performance for the down select.
- Reduction of the anode catalyst loading by a factor of four with no loss in performance.

6.2 Fuel Cell Performance Testing

A number of different test protocols were used for testing fuel cell performance. One centered on measuring performance and HFR as a function of temperature for a fixed dewpoint at two different currents (0.5 and 0.8 Amps/cm^2). In this script, testing was carried out under hydrogen/air flows with a constant stoichiometry of 2/2 under ambient pressure outlets. The inlet dewpoint was held at 80℃ which would result in an outlet dewpoint of approximately 85℃ over all the conditions tested. The cell temperature was varied from 80° to 120℃ with each condition being held for 25 minutes where the values of the last five minutes are reported at each current. The resultant outlet RH at each temperature is shown in Figure 63. One of the advantages of this test is that essentially only one dewpoint needs to be calibrated.

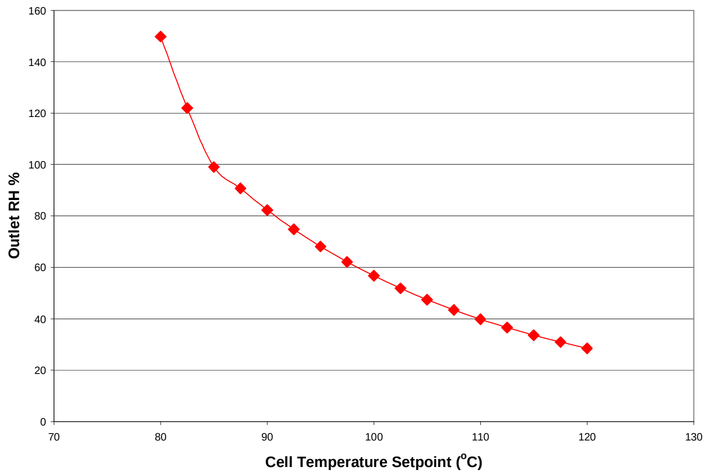

Figure 63. Outlet RH vs. cell temperature for MEA screening test.

Cell testing diagnostics used and/or developed in this contract include protocols for electrochemical surface area measurements, hydrogen crossover as a function of anode over pressure, oxygen permeability measurements, fluoride release rates, full spectrum impedance, electrode resistance, etc.

Performance testing began with examining variables such as EW of the 3M PFSA and PEM thickness. The effect EW can be seen in Figure 64 and Figure 65. Thinner PEMs also can have a large effect on HFR and MEA performance but there are diminishing returns with lower equivalent weight. That gain in performance is greater than that shown with a simple IR correction. This is consistent with the concept of better water management helping not just the resistivity but also the ORR.

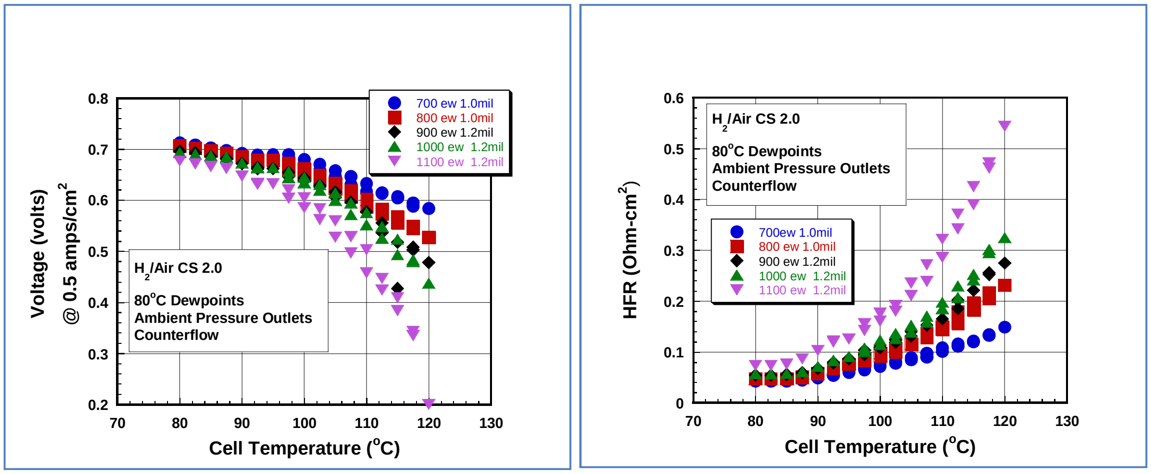

Figure 64. Fuel cell performance and HFR as a function of PEM equivalent weight.

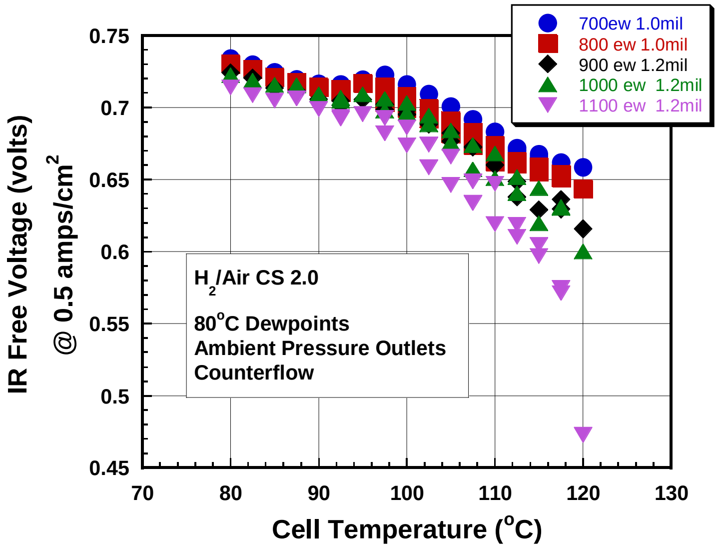

Figure 65. IR-Free performance as a function of PEM equivalent weight.

Many new ionomers, PEM constructs (blends and structures), peroxide mitigating additives, and process variables were all tested for performance. At times, contaminants from new synthetic processes masked the true performance of the new PEMs, so studies had to be done to understand and eliminate those in order to gain the true measure of the PEM. The ionomer that was selected for our final MEA testing was PFIA (Figure 1) data generated for other new PEMs provided important insights and understanding as well. Some of those observations are:

1. PFSAs with pendant benzene rings at the end of the side chain (ortho bis acid, meta bis acid, etc.) and hydrocarbon PEMs like SPES were much more prone to early, if not immediate edge failure in fuel cell tests, due to their mechanical brittleness. Tensile measurements were an excellent predictor of this tendency. The use of a subgasket could mitigate this to various degrees.
2. More often than not the performance was related to the effective equivalent weight, which would be the weighted average of a blend of different EWs or different ionomers.

A number of studies looked at new 3M proprietary additives and their effect on performance. In almost all studies performance was affected at only the driest conditions with increasing additive level, typically at additive levels higher than what was necessary for sufficient durability, and where the fluoride release rate had begun to plateau (e.g. Figure 75).

A great deal of work was put into optimizing ionomer filling of the support in coating. In most cases the performance and HFR matches that of the weighted average of the effective equivalent weight.

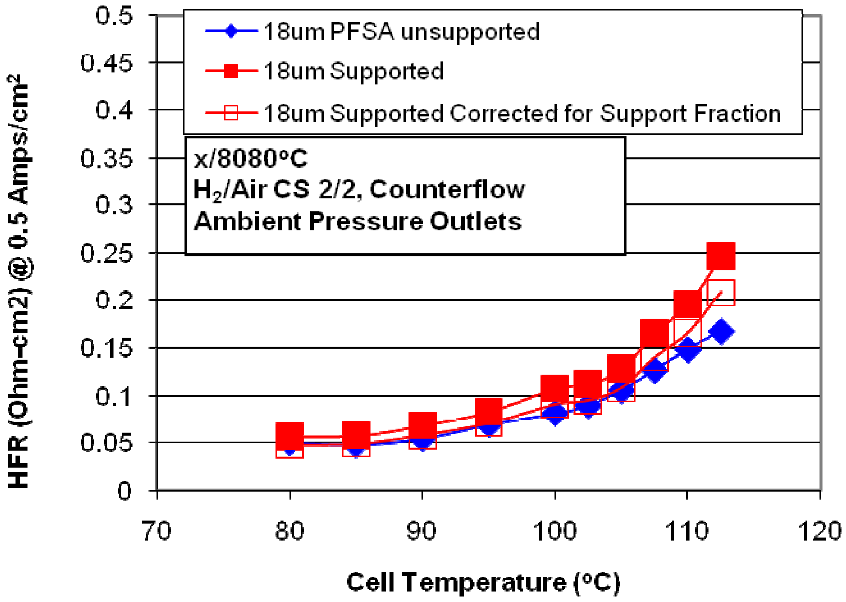

Figure 66. Comparison of HFR of supported, unsupported and theoretical based on volume fraction.

Performance for the PFIA 625 EW polymer both, as is and in supported its form, is shown in Figure 67. The lower performance of the unsupported PEM in this example is related to a contamination issue due to an impurity that was not present in subsequent preparations. The HFR values are consistent and not affected by the contamination issue.

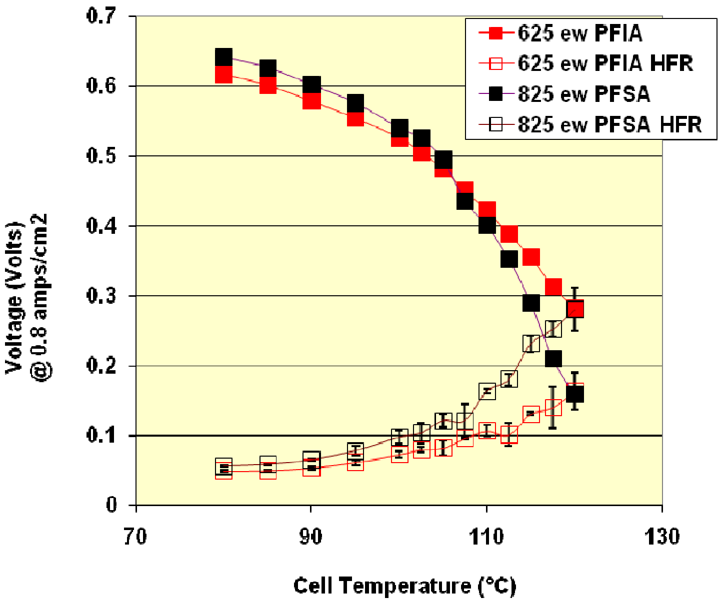

Figure 67. 825 PFSA and 625 PFIA fuel cell results (H^2/Air, CS 2/2, 80°C dewpoint inlets, ambient pressure outlets, 20um PEM thickness)

6.3 Accelerated Durability Testing

One approach to understanding the degradation process was the use of multiple PEMs to look at additive level, test conditions, where and how the degradation occurs, how additives move, etc. Much of this work is summarized in reference 27. Some of the conclusions of this work are that additives can change their distribution in the MEA, degradation is associated with the highest concentration of platinum in the MEA and is manifest as highly localized degradation resulting in a mechanically weakened layer consistent with a Swiss cheese type morphology. We saw no indication of change in conductivity, EW, IR spectra, or NMR spectra of the degraded polymer. This is consistent with localized unzipping of whole polymer chains that resulted in a thinning of the PEM from the inside out under OCV H_2/O_2 testing. The Pt band location was dependent on the fuel and oxidant partial pressures and corresponded to the area of maximum degradation as measured by tensile properties.

RH cycle testing

Based on the test recommended by the DOE, 3M built a RH cycle station that could run this mechanical fatigue protocol.[2] Development of the RH cycle test was more difficult than expected, since there were many minor details that strongly affect results. Many iterations and changes to the RH cycle equipment were attempted over the first two years of the contract until the final state was selected in the fall of 2009. Since then, over 60 samples have been run with consistent results.

A schematic of the RH cycle equipment built at 3M in its final working state is shown in Figure 68. 3M utilized two such set ups to run 4 cells constantly.

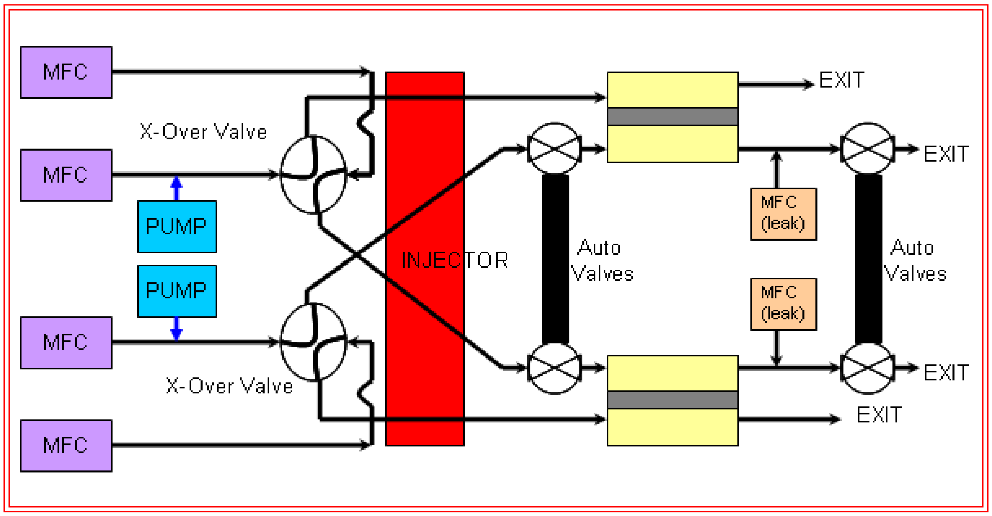

Figure 68. Schematic of the RH cycle station developed at 3M to run the mechanical testing cycle defined in Table B4 by the DOE.

Critical knowledge learned during development of this test method is given below:

1. The fuel cell flow field channels have a significant effect on the drying time of the MEA. It is necessary to dry the MEA as fast as possible therefore a wide channel straight flow works the best. The FCT (Fuel Cell Technologies) standard quad serpentine 40 mil wide channel flow field typically used in 50cm2 cells did not work well leading to false positives
2. It is necessary to make the exit gas during the dry cycle reach 20%RH or less. If it does not dip below 20%RH within the cell during the dry cycle the membrane does not change enough dimensionally to cause fatigue. We measured the exit RH using a humidity sensor and then optimized our heating elements to get the exit gas below 20%RH. It is essential to measure the exit gas RH to verify this. If the exit RH is not controlled to less than 20%, the MEA will last much longer than expected and therefore many membranes would pass the test when they otherwise should not.
3. For our test stand we wanted to automate the leak measurement so the stand did not require an operate to manually measure the leak of each cell each day. To accomplish this we used a small 50sccm mass flow controller and closed off one side of the cell and measured the leak rate. During development of this automation we found it necessary to physically close off each side of the cell with an automated valve instead of using a check valve to stop backward flow. It was found the check valves would fail occasionally causing errors in our leak measurement.

We found that MEA construction has a significant effect on the lifetime in the RH cycle test. MEAs that are bonded prior to the test last much longer than MEAs where the components are laid in individually into the cell without bonding. Nearly all bonded MEAs will pass the test. Presumably by bonding it provides added strength to the PEM. A typical sample run the 3M RH cycle equipment would show leak data over time as depicted in Figure 69. The lifetime target is 20,000 cycles.

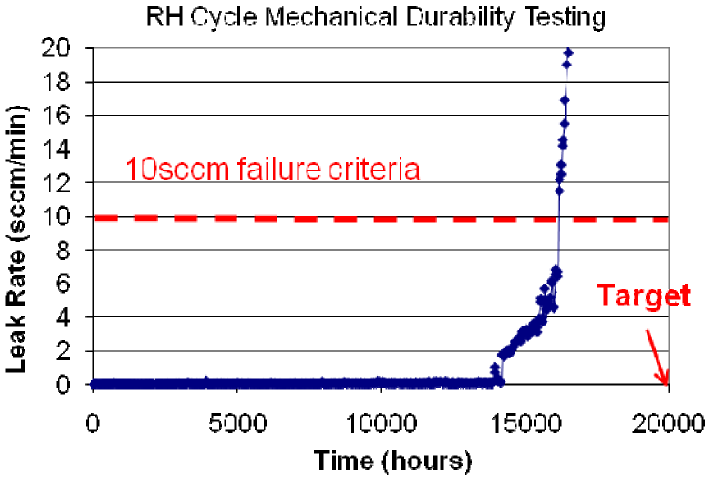

Figure 69. Typical data set for samples running the 3M modified RH cycle test to allow automated leak measurement every 12 hours.

After the RH cycle test stand was optimized and protocol setup, several sets of data were produced including a comparison of PEM process conditions of the membrane. It is known the membrane process conditions have an effect on mechanical strength and Figure 70 confirms this result, comparing two different process conditions.

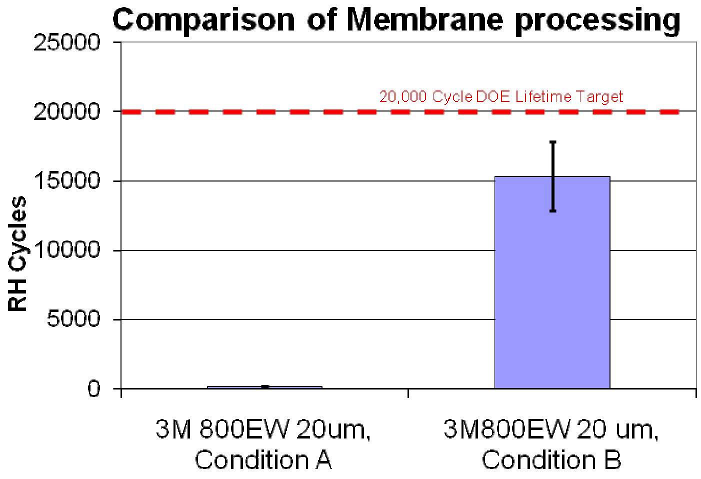

Figure 70. Comparison of membrane processing conditions in the RH cycle test.

Supported membranes provide a significant improvement in this test. Comparing the supported membranes in Figure 71, several different support types were able to pass the 20,000 cycle target. Note that in the interest of time, once the sample reaches 20,000 cycles it was removed regardless of whether it had failed or not. Hence many samples did not fail at 20,000 and could have kept running.

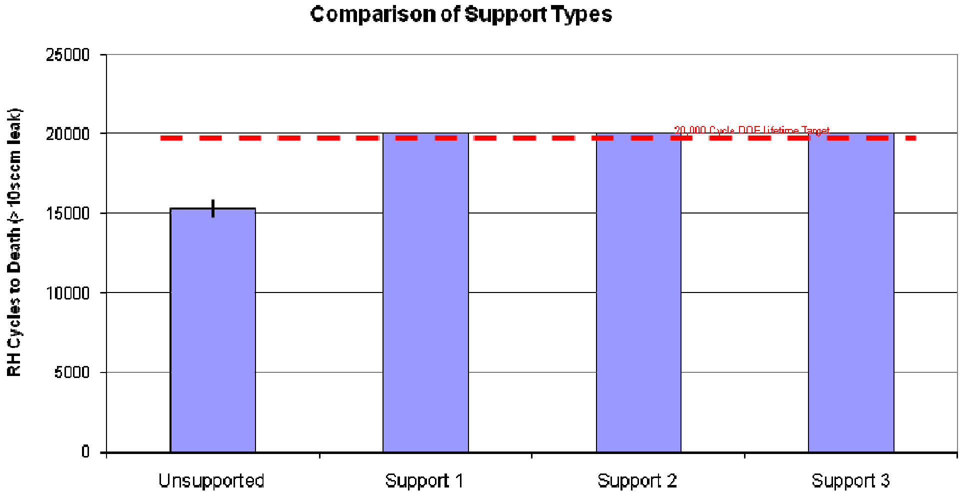

Figure 71. Various support types compared to no support show ability to reach the target # of cycles in the mechanical RH cycle test. Samples reaching 20,000 cycles were removed but had not failed. At least two samples were run for each of these sample sets.

The PFIA membrane was evaluated in the RH cycle test both with and without support. Figure 72 demonstrates the need for support in lower EW membranes to compensate for their lower dimensional stability. It also shows the down selected PFIA ionomer with the down selected support material meets the DOE target for the mechanical cycle test.

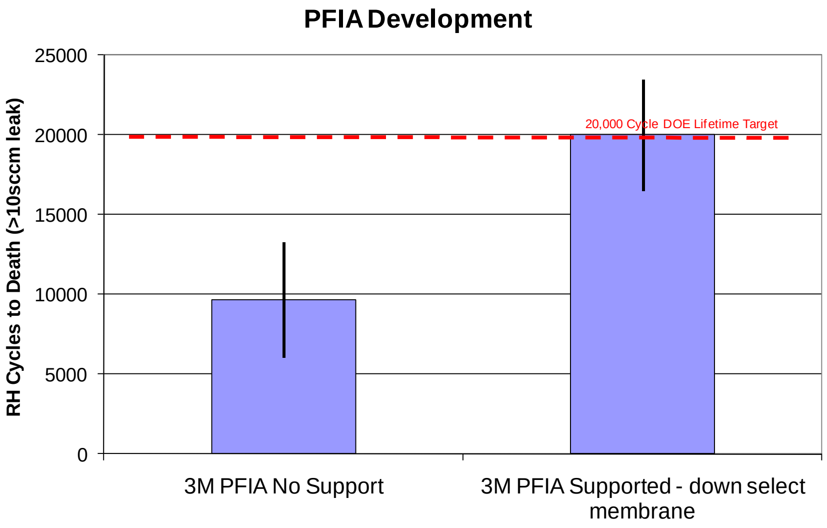

Figure 72. PFIA with and without in the RH cycle test.

OCV Testing

During the course of the contract over 100 samples were tested for OCV lifetime. The samples were run according the DOE test from Table B3 with a target lifetime of 500.

The Chemical Durability test procedure described in Reference 2 was followed closely for the tests completed at 3M, however impedance monitoring was not available for some of the testing. The samples failed when they reached 80% of initial OCV or when it was imminently approaching. For example, samples would often remain fairly steady in OCV in the test until a point when the OCV would degrade very quickly and the sample was removed as failure was very close, usually near to 800mV.

Many sets of experiments were run in this chemical OCV test, largely encompassed by the list below

1. New ionomers.
2. Membranes made from blending polymers with 3M ionomer for improved dimensional stability.
3. New additives or combinations of stabilizing additives.
4. Membranes where the location of stabilizing additive within the MEA was varied.
5. Membranes that were processed at various conditions.
6. New 3M supported membrane developments.

Chemical OCV testing was also completed on PFIA based membranes and the final DOE 7 down selected MEA. Some PFIA materials remain under test at the time of the writing of this report. PFIA made materials surpassed the 500 hour goal in several instances and has event shown to be similar in life to standard PFSA membranes in this test (Figure 73).

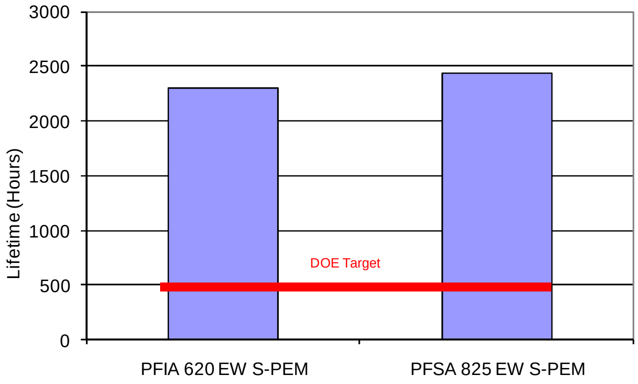

Figure 73. Lifetime DOE OCV test comparing PFIA supported membranes to PFSA supported membranes.

In early OCV testing of PFIA samples it was observed that there was a marked drop in OCV that was not related to any increase in measured crossover values. Typically, a PFSA-based PEM with such a low OCV would have an increased crossover value and would not plateau in voltage but drop quickly. An improvement of PFIA processing resolved this, as shown in Figure 74. This was most likely due to an impurity that impacted the cathode catalyst ORR.

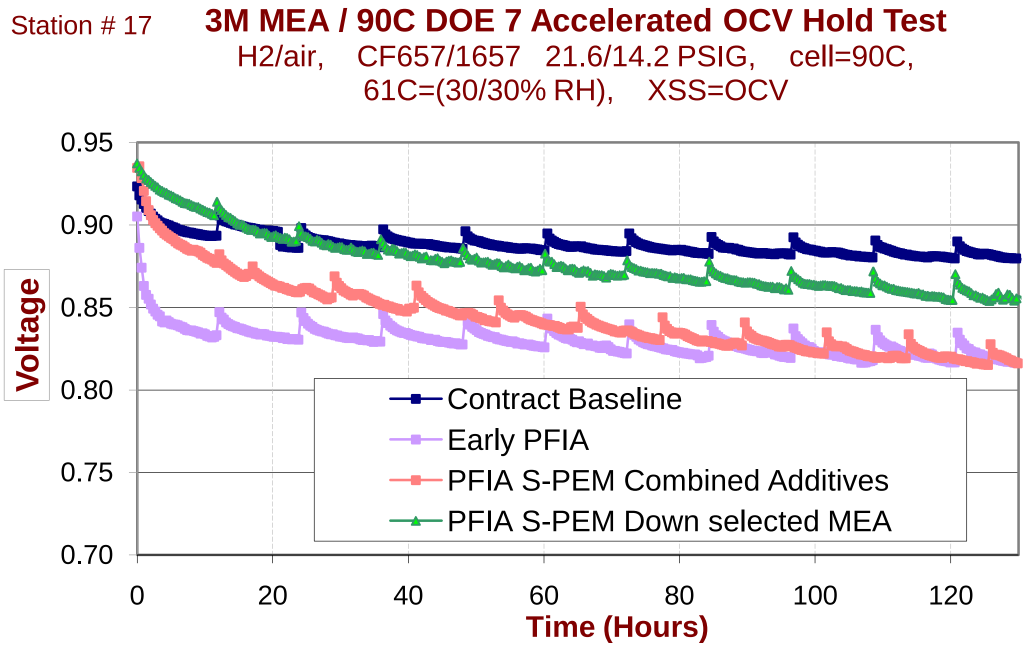

Figure 74. Starting OCV value improvement as PFIA synthesis process was improved and contaminants removed.

Many of our additives were screened using a very aggressive test protocol – H_2/O_2, 90℃ 30%rh OCV hold. This test was not a lifetime test but used only to determine initial FRR values. Final down selects and additional screening using the DOE prescribed OCV test protocol was also carried out. Our additive work focused on screening new additives, new combinations of additives, and new ways of incorporating them. One example is shown in Figure 75, showing FRR as a function of mole % of additive vs. acid groups.

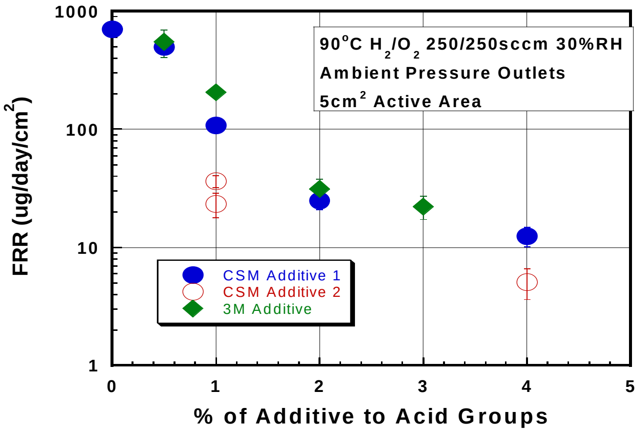

Figure 75. FRR for a variety of additives and combinations tested under this program.

3M utilized two multi cell test stands for accelerated durability tests throughout the program to run over 300 samples to failure. Each of the two accelerated test stands (SHIVA 1 and SHIVA 2) has the ability to run 10 cells in parallel with a load and humidity cycle protocol. Prior to the beginning of the program an automotive based accelerated protocol was developed for SHIVA 1. It runs continuously through the conditions given in
Table 5.

Table 5. Load cycle conditions used on SHIVA 1 durability test stand for continuous accelerated testing of 10 cells at once.

Test point	Current Density (A/cm^2)	Duration (min)	Stoich	Outlet Percent RH
1	0.20	5	5.0	72
2	0.02	20	15.0	60
3	0.80	15	1.7	115
4	0.80	10	3.0	87
5	0.02	20	15.0	60
6	0.80	15	1.7	115
7	0.20	20	5.0	72
8	1.00	20	1.7	115

Some of MEAs lasted a very long time on SHIVA 1, in some cases over 18,000 hrs (over 2 years). To facilitate sample throughput and in order to make advancements in MEA components, a new protocol was developed for SHIVA 2 to allow faster testing. The new protocol was patterned after the SHIVA 1 protocol but added in 4 thermal cycles each day that go up to 120℃ and down to 30℃. SHIVA 2 protocol is outlined in Table 6.

Table 6. SHIVA 2 protocol utilizing a section of the SHIVA 1 protocol as well as 4 thermal cycles between 30℃ and 120℃

Cycles/Day	Cell Temp	Conditions Description	Time
1	80	Long scan @ 0.6A/cm2 to used collect fluoride data	4.5 hrs
1	80	Short anode overpressure OCV to monitor lifetime	5 min
4	120	Hot Temperature Low RH to degrade MEA (up to 80ºC dewpoint)	15 hrs
	30	Low Temperature to Thermal and Humidity Cycle MEA	
2	80	Load Cycle at Various RH to monitor performance (SHIVA 1 protocol)	4.5 hrs

After the new SHIVA 2 protocol was implemented, it seemed the more aggressive conditions worked well to bring improved MEAs to failure more quickly to better facilitated test throughput. The two SHIVA stands complimented each other well, to produce a large amount of durability data. Baseline studies on thickness, membrane processing conditions, and casting solvent were done. An example evaluating the effect of membrane thickness on MEA lifetime is shown in Figure 76. Each data point on the graphs represents the average of five samples.

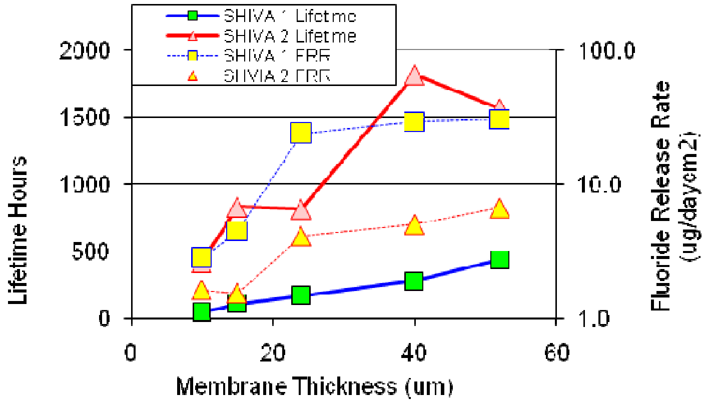

Figure 76. Membrane thickness study carried out with the two different protocols to determine FRR and lifetime.

In addition to the SHIVA 2 studies with 120℃ test excursions, complementary studies were carried out looking at 120℃ static testing to provide an upper bound for lifetimes removing the dimensional stability component to the testing that comes with changes in humidity, temperature and current. Shiva 2 testing forces many of the mechanisms expected in a normal drive cycle. The purpose of the steady state 120℃ testing was to decouple the mechanical humidity/temperature cycling and focus on chemical durability near the Tg of the polymer. By seeing long lifetimes in the steady state test at 120℃

we can surmise that shorter lifetimes in the Shiva 2 test were not just from going to near the Tg of the PEM. Our first experiments were testing under water balance conditions at 120℃ as we did in our previous contract. There we equaled or surpassed our previous lifetimes of NSTF catalyst using dispersed catalysts. From there we went to more aggressive conditions (drier) and higher current densities. Results for a variety of MEA compositions can be seen in Figure 77. All of these results are for unsupported PEMs that had a subgasket assembly in the MEA to protect against edge failures. The gains in lifetime that were realized over the life of the contract came with proper additive level, electrode type and PEM process variables. Probably the most important factor was the electrode, however due to it being a single test stand with a long test time, relatively few variables were tested. The results are very promising representing lifetimes at that temperature and low RH that no one else has published. We expect further gains in lifetime and performance would be achieved with our down selected supported PFIA PEM with combined additives.

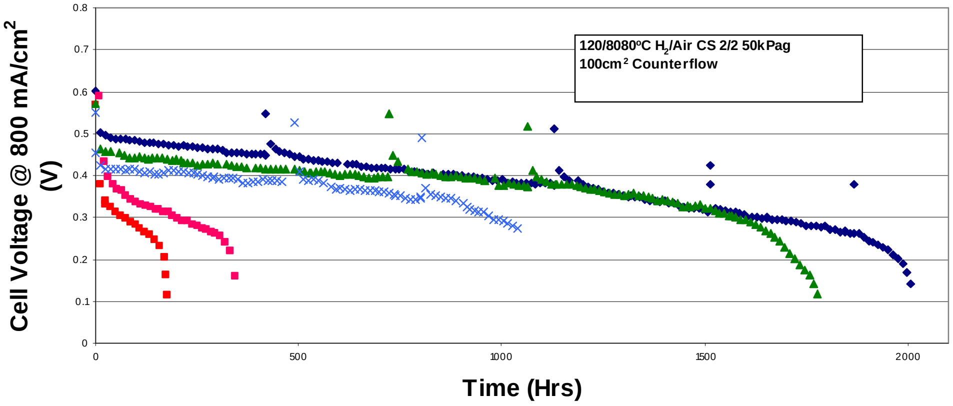

Figure 77. Results of testing of a variety of MEA constructions at 120℃ steady state conditions.

Many of the samples that were run until failure in the tests described above had post mortem analyses performed on them. The general procedure after a cell is removed from the test stand is to first run a physical leak check on the samples to determine if it has a hole. In most cases there is a hole that produces a leak rate of 10-30 sccm at 5psi. The samples were then run in an imaging test where one side of the MEA is exposed to a low concentration of H_2 and an IR image is produced to look for hot spots where the H_2 is coming through. These images show where holes are located in the membrane and also the relative size of the hole.

Specific trends could be observed in these images that provided insight as to where a membrane was failing. For example Figure 78 shows two samples from a SHIVA 1 membrane thickness experiment (10um thick membrane). In this case both samples seem to have produced a hole near the center active area of the MEA. As a contrast to the 10um membranes, the 40um membranes showed only holes or tears near the edge peripheral areas as shown in Figure 79.

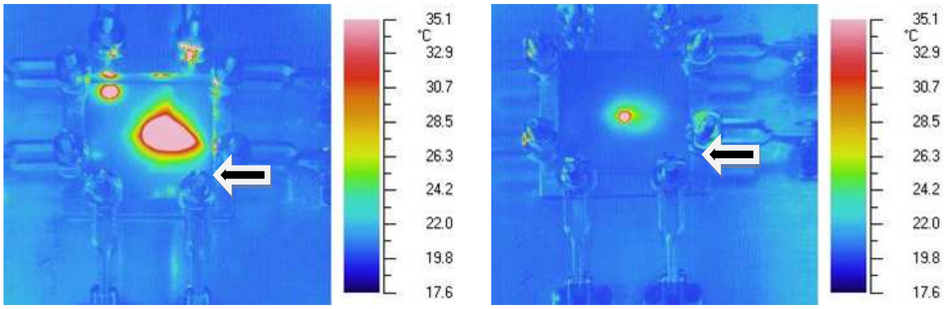

Figure 78. Post Mortem IR imaging of MEAs tested to failure in the SHIVA durability test. These samples were 10um thick membrane and showed primarily holes in the center area of the active area. The black arrow represents the location of the anode inlet

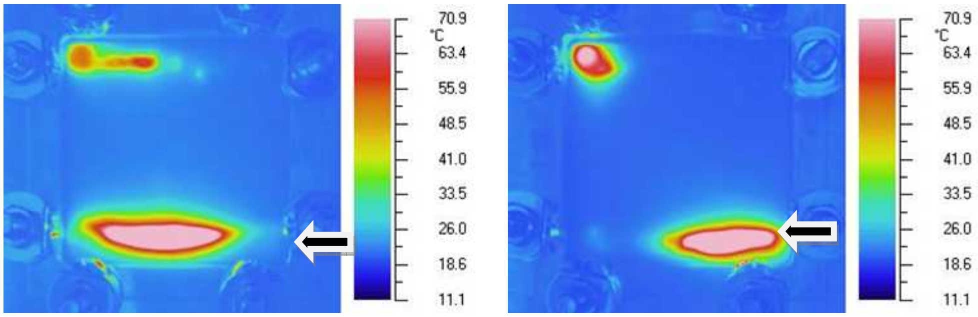

Figure 79. Post Mortem IR imaging of MEAs tested to failure in the SHIVA durability test. These samples were 40um thick membrane and showed primarily holes on the outer peripheral edges. The black arrow represents the location of the anode inlet

Post mortem analysis of supported membranes gave results that contrasted from unsupported PEMs. The failure method was different from neat membranes typically tested in our durability tests. For example Figure 80 shows typical 800EW 3M membrane without any support tested on SHIVA until failure. The holes occur near the edges and usually form a tear or larger hole that creates a fairly large hot spot. Often these large hot spots are discovered in similar locations for a set of MEAs. In contrast, supported membranes often show much smaller localized holes that are completely random throughout the MEA (Figure 81). The supported membranes may have longer life because these random small holes are not propagating to create a larger hole or tear, thus mitigating a catastrophic failure. Also, since the holes appear randomly located, it suggests that the MEAs failed at a spot where the weakest area was located instead of an area of the cell like an inlet or outlet where flows, currents, and potentials may be very different.

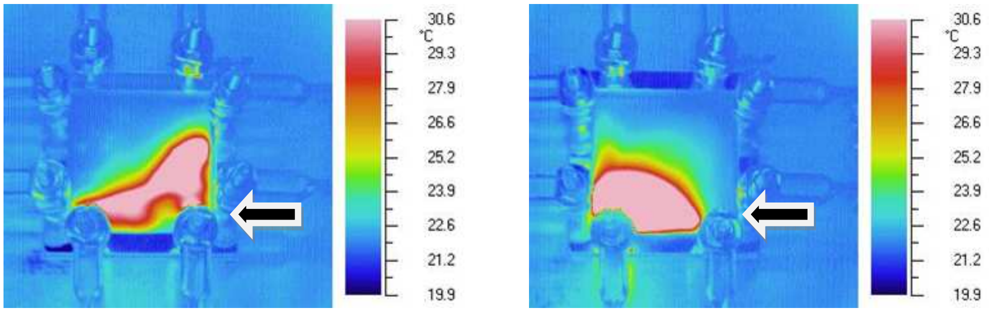

Figure 80. Post Mortem IR imaging of MEAs tested to failure in the SHIVA durability test. These samples were standard 3M 800EW membrane without support.

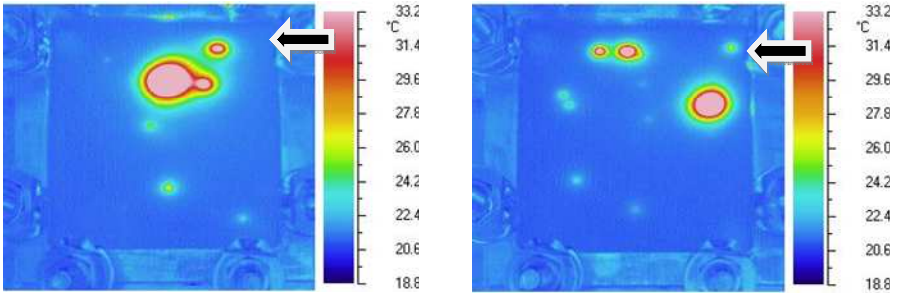

Figure 81. Post Mortem IR imaging of MEAs tested to failure in the SHIVA durability test. These samples clearly exhibit the smaller random location of failures instead of the large tear.

Samples from the RH cycle mechanical testing were also examined using the IR post mortem method. Examples of PFIA unsupported membranes that did not pass the 20,000 cycles are shown in Figure 82. These samples had small edge holes that contributed to the crossover. Also shown are two samples from the RH cycle test that passed the 20,000 cycles. These samples are shown in Figure 83 and some evidence of a thin spot (lighter color) can be witnessed. These thin spots however did not produce a measurable leak rate and therefore suggest places where the membrane is still holding together mechanically despite the fatigue generated in the test.

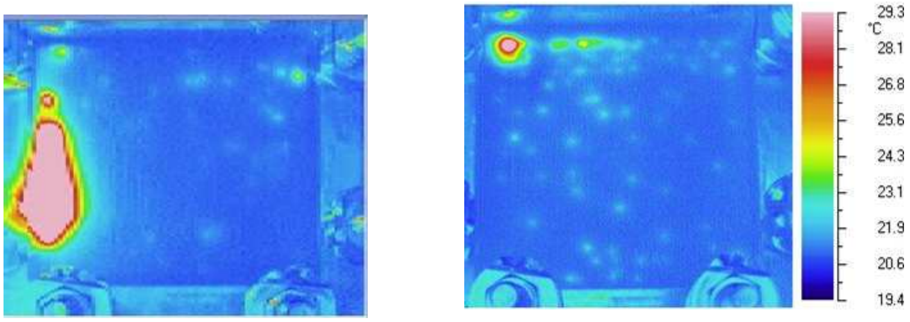

Figure 82. Post Mortem IR imaging of MEAs tested to failure in the RH Cycle mechanical test. These samples were PFIA samples made without support and lasted about 7000 cycles and did not pass the test.

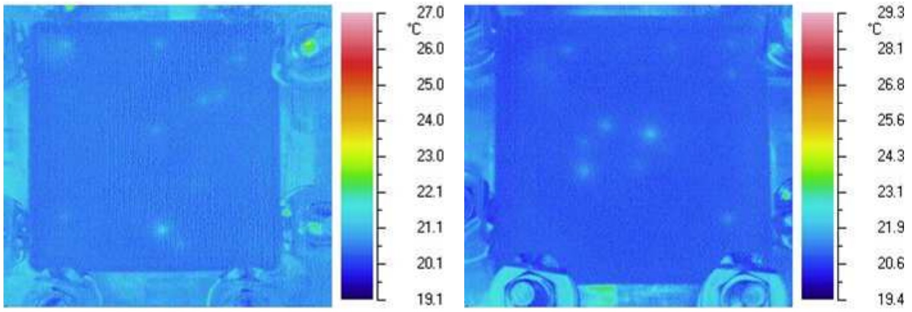

Figure 83. Post Mortem IR imaging of MEAs tested to failure in the RH Cycle mechanical test. These samples were supported PFIA that passed the 20,000 cycles

In summary, the post mortem analysis revealed that membranes with support have a random localization of holes compared to unsupported membranes where it seems one large hole propagates quickly and leads to a faster failure of the membrane. This is consistent with OCV test data where lifetimes were improved but FRR was not reduced.

7. Modeling - Carried Out in Collaboration with the University Of Tennessee

7.1 Multi-scale Materials Modeling

Coarse-grained Modeling of Morphology
This investigation involved the application of 2 distinct methods to study the hydrated morphologies of PFSA membranes as a function of membrane side-chain chemistry, degree of hydration, equivalent weight, and molecular weight. The two methodologies utilized were dissipative particle dynamics (DPD) and coarse-grained molecular dynamics (CGMD). During the project we successfully applied the DPD methodology to explore the hydrated morphologies of the Nafion™ ionomer, the short-side-chain PFSA ionomer, and the 3M PFSA ionomer as function of water content, equivalent weight (EW), and molecular weight (MW).

Initially we undertook a comparative study of the hydrated morphology of Nafion™, the short-side-chain (SSC), and 3M perfluorosulfonic acid (PFSA) fuel cell membranes with DPD simulations as a function of ionomer equivalent weight (EW) and degree of hydration. Coarse-grained mesoscale models were constructed by dividing each hydrated ionomer into components consisting of: a common poly(tetrafluoroethylene) (PTFE) backbone bead, ionomer specific backbone beads, a terminal side chain bead, and a bead consisting of a cluster of six water molecules. Flory–Huggins χ-parameters describing the interactions between the various DPD particles were calculated. Equilibrated morphologies were determined for the SSC and 3M PFSA membranes both at EW's of 678 and 978 g/mol, and Nafion™ membranes with an EW of 1244 g/mol. The hydration level was varied in each system with water contents corresponding to 5, 7, 9, 11, and 16 H_2O/SO_3H. The high EW ionomers exhibit significantly greater dispersion of the water regions than the low EW membranes. Water contour plots reveal that as the hydration level is increased, the isolated water clusters present at the lower water contents increase in size eventually forming continuous regions resembling channels or pores particularly at a hydration of 16 H_2O/SO_3H. The DPD simulations reveal differences in the hydrated morphology when only the side chain length was altered and indicate that the 3M PFSA ionomer exhibits much larger clusters of water when compared to the SSC ionomer at the same EW and water content above 9 H_2O/SO_3H. The average size of the clusters were estimated from the water–water particles' RDFs and vary from about 2 nm to nearly 13 nm for hydration levels from $\lambda = 5$ to $\lambda = 16$. Finally, computed Bragg spacing in each of the hydrated membranes indicate separation of the domains containing the water from 2 to 6 nm, exhibiting an approximately linear relationship with hydration.

In a subsequent investigation the swelling behavior of the SSC PFSA polymer was examined using DPD simulations and the results indicate that there is a strong influence of MW on both the shape and size of water-rich ionic aggregates formed as a function of water content, particularly for high EWs where there is a low concentration of sulfonic acid groups. This is likely due to the increased propensity for the PTFE backbones to aggregate and form fibrillar structures as the MW is increased in order to minimize total chain bending energy while maintaining phase separation between the ionic and perfluorinated components. Given that all previous molecular simulations of PFSAs have used MWs well below the values studied here, it is not surprising that these effects have not been seen previously, and that nearly all atomistic models of PFSA morphology predict spherical ion-clustered domains. Since even our largest DPD simulations were with SSC ionomers with molecules whose MW is just below the lower limit of the MW range observed for real PFSAs, this effect is likely to be even more pronounced than found here, and may be one of the reasons why there is still so much disagreement between the various different morphologies predicted for PFSAs through modeling studies. Our study has shown that MW does have a significant effect on the hydrated morphology particularly at an upper hydration limit where $\lambda = 16$ and swelling of SSC PFSAs, and this finding is likely to be general across PFSA membranes with different side-chain length.

Finally, in a separate study the hydrated morphologies of 3M PFSA membranes were investigated using DPD simulations as a function of the EW, MW, and hydration level. The 3M PFSA ionomers were modeled using typical EWs of 578, 640, and 790 g/mol, and molecular weights were varied from about 45 000 to 90 000 g/mol in order to be close to the experimental range. The morphology changes corresponding to the EW, MW, and hydration level were comparatively investigated by inspecting the water distributions, followed by quantitative analysis by radial distribution functions and Bragg spacing according to the periodicity of water domains. Compared to the morphologies of short-side-chain PFSA membrane, the longer side chain in 3M PFSA membrane provides more flexibility for the sulfonate-terminated side chains and generally results in the stronger aggregation of water clusters. This results in lower water uptake for higher EW, corresponding to a lower ion-exchange capacity (IEC), which is attributed experimentally to a higher crystallinity of the fluorocarbon phase, although our simulations were not able to observe the crystallites directly. As the water content increases, the locally isolated water clusters at a low hydration level become a continuous water domain at a high hydration level. The MW appears to have a strong influence on both the shape and size of the water clusters. The longer PTFE backbone, corresponding to a higher MW, drives the elongated form in water-rich ionic phase.

<u>Highlights</u>:

1. Successful application of DPD to study hydrated morphologies of hydrated PFSA ionomers.
2. Results suggest that as the hydration level is increased, the isolated water clusters present at the lower water contents increase in size eventually forming continuous regions resembling channels or pores.
3. The 3M PFSA ionomer exhibits much larger clusters of water when compared to SSC ionomer due to the small structural difference in the ionomers, while the Nafion ionomer shows narrowed water channels (or certainly elongated domains).
4. The ion and water-containing domains or regions was observed to increase with MW particularly for very low MW (i.e., from 15K to 40K). The systems with higher MW ionomers display greater aggregation of the PTFE backbones, which in turn drives formation of larger water-rich domains and greater phase separation.

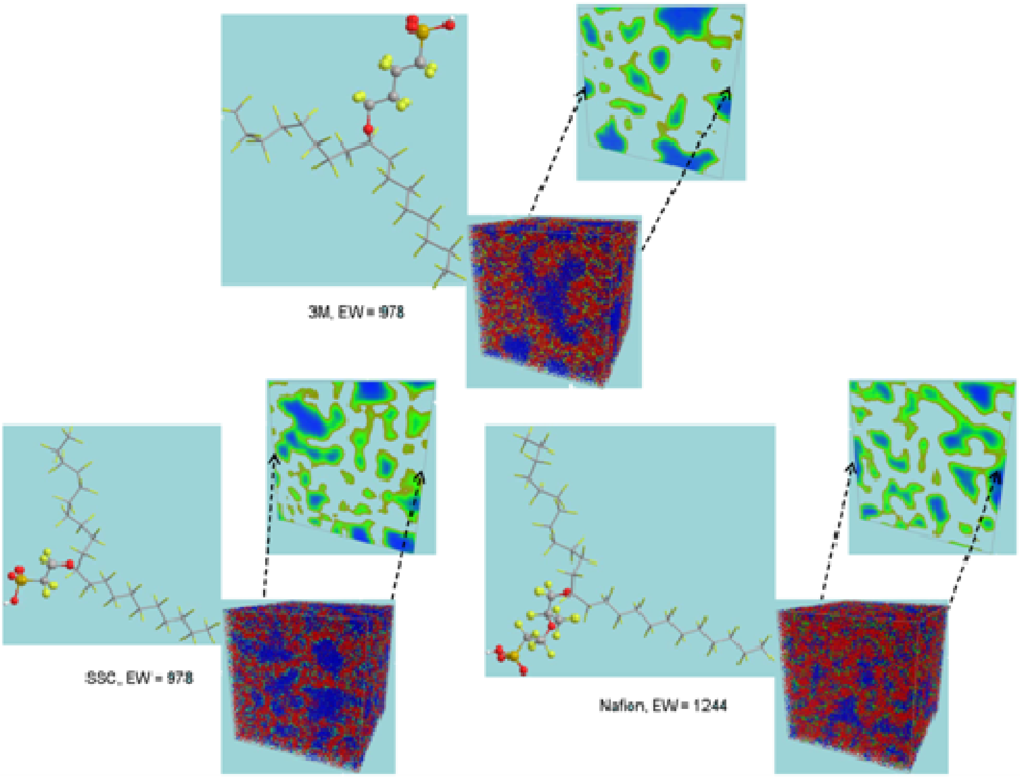

Figure 84. Featured on the front cover of Energy and Environmental Science[31]. DPD simulations of 3 PFSA membranes each at the same water content of 9 H¬2O/SO3H. In the simulation boxes the water phase is shown in blue and the polymer backbone phase in red. The 2D slices show the water densities.

7.2 Chemical Degradation of PFSA Membranes

The Gaussian 03 suite of programs was used for the determination of all structures and the associated energetics of the species involved in the various reactions.[32] These calculations were performed by employing hybrid density functional (DFT) theory with Becke's 3 parameter functional (B3LYP)[2-5] with 6-311++G** basis set. Three types of energy were calculated: (a) the energy of homolytic bond cleavage, (b) the energy of reaction, and (c) the activation energy of reaction. The homolytic cleavage of a bond in a fragment produces two radical components, having one unbound electron on the respective atom of each radical component. The energy of a homolytic bond cleavage was calculated by $E_{radical1} + E_{radical2} – E_{fragment}$, where, E_x represents the energy of the component, x. The energy of a reaction was calculated by $E_{products}$-$E_{reactants}$, where, $E_{products/reactants}$ represents the summation of the energies of all products/reactants. The activation energy of a reaction is the difference between the energy of the transition state (TS) of the reaction and the energy of the reactants-complex or the products-complex (E_{TS}-$E_{reactants-/products-complex}$). The energy of the reactants-/products-complex is the energy of the system when all reactants (products) are optimized together.

Four types of calculations were carried out: (1) optimization of radicals/anions/molecules along with frequency calculation, (2) location of the transition states, (3) potential energy surface (PES) scan and (4) intrinsic reaction co-ordinate (IRC) calculation at the transition state structure. The optimization of the molecules, anions and radicals was performed without any symmetry constraints. Frequency calculation was also performed on the optimized geometries. The energy of the optimized structure was corrected with zero-point energy (ZPE). This corrected energy of the optimized structure represents the total energy of the component in the gas phase at room temperature and standard atmospheric pressure. Transition states of the reactions were located by one of two methods: (a) the optimization of the structure, representing the peak point of a PES scan curve, by a TS method and (b) the synchronous transit-guided quasi-Newton (STQN) method (QST2/QST3). A PES scan was performed on the reactants-complex (or products-complex) by varying the distance of the departing atoms in the reactants-complex (or products-complex), which could lead to the products-complex (or reactants-complex). The structure representing the peak (maxima) on the PES curve was optimized using a TS method to obtain the transition state structure. The electronic structure calculation of a transition state via an STQN method was performed using the geometries of reactants-complex and the products-complex for the corresponding reaction. The transition state obtained, using the above methods, was confirmed by observing one imaginary frequency for the optimized structure. Finally, an IRC calculation was performed for every reaction at its respective transition state to confirm its connectivity to reactants and products.

Side-chain Degradation
The calculation for the side-chain degradation was performed by determining the energy of homolytic bond cleavage for both the anionic and radical side chain fragment shown in Figure 85.

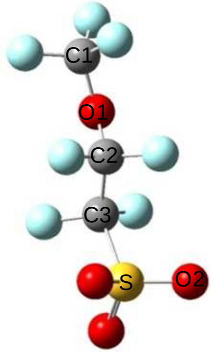

Bond type	Energy of bond dissociation (kcal/mol)
S-O2	128.09
C3-S	60.57
C2-C3	84.74
O1-C2	88.75
C1-O1	90.02
C-F	106.00

Bond type	Energy of bond dissociation (kcal/mol)
S-O2	62.12
C3-S	47.16
C2-C3	77.75
O1-C2	84.94
C1-O1	89.92
C-F	106.00

Figure 85. Homolytic bond cleavage of anion and radical fragments.

These calculations indicate that the C–S bond is the weakest among all bonds. The anionic fragment can react with a hydroxyl radical to produce a radical fragment and a hydroxide ion, which, further, can react with a hydrated proton to yield a water molecule.

$$CF_3O(CF_2)_2SO_3^- + \bullet OH \rightarrow CF_3O(CF_2)_2SO_3\bullet + OH^- \qquad (1)$$

Reaction (1) is endothermic and requires 82.32 kcal/mol of energy. The radical product further decomposes to produce a radical and SO_3 with the cleavage of the C–S bond.

$$CF_3O(CF_2)_2SO_3\bullet \rightarrow CF_3O(CF_2)_2\bullet + SO_3 \quad (2)$$

The energy of reaction (2) is 0.93 kcal/mol, and it is endothermic in nature. To obtain the transition state structure of the reaction, a PES scan was performed on products-complex by decreasing C–S bond distance (Figure 86). The potential energy of the complex increases and attains maximum at structures (4) and (2). Structure (4) is achieved due to the lateral movement of SO_3 from structure (5) and structure (2) is achieved due to axial movement of SO_3 from structure (3). In this course, the structure of SO_3 remains planar. If the C–S bond distance further decreases from structure (2), the structure of SO_3 changes from planar to pyramidal. The potential energy decreases and attains minimum at structure (1), which is the structure of the reactant.

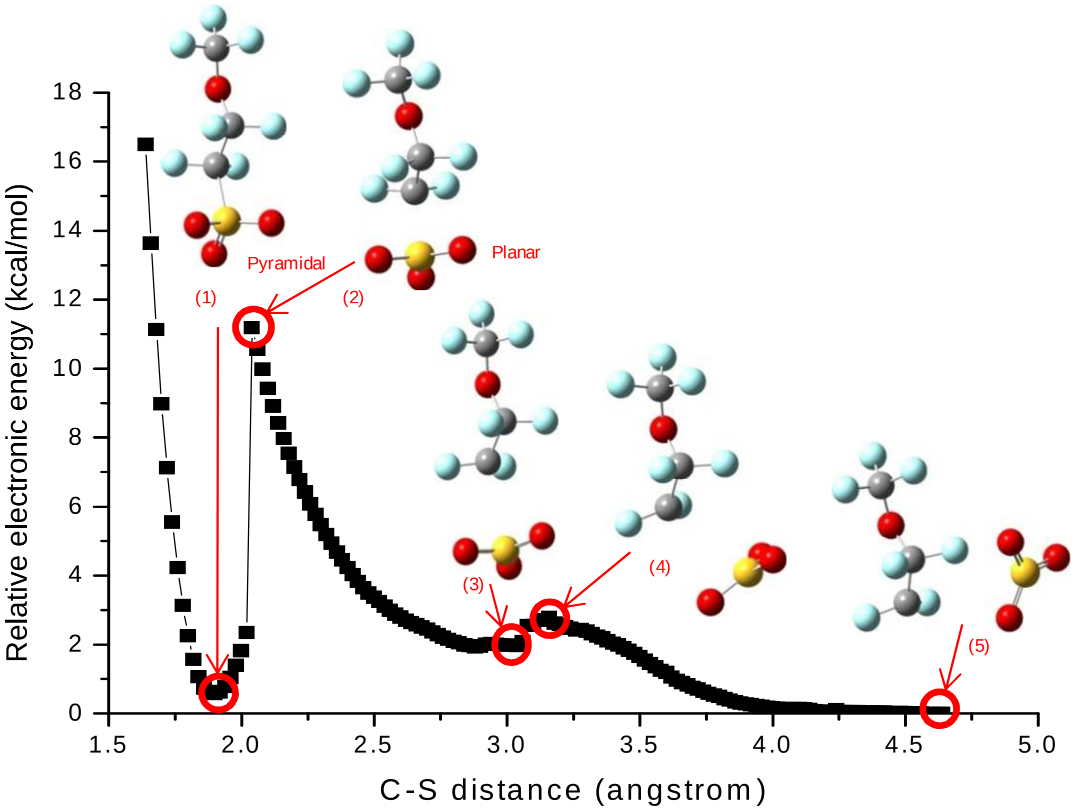

Figure 86. Potential energy surface scan of products complex, CF3O(CF2)2…SO3, radical by decreasing C–S atomic distance.

A PES scan was also performed on the reactant by increasing C–S distance, but the change in the structure of SO_3 form pyramidal to planar was not observed in this case. The scanned potential energy attains a plateau. The radical product of reaction (2) can react with a hydroxyl radical to produce an alcohol, which can further degrade like backbone degradation.

$$CF_3O(CF_2)_2OH \rightarrow CF_3OCF_2CFO + HF \qquad (3)$$

$$CF_3OCF_2CFO + H_2O \rightarrow CF_3OCF_2COOH + HF \qquad (4)$$

Backbone Degradation

The backbone degradation of PFSA membranes starts with the abstraction of the H atom from the –COOH end group by a •OH.

$$CF_3CF_2COOH + \bullet OH \rightarrow CF_3CF_2COO\bullet + H_2O \qquad (5)$$

$$\Delta E_{rxn} = -7.54\,\mathrm{kcal/mol}$$

$$\Delta E_{activation} = 1.70\,\mathrm{kcal/mol}$$

$CF_3CF_2COO\bullet \rightarrow CF_3CF_2\bullet + CO_2$ (6)

$\Delta E_{rxn} = -28.52\,kcal/mol$

$\Delta E_{activation} = 3.25\,kcal/mol$

$CF_3CF_2\bullet + \bullet OH \rightarrow CF_3CF_2OH$ (7)

$\Delta E_{rxn} = -100.37\,kcal/mol$

$CF_3CF_2OH \rightarrow CF_3CFO + HF$ (8)

$\Delta E_{rxn} = 2.26\,kcal/mol$

$\Delta E_{activation} = 41.52\,kcal/mol$

$CF_3CFO + H_2O \rightarrow CF_3COOH + HF$ (9)

$\Delta E_{rxn} = -8.75\,kcal/mol$

$\Delta E_{activation} = 34.34\,kcal/mol$

The mechanism reproduces a –COOH end group in the backbone at the end of one series of reactions. These reactions are exothermic in nature (except reaction [8]). The activation energies for the first two reactions in the unzipping mechanism are very low; these reactions are very fast. The activation energies for the last two reactions are high; these reactions are slow. Figure 87 shows the change in the potential energy of reactants to occur the reaction (8). An IRC calculation at the transition state structure shows its connectivity with the reactant and products. The activation energies for the slow reactions can be compensated by the radical addition reaction (7), which is highly exothermic.

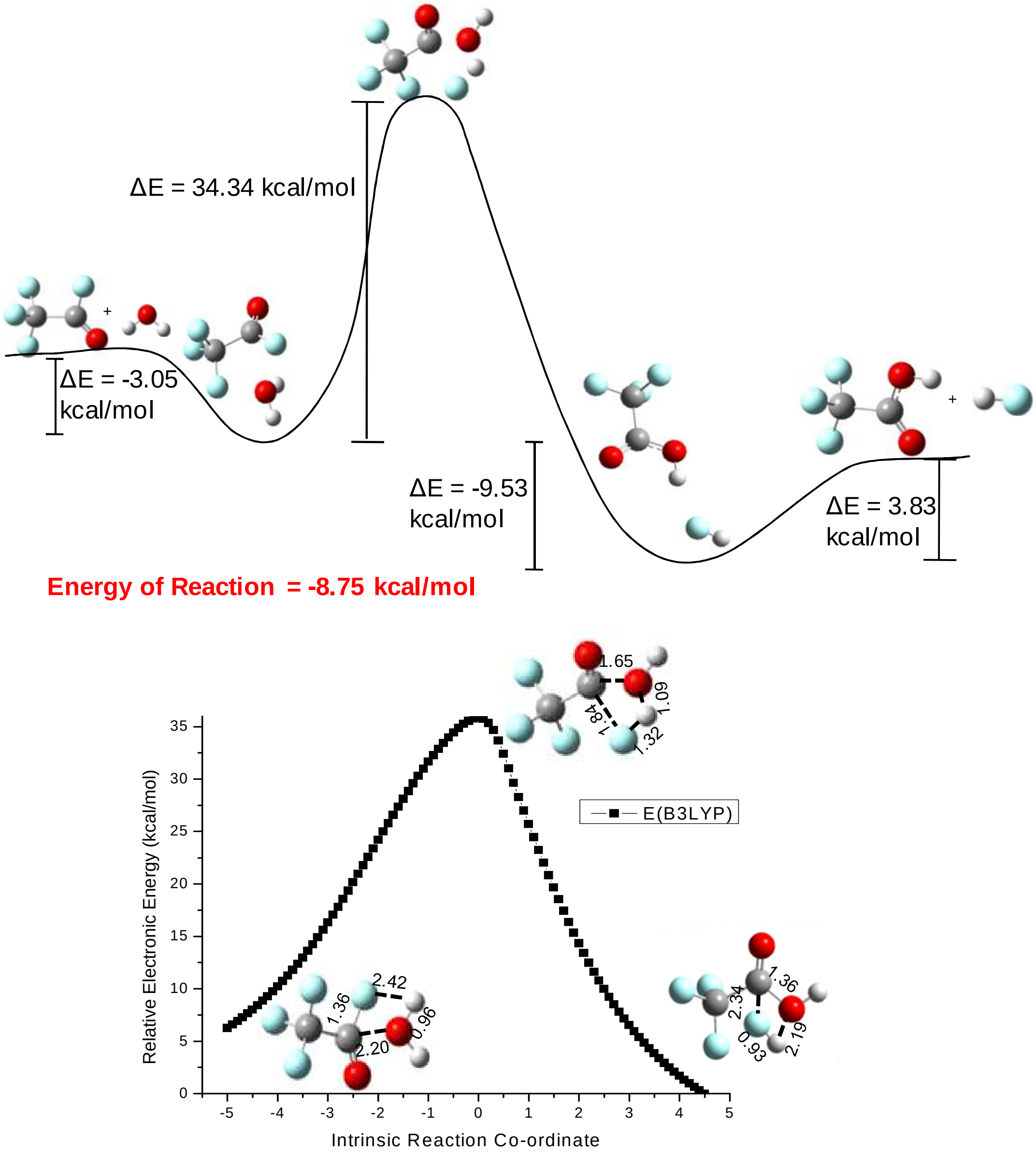

Figure 87. Change in the potential energy of reactants to occur the reaction and IRC calculation at the transition state structure of the reaction.

Highlights

The C–S bond is the weakest bond in the side-chain; hence, the side-chain degradation will start with the cleavage of this bond.

A backward PES scan of the radical fragment of side-chain shows the change in the structure of SO_3 from planar to pyramidal on the expense of ~11.0 kcal/mol of energy.

1. The first two reactions in the backbone degradation mechanism are fast and the last two reactions are slow. The radical addition reaction is highly exothermic which can provide sufficient energy to the slow reactions to cross the activation energy barrier.
2. The backbone degradation mechanism reproduces the –COOH end group in the backbone at the end of one series of reactions which can lead to another series of reactions in the presence of the hydroxyl radical.

7.3 Quantum Chemical Calculations of Hydration and Proton Transfer

Proton Exchange Membrane (PEM) fuel cells offer tremendous potential as clean alternative energy conversion systems. Critical to these devices is the proton-conducting polymer electrolyte membrane. The PEM functions not only as the electrolyte in current hydrogen fuel cells but also as the separator of the electrodes and reactant gases and, importantly, as the internal ion conductor. It is widely known that proton conductivity in these membranes depends on the level of hydration. However, a molecular-level understanding of the factors that contribute to proton transport in PEMs at low hydration levels is of vital importance in the development of novel proton conducting electrolyte materials for fuel cell application. Among these factors are the effects local hydration and neighboring side chain connectivity have on facilitating proton dissociation and the energetics of proton transfer reactions. These were explored via explicit water electronic structure calculations on fragments of the 3M perfluorosulfonic acid (PFSA) ionomer.[33] The fragments consisted of a poly(tetrafluoroethylene) (PTFE) backbone with two pendant side chains each functionalized by a terminal sulfonic acid group. Two different side chain separations along the PTFE backbone were used model different equivalent weight (EW) ionomers with chemical formula $CF_3CF(–O(CF_2)_4SO_3H)(CF_2)_nCF(–O(CF_2)_4SO_3H)CF_3$, where n = 5 and 7 which correspond to equivalent weights (EWs) of 590 and 690 grams ionomer per mole acid, respectively. The fully optimized (B3LYP/6-311G**) geometries revealed that increasing the separation between side chains also increased the number of water molecules required to 'bridge' side chains together through hydrogen bond interactions. The same trend was also observed in the number of water molecules required to facilitate proton dissociation of the side chain sulfonic acid groups. Specifically, dissociation of a single acidic proton was observed in the EW 590 fragment at a water content of only $\lambda = 1$ (where λ is defined as the number of water molecules per sulfonic acid group); but the system with greater separation of the side chains (EW 690) did not exhibit first proton dissociation until four water molecules (i.e. $\lambda = 2$) were added as the greater side chain separation precluded the cooperative interaction through hydrogen bonding that promotes proton dissociation at low hydration in membranes of this type. Furthermore, dissociation of the second acidic proton occurred upon addition of only three water molecules in the EW 590 system while this was not observed in the EW 690 system until addition of five water molecules. The differences in the hydration level required for proton dissociation in these systems was attributed to the interactions between side chains and stronger hydrogen bond capabilities in systems with less separation between side chains.

To investigate the energetics of proton transfer in the PFSA systems at different equivalent weights, potential energy scans (PES) for the forced proton transfer across hydrogen bonds of individual protons bound to sulfonic acid, water molecules, or ionic complexes were performed in minimally hydrated systems using fully optimized geometries obtained from the electronic structure calculations. The scans involved incrementally increasing a specified O-H bond length in steps of 0.02 Å with geometry optimizations at the B3LYP/6-31G** level performed at each step over all other degrees of freedom. It was found that, at low water content, the nature of the hydrogen bond network and the degree of dissociation were critical factors in the resulting energetic barrier for proton transfer. Namely, systems with only one dissociated proton in which the hydrogen bond network could easily reorient to accommodate charge transfer and, generally, return to a similar state (i.e. equivalent number of hydrogen bonds and dissociated protons) exhibited significantly lower energetic barriers for proton transfer than in systems that did not have these qualities. These traits were more dominantly found in the system with less separation between side chains (EW 590) as continuous, cyclical hydrogen bond networks were more readily formed between the water molecules and the sulfonic acid/sulfonate terminal side chain groups. The hydrogen bond network in the EW 690 system, on the other hand, contained less order making the reorientation process less viable at low hydration. This is effectively demonstrated in the PES of the forced transfer of a proton from a water molecule to a sulfonic acid group in the EW 590 and EW 690 systems at a hydration of λ = 2 shown in Figures 1 and 2, respectively.

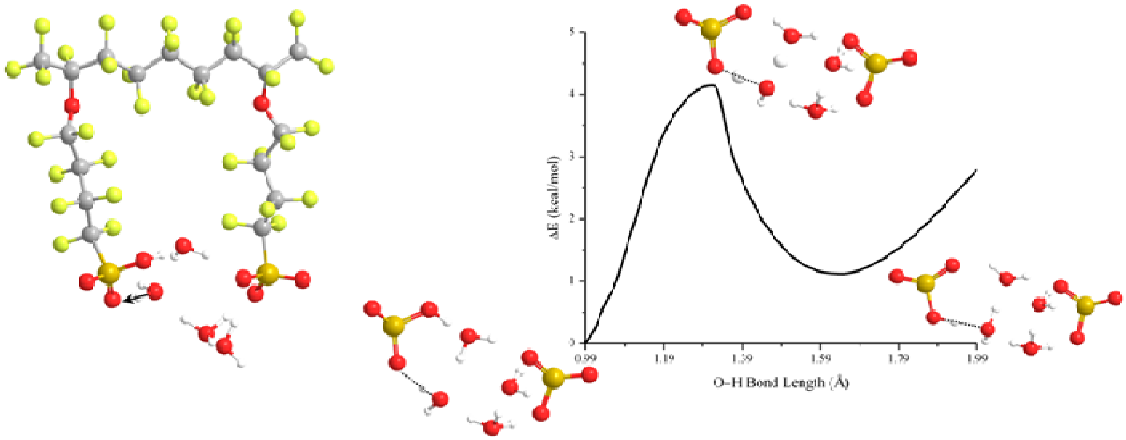

Figure 88. Left: Fully optimized (B3LYP/6-311G) structure of the EW 590 3M PFSA ionomer with the addition of four explicit water molecules used in PES of the forced transfer of the proton indicated by the arrow to an oxygen atom of the sulfonic acid group. Right: The change in energy with respect to the original configuration as a function of the O–H bond length obtained from the proton transfer PES with the bottom view of the sulfonic acid/sulfonate and water molecules at the initial, transition state, and local minimum points of the scan. The hydrogen bond across which the proton is being transferred is indicated by a dotted line. The different colored spheres represent different atom types where: grey–carbon, green–fluorine, red–oxygen, yellow–sulfur, and white–hydrogen.**

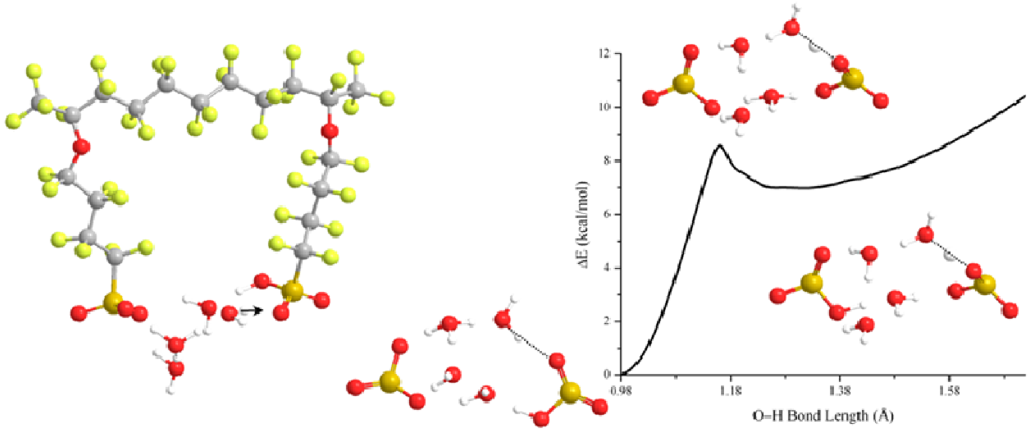

Figure 89. Fully optimized (B3LYP/6-311G) structure of the EW 690 3M PFSA ionomer with the addition of four explicit water molecules used in PES of the forced transfer of the proton indicated by the arrow to an oxygen atom of the sulfonic acid group. Right: The change in energy with respect to the original configuration as a function of the O–H bond length obtained from the proton transfer PES with the bottom view of the sulfonic acid/sulfonate and water molecules at the initial, transition state, and local minimum points of the scan. The hydrogen bond across which the proton is being transferred is indicated by a dotted line. The different colored spheres represent different atom types where: grey–carbon, green–fluorine, red–oxygen, yellow–sulfur, and white–hydrogen.**

The left side of Figure 88 represents a fully optimized geometry of the EW 590 PFSA ionomeric fragment with dissociation of only one proton. While this is not the global minimum energy structure found, it provides a means of comparison to the similar EW 690 fully optimized geometry with a single dissociated proton shown in the left side of Figure 89. In each system, the proton being transferred is indicated by a black arrow, and the images shown with the PES are bottom views of the sulfonic acid/sulfonate and water molecules at different points throughout the scan with the hydrogen bond in which the proton is transferred over indicated by dotted lines. The energetic barrier for proton transfer in the EW 590 system is slightly higher than 4 kcal/mol with the transition state shown above the maxima on the PES. The local minimum is only ~1 kcal/mol higher in energy than the initial structure with a similar state of the hydrogen bond network, as shown in the rightmost image of Figure 88. The energetic barrier for transferring a similar proton in the EW 690 system is nearly 9 kcal/mol with a local minimum ~7 kcal/mol higher than the original configuration. This proton transfer reaction led to the breaking of hydrogen bonds and the lack of a continuous, all-inclusive hydrogen bond network precluded the reorientation of the system needed for stabilization. These results provide insight into how side chain separation and the nature of the hydrogen bond network affect the energetics of proton transfer from a water molecule to a sulfonic acid group in systems with one dissociated proton. Proton transfer back to a sulfonate group after dissociation, on the other hand, more strongly resisted reprotonation in each system; this was especially noted in the global minimum energy structure of the EW 590 system (top left panel in Figure 90) where both protons had dissociated and reprotonation of the sulfonic acid group required the disruption of a fully connected, highly symmetric hydrogen bond network and changed the state of the system. This is shown in the bottom panel of Figure 90 with the hydrogen bond distances (as measured by the O···O separation) between the sulfonate/sulfonic acid groups and water molecules/hydronium ions reported and the hydrogen bond in which the proton is being transferred over indicated by a blue bracket. As the proton is transferred, the hydronium ion in the lowest portion of the figure donates a proton to its neighboring water molecule to compensate for the excess negative charge on the water molecule as the proton is transferred back to the sulfonate group. The final state of the original hydronium ion is that of a water molecule with ‘quasi-hydrogen bonds’ shared between two oxygen atoms of the sulfonate/sulfonic acid groups (red lines) and a much weaker hydrogen bond (as indicated by the hydrogen bond length) to the left sulfonate group (red bracket) than in the initial configuration. As can be seen in the monotonically increasing PES in the top right panel of Figure 90, this disruption of the hydrogen bond network and reprotonation of the sulfonate group is highly energetically unfavorable.

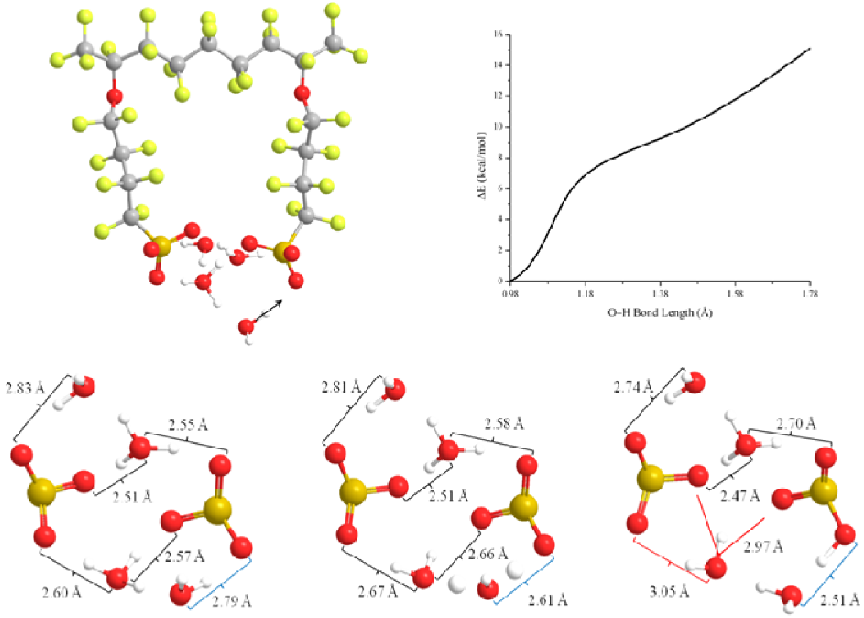

Figure 90. Top left: Fully optimized (B3LYP/6-311G) structure of the EW 590 3M PFSA ionomer with the addition of four explicit water molecules used in PES of the forced transfer of the proton indicated by the arrow to an oxygen atom of the sulfonate group. Top right: The change in energy with respect to the original configuration as a function of the O–H bond length obtained from the proton transfer PES. Bottom: The bottom view of the sulfonic acid/sulfonate and water molecules and the hydrogen bond distances at the initial state, an intermediate state before reprotonation, and the reprotonated points of the scan. The hydrogen bond across which the proton is being transferred is indicated by a blue bracket. The different colored spheres represent different atom types where: grey–carbon, green–fluorine, red–oxygen, yellow–sulfur, and white–hydrogen.**

An additional study used electronic structure calculations to investigate the effects protogenic group separation, side chain chemistry, and local hydration have on proton dissociation in PEMs with multiple and distinct acid groups per side chain on single side chains of various imide-based 3M ionomers. The ionomers associated with this study also consisted of a PTFE backbone, but their functionalized side chains contained two different protogenic groups, an imide and a sulfonic acid group. The fragments had distinct structural differences which mediated the distance separating the acidic groups. Two of these were structural isomers with protogenic group separation determined by the location of a sulfonic acid group on a phenyl ring termed the *meta* and *ortho* bis acids with fully optimized (B3LYP/6-311G**) 'dry' (i.e. no water molecules added) geometries shown in the top panels of Figure 91a and b, respectively. A third imide-based fragment had protogenic groups separated by electron withdrawing $–CF_2–$ groups, denoted as the PFIA ionomer, with the fully optimized 'dry' shown in the top panel of Figure 91c. The images in the bottom panel of Figure 91 represent the electrostatic potential mapped on the total electron density: the darker blue an area is indicates electron deficiency while electron rich areas are indicated by the darkness of red. These figures illustrate key differences in the atomic charges of the protogenic groups in the three systems under 'dry' conditions. Namely, the proximity of protogenic groups in the *ortho* system allowed for hydrogen bonding between the sulfonic acid groups and an oxygen from the nearest sulfonyl group bringing about charge delocalization; this interaction, however, is not sterically possible in the *meta* bis acid system. In the PFIA system, the electron withdrawing $–CF_2–$ groups effectively decrease the negative charge on the sulfonic acid and lower sulfonyl oxygen atoms when compared to the bis acid systems as indicated by the lighter red tone surrounding them.

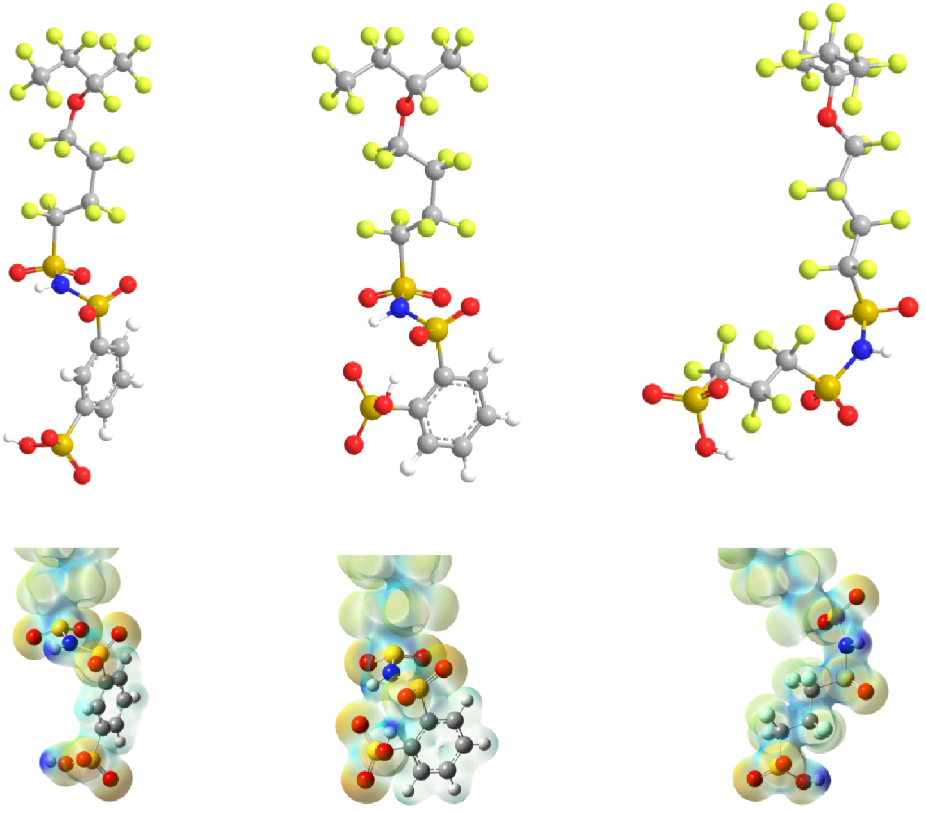

(a) (b) (c)

Figure 91. Top: Fully optimized minimum energy structures of 3M imide-based ionomeric fragments without the addition of water molecules: (a) meta bis acid, (b) ortho bis acid, and (c) PFIA. Bottom: Electrostatic potential mapped on the total electron density: the darker blue an area is indicates electron deficiency while electron rich areas are indicated by the darkness of red. Top atom color: grey – carbon, red – oxygen, yellow – fluorine, orange – sulfur, and white – hydrogen, blue – nitrogen. Bottom atom color: the same as the top aside for the fluorine atoms in the PFIA (c) are represented by large white spheres.

The charge delocalizing effects were found to play critical roles in first proton dissociation at low levels of hydration. Specifically, only three water molecules were required for first proton dissociation in the *ortho* bis acid and PFIA systems, while five water molecules were required for first proton dissociation in the *meta* system (Figure 92). Second proton dissociation, however, required ten water molecules in the *ortho* system as the close proximity of protogenic groups hindered dissociation due to localized excess positive charge in the surrounding water cluster. The two systems with greater protogenic group separation, on the other hand, only required seven water molecules for second proton dissociation as they have a more widely spread charge distribution (Figure 93). These calculations further substantiate prior work on the importance the interaction between protogenic groups through hydrogen bonding, the nature of the hydrated hydrogen bond network, and the side chain hold in the transfer and state of the dissociated protons.

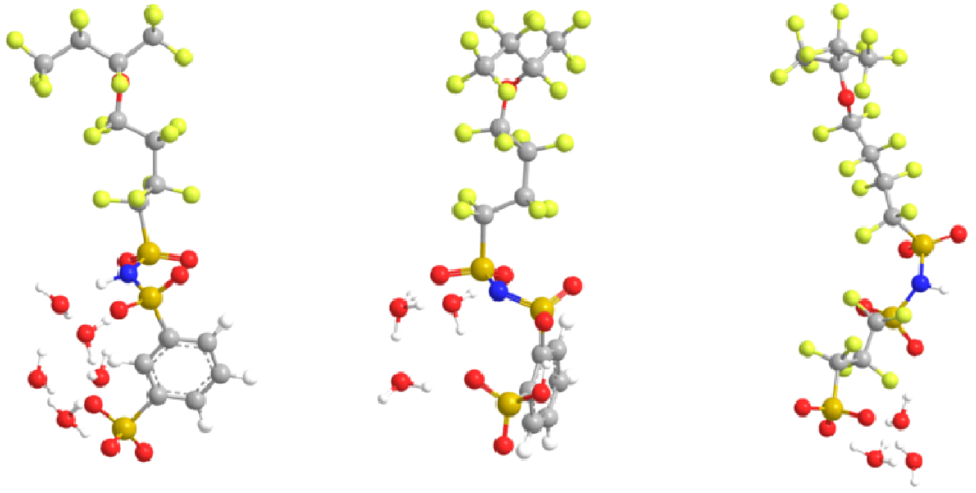

(a) (b) (c)

Figure 92. Fully optimized structures of the 3M imide-based ionomer fragment showing first proton dissociation: (a) the meta bis acid system upon addition of 5 explicit water molecules, (b) the ortho bis acid system upon addition of 3 explicit water molecules, and (c) the PFIA system upon addition of 3 explicit water molecules. Atom color: grey – carbon, red – oxygen, yellow – fluorine, orange – sulfur, and white – hydrogen, blue – nitrogen.

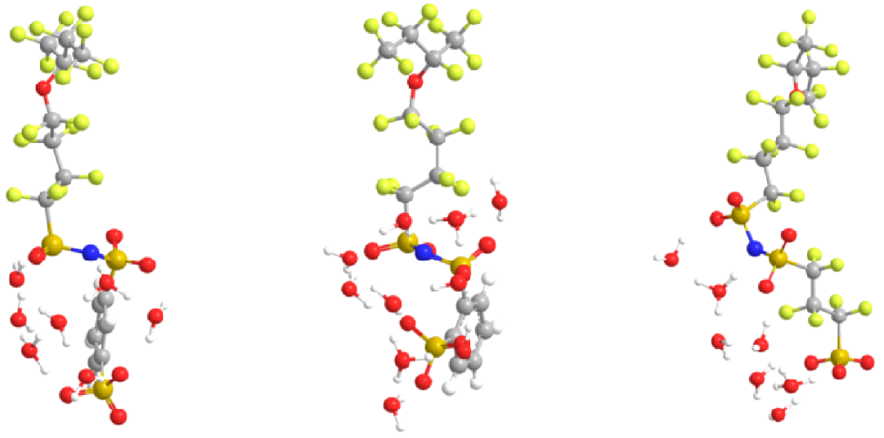

(a) (b) (c)

Figure 93. Fully optimized structures of the 3M imide-based ionomer fragment showing second proton dissociation: (a) the meta bis acid system upon addition of 7 explicit water molecules, (b) the ortho bis acid system upon addition of 10 explicit water molecules, and (c) the PFIA system upon addition of 7 explicit water molecules. Atom color: grey – carbon, red – oxygen, yellow – fluorine, orange – sulfur, and white – hydrogen, blue – nitrogen.

8. Conclusions

- We have developed a new Proton Exchange Membrane (PEM) for PEM fuel cells. This new membrane comprises a new Multi Acid Side-Chain (MASC) ionomer, stabilizing additives for improved chemical stability and polymer nanofibers for improved mechanical stability.
- In out-of-cell tests this new membrane has shown superior mechanical stability, chemical stability and conductivity compared other available membranes. It has met DOE 2015 targets for conductivity and other physical properties, except for the conductivity under the most aggressive condition, 120℃, 40kPa H_2O (about 25% RH at 1 atm).
- In Fuel Cell tests Membrane Electrode Assemblies (MEAs) with this new membrane provides increased performance, lower cell resistance and has met all DOE 2015 durability targets (Table 1).

As stated above, we developed a new ionomer membrane with improved performance and durability. Going forward we intend to build on this new technology to gain further understanding of the factors influencing conductivity and durability in this membranes and develop new materials based on this understanding.

9. References

1. Hamrock S.J. U.S. Department of Energy Hydrogen Program **2009** and **2010** Annual Merit Review Proceedings.
2. Cell Component Accelerated Stress Test and Polarization Curve Protocols for Polymer Electrolyte Membrane Fuel Cells - *http://www.uscar.org/commands/files_download.php?files_id=267*
3. Doyle M,; Rajendran, G. In: Vielstien W, Gasteiger HA, Lamm A, (eds) Handbook of Fuel Cells: Fundamentals, Technology and Applications, Vol 3, John Wiley & Sons: West Sussex, pp 351-395, **2003.**
4. Hamrock, S.J.; Yandrasits, M.A. *Polymer Reviews*, **46**(3) 219 – 244, **2006**.
5. Maritz K.A.; Moore, R.B. *Chem. Rev*. ***104*, ** 4535-4585, **2004**.
6. Mittelsteadt C.K. U.S. Department of Energy Hydrogen Program 2010 Annual Merit Review Proceedings.
7. Paddison S.J. Paul, R. *Phys Chem Chem Phys* ***4,*** 1158–1163, **2002.**
8. K. A. Maritz, and R. B. Moore, *Chem. Rev*. **104,** 4535-4585, (2004).
9. Hamrock, S.J.; Yandrasits, M.A. in *Fuel Cell Chemistry and Operation,* A. M. Herring, T. A. Zawodzinski Jr., S. J. Hamrock, Editors, p. 15, ACS Symposium Series; American Chemical Society: Washington, DC, **2010**.
10. Lai, Y.H.; Mittelsteadt, C.K.; Gittleman, C.S.; Dillard, D.A. *J. Fuel Cell Sci. Technol.* ***6*,** 021002, **2009.**
11. Schaberg, M.S.; Abulu, J.E.; Haugen, G.M.; Emery, M.A.; O'Conner, S.J.; Xiong, P.N.; Hamrock S.J. *Electrochemical Society Transactions, **33 (1)***, 627-633, **2010**.
12. Koppel, I. A.; Taft, R. W.; Anvia, F.; Zhu, S. Z.; Hu, L. Q.; Sung, K. S.; DesMarteau, D. D.; Yagupolskii, L. M.; Yagupolski, Y. L.; Ignat'ev, N. V.; Kondratenko, N. V.; Volkonskii, A. Y.; Slasov, V. M.; Notario R.; Maria, P. C. *J. Am. Chem. Soc., **116***, 3047-3057, **1994**.
13. Savett, S. C.;Atkins, J. R.; Sides, C. R.; Harris, J. L.; Thomas, B. H.; Creager, S. E.; Pennington W. T.; DesMarteau, D. D. *J. Electrochem. Soc*. 2002, ***149*,** A1527, **2002**.
14. Here we are using equivalent weight (EW) to refer to number of grams of polymer needed to give one mole of acidic groups or one mole of acid precursor groups, such as SO_2F. More than one of these groups can be on a single side-chain.
15. Page, K. A. ; Cable, K. M.; Moore, R. B. *Macromolecules*, ***38***(15), 6472–6484, **2005**.
16. G. Alberti, G.; Casciola, M.; Costantino, U.; Leonardi,M. *Solid State Ionics **14***, 289, **1984**.
17. Casciola, D. Bianchi, *Solid State Ionics* 1985, ***17***, 287, **1985**.
18. Carriere, D.; Moreau, M.; Lhalil, K.; Barboux, P.; Boilot, J.P. *Solid State Ionics **185***, 162–163, **2003**.
19. Liu, W.; Ruth, K.; Rusch, G. *J. New Mat. Electrochem. Systems 4*, **2001** (227)
20. Madsen, L.A., Li, J., Hou J., Yandrasits, M.A., Haugen, G.M., **2010** ACS National Meeting Book of Abstracts**.**
21. Hickner, M. A.; Ghassemi, H.; Kim, Y. S.; Einsla, B. R.; McGrath, J. E. *Chem. Rev*., **2004,** *104*, 4587-4612.

22. Paddison, S.J. *Topics in Applied Physics*, ***113,*** 385-412, **2009**.
23. Kreuer, K. D. *et al. Journal of Power Sources* ***178***, 499-509, **2008**.
24. Danilczuk, M.; Perkowski, A.J.; Schlick, S. *Macromolecules*, *43*, 3352-3358, **2010**.
25. Danilczuk, M.; Coms, F.D.; Schlick, S. *Fuel Cells*, *8(6), 436-452,* **2008.**
26. (a) Spulber, M.; Schlick, S. *J. Phys. Chem.* A, *114(21)*, 6217-6225, **2010**. (b) Spulber, M.; Schlick, S., manuscript in preparation.
27. Haugen, G.M.; Emery, M.M.; Hamrock, S.J.; Yandrasits, M.A.; Barta, S. in "*ACS Symposium Series: Fuel Cell Chemistry and Operation I",* pp 137-151, **2010**.
28. Danilczuk, M.; Lancucki, L.; Schlick, S.; Hamrock, S.J.; Haugen, G.M. manuscript in preparation.
29. Emery, M.; Frey, M.;, Guerra, M.; Haugen, G.; Hintzer, K.; Lochhaas, K.H.; Pham, P.; Pierpont, D.;, Schaberg, M.; Thaler, A.; Yandrasits, M.A.; Hamrock, S.J. *Electrochemical Society Transactions,* ***11(1),*** 3-14, **2007**.
30. Schwiebert, K.E.; Raiford, K.G.; Escobedo, G.; Nagarajan, G. *Electrochemical Society Transactions*, ***1(8)*** 303-311, **2006.**
31. Wu, D.-S.; Paddison S.J.; Elliott, J.A. *Energy and Environmental Science* ***1***, 284-293, **2008**.
32. Frisch, M.J., et al., *Gaussian 03*., Gaussian Inc.: Wallingford, CT, **2004**.
33. Clark II, J. K.; Paddison, S. J. *Solid State Ionics* **Submitted.**

10. Project Management and Reporting

- Sixteen quarterly reports and four annual progress reports were submitted.
- Five public presentations were made by S. Hamrock at the DOE Hydrogen Program Annual Merit Review.
- Three presentations were made by S. Hamrock (one with A. Herring) to the Freedomcar Tech team.
- Two presentations were made by S. Hamrock to the DOE at the Golden Field Office in Golden CO.
- Three presentations were made by S. Hamrock and other team membranes to the DOE at 3M in St. Paul, MN.
- All subcontactors provided quarterly reports to 3M.
- Teleconferences were held periodically with either the whole team or sub teams as needed.
- Five internal meetings including all team members and subcontractors were held, two in St. Paul, MN and one in Golden, CO.

11. List of Acronyms

- CCB – catalyst coated backing
- CCM – catalyst coated membrane
- CCR – carbon centered radical
- CF – constant flow
- CGMD - coarse-grained molecular dynamics
- CS – constant stoichiometry
- DOE – Department of Energy
- DMA – dynamic mechanical analysis
- DPD - dissipative particle dynamics
- DSC – differential scanning calorimetry
- ECSA – electrochemical surface area
- EDAX – energy dispersive x-ray spectroscopy
- ESR – electron spin resonance
- EW – equivalent weight
- FCT – Fuel Cell Technologies Inc.
- FRR - fluoride release rate
- FTIR – Fourier transform infrared
- GDL – gas diffusion layer
- GDS – galvanodynamic scan
- GSS – galvanostatic scan
- HFR – high frequency resistance
- IC – ion chromatography
- IEC – ion exchange capacity
- IR – Infrared red
- LC-MS – liquid chromatography-mass spectrometry

- MASC – multi acid side chain
- MEA – membrane electrode assembly
- MW – molecular weight
- NMR – nuclear magnetic resonance
- OCV – open circuit voltage
- ORR – oxygen reduction reaction
- PDS – potentiodynamic scan
- PSS – potentiostatic scan
- PEM – oroton exchange membrane
- PES – poly ether sulfone
- PFIA – perfluorinated imide acid
- PFSA – perfluorosulfonic acid
- PTFE – polytetrafluoroethylene
- PVDF – polyvinylidene fluoride
- RH – relative humidity
- SAXS – small angle x-ray scattering
- SCCM – standard cubic centimeter per minute
- S-PEM – supported PEM
- SSC – short side chain PEM
- TFE - tetrafluoroethylene
- TGA – thermal gravimetric analysis
- WAX – wide angle x-ray scattering

12. Publications / Presentations

1. **Ghassemi, H.; Zawodzinski, T.A.jr.; David Schiraldi, D.A.; Hamrock, S.J.** “Perfluoro Ionomers with Crosslinked Structure for Fuel Cell Application” Presented at the 241st ACS National Meeting, March 30, **2011**, Anaheim CA.
2. **Hamrock, S.J.; Schaberg, M.; Abulu, J.; Haugen, G.; Emery, M.; Yandrasits, M.A.; Xiong, P.** “New Proton Exchange Membrane Development at 3M” Presented at the 241st ACS National Meeting, March 30, **2011**, Anaheim CA.
3. **Janarthanan,R.; Haugen, G.; Hamrock, S.J.; Herring, A.M.** “Application Of Zirconia and Ion Exchanged Heteropolyacid Nanocomposite Modified PFSA Ionomers for Proton Exchange Membrane Fuel Cells” Presented at the 241st ACS National Meeting, March 30, **2011**, Anaheim CA.
4. **Hamrock, S.J.** “New Fluorinated Ionomers for Proton Exchange Membrane Fuel Cells” Presented at the Sustainable Technology through Advanced Interdisciplinary Research Seminar, University of Tenneessee, March 21, 2011, Knoxville, TN.
5. **Schiraldi, D.A**. “Durability in PEM Polymers” Presented at Advances in Materials for Proton Exchange Membrane Fuel Cells Systems, February 21, **2011**, Pacific Grove CA.

6. **Yandrasits, M.A.** “New Fluorinated Ionomers for Proton Exchange Membranes” Presented at Advances in Materials for Proton Exchange Membrane Fuel Cells Systems, February 20, **2011**, Pacific Grove CA.
7. **Schlick, S. “**Fragmentation and Stabilization of Proton Exchange Membranes Used in Fuel Cells: Direct ESR and Spin Trapping Methods” Faculty of Chemistry, Jagiellonian University, December 10, **2010**, Krakow, Poland.
8. **Schlick, S. “**A Dream of Hydrogen. Degradation of Fuel Cell Membranes Using ESR Methods: Ex Situ and In Situ Experiments” Institute of Nuclear Chemistry and Technology, December 8, **2010**, Warsaw, Poland.
9. **Hamrock,S.J. “**New Fluorinated Ionomers for Proton Exchange Membrane Fuel Cells” Department of Polymer Science, University of Southern Mississippi, Decmber1, **2010**, Hattiesberg, MS.
10. **Schlick, S.** “Fuel Cells for Automotive, Stationary and Portable Applications: Challenges and Potential” Solvay Science for Innovation Congress, October 12-14, **2010**, Brussels, Belgium.
11. **Maalouf, M.; Bai, Y.; Paddison, S.; Schaberg, M.; Emery, M.; Hamrock, S.; Ghassemi, H.; Zawodzinski T.,** New Ionomeric Membranes for High Temperature Proton Exchange Membrane Fuel Cells: Effects of Different Side Chains' Acidity on Conductivity, Presented at 218th ECS Meeting, October 10-15, **2010** in Las Vegas, NV.
12. **Kumar M.; Paddison S.,** Chemical Degradation of the Side Chains of PFSA Membranes: An Ab Initio Study, Presented at 218th ECS Meeting, October 10-15, **2010** in Las Vegas, NV.
13. **Hamrock,S.J.; Schaberg, M.S.; Abulu, A.E.; Haugen, G.M.; Emery, M.A.; O'Conner, S.J.; Xiong, P.N.,**New Proton Exchange Membrane Development, Presented at 218th ECS Meeting, October 10-15, **2010** in Las Vegas, NV.
14. **Liu, Y.; Horan, J.L.; Schlichting, G.J.; Hamrock, S.J.; Haugen, G.M.; Herring, A.M.,** Morphology Study of Perfluorosulfonic Acid Ionomer for PEM Fuel Cell Application, Presented at 218th ECS Meeting, October 10-15, **2010** in Las Vegas, NV.
15. **Danilczuk, M.; Perkowski, A.J.; Schlick, S.** Ranking the Stability of Perfluorinated Membranes to Attack by Hydroxyl Radicals, *Macromolecules* **2010**, *43*, 3352-3358.
16. **Wu, D.; Paddison, S.J.; Elliott, J.A.; Hamrock, S.J.,** Mesoscale Modeling of Hydrated Morphologies of 3M Perfluorosulfonic Acid-Based Fuel Cell Electrolytes, *Langmuir,* **2010**, *26 (17),* 14308–14315.
17. **Schaberg, M.S.; Abulu, A.E.; Haugen, G.M.; Emery, M.A.; O'Conner, S.J.; Xiong, P.N.; Hamrock,S.J.,** New Multi Acid Side-Chain Ionomers for Proton Exchange Membrane Fuel Cells, *ECS Trans.* **2010**, *33 (1),* 627.
18. **Maalouf, M.; Bai, Y.; Paddison, S.; Schaberg, M.; Emery, M.; Hamrock, S.; Ghassemi, H.; Zawodzinski T.,** New Ionomeric Membranes for High Temperature Proton Exchange Membrane Fuel Cells: Effects of Different Side Chains' Acidity on Conductivity, Presented at 218th ECS Meeting, October 10-15, **2010** in Las Vegas, NV.

19. **Kumar M.; Paddison S.,** Chemical Degradation of the Side Chains of PFSA Membranes: An Ab Initio Study, Presented at 218th ECS Meeting, October 10-15, **2010** in Las Vegas, NV.
20. **Hamrock,S.J.; Schaberg, M.S.; Abulu, A.E.; Haugen, G.M.; Emery, M.A.; O'Conner, S.J.; Xiong, P.N.,**New Proton Exchange Membrane Development, Presented at 218th ECS Meeting, October 10-15, **2010** in Las Vegas, NV.
21. **Liu, Y.; Horan, J.L.; Schlichting, G.J.; Hamrock, S.J.; Haugen, G.M.; Herring, A.M.,** Morphology Study of Perfluorosulfonic Acid Ionomer for PEM Fuel Cell Application, Presented at 218th ECS Meeting, October 10-15, **2010** in Las Vegas, NV.
22. **Schlick, S.; Lin, L.; Danilczuk, M.; Hamrock, S.J.; Schaberg, M.S**., FTIR Study of Perfluorinated Ionomers and Model Compounds, *Prepr. Pap.-Am. Chem. Soc., Div. Fuel Chem.* **2010,** *55*, 231-232. Presented at 240th ACS National Meeting, August 22-26, **2010** in Boston, MA.
23. **Savant, D.M.; Zaowdzinski Jr., T.A.; Schiraldi,D.A.,** Chemical degradation studies of aromatic model compounds for fuel cell membrane applications, *Polym. Mat. Sci. Eng.* Presented at 240th ACS National Meeting, August 22-26, **2010** in Boston, MA.
24. **Schlick, S.; Spulber, M.,** ESR Detection of Early Events in the Fragmentation of Perfluorinated Model Compounds and Relevance to the Stability of Polymeric Membranes Used in Fuel Cells, *Polym. Mat. Sci. Eng. (Proc. ACS Div. PMSE)* **2010**, *103*, 137-138. Presented at 240th ACS National Meeting, August 22-26, **2010** in Boston, MA.
25. **Schaberg, S.; Abulu, J.; Emery, M.; Haugen, G.; Xiong, P.; Hamrock, S.** New fuel cell membrane development at 3M, *Prepr. Pap.-Am. Chem. Soc., Div. Fuel Chem.* **2010,** *55*, 285. Presented at 240th ACS National Meeting, August 22-26, **2010** in Boston, MA.
26. **Danilczuk, M.; Lin, L.; Schlick, S.; Hamrock, S.J.; Schaberg, M.S.**, ATR-FTIR and DFT Study of Perfluorinated Ionomer Membranes and Model Compounds, Poster presentation at the University of Detroit Mercy research Symposium, September 21, **2010**.
27. **Schlick S.,** Fuel Cells for Automotive, Stationary and Portable Applications: Challenges and Potential, Solvay Science for Innovation Congress, October 12-14, **2010**, Brussels, Belgium.
28. **Spulber, M.; Schlick, S. "**Using Cyclodextrins to Encapsulate Oxygen-Centered and Carbon-Centered Radical Adducts: The Case of DMPO, PBN, and MNP Spin Traps", J. Phys. Chem. **2010**, Web posting 12 May 2010.
29. **Yandrasits, M.A.; Hamrock, S.J.** "Membranes for PEM Fuel Cells" in "ACS Symposium Series: Fuel Cell Chemistry and Operation I", pp 1-13, **2010**.
30. **Haugen, G.M.; Emery, M.A.; Hamrock, S.J.; Yandrasits, M.A.; Barta, S.** "Open Circuit Voltage Fuel Cell Durability Testing using Multiple PEM MEAs" in *ACS Symposium Series: Fuel Cell Chemistry and Operation I*, pp 137-151, **2010**.
31. **Wu, D.-S.; Paddison,** "S.J. Mesoscopic Simulations of the Hydrated Morphology of the Short-Side-Chain Perfluorosulfonic Acid Ionomer", in *ACS Symposium Series: Fuel Cell Chemistry and Operation I*, pp 83-96, **2010**.

32. Schiraldi, D.A.; Zhou, C.; Savant, D.; Zawodzinski, T.A. Jr. "Chemical Durability Studies of PFSA and Nonfluorinated PEM Materials" in *ACS Symposium Series: Fuel Cell Chemistry and Operation I*, pp 125-136, **2010**.
33. **Maalouf, M. ;Pyle, B. ; Sun, C-N. ; Wu, D. ; Paddison, S.J. ; Schaberg, M.S.; Emery, M.A.; Lochhaas, K.H.; Hamrock, S.J.; Ghassemi, H.; Zawodzinski T.A. Jr** "Proton Exchange Membranes For High Temperature Fuel Cells: Equivalent Weight and End Group Effects on Conductivity*" ECS Transactions, 25(1),* 1473-1481, **2009.**
34. **Herring, S. Sachdeva, J. Rajeswari, G. Haugen, S. Hamrock,** "New Approaches to Composite PFSA Membranes for Enhanced Fuel Cell Performance" at the 217th Electrochemical Society Meeting, Vancouver, BC, Canada, April 25, **2010.**
35. **Zawodzinski, T.A. jr; Maalouf, M.; Pyle, B.; Sun, C-N.; Schaberg, M.; Hamrock, S.J.** "Proton Transfer and Water Motion in Low EW PFSAs" at the 217th Electrochemical Society Meeting, Vancouver, BC, Canada, April 25, **2010.**
36. **Janarthanan,R.; Haugen, G.; Hamrock, S.J.; Herring, A.M.** "Immobilization Of Composite Inorganic Additive On PFSA Ionomers For Improved Performance" at the ACS National Meeting, San Francisco, CA, 21-25 March, **2010**.
37. **Schlick, S. "**Polymer Degradation and Stabilization by ESR and ESR Imaging Methods: From Heterophasic Polymers to Ionomer Membranes Used in Fuel Cells" Seminar at the Georgia Institute of Technology, Atlanta, GA, March 8, **2010**.
38. **Danilczuk, M.; Perkowski, A.J.; Schlick, S.** "Ranking the Stability of Perfluorinated Membranes Used in Fuel Cells to Attack by Hydroxyl Radicals and the Effect of Ce(III): A Competitive Kinetics Approach Based on Spin Trapping ESR", *Macromolecules*, **43**, 3352–3358, **2010**.
39. **Kumar K.; Paddison, S.J.** "Ab initio calculations of chemical degradation of PFSA membranes", AIChE Annual Meeting, Nashville TN, November 12, **2009.**
40. **Hamrock, S.J.** "New Fuel Cell Membrane development at 3M", Fuel Cell Seminar, Palm Springs CA, November 2, **2009.**
41. **Maalouf, M.; Pyle, B.; Sun, C-N.; Wu, D.; Paddison, S.; Schaberg, M.; Emery, M.; Hamrock, S.; Ghassemi, H.; Zawodzinski T.A. jr,**"Proton Exchange membranes for high temperature fuel cells: Equivalent weight effects on conductivity" 216th Electrochemical Society Meeting, Vienna, Austria, October 9, **2009**.
42. **Schlick, S.; Perkowski, A.J.; Lin, L.; Mao Q.; Danilczuk**, M. "Stabilization of Perfluorinated Membranes Used in Fuel Cells: The Case of Cerium Ions" presentation at the ACS National Meeting, Washington DC, 16-20 August, **2009**.
43. **Sachdeva, S.; Herring A.M.; Janarthanan R.** "Synthesis ond Characterization of Heteropolyacid Immobilized Membranes" at the ACS National Meeting, Washington DC, 16-20 August, **2009.**
44. **Savant, D.; Schiraldi, D.A.; Zawodzinski T.A. Jr.** "Chemical durability study of nonperflorinated materials for fuel cell membranes" at the ACS National Meeting, Washington DC, 16-20 August, **2009.**

45. **Schlick, S.; Danilczuk, M.; Coms, F.D.** "Degradation of Fuel Cell Membranes Using ESR Methods: *Ex Sit*u and *In Situ* Experiments" at the ACS National Meeting, Washington DC, 16-20 August, **2009**.
46. **Spulber, M.; Schlick,S. "**Effect of Cyclodextrins on Encapsulation and Lifetimes of Spin Adducts: DMPO, PBN, and MNP as Spin Traps" at the ACS National Meeting, Washington DC, 16-20 August, **2009**.
47. **Schlick**, **S. "**Degradation of Fuel Cell Membranes Using ESR Methods: *In Situ* and *Ex Situ* Experiments" Polymer Degradation Discussion Group (PDDG), Sestri Levante, Italy, 6-10 September **2009**.
48. **Maalouf, M.; Pyle, B.; Sun, C-N; Wu, D: Paddison, S.J.; Schaberg, M; Emery, M; Lochhaas, K.H; Hamrock, S.J; Ghassemi, H.; Zawodzinski Jr, T.A.** "Proton Exchange Membranes for High Temperature Fuel Cells: Equivalent weight and end group effects on conductivity" *Electrochemical Society Transactions, **25(1),*** 1473-1481, **2009**.
49. **Aieta, N.V.; Stanis, R.J.; Horan, J.L.; Yandrasits, M.A.; Cookson, D.J.; Ingham, B.; Hamrock, S.J.; Herring, A.M.** "Clipped Random Wave Morphologies and the Analysis of the SAXS of an Ionomer Formed by Co-Polymerization of Tetrafluoroethylene and CF2=CFO(CF2)4SO3H." *Macromolecules, **42(15)**,* 5774–5780, **2009***.*
50. **Yandrasits M.A.; Hamrock, S.J.** "Membranes for PEM Fuel Cells" in "*ACS Symposium Series: Fuel Cell Chemistry and Operation I"*, pp 1-13, **2010**.
51. **Haugen, G.M.; Emery, M.M.; Hamrock, S.J.; Yandrasits, M.A.; Barta, S.** "Open Circuit Voltage Fuel Cell Durability Testing using Multiple PEM MEAs" in "*ACS Symposium Series: Fuel Cell Chemistry and Operation I",* pp 137-151, **2010**.
52. **Schlick, S.; Perkowski, A.J.; Lin, L.; Mao, Q.; Danilczuk, M.** "Stabilization of Perfluorinated Membranes Used in Fuel Cells: The Case of Cerium Ions" ACS National Meeting, Washington DC, 16-20 August, **2009**.
53. **Aieta, N.V.; Stanis, R.J.; Horan, J.L.; Yandrasits, M.A.; Cookson, D.J.; Ingham, B.; Hamrock, S.J.; Herring, A.M.** "Clipped Random Wave Morphologies Derived From SAXS Of Differing Equivalent Weights Of The 3M Ionomer : A New Way To Visualize Copolymers" Advances in Materials for Proton Exchange Membrane Fuel Cell Systems; Pacific Grove: California, February 17, **2009**.
54. **Sachdeva, S.; Sharma, N.; Hamrock, S.J.; Herring,A.M.** "Characterization of Heteropolyacid Immobilized Proton Exchange Membranes" Advances in Materials for Proton Exchange Membrane Fuel Cell Systems; Pacific Grove: California, February 17, **2009**.
55. **Danilczuk, M.; Perkowski, A.J.; Schlick, S. "**Comparing the Stability of Nafion™ and 3M Membranes Exposed to Hydroxyl Radicals: Spin Trapping Experiments, Advances in Materials for Proton Exchange Membrane Fuel Cell Systems" Pacific Grove: California, February 17, **2009**.
56. **Hamrock, S.J.** "Proton Exchange Membrane Development at 3M", Advances in Materials for Proton Exchange Membrane Fuel Cell Systems; Pacific Grove: California, February 16, **2009**.

57. **Schiraldi, D.A.** “Durability of Non-perfluorinated Membrane Materials for Fuel Cells” Advances in Materials for Proton Exchange Membrane Fuel Cell Systems; Pacific Grove: California, February 16, **2009**.
58. **Aieta, N.V.; Yandrasits, M.A.; Hamrock, S.J.; Stanis, R.J.; Horan, J.L.; Herring, A.M.** “Representative Morphologies of Nafion™ and Other PFSA Membranes Using a Fourier Transform Approach to the Reduction of SAXS Data at Different Levels of Hydration” 214th ECS National Meeting, Honolulu, HI, October 12, **2009**.
59. **Schlick, S.** “Fragmentation of Proton Exchange Membranes Used in Fuel Cells: Direct ESR and Spin Trapping Methods” Commissariat a l’Energie Atomique (CEA), Grenoble, France, October 23, **2008**.
60. **Hamrock, S.J.** “Membranes for PEM Fuel Cells”, Gordon Research Conference - Membranes: Materials & Processes, August 11, **2008**, Colby-Sawyer College New London, NH.
61. **Paddison, S.J.** “Mesoscopic modeling of the morphology and state of water in hydrated PFSA fuel cell membranes”, 236th ACS National Meeting & Exposition, August 18, **2008**, Philadelphia, PA, USA
62. **Yandrasits, M.A.** “ PEMFC membrane development at 3M”, 236th ACS National Meeting & Exposition, August 18, **2008**, Philadelphia, PA, USA
63. **Schiraldi, D.A.** “Chemical durability studies of PFSA and nonfluorinated PEM materials”, 236th ACS National Meeting & Exposition, August 20, **2008**, Philadelphia, PA, USA
64. **Wu, D.; Paddison, S.J.; Elliott, J.A.** “A comparative study of the hydrated morphologies of perfluorosulfonic acid fuel cell membranes”, *Energy and Environmental Science* DOI:10.1039/b809600G, **2008**.
65. **Schlick, S.** “Direct ESR and Spin Trapping Methods for the Study of Fragmentation in Polymer Membranes Used in Fuel Cells”, ESR Group, Department of Chemical Physics, Weizmann Institute of Science, Rehovot, Israel, 3 June **2008**.
66. **Herring, A.M.; Aieta, N.; Kuo, M-C.; Dec, S.; Frey, M.; Genupur, A.; Haugen, G.M.; Hamrock, S.J.** “*Improving the effect on proton conduction in PFSA polymers by the smart addition of Heteropoly Acids*” 213th ECS National Meeting, Phoenix, AZ, May 18, **2008**.
67. **Hamrock, S.J.** “*New Membranes for PEM Fuel Cells*”, 212th ECS National Meeting, Washington D.C. October 8, **2007**.
68. **Emery, M.; Frey, M.;, Guerra, M.; Haugen, G.; Hintzer, K.; Lochhaas, K.H.; Pham, P.; Pierpont, D.;, Schaberg, M.; Thaler, A.; Yandrasits, M.A.; Hamrock, S.J.** "The Development of New Membranes for Proton Exchange Membrane Fuel Cells", *Electrochemical Society Transactions,* ***11(1),*** 3-14, **2007**.

13. Published Patent Applications

- **US 20110151350** Fuel Cell Subassemblies Incorporating Subgasketed Thrifted Membranes.
- **US 20090269644** Proton Conducting Materials.

14. Task Schedule

Task	Project Milestones	Milestone Completion Date			Progress Notes
		Original Plan	Revised Plan	Percent Complete	
1	Complete the test method development Install and modify new equipment	04/01/08		100%	Completed.
2	Identify first set of more conductive and durable materials	04/01/09		100 %	Completed
3	Identify material classes showing the higher promise based on performance in ex situ and single cell tests	10/01/09		100%	Completed.
4	Down select best performing catalyst/GDL/process based on performance in ex situ testing and single cell testing	10/01/10	12/01/10	100%	Completed.
5	Perform final testing with the best components.	03/31/10		100%	Completed.

Appendix 1 - Additional Polymer Modifications - Carried out with in Collaboration with Case Western Reserve University

Several approaches have been studied to prepare ionomers for a high temperature proton exchange membrane (PEM) fuel cell. The goal is for these ionomers to be very low equivalent weight (EW), chemically stable, solvent resistant and highly conductive. The synthetic approaches included grafting, multiblock and hybrid formation and cross-linking. The approaches described here are:

e) Tethering perfluorosulfonic side-chain into polyarylene backbone.
f) Hybrid materials from PFSA and polyarylenes
g) Cross-linking of low EW PFSA

a) Tethering perfluorosulfonic side-chain into polyarylene backbone

There are numerous examples of sulfonated aromatic polymers in the literature designed for PEM fuel cells. The idea of using aromatic polymers such as polyethersulfones and ketones comes mainly from the fact that these materials have high glass transition, exceptional thermal and chemical stability and outstanding mechanical properties. Sulfonic acid groups in most of these sulfonated aromatic polymers are directly attached to the benzene rings on the backbone by direct sulfonation of polymers or starting monomers. Among others, polymer electrolyte membranes carrying sulfonic acid groups on their aromatic backbone demonstrate excellent thermal stability. It has been suggested that proton conductivity of the sulfonated polymers and acidity of the sulfonic group are strongly related. One approach to prepare materials with both high glass transition and super acid groups is to insert perfluorinated methylene spacer between sulfonic and benzene ring. The following methods have been investigated to prepare materials with aromatic backbone and perfluorosulfonic side chain:

Friedel-Crafts acylation of aromatic rings using 4-(sulfonylfluoride)butyryl fluoride (SFBF)

One key reagent available for grafting PFSA side chain to aromatic ring is 4-(sulfonylfluoride)butyryl fluoride and Friedel-Craft was considered as the method of grafting. Friedel-Crafts acylation of aromatic rings by perfluoroalkylacyl fluoride is not very common and very few examples with little detail exist. To investigate this reaction a set of experiments was designed between SFBF and phenylether as a model compound. The structures of expected products are shown on Figure 94. Boron trifluoride (BF_3) is a strong Lewis acid commonly used in acylfluoride acylation reactions. BF_3 in the form of gas or solution of $BF_3.Et_2O$ in dry dichloromethane was used under various conditions (temperature, pressure, etc.) and in all cases only partially hydrolyzed SFBF was observed by F-NMR with no detectable acylated or sulfonylated products. The structure of the hydrolyzed SFBF is shown in Figure 95. ^{19}F NMR study of the byproducts revealed only the disappearance of the fluorine atom (25.23 ppm) in the acylfluoride presumably due to hydrolysis (Figure 96). It was concluded that fluorine atoms surrounded the carbonyl group of perfluorinated acylfluoride in SFBF cause acylium ion intermediate necessary for Friedel-Crafts acylation become very unstable and therefore unlikely to form. These experiments also confirmed that perfluorinated sulfonylfluoride group of SFBF is hydrolytically more stable compared with acylfluoride.

Figure 94. Target compounds for Friedel Crafts reactions.

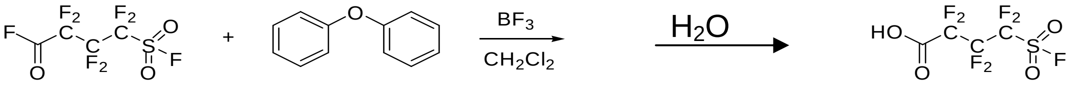

Figure 95. Friedel Crafts reaction on model compound.

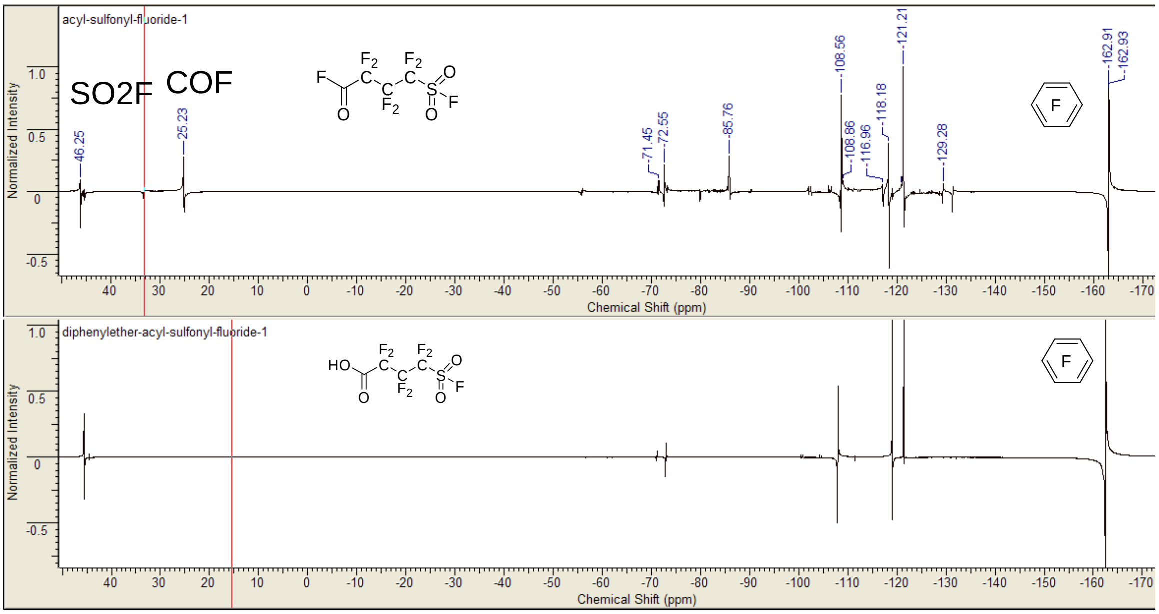

Figure 96. F-NMR spectra of SFBF (top) and crude product of acylation reaction (bottom).

Grafting SFBF into sulfonated polyethersulfone (SPES) through sulfonamide linkages

A commercially available polyethersulfone (PES) was selected and sulfonated with chlorosulfonic acid to form SPES polymers with wide range of degree of sulfonation. SPES-550 (EW=550 g/mol) was chosen for preparation of grafting system. It was treated with a chlorinating reagent to convert sulfonic acid groups into sulfonylchloride followed by ammonolysis to form sulfonamide groups. The SPES in sulfonamide form treated with excess 4-(sulfonylfluoride)butyryl fluoride to generate imide linkages. Based on our previous experiments which showed high reactivity of carbonylfluoride compared with sulfonylfluoride the imide linkage was expected to be an unsymmetric type (Figure 97). Therefore, the final product after hydrolysis of sulfonylfluoride groups contains imide, perfluorosulfonic and probably unreacted sulfonated aromatic groups. However, experimental ion exchange capacity (IEC) was only 0.5 mmol/g which is much lower than the starting SPES-550 (1.8 mmol/g). This might be due to poor conversion during each step and presence of significant amount of Ar-SO3H and Ar-SO2NH2. They are considered as weak acids compared with Rf-SO3H. Proton conductivity of the membrane was 21 mS/cm at room temperature and 100% RH which is relatively high when compared with an aromatic analog. SPES-2000 (IEC=0.5 mmol/g) would have conductivity below 5 mS/cm under the same condition (IEC of BPSH-20 is about 0.9 mmol/g with conductivity around 10 mS/cm). This relatively high value of proton conductivity can be explained by the presence of perfluorsulfonic groups without considering the effect of protons from SO2-NH-CO group. Solution NMR was unsuccessful due to low solubility of the product in common solvents. Partial crosslinking and formation of two imide groups is possible which cause low solubility of the product.

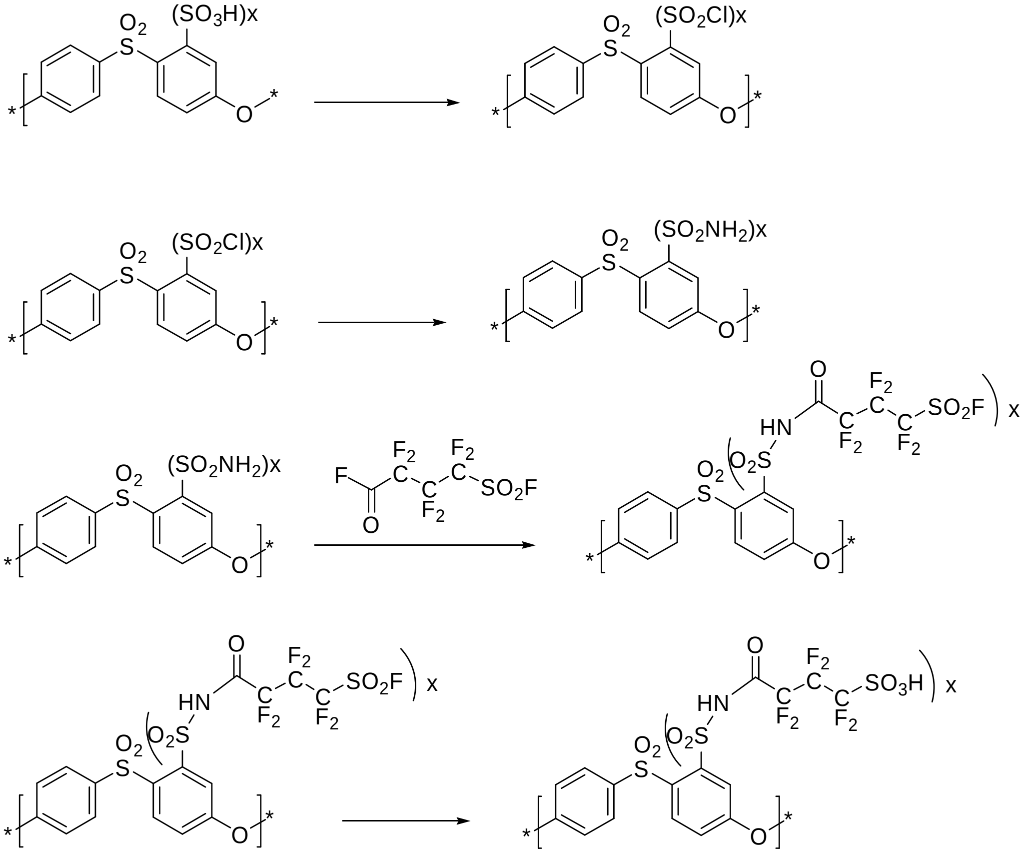

Figure 97. Grafting SFBF into sulfonated polyethersulfone (SPES) through sulfonamide linkages.

Grafting PFSA ionomers into sulfonated polyethersulfone

This set of experiments was designed to make hybrid materials by grafting PFSA ionomers into sulfonated polyethersulfones such as SPES and BPSH. The reaction sites are sulfonamide groups of PFSA and sulfonyl chloride of sulfonated polyethersulfone which form sulfonimide linkage. PFSA ionomer used in these experiments was low molecular weight oligomers with EW around 640 g/mol which 25% of the functional groups were converted to sulfonamide. Sulfonated polyethersulfones

were treated with thionyl chloride to generate sulfonyl chloride functional groups. Reaction between two polymers took place in solution at room temperature (Figure 98). Due to the fact that both reacting polymers have multi functional groups cross-linking was expected and in all cases gel formation was observed. The solubility of resulting polymer was limited and films cast from solution were opaque. Experimental IEC values of the resulting materials were in the range 0.6-1.2 mmol/g which were lower than calculated values possibly due to the presence of residual tertiary amine or sulfonamide. Proton conductivity of the membranes at 18℃ inside water was in the range of 25-35 mS/cm except for the sample made from SPES-1100 and three times 3M ionomer which was 150 mS/cm. All the membranes swell extensively in hot water resulting poor mechanical strength. Anisotropic swelling was observed in three samples which membranes swell in one direction more than the other two directions (
Table 7).

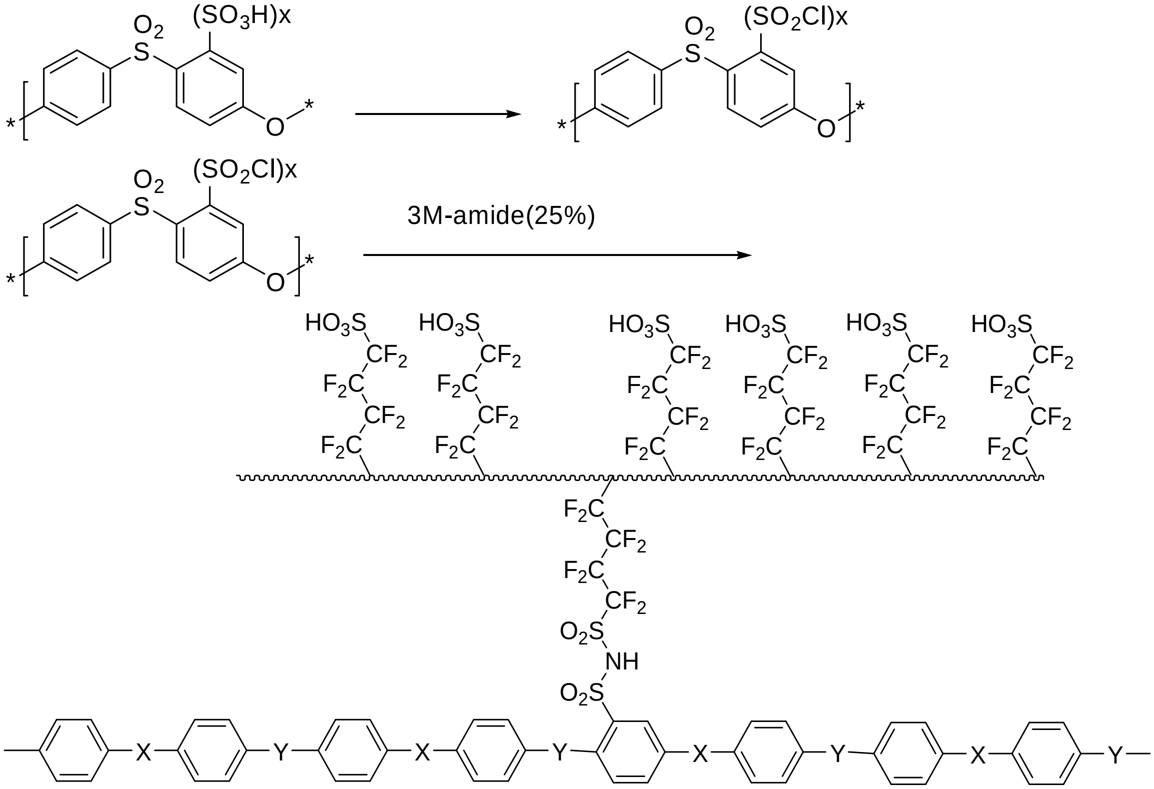

Figure 98. Grafting PFSA ionomers into sulfonated polyethersulfone

Table 7. Properties of PFSA ionomers after grafting into sulfonated polyethersulfone.

		wt. ratio[a]	IEC (meq/g)	Cond. (mS/cm)[b]	Swelling Δx,y -Δz
1	SPES-850	1:1.5	0.35	30	

2	BPSH-35	1:1.5	0.75	25	
3	SPES-1100	1:1.8		35	5-60
4	SPES-850	1:1.3		35	9-20
5	SPES-1100	1:3		150	30-10

a) wt ratio of aromatic polymer to 3M-sulfonamide. b) Measured at r.t. in water

Poly(arylene ether)s with PFSA pendent groups

Figure 99 shows the synthetic route for the preparation of polysulfone (PSU) with perfluorosulfonic side-chain. Lithiation of the polysulfone was achieved in a 3 wt% THF solution with 10M n-buthyllithium, at temperatures ranging from -60°to -80℃ under argon. The lithiation proceeds very fast (0.5 h) as demonstrated by rapid color change from pale yellow to pink/red. Introduction of perfluoroalkyl side chain to an aromatic ring has been demonstrated by the reaction of perfluoroacylfluoride with the lithiated PSU. In several experiments addition of SFBF to the lithiated PSU solution produced cross-linked gels. This behavior can be explained by the fact that SFBF has two potentially reactive sites of acylfluoride and sulfonylfluoride and high reactivity of nucleophile in lithiated aromatic rings in PSU. The problem of gel formation was greatly reduced by careful addition of lithiated PSU solution into excess SFBF. F-NMR of starting SFBF and product confirmed the formation of product.

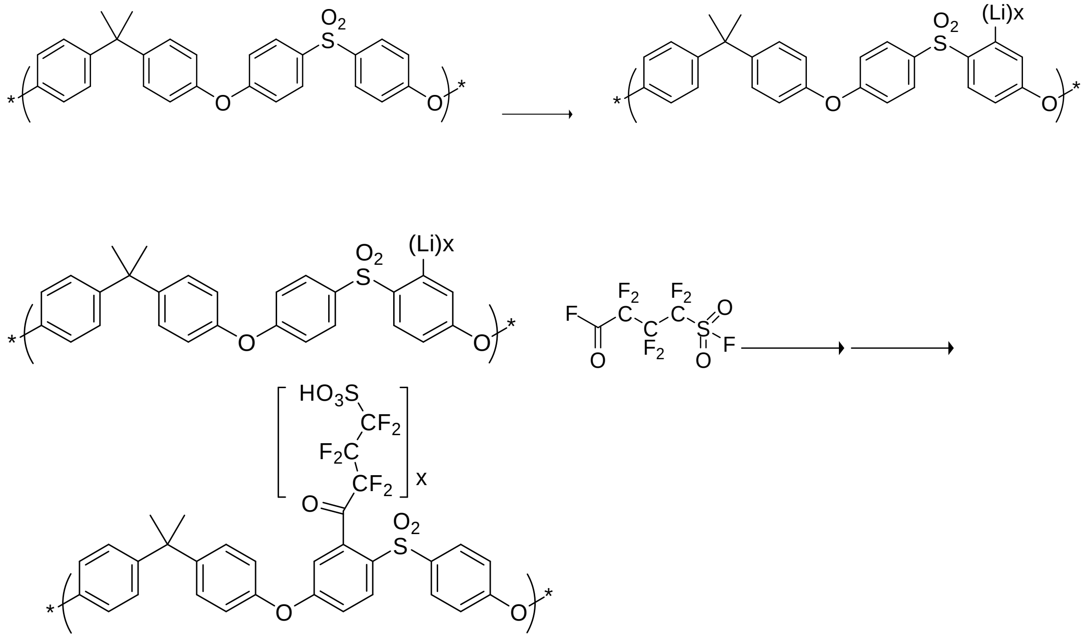

Figure 99. Synthesis of Poly(arylene ether)s with PFSA pendent groups

Table 8 summarizes the results of the characterization of the grafted polymers and sulfonated polyethersulfone (SPES). The proton conductivity values of PSU-PFSAs were higher than those of SPESs at any IEC. One should consider the possibility that the acidity of the perfluoroalkyl sulfonic acid of PSU-PSA is significantly high compared with that of the aromatic sulfonic acid of the SPES, which caused easy dissociation of sulfonic acid and showed higher proton conductivity. PSU-PSA membranes showed relatively high water absorption and λ values compared with SPES having similar IEC which also affect the proton exchange properties of these membranes. This distinctive behavior is believed to be partly related to the microphase separation in the membrane. Presence of perfluoroalkyl spacers in PSU-PFSA provide higher mobility for sulfonic acid groups as well as more free volume between the packed polymer chains may explain some of these results.

Table 8. Properties of poly(arylene ether)s with PFSA pendent groups compared with SPES.

Sample	IEC (meq/g)	Water uptake (%)	λ (H_2O/SO_3H)	Conductivity (mS/cm) (100%RH)		
				20℃	40℃	80℃
PSU-PSA-1	1.12	100	49	60	73	91
PSU-PSA-2	0.66	78	65	56	63	80
PSU-PSA-3	0.45	30	36	45	50	62
PSU-PSA-4	0.04	-	-	5	5	6
SPES-850	1.17	34	16	48	52	64
SPES-1150	0.87	10	6	11	15	22

The dynamic mechanical analysis (DMA) and tensile test of polymeric electrolytes in various temperatures and water content provide valuable information about durability of the membranes. The dynamic mechanical properties (DMA) of PSU-PSA between 50 and 250℃ have been investigated (Figure 100). The loss tangent curve for this membrane showed a maximum at 196.5℃ which is the c haracteristic peak of α-relaxation of polysulfone. The tan δ value for unsulfonated starting polymer is lower and recorded around 187℃ which is partially due to the interaction of sulfonic acid groups in PSU-PSA. The tan δ peak for PSU-PSA is not entirely represented because the material becoming too brittle and failed at higher temperatures. Tensile properties of PSU-PSA membrane were compared with SPES and Nafion™ membranes after the samples being equilibrated at 60% RH for 48 hours. The result showed higher tensile modulus for PSU-PSA-1 (168 MPa) and SPES-850 (770 MPa) compared with Nafion™ (99 MPa) which is expected from less flexible backbone in aromatic polymers. Tensile strength of these membranes showed values of 7, 57 and 11 Mpa for PSU-PSA-1, SPES-850 and Nafion™, respectively. Samples of PSU-PSA snapped prematurely before reaching the yield point. This behavior can be mainly due to the presence of submicron gel particles produced during the synthesis of the polymer.

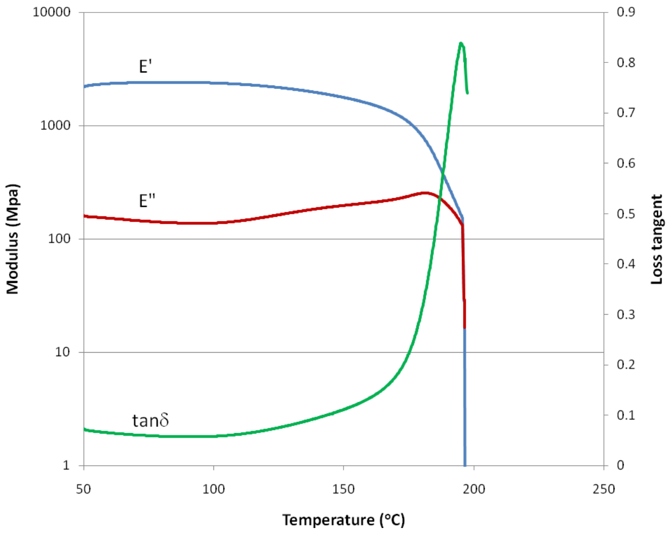

Figure 100. DMA traces of PSU-PSA-1. Storage modulus (E'), loss modulus (E"), and loss tangent (tanδ¨).

The H2/air fuel cell performance of PSU-PSA membrane (70 µm) was compared with that of Nafion™ 112 membrane (50 µm) in Figure 101. The experiment was performed at 30℃ and 75% relative humidity using commercially available gas diffusion electrode coated with Pt/C which was impregnated with Nafion™ ionomer. A power output of 0.26 Wcm-2 was recorded at a current density of 0.65 Acm-2 and cell voltage of 0.4 V for PSU-PSA. In comparing the two membranes, there are similarities in the polarization curves and power output in spite of differences in thickness and proton conductivities between PSU-PSA-1 (0.060 S/cm) and Nafion™112 (0.087 S/cm) under the test conditions.

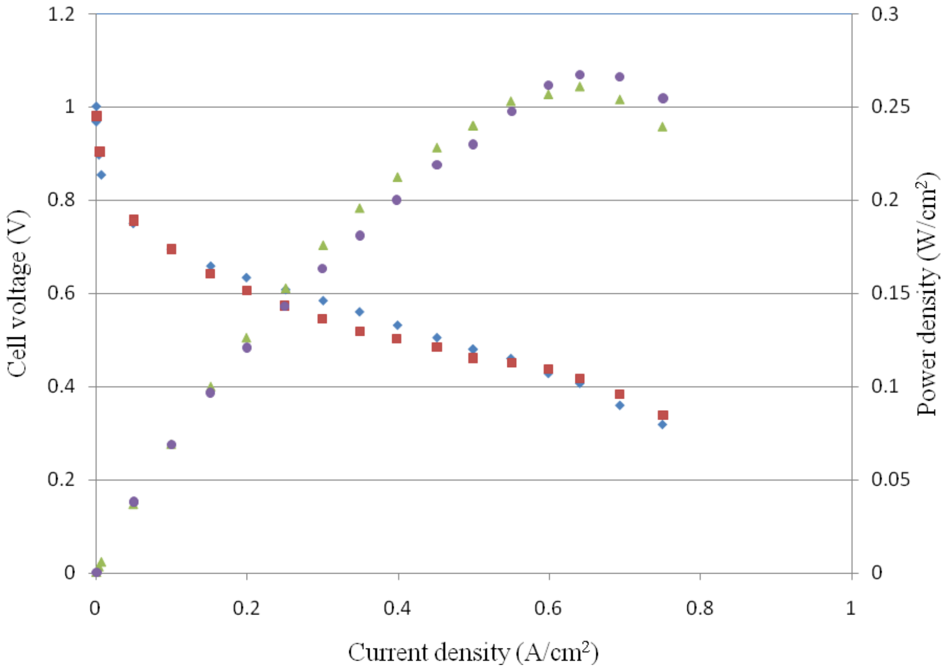

Figure 101. Polarization curves of PSU-PSA-1 (71 μm; cell voltage:■, power output:●) and Nafion™112 (50 μm; cell voltage:♦, power output: ▲); Conditions: cell temperature = 35℃; H2/air; atmospheric pressu re; bubbler temperature = 30℃; electrode area = 5 cm2.

b) Hybrid materials from PFSA and polyarylenes

The goal of this work was to prepare hybrid materials with defined comb shape structure using PFSA ionomers as main chain and highly sulfonated poly(ether sulfone)s as side-chains (Figure 102). It was expected that the material with comb structure generate suitable morphology for proton transport under dry condition. Three PFSA ionomers with arylhalide groups and BPSH-100 oligomers with phenol end-groups were tested (Figure 103).

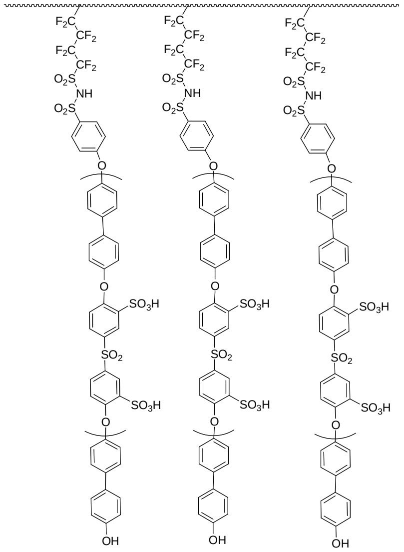

Figure 102. Proposed hybrid structure.

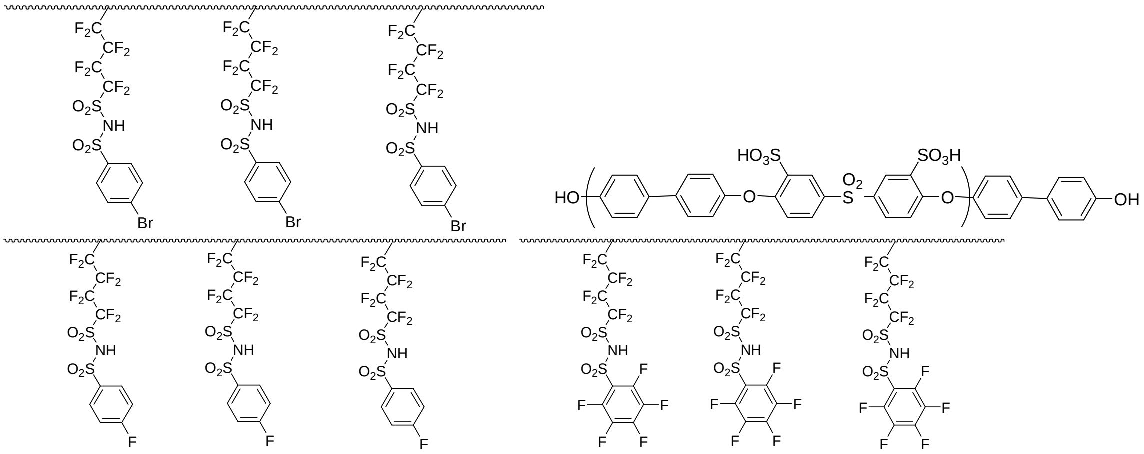

Figure 103. Starting materials for hybrid compounds

All the aryl functionalized PFSAs were prepared from PFSAmide (PFSA with sulfonamide groups) and corresponding arylsulfonyl chloride (Figure 104). Reaction between phenol-terminated BPSH-100 and each functionalized PFSA was designed in order to form ether linkages through nucleophilic aromatic displacement. Unfortunately, in all cases final products were poor quality brittle films due to low reaction yield or side-reactions. Knowing that all the starting materials were fully characterized and their structures were confirmed by analytical methods such as NMR the final step of attaching sulfonated polyarylene to PFSA was considered as the critical step and responsible for undesired product.

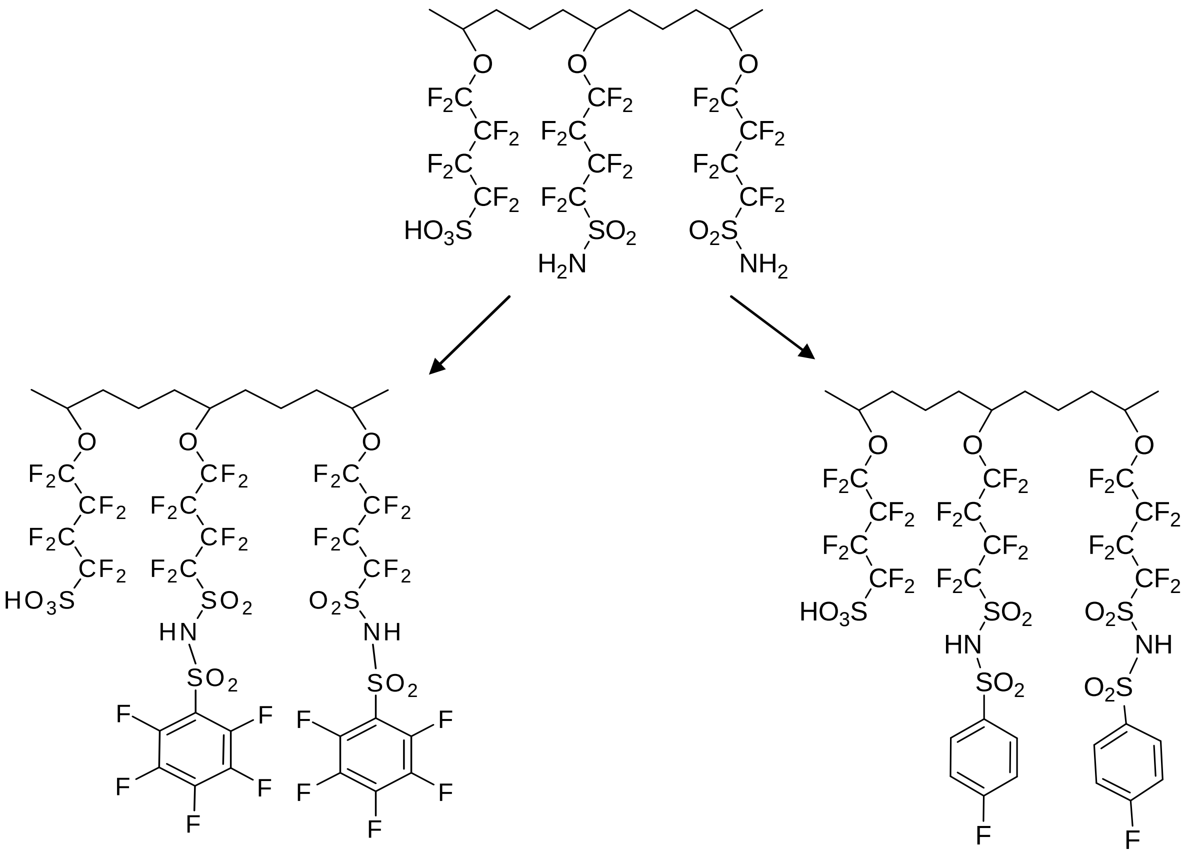

Figure 104. PFSA derivatives with 4-fluorophenysulfone and pentafluorophenyl sulfone

c) Cross-linked low EW PFSA

As discussed above, low EW gives high conductivity, but mechanical properties and durability are compromised. At low EW, membranes swell excessively and become nearly soluble in water at higher temperature. One way to stabilize polymers and prevent from dissolving is by chemical modification to form crosslinking structure. Two main approaches were studied; crosslinking through the use of a cure site monomer (reactive side chain) or crosslinking via the sulfonyl fluoride precursor to the ionomer.

Bromine Cure Site Monomer Approach

The initial focus was on the use of bromine containing cure site monomers. The structure shown in Figure 105 has the same backbone and sulfonic acid side chain as the standard ionomer but also has a small amount of a third monomer that has a bromine in the side chain.

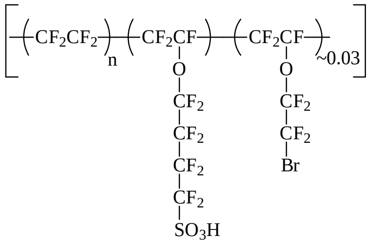

Figure 105 3M Ionomer containing bromine cure site monomer

The bromine can be abstracted in the presence of a multifunctional crosslinker, such as triarylisocyanurate, to form covalent bonds. This chemistry is well established in the fluoroelastomer industry and was considered a promising path for crosslinking our ionomer membranes. Preliminary data showed that the bromine functionality was reactive and it was possible to make a crosslinked network. Despite the evidence of some reaction, significant problems exist in this approach. Most notably, the hydrocarbon crosslinker and peroxide initiators are not miscible with the fully fluorinated ionomer. Melt bending of these compounds would result in small phase separated domains and effective reaction with the ionomer polymer was difficult to reproduce.

An ultraviolet light (UV) light cured approach was also attempted in a means of initiating the cure reaction. This approach was also subject to phase separation problems with the reactants. In addition, it was recognized that the stoichiometery was an issue. An equal molar amount of reactants would result in incomplete cure. In order to ensure the bromine was completely reacted an excess of crosslinker was required. Ultimately, this approach was abandoned due to these difficulties.

Nitrile Cure Site Monomer Approach

Another well used crosslinker in the fluorpolymer industry is a side chain nitrile group which can trimerize to form a triazine ring crosslink. The polymer shown in Figure 106 was made and reaction with the side chain nitrile (-CN) were attempted.

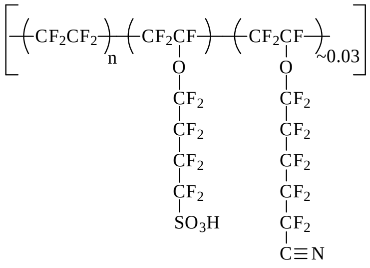

Figure 106 3M ionomer containing nitrile cure site monomer

Several attempts were made to compound this polymer with the appropriate catalyst followed by a heat cure. In all cases there was no evidence of reaction. It is speculated that the sulfonyl fluoride or sulfonic acid functionality in the ionomer was poisoning the nitrile trimeriztion catalyst.

Cross-linked PFSA: sulfonylfluoride approach

PFSA ionomers before hydralysis contain sulfonyl fluoride groups which were considered and studied as reactive sites. Sulfonyl fluoride is susceptible for nucleophilic attack to form sulfonate, sulfonamide or sulfonic ester.

An alternative approach to the cure site monomer method is to use the reactive sulfonyl fluoride group as crosslink site. The reaction of a perfluorinated sulfonamide with the sulfonyl fluoride in the presence of a HF scavenger will form the perfluoro sulfonamide and shown in Figure 107.

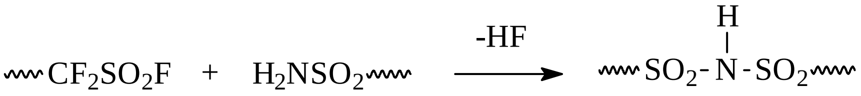

$$\sim CF_2SO_2F + H_2NSO_2\sim \xrightarrow{-HF} \sim SO_2-\overset{H}{\overset{|}{N}}-SO_2\sim$$

Figure 107. Reaction of a sulfonyl fluoride with a sulfonamide to form a sulfonamide

The procedure for making the sulfonamide from the sulfonyl fluoride by reaction with ammonia has been worked out in the PFIA synthetic work and was used in the crosslinking experiments. Two approaches were considered. The first is to partially react some of the sulfonlyl fluoride groups in the precursor polymer to the sulfonamide form followed by the intramolecular reaction with remaining sulfonyl fluorides to form the imide crosslink. This approach was difficult to control and selectively reacting a fraction of the sulfonyl fluoride proved impractical.

Also attempted was cross-linking under melt condition. A series of mono and difunctional aliphatic and aromatic molecules such as, arylsulfonamide, hexamethylene diamine, bisphenol-A and oxydianiline were examined. Various amounts of each of these compounds mixed with the waxy oligomer and pressed several times using a hot press. The temperature of the hot press varied between 100-200℃ and each time the samples were hold around 3 minutes under the press. The amount of difunctional cross-linking compounds was calculated to be 20 mol% of sulfonyl fluoride groups providing a condition for highly crosslinked products. After each press the films were removed and their mechanical behavior was compared with the blank sample. Figure 108 shows a typical structure of PFSA after cross-linking. Only membranes reacted with hexamethylene diamine and oxydianiline formed highly cross-linked products. However, the films were not homogenous due to poor mixing condition which prevent diamino compounds blend thoroughly with the oligomer.

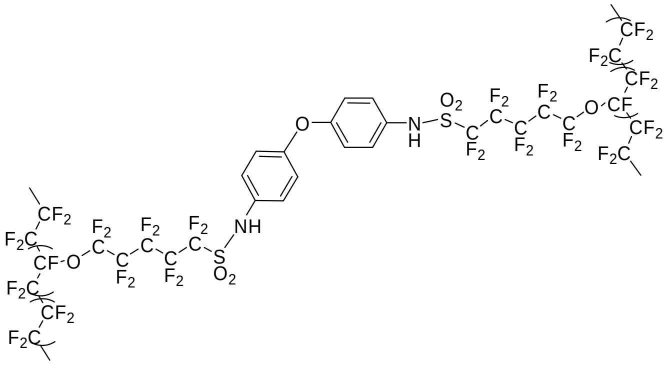

Figure 108. PFSA ionomer cross-linked with an aromatic diamine.

Cross-linked PFSA: sulfonamide-sulfonyl chloride approach

To overcome the problems of working with infusible PFSA precursor, new PFSAs with sulfonamide groups (PFSAmide) were employed. PFSAmides with various degree of functionalization were prepared by partial ammonolysis of sulfonyl fluoride of PFSA precursor followed by hydrolysis of the remaining to sulfonic acid. A set of reactions was design between PFSAmide and functionalized polyethersulfones to form cross-linked membranes. In these experiments sulfonated polysulfones (SPES) with low level of sulfonation were selected as cross-linkers. Several reactions were set up between PFSAmide with various percent of amide groups on the side-chain and SPES carrying sulfonyl chloride. Multiple sulfonyl chloride sites on SPES were expected to react with amide groups and generate sulfonimide cross-linked structure as shown in Figure 109. Qualitative swelling test in hot water showed that in most cases the final products had better dimensional stability compared with the control one. The highest cross-linking occurred when PFSAmide with high level of amide groups were used.

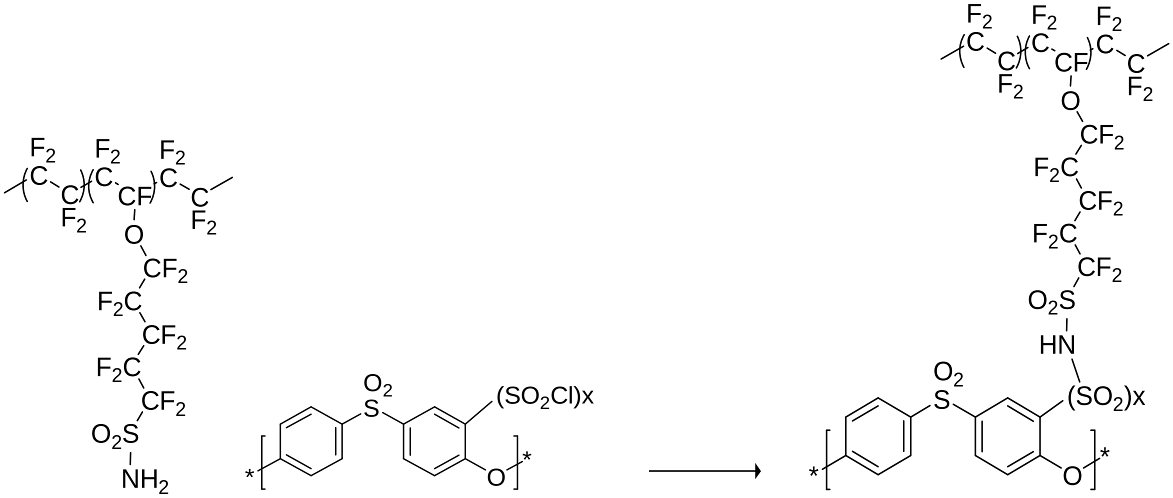

Figure 109. Cross-linking PFSA via sulfonamide-sulfonyl chloride approach

Cross-linked PFSA: sulfonamide-activated arylfluoride approach

Decafluorobiphenyl reacts with bisphenols to form linear poly(arylene ether)s. High reactivity of fluoro atoms in decafluorobiphenyl provides an easy route to do further chemistry and produce new materials. Two poly(arylene ether) oligomers with Mw of 3k and 5k were synthesized from 6F-bisphenol-A and decafluorobiphenyl. Molecular weight of the oligomers was controlled by using slight excess of decafluorobiphenyl which also serve as reactive end-groups. Reaction of PFSAmide (88% sulfonamide) with these two oligomers in NMP resulted products which were insoluble in many organic solvents (Figure 110). Films cast from mixtures of PFSAmide and either of these oligomers remain flexible after heating at 120℃ for one hour and show small degree of swelling after treating in hot water. Films prepared from 88% amide containing PFSAmide show much better dimensional stability compared with those made from PFSAmide with 7% amide content. However, proton conductivity of the samples made from low amide content materials was higher and measured in the range of 80-250 mS/cm depending on the ratio of PFSAmide to oligomers.

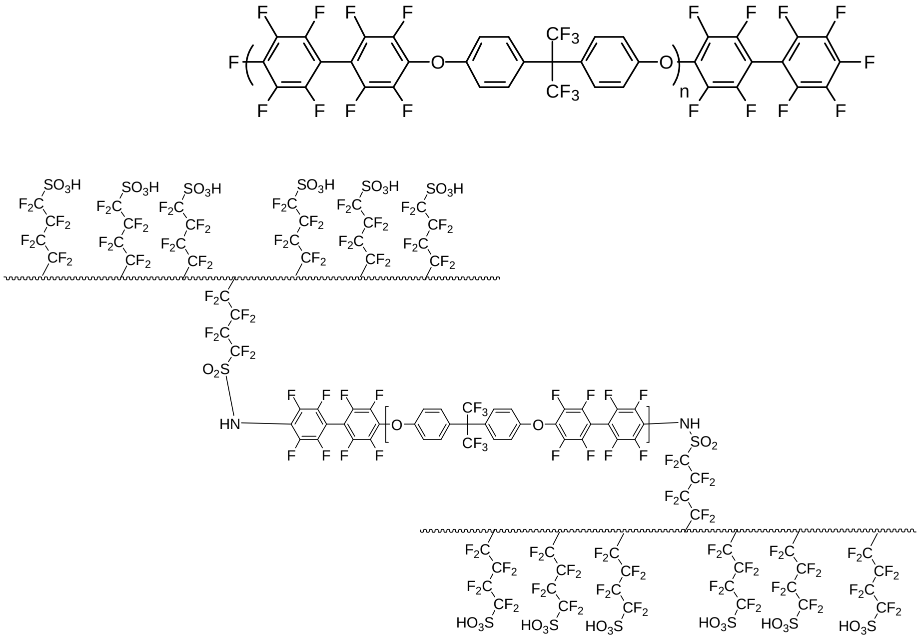

Figure 110. Cross-linking PFSA via sulfonamide-activated arylfluoride approach.

Cross-linked PFSA: PFSA with pendent fluorobenzene rings

Two functionalized PFSA ionomers prepared from PFSAmides and 4-fluorobenzenesulfonyl chloride and pentafluorosulfonyl chloride (Figure 111). Fluorobenzene groups are reactive sites toward phenolates and used to form cross-linked materials. These functionalized PFSA when reacted with various bisphenolate salts, such as biphenol dipotassium salt, form cross-linked products (Figure 112). The highest degree of cross-linking obtained when highly functionalized PFSA (89% amide content) with pentafluorobenzene groups reacted with biphenolate in DMSO. The amount of biphenolate was calculated to be about 8 wt% of the total ionomer and 30 mole% of the fluorobenzene groups. The whole process of casting and curing was complete in less than an hour. Film was clear and show very small swelling before and after treating in boiling water. Conductivity of the cross-linked ionomer was 40 mS/cm (in water) and 7 mS/cm (at 60% RH). Cross-linked product was not soluble or even swelled in acetonitrile while the starting ionomer readily swelled and disintegrated in acetonitrile.

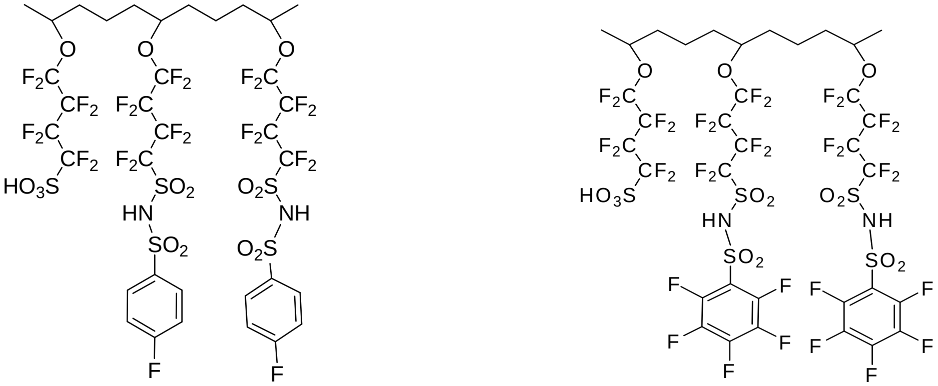

Figure 111. PFSA with fluorobenzene rings on the side-chain.

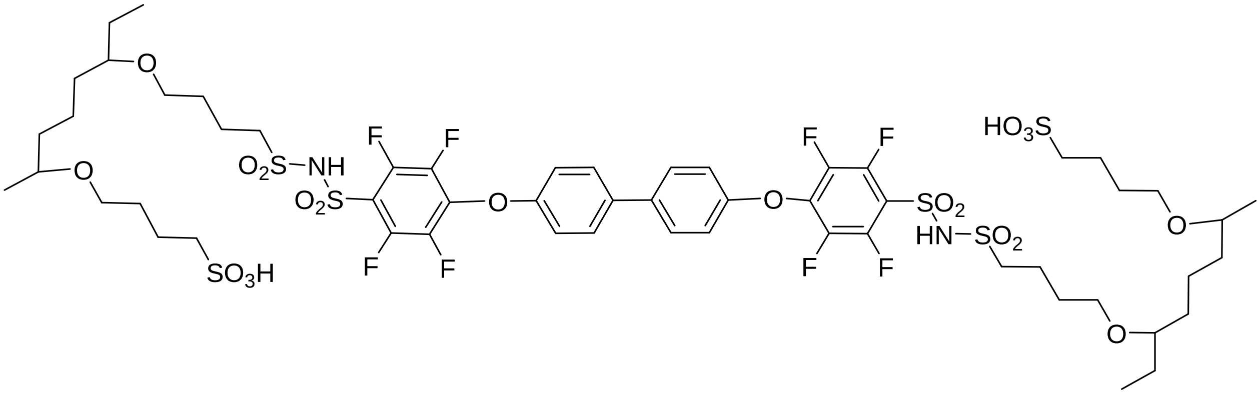

Figure 112. Proposed structure of cross-linked PFSA with biphenol.

The membranes with least dimensional stability were those made from low amide content (28%) and 4-fluorobenzenesulfonyl chloride which produced materials with lower cross-linked density. This can be explained by the fact that pentafluorobenzene has more reaction side and fluorine atoms are more reactive compared with 4-fluoro derivative. As expected samples made from low amide content had relatively higher proton conductivity. Table 9 shows the summary of the results.

Table 9. Summary of curing experiments between functionalized PFSA and biphenolate

Exp	Imide	BP wt%	Rx condition	Film quality	Cond.
1	89-F5	8	Gelled in solution, hot pressed at 190C	Lot of small gel particles	
2	89-F5	8	Two sol. Mixed and cast. Dried at 120C	Clear, low swelling	40 mS/cm(100%)

3	28-p-F	4	Two sol. Mixed and cast. Dried at 120C	Opaque, high Swelling	
4	28-F5[1]	4	No gel in solution	Semi-transparent High swelling	90-110 mS/cm (100%)
5	28-F5	4	Two sol. Mixed and cast. Dried at 120C	Transparent High swelling	90-110 mS/cm (100%)

1) conductivity: 115 mS/cm (100%), 6 mS/cm (75%), 1 mS/cm (60%)

An alternative approach to generate bisphenolates in situ is to use masked bisphenols. Masked bisphenols are synthesized from bisphenols and an alkylisocyanate and easily purified by crystallization. They decompose at high temperature in the presence of a carbonate ion and generate bisphenoxides and gases biproducts. To alleviate some of the problems associated with the preparation and introduction of biphenoxide ion in the reaction masked biphenol (Figure 113) was utilized. Masked biphenol and functionalized PFSA (with pentafluorobenzene) formed transparent film after casting and curing at 230℃ for 3 minutes. Presence of small voids were noticed in all cured membranes which caused probably by evolution of volatile gases generated during decomposition of the masked biphenol. Samples made from highly functionalized PFSA showed lower swelling in hot water compared with those made from low imide content.

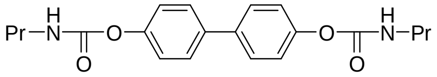

Figure 113. Structure of masked biphenol

Cross-linked PFSA: sulfinated polyarylenes (S-alkylation)

Sulfinated aromatics react with activated halides to form sulfone linkage (monomers and polymers based on sulfine chemistry have been made by author and presented in ECS meeting, Fall 2006). To study the possibility of using sulfinated aromatic compounds as cross-linker, UDEL was converted into sulfinated UDEL through lithiation followed by reaction with sulfur dioxide. The degree of sulfination was estimated to be at least two sulfinate groups per diphenylsulfone moiety (Figure 114). The reactivity of sulfinated polymer toward fluorinated aromatic compounds was demonstrated by performing a model reaction between sulfinated UDEL and decafluorobiphenyl. A solution of these two compounds in NMP at 100℃ turned into gel in just a few minutes (Figure 115).

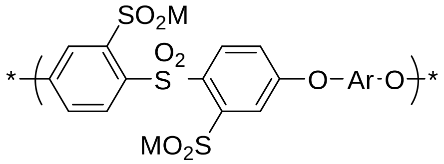

Figure 114. Structure of a sulfinated poly(arylene ether).

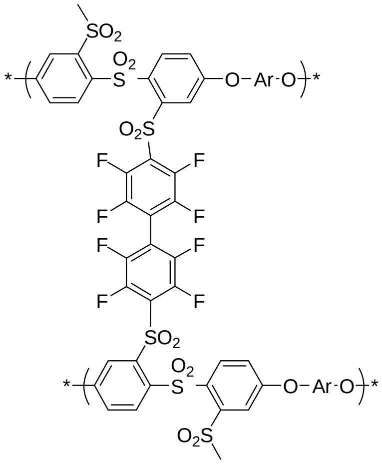

Figure 115. Proposed structure of sulfinated poly(arylene ether) cross-linked with decafluorobiphenyl.

Reaction of PFSA having 7% pentafluorophenylsulfonimide groups with 5 wt% sulfinated UDEL formed a membrane which showed high swelling. When PFSA with higher level of functional groups was used resulting product showed slightly better swelling properties. Increasing the curing temperature up to 260℃ improved the swelling properties of the membrane. Discoloration of the membranes after exposing to high temperature even for short period of time (< 3 min) was noticeable.

Cross-linked PFSA: 1,3,5-benzenetrisulfonyl chloride

Another method of cross-linking was designed in a way that sulfonamide groups of PFSAmide react with 1,3,5-benzenetrisulfonyl chloride (BTS) to generate cross-linked network. Reaction of PFSAmide with BTS in the presence of triethylamine (TEA) in NMP at 60℃ turns into gel in a few minutes. However, controlled addition of PFSAmide to excess BTS in the presence of TEA at room temperature generates soluble polymer with benzene disulfonic acid side-groups (Figure 116). Proton NMR of the product shows two peaks at 7.9 and 8.8 ppm with the ratio of 2 to 1 assigned as aromatic protons and the broad peak at 8.9 is assigned to the exchangeable acidic protons of NH and SO_3H (Figure 117).

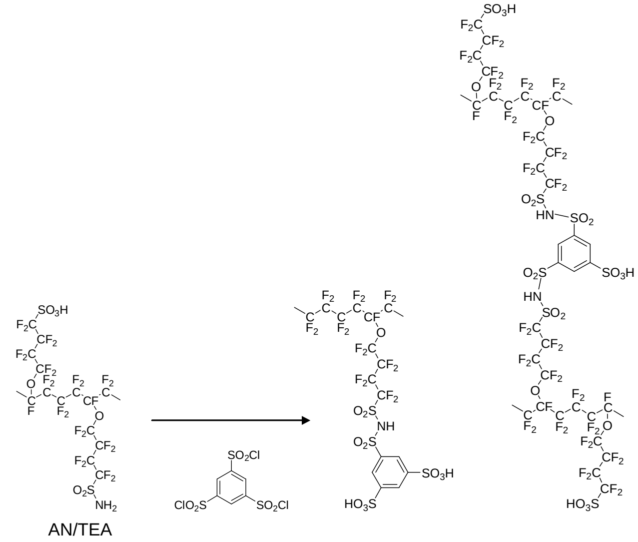

Figure 116. Reaction of PFSA with 1,3,5-benzenetrisulfonyl chloride

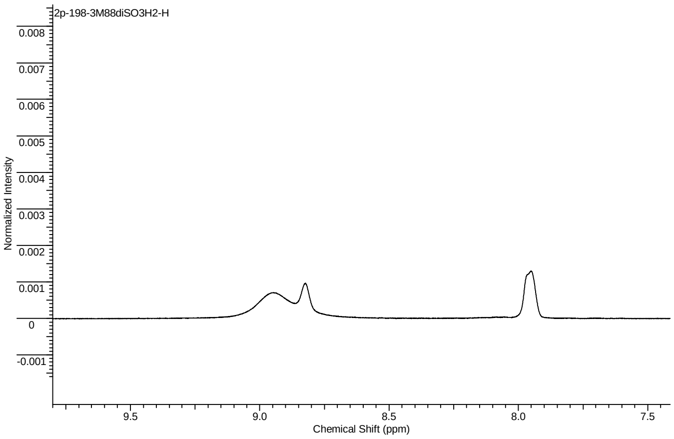

Figure 117. Proton NMR spectrum of PFSA cross-linked with 1,3,5-benzenetrisulfonyl chloride.

To form cross-linked membranes PFSAmides and controlled amount of BTS reacted at low temperature (< 0℃). Acetonitrile was a typical solvent for both reactants during the reaction and casting. Reaction between sulfonamide and sulfonyl chloride presumably occurs during the mixing of reactant at low temperature for a few minutes and casting at room temperature for 24 hours. Films were completely dried after heating at 60℃ for 2 hours and 170℃ for 1 hour. Films were evaluated for the extent of cross-linking by soaking in acetonitrile at 40℃ for many days and their weights before and after treatment in acetonitrile were recorded for this purpose. The membranes made from high SO_2NH_2 content (89%) showed almost zero weight loss and only little swelling after soaking in acetonitrile. Those made from low SO_2NH_2 content (28%) however, only swelled in acetonitrile with little weight loss. Cured membranes also showed significant improvement in their dimensional stability before and after treatment in hot water. The level of swelling depends on the sulfonamide content and the amount of BTS used in each case. Figure 116 represents possible structure of cross-linking group. Proton conductivity of the cross-linked membranes in water at room temperature showed a wide range from 3 - 340 mS/cm. The highest values were recorded from membranes with low sulfonamide content. Table 10 shows the summary of the results.

Table 10. Properties of PFSA cross-linked with 1,3,5-benzenetrisulfonyl chloride.

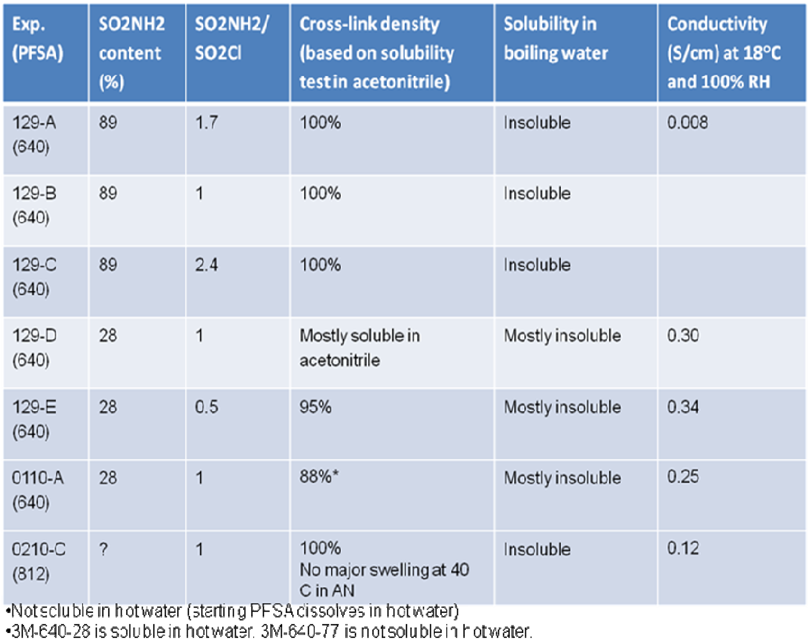

Exp. (PFSA)	SO2NH2 content (%)	SO2NH2/ SO2Cl	Cross-link density (based on solubility test in acetonitrile)	Solubility in boiling water	Conductivity (S/cm) at 18°C and 100% RH
129-A (640)	89	1.7	100%	Insoluble	0.008
129-B (640)	89	1	100%	Insoluble	
129-C (640)	89	2.4	100%	Insoluble	
129-D (640)	28	1	Mostly soluble in acetonitrile	Mostly insoluble	0.30
129-E (640)	28	0.5	95%	Mostly insoluble	0.34
0110-A (640)	28	1	88%*	Mostly insoluble	0.25
0210-C (812)	?	1	100% No major swelling at 40 C in AN	Insoluble	0.12

- Not soluble in hot water (starting PFSA dissolves in hot water)
- 3M-640-28 is soluble in hot water. 3M-640-77 is not soluble in hot water.

Cross-linked PFSA: 4-(sulfonylfluoride)butyryl fluoride (SFBF)

A functionalized ionomer was synthesized by reaction of PFSAmide with 4-(sulfonylfluoride)butyryl fluoride (Figure 2). The main idea is to take advantage of reactivity difference of two functional groups in SFBF and synthesize a cross-linked membrane in two steps. In first step sulfonamide groups of PFSAmide reacts with excess acylfluoride of SFBF to form an extended side chain with a new $-CF_2-SO_2-NH-CO-CF_2-$ linkage (Figure 118). Fluorine NMR showed complete disappearance of sulfonamide groups and formation of imide group. This intermediate then reacts with the starting PFSAmide to form a cross-linked product (Figure 119). The final product contains one unsymmetrical imide and a symmetrical sulfonamide on every connecting linkage between two main chains. Acyclic imides are generally known for their poor hydrolytic stability under basic or acidic environment. This was tested by treatment of intermediate product in 0.5 M sulfuric acid at 60°C for 48 hours. The result showed complete hydrolysis of unsymmetrical imide. Fluorine NMR spectra of starting PFSAmide, SFBF and intermediate before and after hydrolysis are shown in Figure 120. The top spectrum is for crude SFBF and the middle and bottom spectra are for intermediate product before and after hydrolysis, respectively. The new peaks indicated by arrows in the middle spectrum indicate formation of extended side-chain which completely disappeared after hydrolysis.

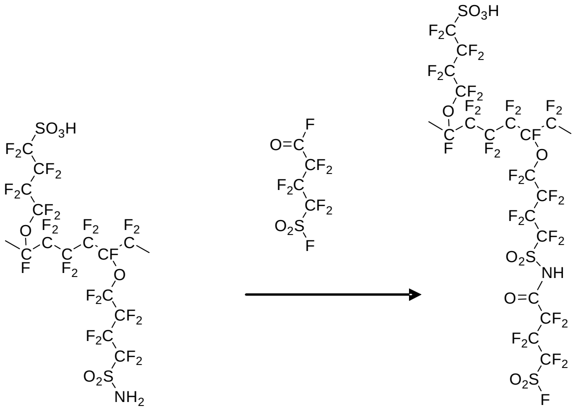

Figure 118. Reaction of PFSA with SFBF; formation of an intermediate.

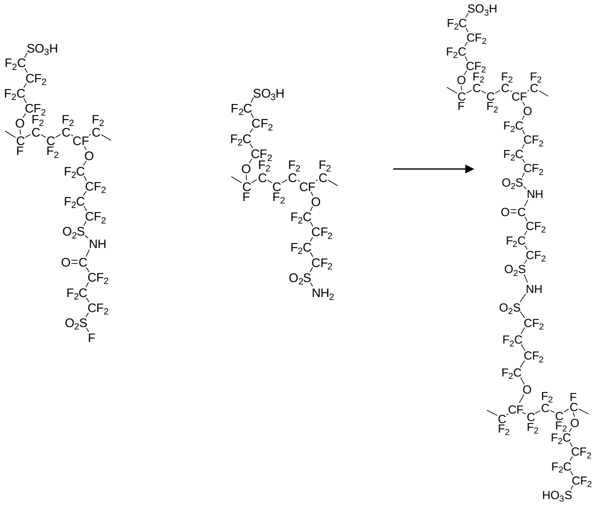

Figure 119. Cross-linked PFSA

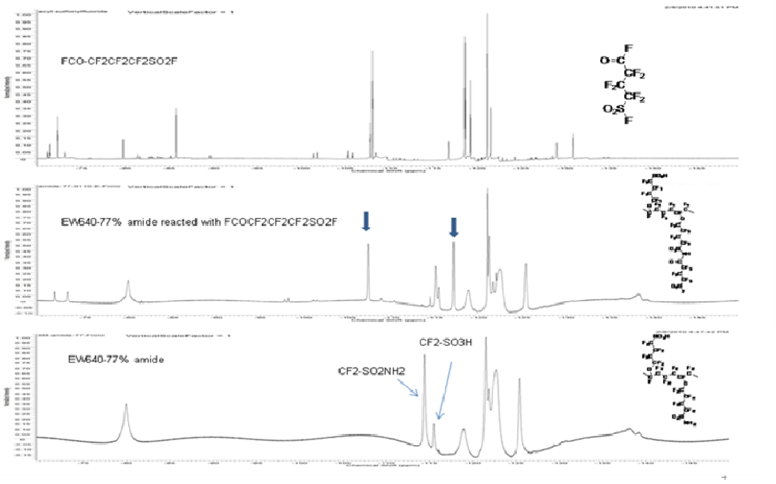

Figure 120. Fluorine NMR spectra of SFBF (top), PFSA intermediate before (middle) and after (bottom) hydrolysis

Cross-linked PFSA: Perfluoropropylene disulfonyl fluoride (PPDSF)

In this section a symmetrical difunctional PPDSF was used as a cross-linking agent. Reaction between sulfonamide containing PFSAmide and sulfonyl fluoride of PPDSF in acetonitrile produced intermediate B with sulfonimide linkages (**Figure 121**). Nearly complete conversion of sulfonamide groups into imide was evidenced by ^{19}F NMR (Figure 122) which showed disappearance of sulfonamide peak at -115 ppm. Mixture of the intermediate B and starting ionomer A in acetonitrile formed a clear film after casting under IR lamp followed by heat treatment at 170℃ f or one hour. All films prepared using various ratio of A and B became insoluble in water, methanol and acetonitrile after curing indicating formation of cross-linked structure (membranes swell up to 75% after soaking in water). The extent of cross linking was qualitatively examined by monitoring the swelling behavior of the films in hot water. Films made with high ratio of ionomer A to B showed little swelling meaning high degree of cross linking and the film made with low ratio of ionomer A showed relatively high swelling resulting from lower level of cross linking.

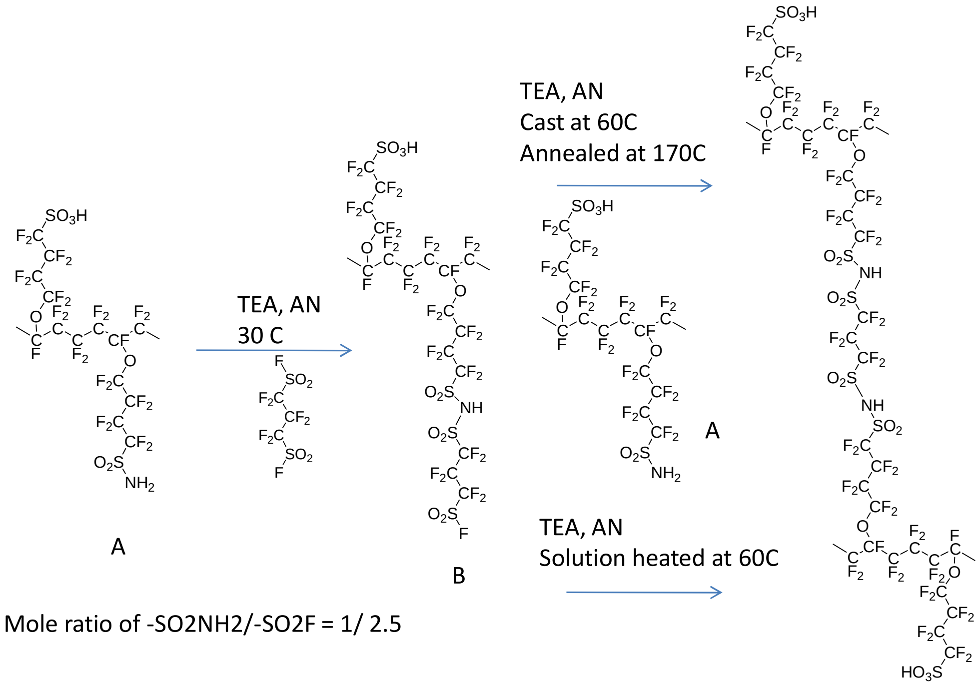

Figure 121. Reaction of PPDSF with PFSA

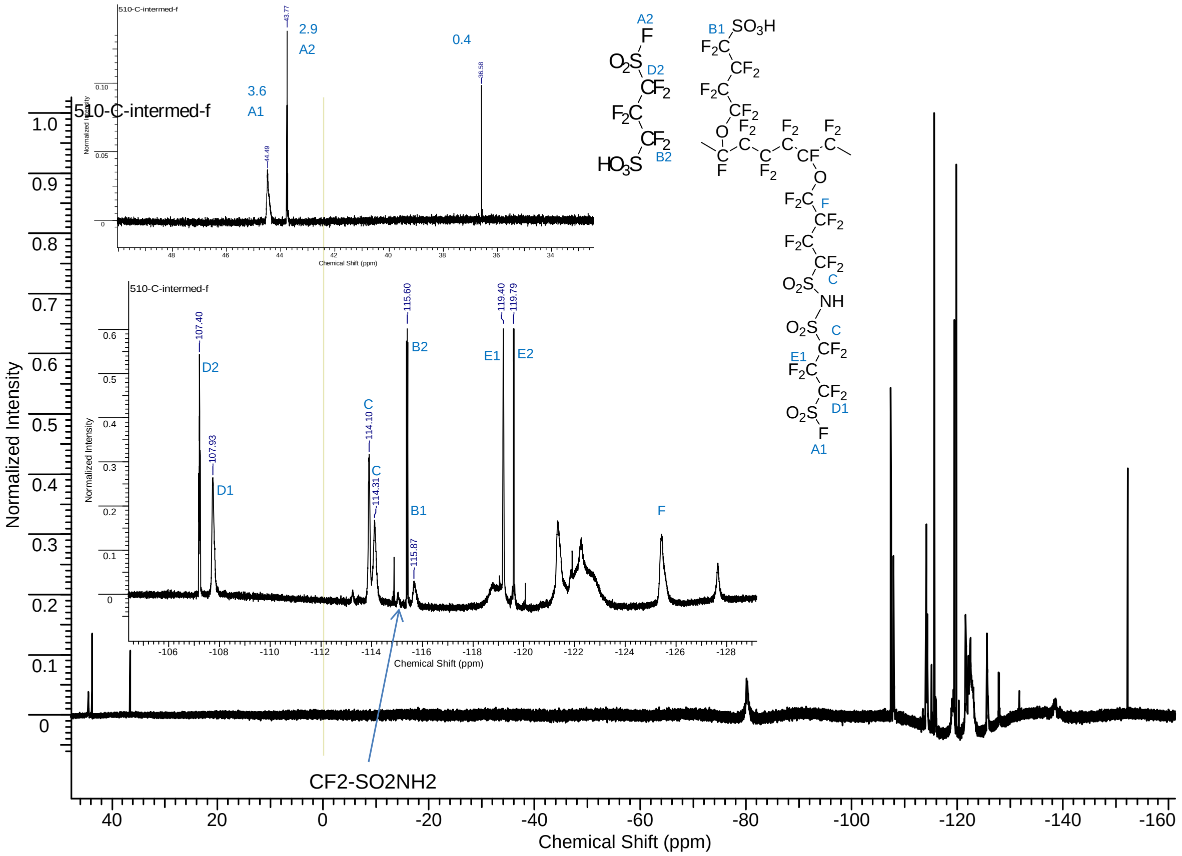

Figure 122. 19F NMR spectrum of the intermediate B.

When intermediate B and ionomer A were mixed in acetonitrile and heated at 60℃ for several hours the mixture became viscous and finally gelled. The fluorine NMR spectrum of the solution cured product showed no trace of sulfonamide group which appears around -114.8 ppm and reveals new peaks assigned for sulfonimide linkages (Figure 123). It is obvious that the cured products contain at least three acid functional groups including sulfonimide, sulfonic acids from starting PFSA and intermediate B. Peaks labeled as A at -115.8 and D at -115.3 ppm were assigned as CF_2 groups next to sulfonic acids on the short and long side-chain, respectively. The fluorine NMR of samples cured in solid phase and solution looks almost identical (Figure 124). Equivalent weights of the cross-linked membranes determined by titration show higher values compared with theoretical numbers. Presence of residual triethylamine or sulfonamide groups might be the reason for this deviation. Proton conductivity of the membranes at 15℃ and 100% RH was estimated around 0.12 S/cm (thickness of the membranes in fully hydrated condition used in calculation). Summary of the results is tabulated in Table 11.

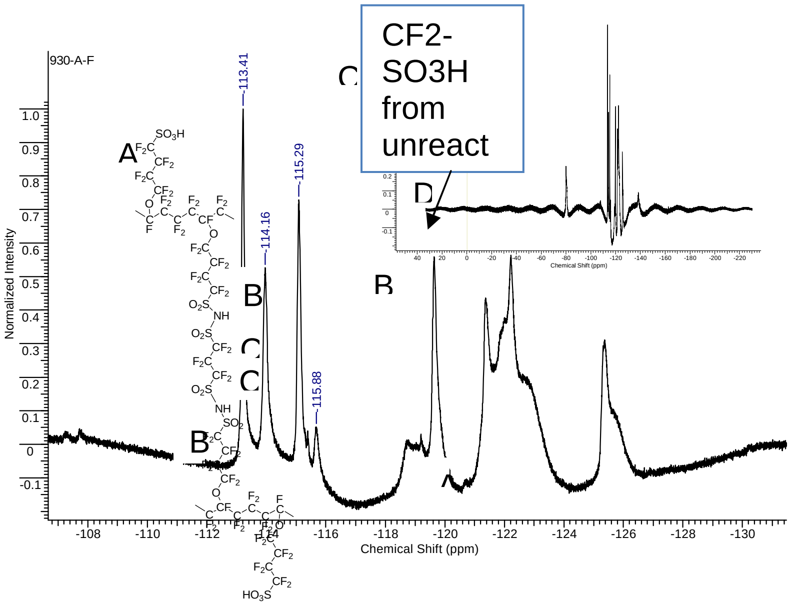

Figure 123. 19F NMR spectrum of the crosslinked ionomer made in solution

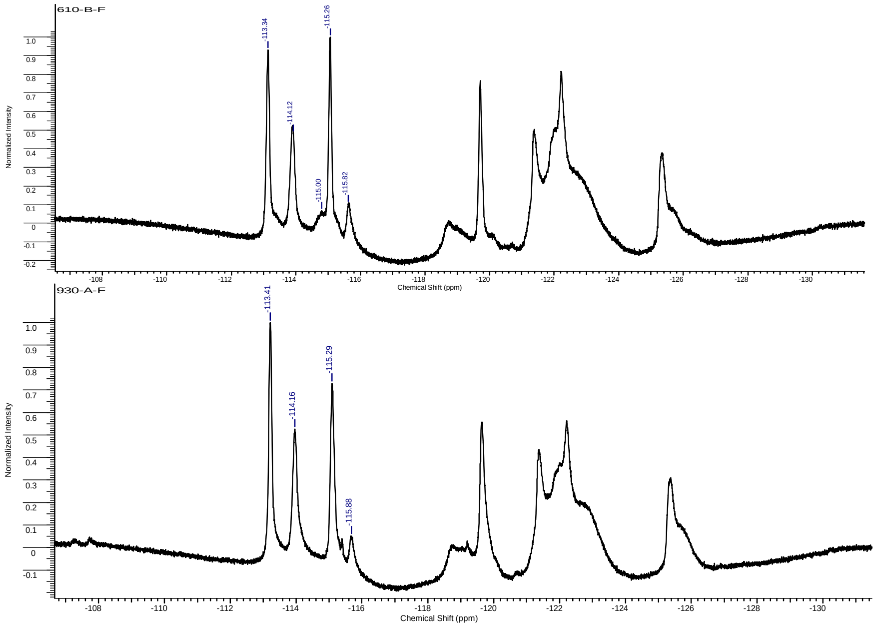

Figure 124. Comparing 19F NMR spectra of the crosslinked ionomers in solid state (top) and in solution (bottom)

Table 11. Properties of ionomers cross-linked with PPDSF

Sample	EW (g/mol)	Conductivity	Swelling	Solubility

	Calc.	Exp.	(S/cm)[3]	(%)[4]	Acetonitrile	Methanol	Water
640-77[1]	470	585	0.12	60	NS	NS	SW
640-77[2]	470	570	-	75	NS	NS	SW

Sample cured in solid state. 2) Sample cured in solution. 3) Measured at 15℃ and 100% RH. 4) By measuring dimension after soaking the sample in water for 24 hr and dried in ambient condition for 24 hr.

Appendix 2 - Zirconium Based Additives for Enhanced Conductivity

Introduction
The layered *α*-zirconium phosphate is the most interesting in terms of its proton conductivity because it has a pendant –OH group which extends into the interlayer region and forms a hydrogen bonded network with water (Figure 1). The transport mechanism in *α*-ZrP at room temperature is dominated by surface transport four orders of magnitude greater than the bulk transport; however, the crystallinity also plays an important role.[1] In addition, conductivity in *α*-ZrP is highly dependent on the hydration, varying by two orders of magnitude as the relative humidity is increased from 5 to 90%.[2] Recent research has confirmed the dominance of the surface transport and demonstrated enhancements that can be made through modification of the P–OH groups.[3] Based on this understanding of *α*-ZrP, attempts to enhance the proton conductivity have been made in the following directions

Intercalation of functional groups.
(ii) Composite *α*-ZrP membranes.
(iii) External surface area maximization (mechanical and colloidal synthesis).
(iv) Internal surface area maximization (sol–gel synthesis and pillaring).

Attempts to improve the conductivity of solid acid membranes have included the synthesis of new layered compounds, where Brønsted bases are intercalated in the interlayer region or functionalized organic radicals replace the hydroxyl of the phosphate group.[4] Significant improvement was achieved with the intercalation of strong acidic functional groups like $–SO_3H$ (there was little improvement for the weak –COOH) into the interlayer region. Metal^{IV} sulfophosphonates and zirconium sulfophenyl-phosphonates have been investigated for their conductivity under different temperature and relative humidity regimes (Figure 125).[5]

In past we investigated the synthesis of sulfonated Zirconium phosphates of the type described above, however the conductivity of $–SO_3H$ groups is highly humidity dependent. To increase the acid strength relative to that provided by a sulfonic acid substituted onto an aromatic ring, sulfonamide substituted materials represent another possible candidate. Aryl sulfonimides have been found to be hydrolytically stable We have tried to synthesize new Zirconium phosphonates from new phosphonic acid molecules containing $–SO_2$-NH-SO_2- bissulfonyl imide functionalities in order to achieve higher proton conductivity under hot and dry conditions. Figure 126 shows a schematic of Zirconium phenyl phosphonate layers linked via $–SO_2$-NH-SO_2- moieties. In order to realize these novel zirconium phosphonates we had to first prepare the phosphonic acids containing these $–SO_2$-NH-SO_2- bissulfonyl imide functionalities. The report describes various synthetic approaches taken to prepare the phosphonic acid, zirconium phosphonates, composites membranes containing 3M ionomer and zirconium phosphonates, the conductivity measurements, fuel cell performance measurements of these composite membranes and the structure of one zirconium phosphonate of interest in the membrane. There was also a limited effort on preparing polymers containing both phosphonic and bissulfonyl imide acid acid groups.

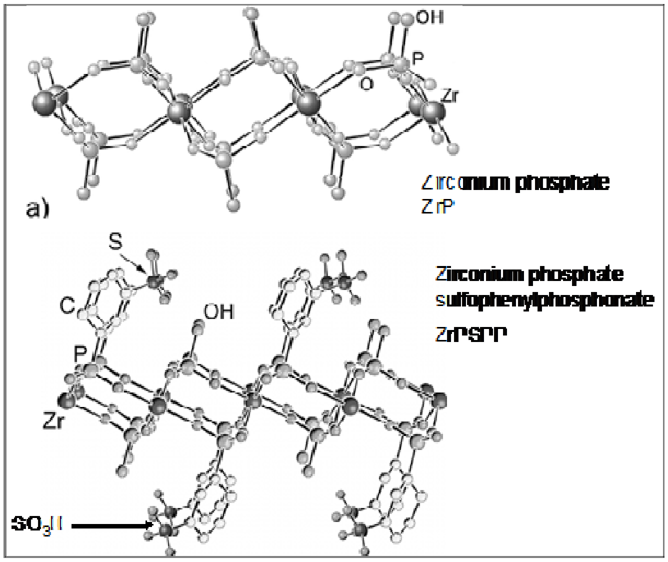

Figure 125. Single layer of α Zr(HPO4)2 ,ZrP and Zirconium phosphate sulfophenylphosphonate showing similarity in their layer structures.

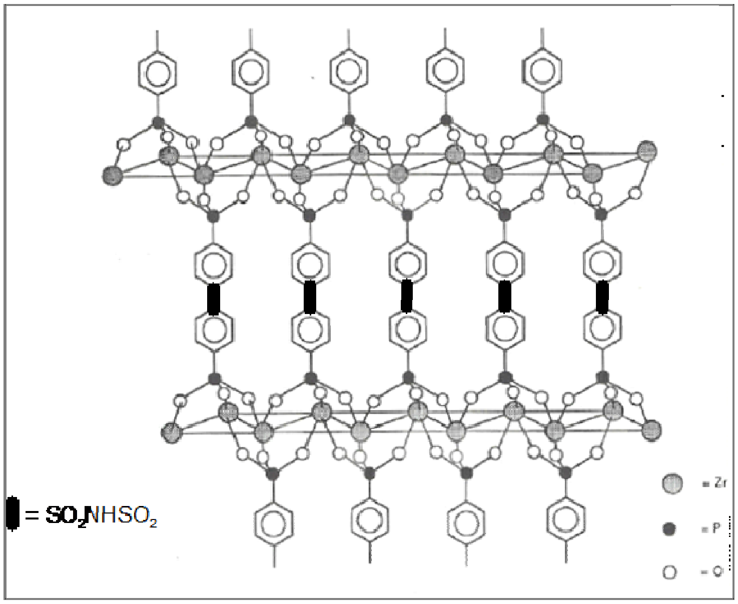

Figure 126. Schematic of Zirconium phosphonate containing bis sulfonylimide group. The bis phosphonate bissulfonylimide acid is assumed to link the two layers.

Phosphonic acid molecules

Keeping in mind the oxidative stability of the phosphonate molecules we focused our efforts on aromatic and fluorinated phosphonate molecules. Two of the phosphonate molecules which were synthesized during the program are shown in Figure 127.

Various synthetic approaches were attempted to synthesize the phosphonate molecules shown in Figure 127.

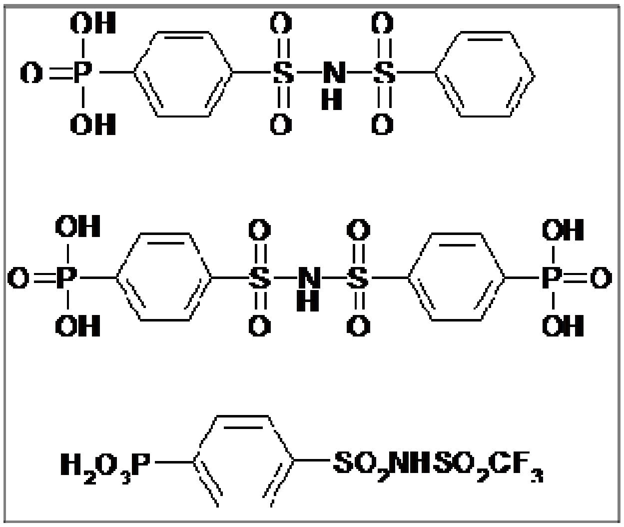

Figure 127. Scheme of phosphonate molecules synthesized during the course of study.

Synthesis and Characterization

Chlorosulfonation of Phenylphosphonic acid

The intended reaction scheme is shown in Figure 128. Chlorosulfonation of Phenylphosphonic acid was carried out using Chlorosulfonic acid. This was confirmed by ^1H (Figure 129), ^{31}P and ^{13}C NMR. The product is highly prone to hydrolysis as observed by NMR. After 2 days the most of the reaction mixture was hydrolyzed to yield Sulfophenylphosphonic acid. After the sulfonation excess $ClSO_3H$ was removed from the chlorosulfonated phenylphosphonic acid by rotary evaporation under vacuum. The resulting mixture was treated with 7N NH_3 solution in methanol to yield an off-white solid.

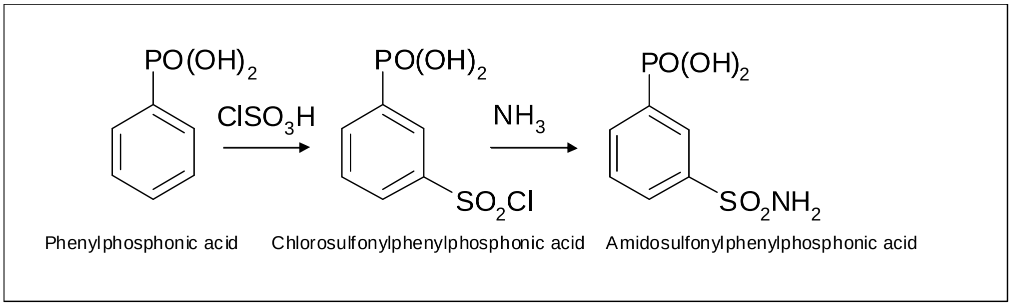

Figure 128. Reaction scheme showing chlorosulfonation followed by amidation of phenylphosphonic acid.

NMR characterization of the product from above reaction after ammoniation shows a different proton NMR spectrum when compared to either sulfonic acid or sulfonyl chloride. Powder X-Ray characterization of ammonia treated chlorosulfonated phenylphosphonic acid material shows a layered product with 15.0-15.5Å spacing which might correspond to the final sulfonamide product, however, ^{15}N NMR shows evidence for ammonium ion and another unidentified peak at 40ppm, however the sulfonamide Nitrogen is expected to appear at ~80ppm. Hence, no sulfonamide was formed.

In a repeat of the of the sulfonation reaction of phenylphosphonic acid excess chlorosulfonic acid was removed after the reaction under reduced pressure and the resulting viscous oil chlorosulfonated phenylphosphonic acid was reacted with anhydrous ammonia in a pressure vessel. ^{15}N NMR for the product shows a peak at ~20ppm for Ammonium ion and another unidentified peak at ~40ppm (Figure 130). A search of the literature revealed that the unidentified may be due to a P-N bond. This led us to believe that chlorosulfonation of phenylphosphonic acid leads to chlorination of phosphonic acid group in addition to chlorosulfonation to yield 3-sulfophenylphosphonic dichloride instead of 3-chlorosulfonylphenylphosphonic acid. The chlorination of phosphonic acid group ($PO(OH)_2 \rightarrow POCl_2$) followed by reaction with ammonia leads to a P-N bond phosphamide (Figure 130). This led us to believe that we needed to find alternate ways to prepare the desired phosphonic acid containing bissulfonylimide functionalities.

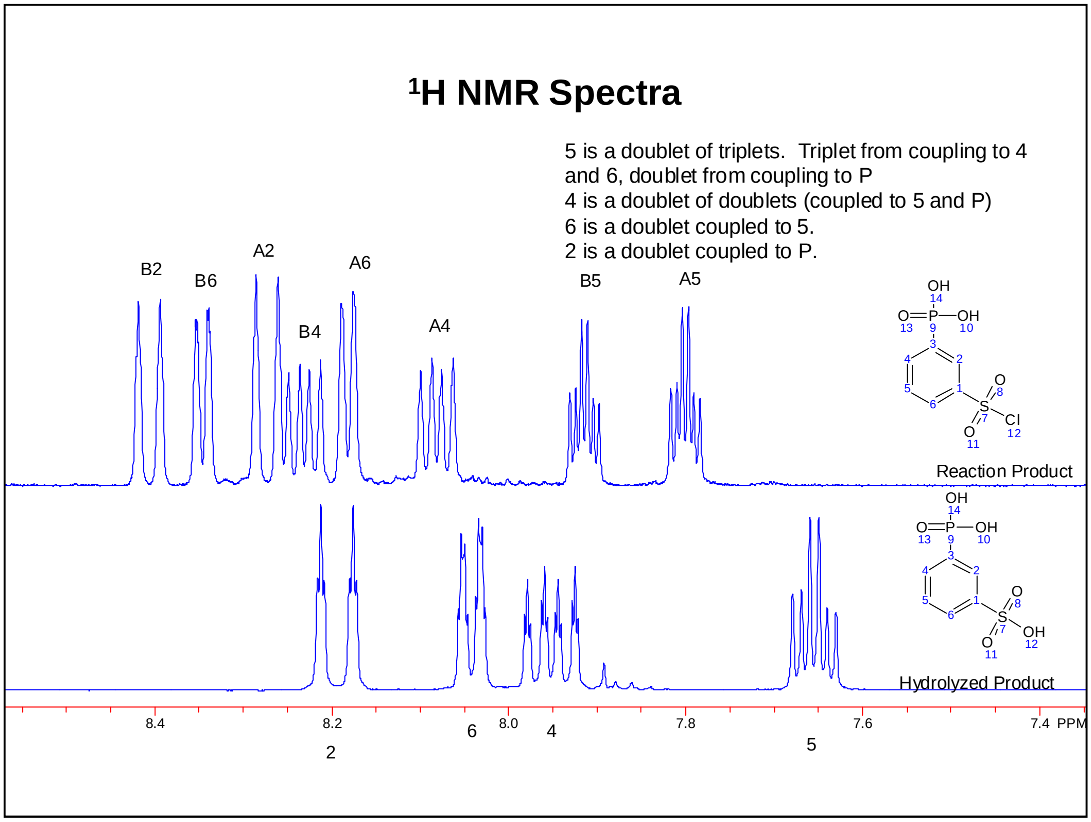

^{1}H NMR Spectra

5 is a doublet of triplets. Triplet from coupling to 4 and 6, doublet from coupling to P
4 is a doublet of doublets (coupled to 5 and P)
6 is a doublet coupled to 5.
2 is a doublet coupled to P.

Figure 129. 1H NMR spectra of sulfonated product of phenylphosphonic acid.

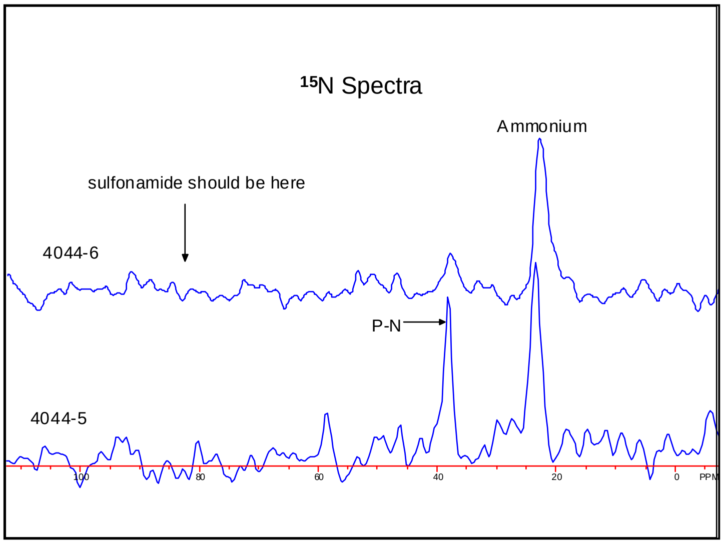

Figure 130. 15N NMR spectra of amidation product of sulfonated phenylphosphonic acid.

Alternate synthetic methods for phosphonic acids

Synthesis of Bisphosphophenyl bis sulfonyl imide acid, I

In order to avoid the hydrolysis related problems we attempted to synthesize the bromo bissulfonyl imide salts by reacting 4-bromobenzenesulfonamide with 4-bromobenzenesulfonyl chloride followed by phosphonation of the brominated bissulfonimide product. The complete reaction scheme is shown in Figure 131.

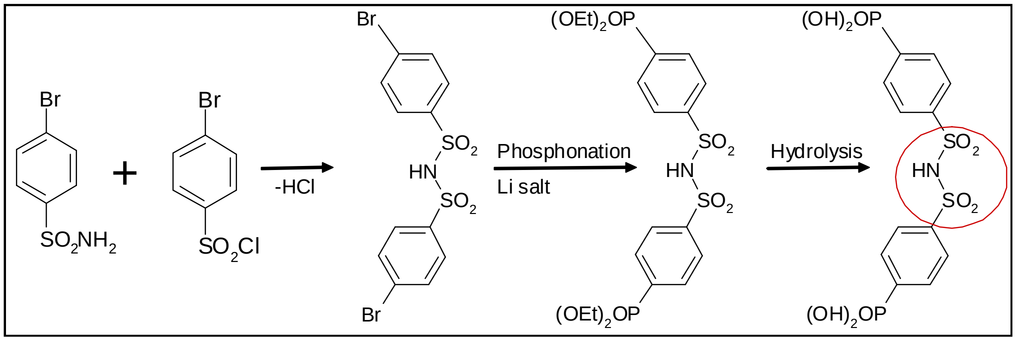

Figure 131. Complete reaction scheme for synthesis of Bisphosphophenyl bissulfonylimide acid, I, from brominated starting materials.

The detailed reaction sequence and relevant ^{31}P NMR spectra are shown in Figure 132.

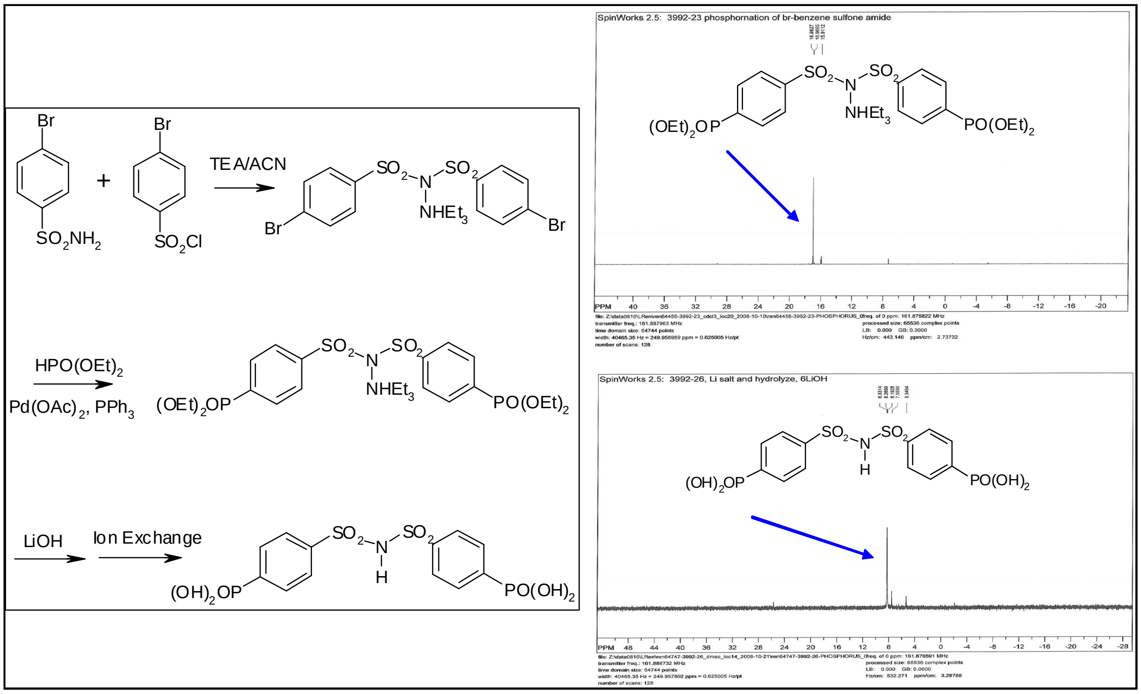

Figure 132. Reaction sequence and 31PNMR of phosphonate ester and acid, I products.

Synthesis of (4-benzenedisulfonimide) phenyl phosphonic acid, II
The detailed reaction scheme is shown in Figure 133. 4-bromobenzene sulfonamide is first phosphonated to yield product in stage 1 which is reacted in subsequent steps to finally yield the phosphonic acid product in stage 3.

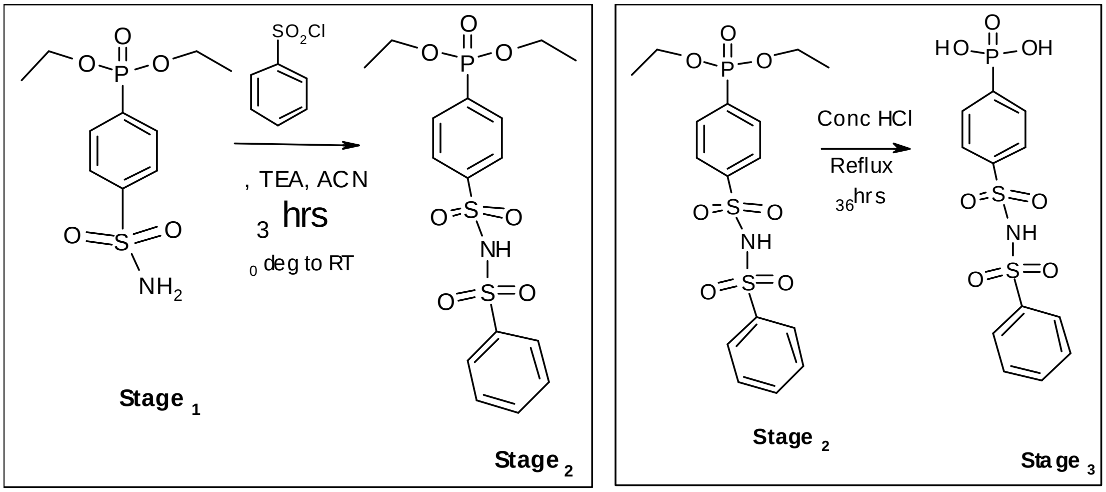

Figure 133. Reaction scheme for synthesis of (4-benzenedisulfonimide) phenylphosphonic acid.

Synthesis of (4-Trifluoromethane bissulfonimide) phenyl phosphonic acid, III
The reaction scheme is described in Figure 134for synthesis of ester form of **III** is very similar to that for **I**.

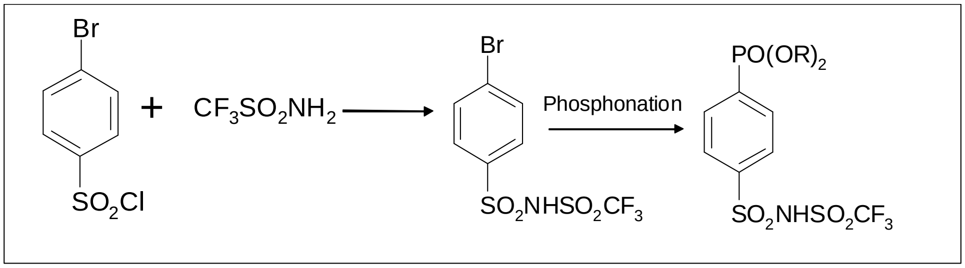

Figure 134. Reaction scheme for synthesis of ester form of III.

Synthesis of Zirconium phosphonates with above phosphonic acids
Zirconium salts were reacted with phosphonic acids, **I**, **II** and **III** synthesized in the preceding sections.

$Zr(O_3P\text{-}C_6H_4\text{-}SO_2NHSO_2\text{-}C_6H_5)_2$, IV
0.5gm of $ZrOCl_2.8H_2O$ was dissolved in 30gm of deionized water in a Polypropylene bottle. To this solution 2gm of (50wt%) Hydrofluoric acid was added under stirring. After 5 min 1.3gm of phosphonic acid $H_2O_3P\text{-}C_6H_4\text{-}SO_2NHSO_2\text{-}C_6H_5$, **II** synthesized in Example 3 was added to the above mixture. The polypropylene bottle containing the mixture was heated in an oil bath under stirring at 80˚C for 16 hours. The dried product was washed with methanol and centrifuged. The supernatant was decanted. The precipitate was dried in a hot air oven at 110˚C for 15 minutes. X-ray diffraction (XRD) shows peaks for a layered zirconium phosphonate solid, **IV**, (001 reflection at 23.5Å, 002 reflection at 11.7 Å and 003 reflection at 7.85 Å) (Figure 135).

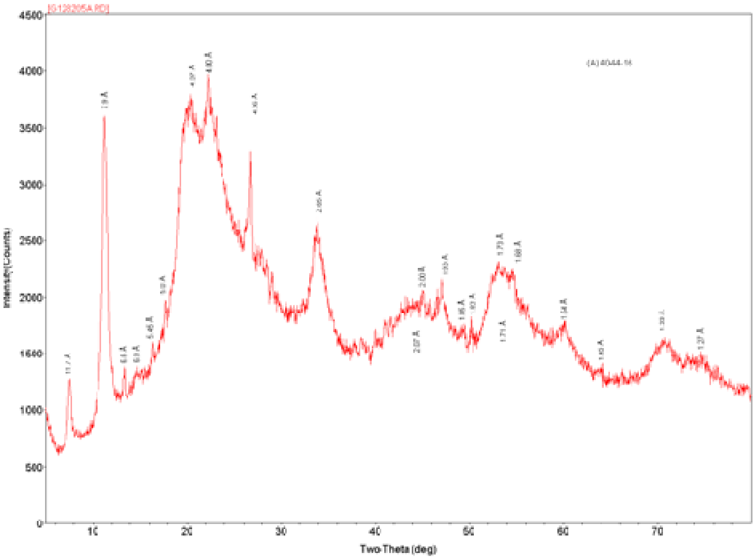

Figure 135. XRD pattern of IV showing a layered structure.

$Zr(O_3P\text{-}C_6H_4\text{-}SO_2NHSO_2\text{-}C_6H_4PO_3)$, V

Confidential: Use or disclosure of data contained on this page is subject to the restriction noted on the first page of this document.

$ZrOCl_2.8H_2O$ was reacted with phosphonic acid $H_2O_3P\text{-}C_6H_4\text{-}SO_2NHSO_2\text{-}C_6H_4PO_3H_2$, **I** to yield a zirconium phosphonate **V**. X-ray diffraction shows peaks for a layered the zirconium phosphonate.

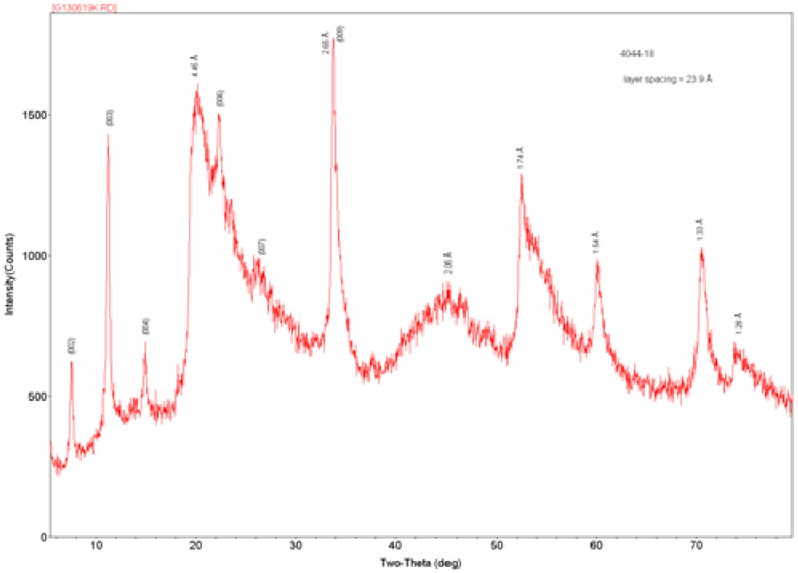

Figure 136. XRD pattern of V showing a layered structure.

Membrane Preparation

Zirconium phosphonates with bissulfonyl imide ($-SO_2NHSO_2-$) groups prepared in this study have lower equivalent weight than the control 3M ionomer and have been added to the 3M ionomer to obtain composite membranes with lower equivalent weights in order to obtain improve proton conductivity and fuel cell performance under hot and dry conditions. The schematic for the preparation of composite membrane is shown in Figure 137.

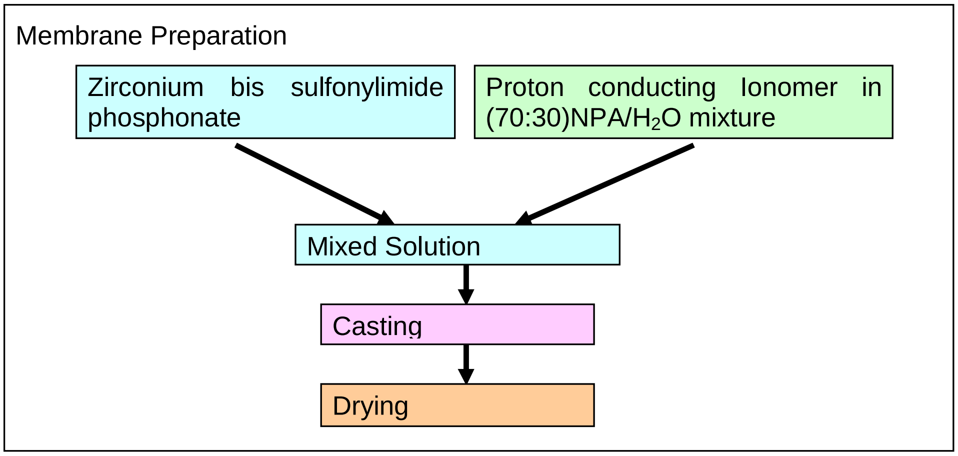

Figure 137. Schematic for preparing composite .

Composite Membranes preparation and testing

Composite Membranes containing $Zr(O_3P\text{-}C_6H_4\text{-}SO_2NHSO_2\text{-}C_6H_5)_2$*, IV or* $Zr(O_3P\text{-}C_6H_4\text{-}SO_2NHSO_2\text{-}C_6H_4PO_3)$*, V*

Zirconium phosphonate **IV** or **V,** was mixed with 3M ionomer 825EW and stirred over a period of 7 days to give 10wt% and 20 wt% (final composition based on actual solids) coating dispersion. 13 mil thick wet membranes were prepared using an adjustable gap coater these coating dispersions on a polyimide film. The membranes were annealed at 80˚C for 10 min, 125˚C for 15min and finally at 200˚C for 10 min. Proton conductivity data for control and composite membranes containing 10 wt% of the zirconium phosphonates is shown in Figure 138. Membranes containing 10wt% of V show proton conductivity similar to control at low humidity conditions.

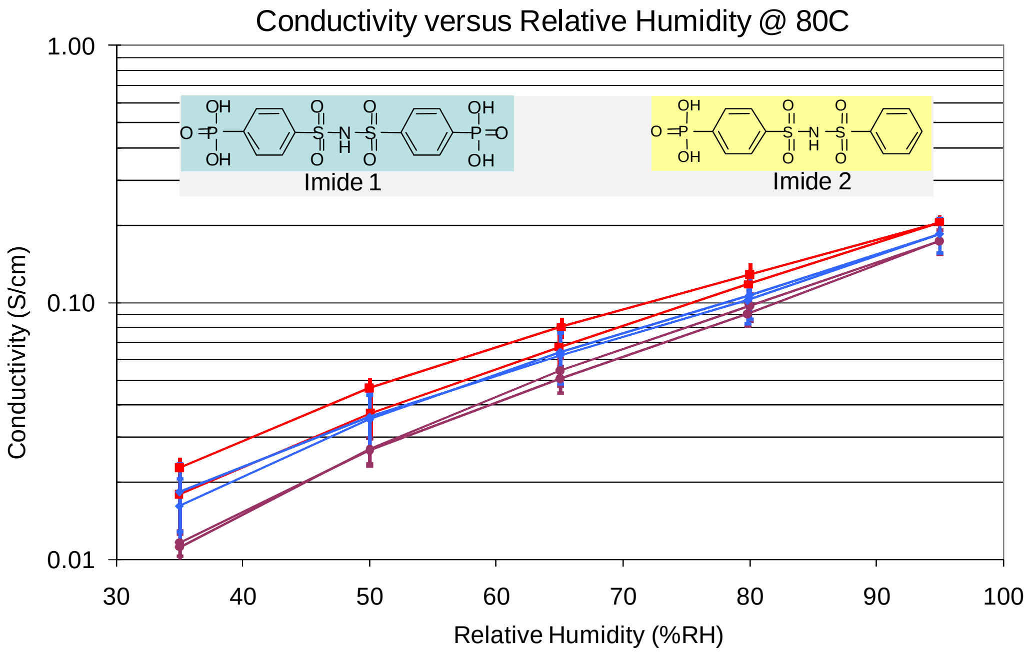

Figure 138. Proton conductivity data for composite membranes containing 10wt% of IV (Imide2, plum color), and V (Imide1, blue color) and control 800 EW (red color).

Further Fuel cell testing was performed on the membranes containing zirconium phosphonate V. The membranes need to be cleaned up with nitric acid wash and hydrogen peroxide to get rid of unreacted material which gets leached out during the wash. Composite membranes show lowed fuel cell performance compared to 825 EW control membrane (Figure 139).

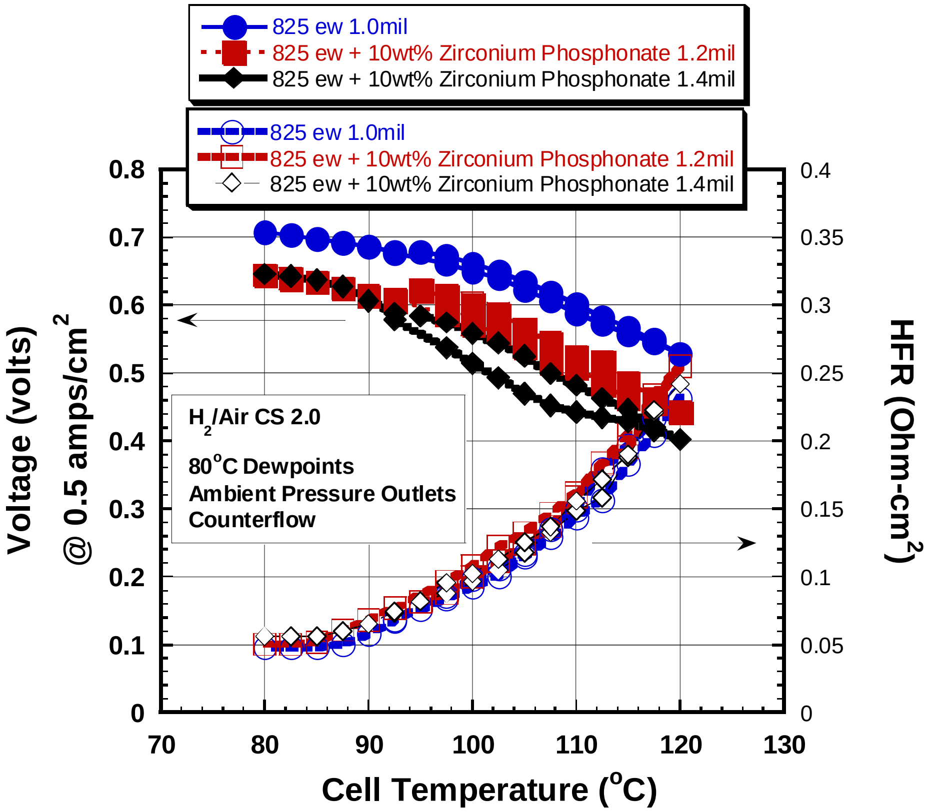

Figure 139. Fuel cell performance data for composite and blank membranes.

Composite Membranes containing $Zr(O_3P\text{-}C_6H_4\text{-}SO_2NHSO_2\text{-}C_6H_4PO_3)$, V, prepared from phosphonate ester of I

Often because of the highly hygroscopic nature of the phosphonic acid as well as zirconyl chloride salt the final zirconium phosphonate ends up with either excess zirconia or phosphonic acid which leads to poor fuel cell performance by increasing EW when excess Zirconia is present, or causing poor catalyst performance when excess phosphonic acid present binds to the catalyst. Excess zirconia can be cleaned by acid wash with nitric acid where as excess organic can be cleaned up by peroxide wash. Excess phosphonic acid on the other hand can be cleaned up by washing with methanol.

$Zr(O_3P\text{-}C_6H_4\text{-}SO_2NHSO_2\text{-}C_6H_4PO_3)$, V,

In this study was prepared from Zirconyl chloride and the corresponding ester of this $O_3P\text{-}C_6H_4\text{-}SO_2NHSO_2\text{-}C_6H_4PO_3$ phosphonic acid. It is hard to weigh the phosphonic acid accurately because of its hygroscopic nature (unlike the phosphonate ester which is much less hygroscopic). The excess unreacted phosphonic acid was removed by repeated washes with methanol. The final zirconium phosphonates was then dried and mixed with 3M ionomer 825EW and stirred over a period of 3 days to give 10wt% (final composition based on actual solids) coating dispersion. A 10 wt% membrane has an effective equivalent weight of 797. 13 mil thick membranes were prepared using an adjustable gap coater these coating dispersions on a polyimide film. The membranes were annealed at 80˚C for 10 min, 125˚C for 15min and finally at 200˚C for 10 min. No further cleaning was carried out on this membrane. Fuel cell testing performance of these membranes is shown in Figure 140.

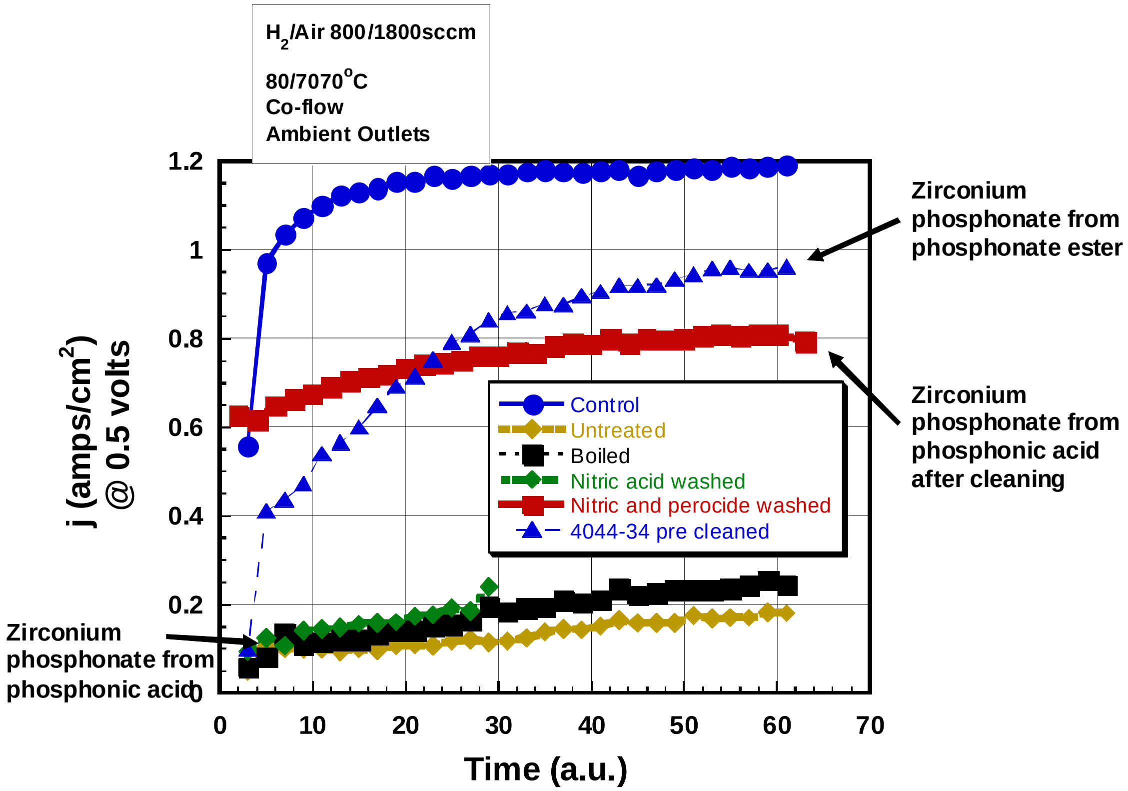

Figure 140. Graph showing Fuel cell testing data for composite membranes containing V .

It can be seen from the Figure 140 that the current membrane (solid blue triangle) required no additional clean up and showed a better startup and seems to improve over time. The previous membranes containing 10 wt% zirconium phosphonates (which were not cleaned of excess phosphonic tan diamonds and black squares, green diamonds nitric acid treated) showed poor start up until a combined nitric acid and peroxide wash was carried out for the membranes.

The temperature challenge plot shown in the Figure 141 indicates that the composite membranes containing **V**, prepared from phosphonate ester (cleaned up of unreacted phosphonic acid) also hold voltage (at constant current density) at higher temperature better than previous membranes including the control 825 EW membrane. HFR measurements shown in Figure 141 indicate that the composite membranes containing **V**, also shows a lower HFR than the control membranes. It can also be seen that the composite membranes containing **V** obtained from using phosphonic acid instead of phosphonate ester despite cleaning show poor fuel cell performance (Figure 141) and higher HFR (Figure 142).

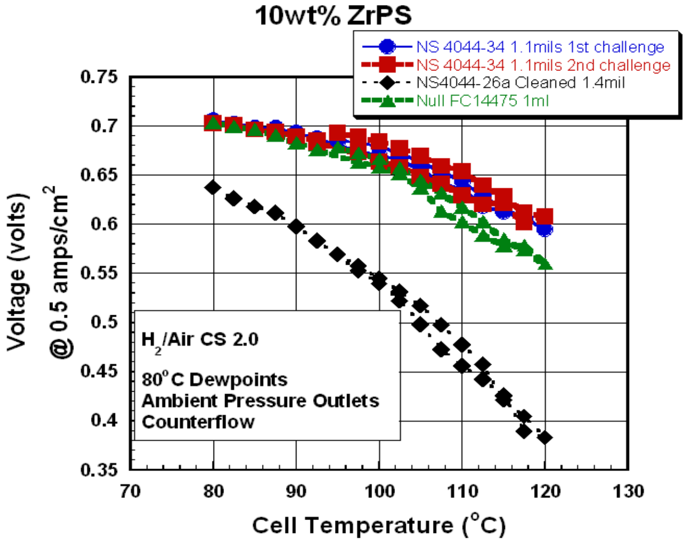

Figure 141. Fuel cell performance for V, Temperature Challenge plots.

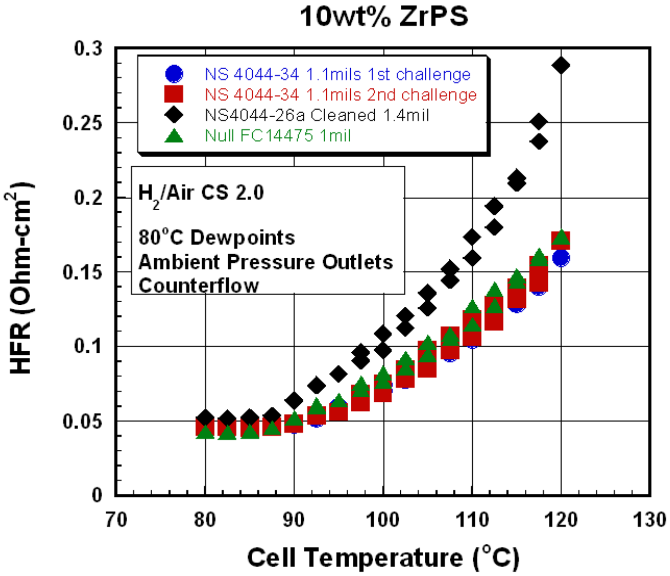

Figure 142. HFR of composite membranes.

Composite Membranes containing 30 wt% Zr(O_3P-C_6H_4-SO_2NHSO_2-$C_6H_4PO_3$), V, prepared from phosphonate ester of I

Zirconium phosphonate, V prepared from phosphonate ester was mixed with 3M ionomer 825EW and stirred over a period of 3 days to give 30wt% (final composition based on actual solids) coating dispersion. A 30 wt% membrane has an effective equivalent weight of 741.

13 mil thick membranes were prepared using an adjustable gap coater these coating dispersions on a polyimide film. The membranes were annealed at 80˚C for 10 min, 125˚C for 15min and finally at 200˚C for 10 min. The membranes were tested both acid washed and as such. Proton conductivity measurements for the composite membranes show that at 80˚C the composite membranes show lower conductivity when compared

to the 700EW control 3M ionomer membrane whereas at 120˚C the composite membranes show similar proton conductivity as 700EW control 3M ionomer membrane (Figure 143).

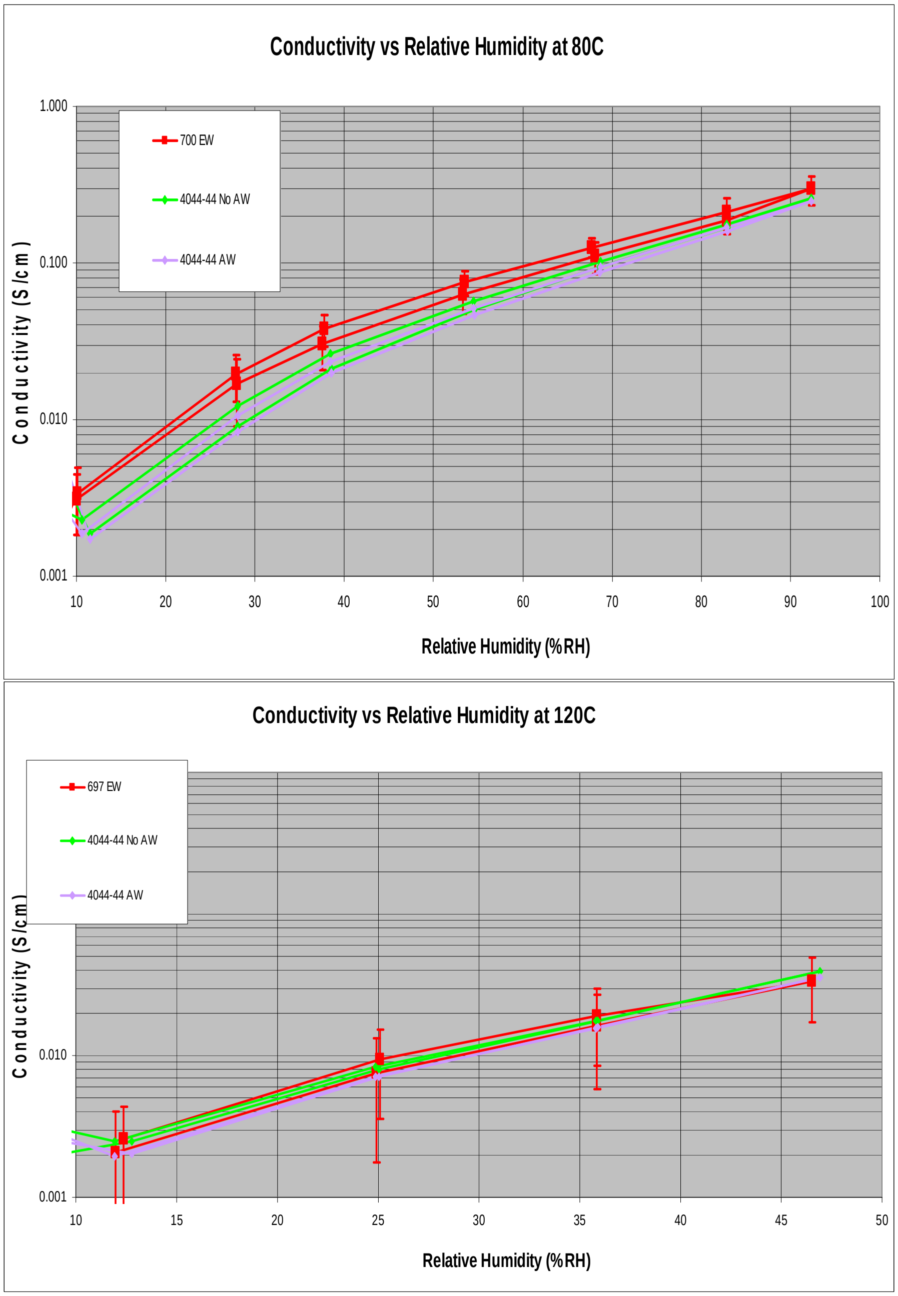

Figure 143. Proton conductivity data for composite membranes containing 30 wt% of V at 80˚C and 120˚C as a function of humidity.

Structural analysis of Zirconium Phosphonates in Ionomer membranes via X-ray scattering

The most promising results in our study were obtained with Zirconium phosphonate $Zr(O_3P\text{-}C_6H_4\text{-}SO_2NHSO_2\text{-}C_6H_4PO_3)$, **V** containing composite membranes. Hence, it would be useful to understand the structure of this material in the fuel cell membrane. To understand the stability of Zirconium phosphonate structure X-ray diffraction was carried out on the composite membranes containing Zirconium phosphonates $Zr(O_3P-C_6H_4-SO_2NHSO_2-C_6H_4PO_3)$, **V** under various conditions.

The X-ray diffraction pattern for the neat powder compound is shown in Figure 136. The XRD pattern for the composite membrane containing the freshly prepared composite membrane containing **V** (labeled as Control) is shown in the Figure 144. Both Figure 136 and Figure 144 clearly illustrate the layered nature of the zirconium phosphonate in neat powder and in composite membrane. Even after cleaning by nitric acid and peroxide the composite membrane shows that the layered zirconium phosphonate material stays intact albeit a decrease in peak intensity, however, there is no signature of layered zirconium phosphonate materials after the fuel cell testing (broad feature no peaks). We wanted to find out if the loss of layered structure of Zirconium phosphonate was happening by some kind of decomposition of the structure under fuel cell test conditions or there is some other mechanism in play.

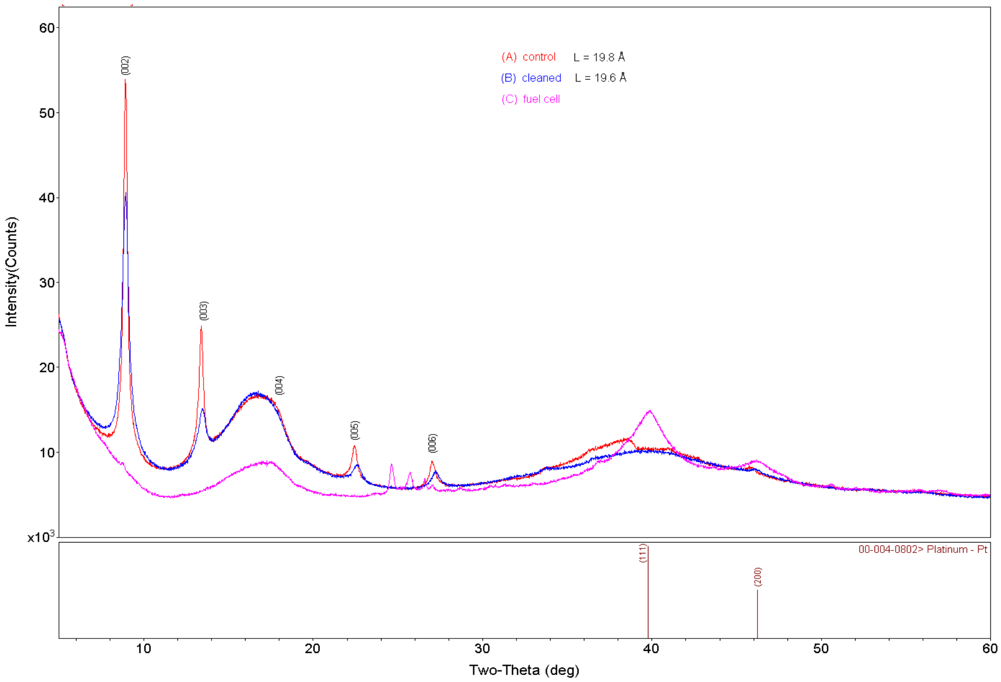

Figure 144. XRD pattern of Zirconium phosphonate V containing composite membranes.

X-ray diffraction of the Zirconium Phosphonate $Zr(O_3P-C_6H_4-SO_2NHSO_2-C_6H_4PO_3)$, V
The XRD pattern of the powdered zirconium phosphonate $Zr(O_3P-C_6H_4-SO_2NHSO_2-C_6H_4PO_3)$, **V** shown previously (Figure 136) as well as in Figure 145 shows *00l* peaks corresponding to a layered structure. Since we do not have a single crystal structure data for this compound we can only speculate the structure. Based on the structure of previous Zirconium bisphosphonates we think the plausible structure for this zirconium phosphonate should look like the one shown in Figure 126.

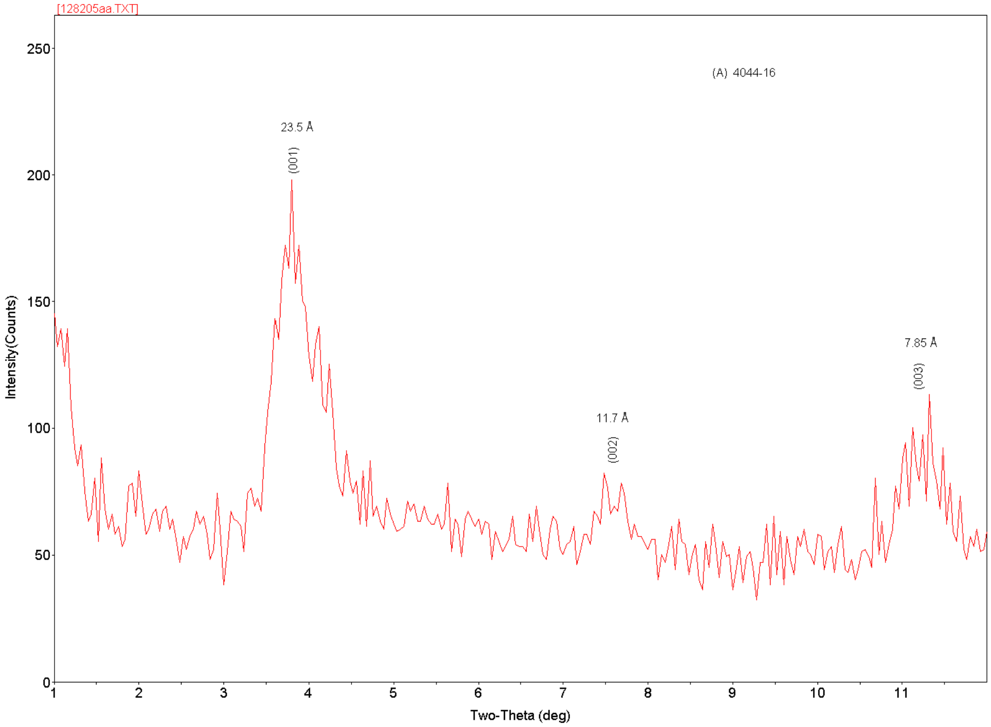

Figure 145. Low angle XRD pattern of V.

X-ray diffraction of the Ionomer dispersions containing zirconium phosphonate

Even if we know the structure of **V** in solid state it is quite likely the structure may not be acid stable either in ionomer dispersion or somehow degrading or transforming in a fuel cell environment. To understand what was happening to the zirconium phosphonate in the membrane we carried out X-ray diffraction study of ionomer solutions of **V** and other zirconium phosphonates (Figure 146).

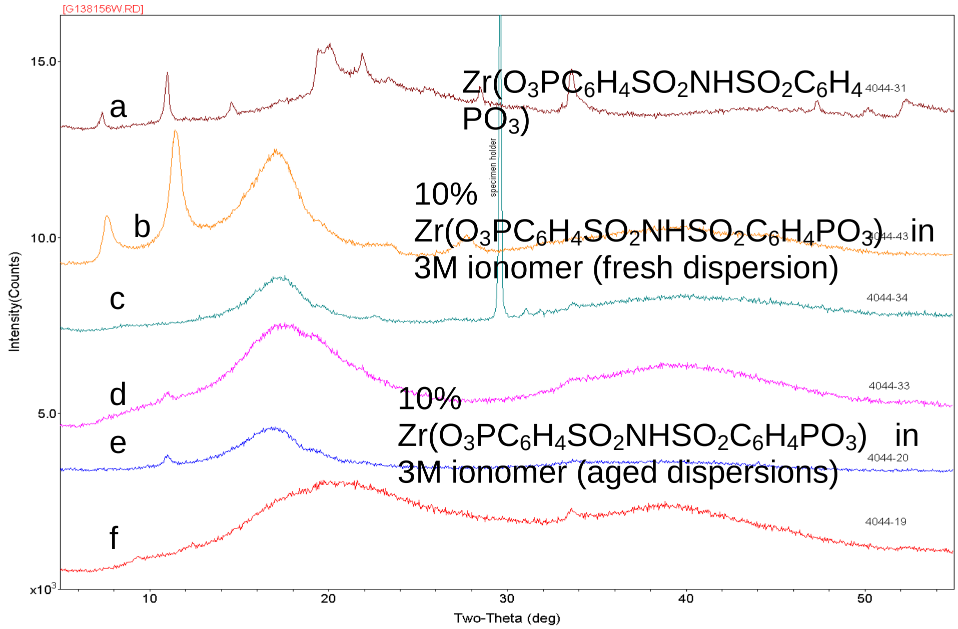

Figure 146. XRD patterns of Ionomer dispersion containing Zirconium phosphonate, V in Ionomer Dispersion.

XRD patterns collected for the Zr(O_3P-C_6H_4-SO_2NHSO_2-$C_6H_4$$PO_3$), **V** (Figure 144a) solid as well as for freshly prepared dispersions containing 3M ionomer and Zr(O_3P-C_6H_4-SO_2NHSO_2-$C_6H_4$$PO_3$), **V** (Figure 146b) shows the presence of reflections corresponding to the layered zirconium phosphonate. As the dispersions are aged (Figure 146c-f) the reflections corresponding to the layered zirconium phosphonate disappear. This may indicate the loss of layered structure which either means the layers have exfoliated or layers have chemically reacted and no longer exist.

Our proposed structure for the Zirconium phosphonate structure shown in Figure 126 shows that the zirconium phosphonate layers are linked via the bis phosphonate linkage and loss of X-ray reflections as witnessed in Figure 144 would seem to indicate that the loss of layered structure which is possible only via hydrolysis of Zr-O-P linkage as bis sulfonyl imide linkage have been proved to be acid stable. There is also evidence of acid stability of both Zirconium phosphates and phosphonates in published literature. We resorted to ^{31}Phosphorus NMR to solve this puzzle because any loss of structure of Zirconium phosphonate, **V** should lead to formation of free phosphonic acid **I,** which should be detected by solution ^{31}P NMR, however, the ^{31}P NMR did not show any signal indicating that no free phosphorus was present in the solution (Figure 147). We also looked at the solid via ^{31}P NMR and indeed we see phosphorus signal around -8ppm corresponding to Zirconium phosphonate (Figure 148). This confirms that all the phosphorus is still bound in the solid to zirconium thereby indicating the stability of the Zr-O-P linkage.

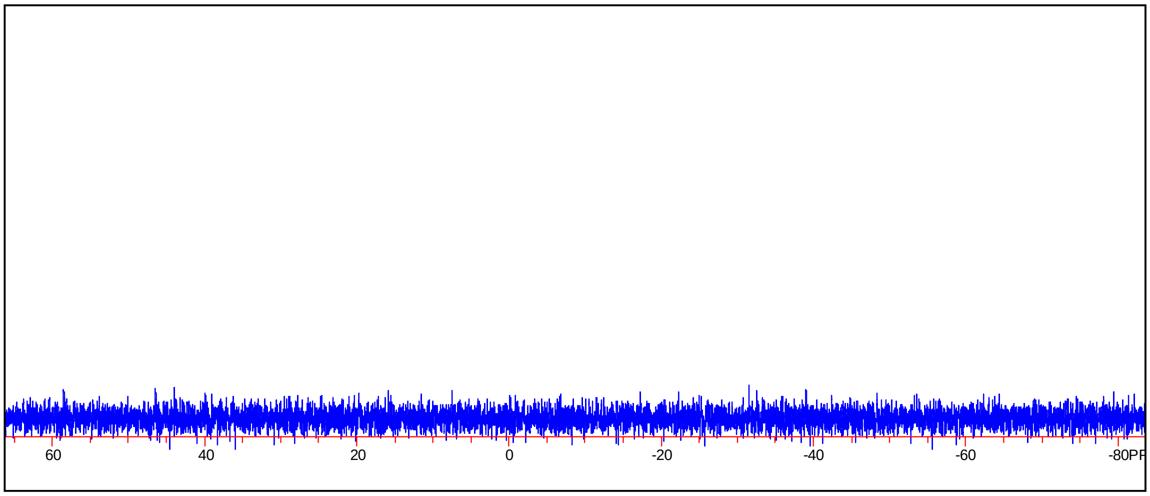

Figure 147. 31P Solution NMR of the ionomer dispersion containing V.

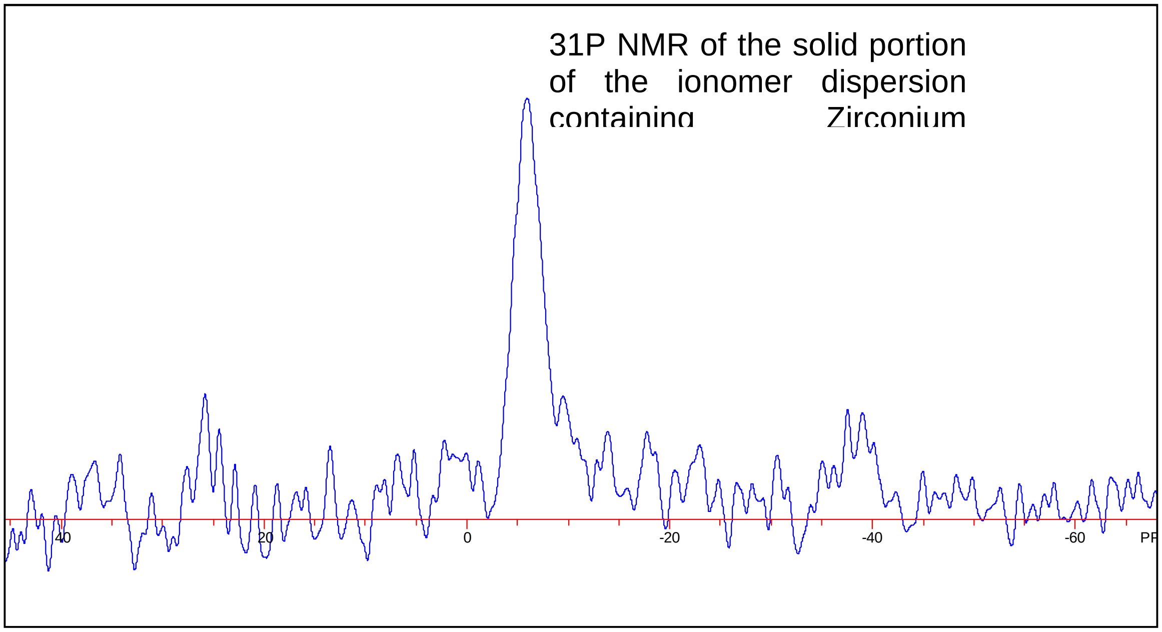

Figure 148. 31P MASNMR of the ionomer dispersion containing V.

In this scenario, the only way the loss of layered structure can be explained is if there is an exfoliation of layers which cannot occur in the current proposed structure of Zirconium phosphonate (as shown in Figure 126). We started to think if there is an alternate structure to the one we have proposed. The only alternate structure which is possible if both the phosphonic acid groups of the bis phosphonic acid $H_2O_3P\text{-}C_6H_4\text{-}SO_2NHSO_2\text{-}C_6H_4PO_3H_2$,**II** molecule link to the same layer (Figure 149) instead of linking to two different layers (Figure 126).

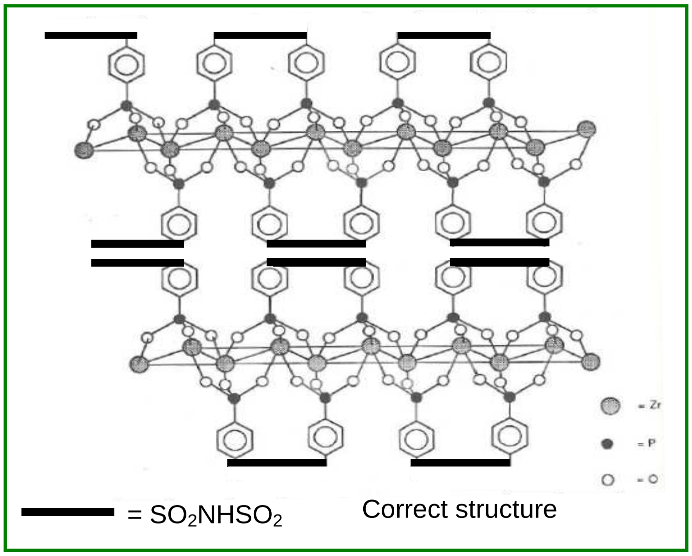

Figure 149. Alternate proposed structure of Zirconium phosphonate, V.

As of now we don't have a crystal structure for the phosphonic acid however, crystal structure of an alkali / alkylammonium salt of 1,1-bis[4-(trifluorovinyl)oxyphenylsulfonyl] imide acid from literature[vi] suggests that it is possible that both the phenyl phosphonic acid groups linked together with bissulfonylimide form letter 'U' and hence can end up binding to the same zirconium phosphonate layer.

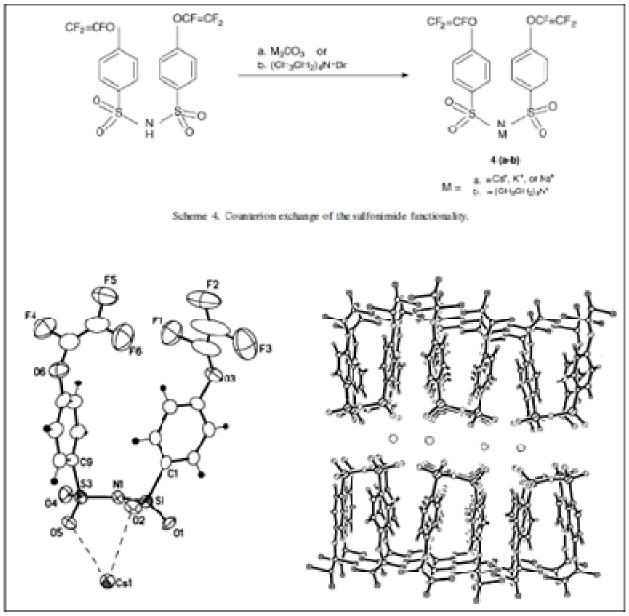

Scheme 4. Counterion exchange of the sulfonimide functionality.

Figure 150. Single crystal structure reprinted from reference .

Phosphonation of 3M ionomer containing aryl-bromide pendant groups

Br-containing 3M ionomer based material was first synthesized by reacting 4-bromobenzensulfonamide with sulfonyl fluoride form of the 3M ionomer. The cleaned up product was phosphonated successfully following the procedure described here (Figure 151). 1gm of this fluoropolymer containing phenylbromide attached to the polymer via a bissulfonylimide group was suspended in 30ml EtOH. To this was added 49mg of Palladium(II) acetate and 173mg of triphenylphosphine followed by dropwise addition of 0.35ml of N,N-dicyclohexylmethylamine and 0.225ml of diethyl phosphite. The reaction mixture was heated for 30min at 70˚C. In order, to dissolve the polymer 4 ml of N-methyl pyrrolidone was added. A clear solution formed, was refluxed for 15 hours at 80˚C. The solvent was removed in a rotary evaporator. The product obtained shows a 31P NMR signal at δ 16.2ppm (referenced to H_3PO_4) confirming the formation of the phosphonate ester. Our studies found that phosphonate ester can be hydrolyzed by trimethylsilyl bromide (TMS-Br) in acetonitrile (structure shown in Figure 152). Reaction was very efficient but needed much excess of TMS-Br. This hydrolysis reaction was confirmed by NMR. $-OCH_2CH_3$ of phosphonate ester peaks at 4.0ppm and 1.3ppm disappeared in ^{1}H-NMR spectrum (see Figure 153) and new phosphonic acid peak appeared at 13.7ppm in ^{31}P NMR spectrum (Figure 154).

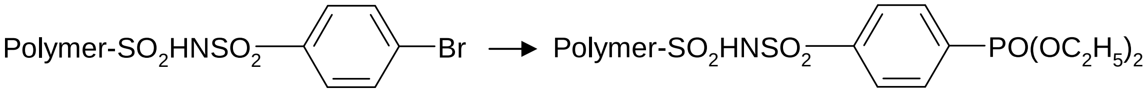

Figure 151. Reaction scheme of phosphonation of the brominated polymer.

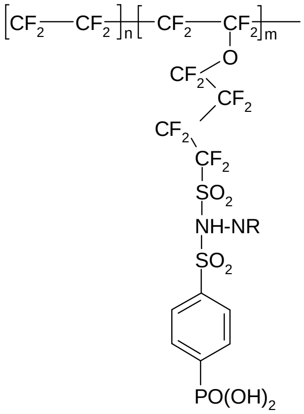

Figure 152. Structure of the phosphonic acid polymer.

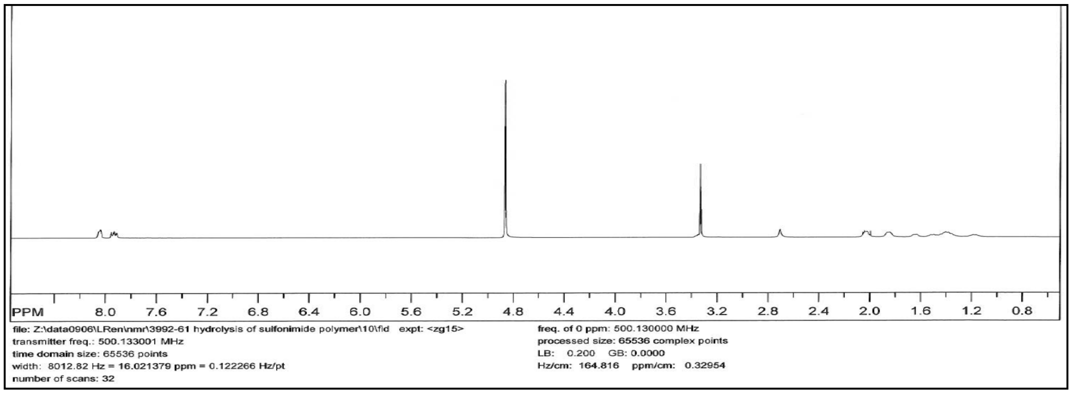

```
file: Z:\data0906\LRen\nmr\3992-61 hydrolysis of sulfonimide polymer\10\fid   expt: <zg15>      freq. of 0 ppm: 500.130000 MHz
transmitter freq.: 500.133001 MHz                                                               processed size: 65536 complex points
time domain size: 65536 points                                                                  LB:   0.200   GB: 0.0000
width:  8012.82 Hz = 16.021379 ppm = 0.122266 Hz/pt                                            Hz/cm:  164.816   ppm/cm:  0.32954
number of scans: 32
```

Figure 153. 1H-NMR spectrum of polysulfonimide phosphonic acid polymer.

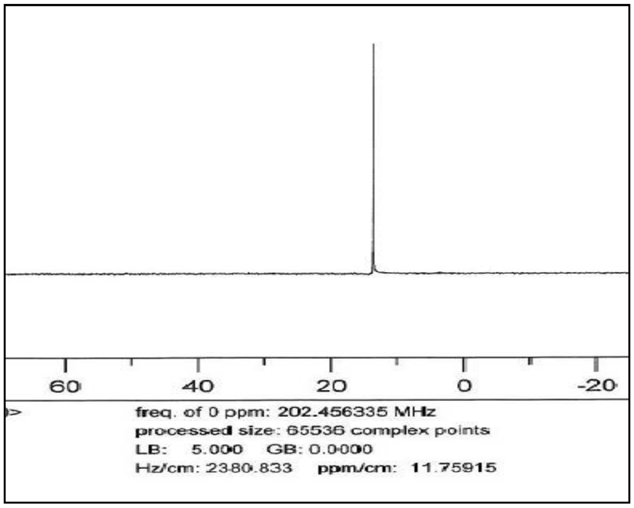

Figure 154. 31P-NMR spectrum of polysulfonimide phosphonic acid polymer.

Further Reaction of Phosphonated/Brominated 3M ionomer

In the preceding section we described the successful phosphonation of 3M ionomer with aryl bromide pendant groups. The phosphonate ester resulting from the above reaction can be hydrolyzed by trimethylsilyl bromide (TMS-Br) in acetonitrile, however, repetition of these reactions and NMR analysis led us to believe that phosphonation reaction is often incomplete and not all bromine pendants are converted to phosphonate groups.

This result led us to intentionally attempt a partial phosphonation of the bromine groups. The overall reaction scheme is given in Figure 155. First, Br-containing polysulfonimide was phosphonated partially to yield polymer bearing two side chains. One is phenylphosphonate sulfonimide and the other one is still phenyl bromide sulfonimide. The phenylphosphonate sulfonimide side chain can then be hydrolyzed to phenylphosphonic acid sulfonimide as shown in Figure 155. From here, the modified polymer can be reacted via three different routes:

Route 1: Heteropolyacids (HPA) can be attached to polymer to aid in increased proton conductivity while render the HPAs stable to dissolution in water.
Route 2: The functional group phenyl bromide on side chain can be reacted with Sodium sulfite to create a sulfonic acid group. This can help in creating three different proton conducting groups, sulfonamide, sulfonic acid and phosphonic acid groups.

Route 3: The modified polymer group containing phosphonic acid can be reacted with Zironium ions to create cross links which can help in improving the strength and decrease water solubility.

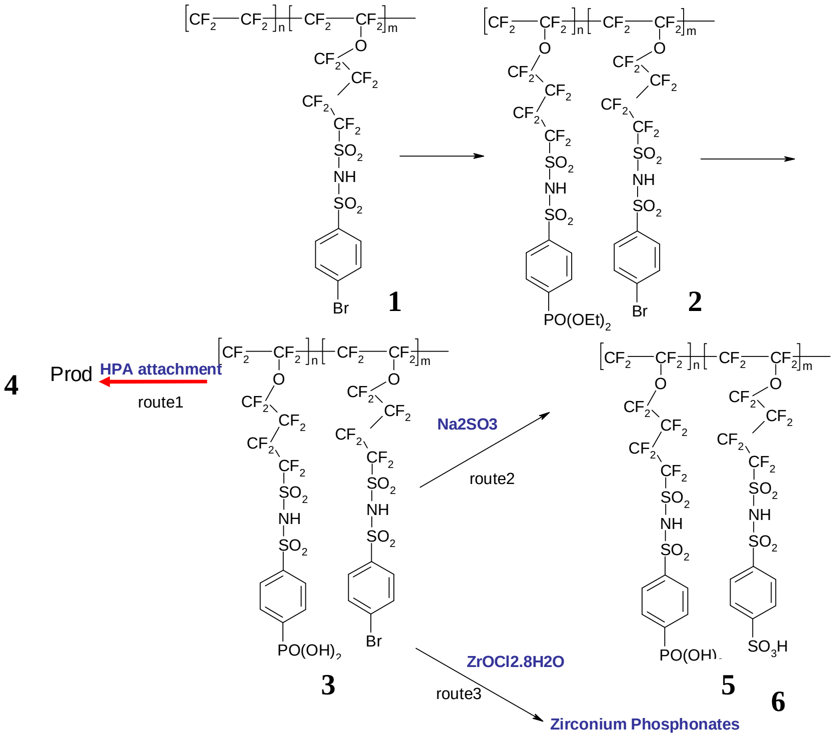

Figure 155. Further reactions of phosphonated/brominated 3M ionomer.

We have carried out experiments have been carried out towards route1 so that HPA can be attached to the polymer **3**. The first trial started from 60% phosphonated phenyl bromide sulfonimide polymer **2**. The phenylphosphonate functional group was then hydrolyzed by Trimethylsilyl iodide (TMSI) to yield phenylphosphonic acid group **3**. The chemical structures of the phosphonated polymer and the hydrolyzed polymer containing phosphonic acid groups were confirmed by NMR. The resulting polymer was then reacted with lacunary heteropolyacid $K_8SiW_{11}O_{39}$, and the resulting product was analyzed by NMR (see Figure 156). ^{31}P-NMR of the product after HPA attachment reaction shows three new peaks at 25.56, 10.93 and 8.31ppm, while the ^{31}P NMR of the starting polymer shows a peak at 12.80ppm which disappeared/shifts during the course of the reaction. ^{1}H-NMR of the product after HPA attachment shows some new peaks at 9.48, 7.31 and 6.67ppm compared with the unreacted polymer. ^{19}F-NMR data shown in Figure 157 clearly indicates that the polymer backbone did not change during the HPA attachment reaction. The NMR data presented here clearly led us to believe that HPA does indeed get attached to the polymer. Further studies to fully establish the attachment of HPA (for example leaching studies would be necessary to establish that HPA phosphonate linkage is indeed stable to water dissolution). Another key study would be to prepare a membrane from the resulting product to study its conductivity.

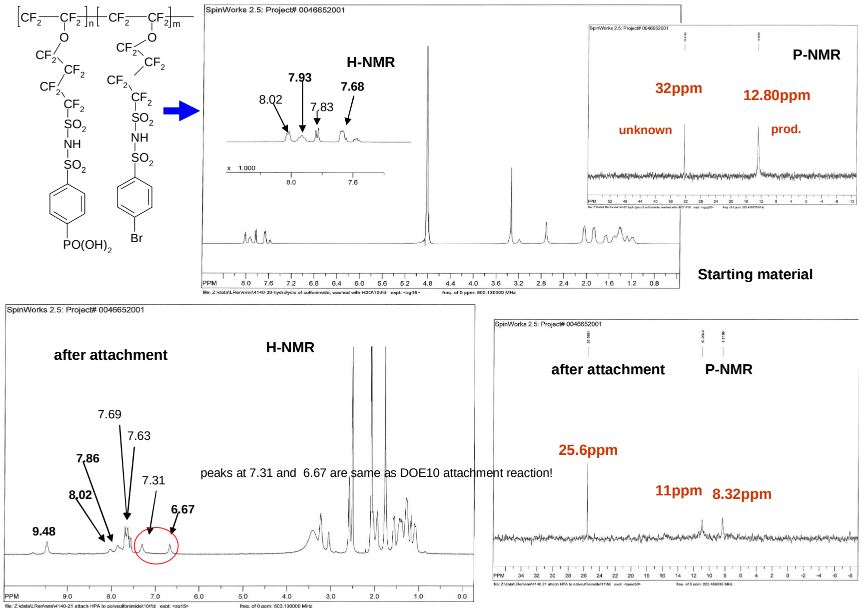

Figure 156. 31P and 1H NMR data for the phosphonic acid containing polymer and its reaction with HPA.

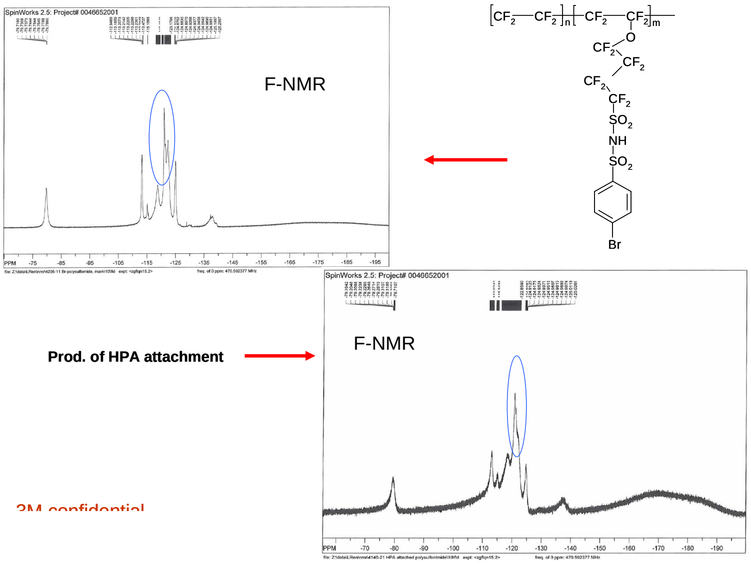

Figure 157. 19F NMR data for the phosphonic acid containing polymer and its reaction with HPA.

We have also carried out cross linking reaction of the polymer containing phosphonic acid groups with Zirconium salts in order to obtain a cross linked material (route 3). The polymer was reacted with Zirconyl chloride hydrate in a fluoride medium. The resulting material was analyzed by ^{31}P NMR in solid state (Figure 158). The peaks at -5.38 and 3.7 ppm clearly indicate that phosphonate groups are linked to Zirconium atoms. The peak at 10.35ppm most likely is inaccessible to zirconium atoms.

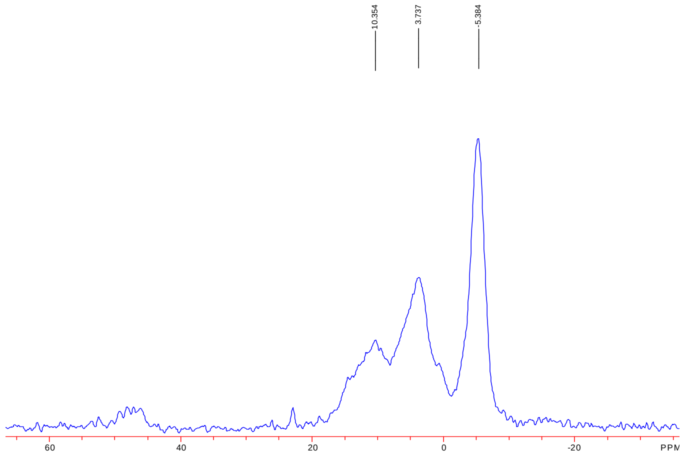

Figure 158. 31P Solid state NMR data for the phosphonic acid containing polymer and its reaction with Zirconium salt.

Conclusions

New proton conducting bis sulfonyl imide containing phosphonic acid molecule and polymer have been synthesized and characterized for the first time in literature. Zirconium phosphonates have been prepared and characterized using these phosphonic acid molecules. Composite membrane containing 3M ionomer and zirconium phosphonate additives were prepared and their proton conductivity and fuel cell performance was tested during the course of study. In many cases the conductivity and fuel cell performance of the composite membranes was inferior compared to the control membranes however in some cases after cleaning the material of residual unreacted compounds better fuel cell performance was observed. Our understanding is that further improvements in the synthesis methods and better choice of molecules can provide new additives which may provide new additives with improved fuel cell performance in composite membranes. These materials also provide phosphonate groups for further anchoring and cross linking points. Initial reactions are a testimony to the fact that phosphonate groups do indeed attach HPA as well as bind zirconium atoms.

References

1. G. Alberti, M. Casciola, U. Costantino, M. Leonardi, *Solid State Ionics* 1984, **14**, 289.
2. M. Casciola, D. Bianchi, *Solid State Ionics* 1985, **17**, 287.
3. D. Carriere, M. Moreau, K. Lhalil, P. Barboux, J.P. Boilot, *Solid State Ionics* 2003, **162–163**, 185.
4. G. Alberti, M. Casciola, U. Constantino, R. Vivani, *Adv. Mater*. 1996, **8**, 291.
5. a) G. Alberti, M. Casciola, U. Costantino, A. Peraio, E. Montoneri, *Solid State Ionics* 1992, **50**, 315. b) E.W. Stein Sr., A. Clearfield, M.A. Subramanian, *Solid State Ionics* 1996, **83**, 113.

Appendix 3 Composites with Mn substituted Heteropoly Acids – Carried out With the Colorado School of Mines

The free radical attack and decomposition of ionomers during fuel cell operation is a severe problem. To mitigate against free radical attack cations, such as Mn or Ce can be added to the ionomer. While these cations decompose the free radicals before they can attack the ionomer and dramatically increase membrane electrode assembly lifetime they take up ion exchange capacity and so increase area specific resistance of the MEA. To improve on this approach we investigated the use of Mn substituted heteropoly acids (HPAs) which are proton conductors. The issue with this approach is that the HPA are water soluble. We show dramatic improvements in fuel cell performance with the Mn substituted HPAs but we were unsuccessful in discovering an immobilization strategy for these useful additives.

The results of the soak tests in Figure 159 show that without the addition of Cs the weight lost during a 24-hour soak in water is equal to the weight percentage of additive added. However, with the addition of the Cs salt of the MnHPA the weight loss becomes significantly less. At the highest loadings tested, 15 wt%, the total mass loss from the composite membrane was between 2 – 7%. This is interpreted as at minimum 50% of the additive that was put into the membrane remains after this soak test. The soak test supports the hypothesis that CsMnHPA can become immobilized within the polymer matrix and persist within an operating fuel cell.

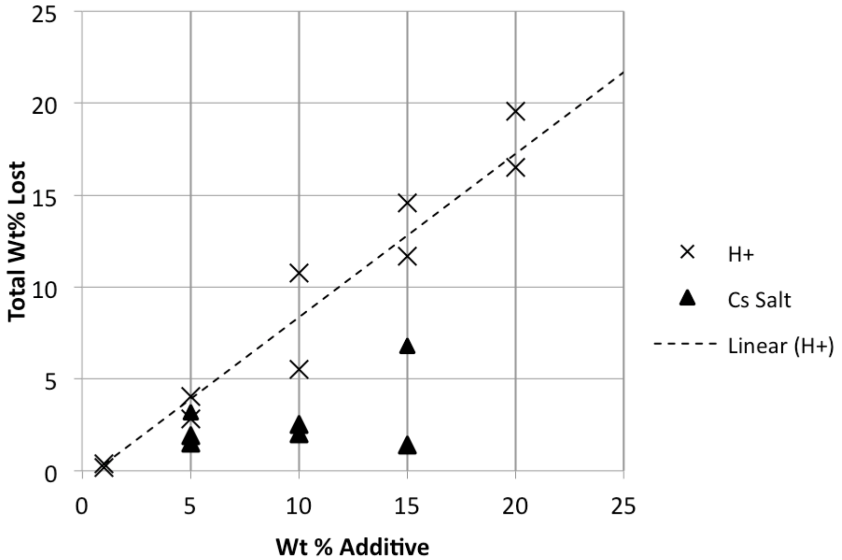

Figure 159. Weight loss after 24h soak in water

EXAFS was used to characterize the interaction of the Mn HPA additive with the 3M ionomer in the composite ionomer. When the additive is put into the membrane all of the long-range structure for the Mn in the EXAFS disappears. This is consistent with the Mn becoming liberated from the Wells-Dawson structure. For comparison $MnSO_4$ in the membrane was also fit and the parameters for the Mn edge in this system are almost identical to that of the Mn edge of the MnHPA in the ionomer. This provides evidence that the MnHPA breaks down into two separate ions, the P_2W_{17} anion and Mn^{II} cation nd that the bonding of the Mn to the HPA is quite weak.

The addition of both 1% and 5% MnHPA improved the initial performance of the MEAs, Figure 160. While the OCV is relatively unchanged in the three samples, the 1% MnHPA MEA shows 110mV improvement at 1 A / cm^2 over the control. This improvement can also be visualized by a 200 mA / cm^2 improvement at 300mV. While both MEA containing additives showed improvements over the control the 1% MnHPA showed the greatest improvement. This may be due to inhibition, at higher weight loadings of additive, of the creation of the pore network that is most effective at H^+ transport. This has been witnessed in the SAXS of HPA composite membranes by the presence of larger ionic domains with the addition of higher loadings of HPA.

Both the 1% and 5% HPA outperformed the control in the temperature challenge experiment. At a cell temperature of 85°C (81.95% Rh) the 1% MnHPA out performs the control by 80mV (at 0.4 A / cm^2). As the cell heats at constant dew point, the magnitudes of the improvements tend to increase. A maximum improvement of 160 mV, vs. the control, at a cell temperature of 100°C (46.8% Rh) was reached. Again, the 1% sample shows increased performance over the 5% in all cases, but as the cell temperature is increased (Rh lowered). The discrepancies in performance between the different weight loadings of the additive decreases at lower Rh. At 100°C cell temperature and 80°C dewpoint the improvements of the two loadings of additives are within experimental error of each other, while showing significant performance gains over the control. This is consistent with the presented theory that at a weight loading at or above 5% the morphology of the pore network is inhibited. At lower RH's this network is already severely disrupted. Therefore, in an already disrupted pore network the increase in H^+ conduction at lower RH (from HPA addition) is more apparent.

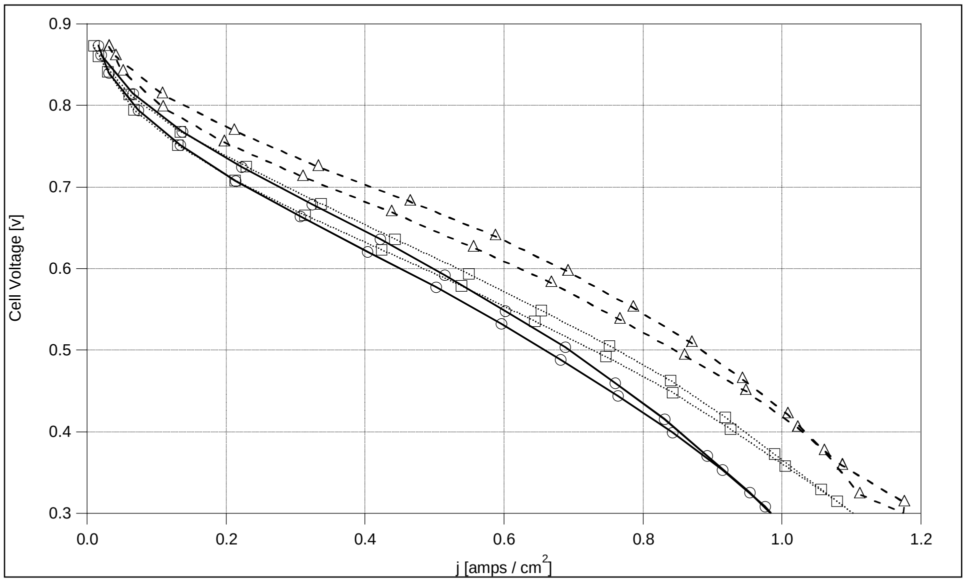

Figure 160 Polarization Scan of 1% MnHPA(△), 5% MnHPA (□), and 1000 EW 3M ionomer Control(○)

As can be seen in Figure 161 the F^- ion measured in the effluent water is approximately half in the additive containing membranes, as compared to the control. The control sample has an initially high FER, around 2 µg/ cm^2 / day, but lowers to 1.5 µg/ cm^2 / day after 20 hours. Both additive samples show FER of less that 1 µg/ cm^2 / day. These rates stay constant throughout the accelerated test.

Observing that the FER remains constant with MnHPA addition, it is interpreted as mitigating the oxy-radical induced degradation and appears to limit other forms of F^- producing degradation. Other groups have confirmed this by simply adding Mn as an ion. However we have shown the Mn HPA offers improvement over simply adding Mn ion. As the chains containing these weak-link end are degraded and there are less of them left and therefore the FER goes down.

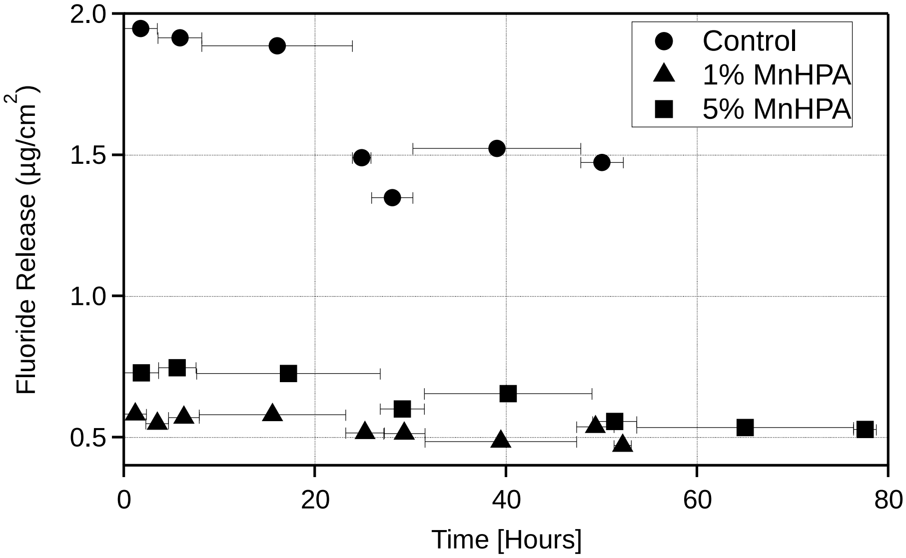

Figure 161. FER vs. Time 1% MnHPA(△), 5% MnHPA (□), and Control(○)

Immobilized Heteropoly acid composites

HPAs are highly soluble in water and easily leach in the presence of water if they are not properly immobilized in the ionomer matrix. Various supports like silica, titania, zirconia have been used to immobilize heteropolyacids as reported in literature. In view of this, we explored the properties of zirconia to immobilize the lacunary heteropolyacids in the PFSAs using sol-gel chemistry to reduce leaching and obtain higher conductivity at temperatures >100 °C. Two sepertae methods were investigated to immobilize HPAs.

In-situ method using lacunary HPAs

A casting dispersion of 825 EW 3M ionomer was obtained from 3M. The lacunary heteropolyacid was synthesized following the procedure reported earlier. A prescribed amount of the zirconia precursor, zirconium propoxide, is weighed out and acetyl acetone (molar ratio acac/Zr=10) is added to it to slow down the hydrolysis. An appropriate amount of propanol water mixture (70/30,v/v) was added to dissolve it completely. To this lacunary heteropolyacid ([α $H_8SiW_{11}O_{39}$].$14H_2O$)) was added, such that the weight ratio of the HSiW to the 3M ionomer is either 1, 5, or 10 (based on the amount of loading) and mixed well with the 20% 3M ionomer solution. Membranes were synthesized with Zr/HSiW molar ratio of 3, 5 and 10. After stirring overnight, the solution was cast on a Kapton® sheet, which is pasted on a glass plate, using a film applicator (using 25 µm gap). The plate is quickly kept in the oven at 80 ^oC for 20 minutes and then further annealed at 160 ^oC or 180 ^oC for 15 minutes. SEM, Figure 162, shows that we obtained sub-µm particles, which appeared to be agglomerates of 2-3 100 nm particles. On boiling the composite membranes lost *ca.* 70% of the HPA by W content but the residual HPA in the composites did show marked improvement in proton conductivity, Figure 163.

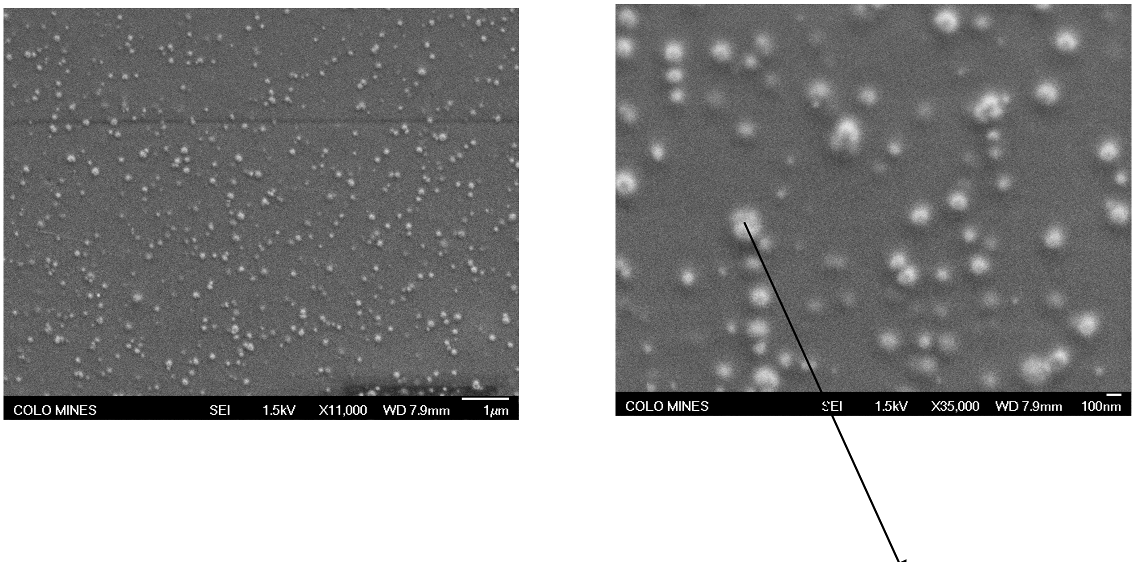

Agglomeration of 2-3 particles

Figure 162. SEM pictures of the composite membranes with Zr/HSiW=3, 1% HSiW loading

Table 12: Leaching results of the zirconia immobilized heteropolyacid membranes using XRF

Memb	ZrO_2/HSiW	HSiW (%)	Amt. before boiling (mg/cm^2) XRF	Amt. after boiling (mg/cm^2) XRF	Tungsten lost (%)
1.	3	10	Zr=0.313 W=0.705	Zr=0.336 W=0.172	W=75.6%
2.	5	10	Zr=0.367 W=0.699	Zr=0.428 W=0.180	W=74.2%
3.	10	10	Zr=0.473 W=0.614	Zr=0.521 W=0.182	W=70.3%

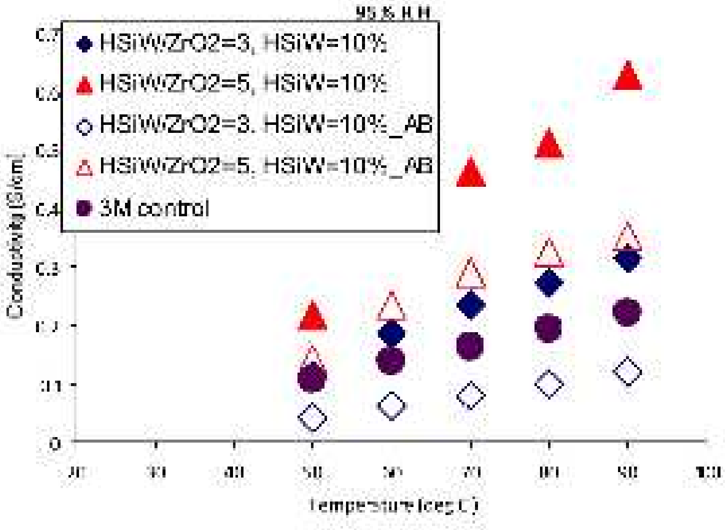

Figure 163. Proton Conductivity of the zirconia immobilized HSiW membranes annealed at 180 °C synthesized by modified sol-gel method as a function of temperature at 95% RH and 50% RH.

In-situ formation of HPAs on preformed ceramic particles

Only *in situ* impregnation of heteropolyacid on the support system appears appropriate to minimize the chance of heteropolyacid leaching out of the composite. The objective of this work is to investigate 3M Membrane (PFSA ionomer) doped with in situ impregnated heteropolyacid on zirconium phosphate by employing the in situ impregnated heteropolyacid demonstrated by Rao et al. In their work, Rao *et al.* supported tungsten oxide on porous zirconium phosphate to achieve phosphotungstic acid supported on zirconium phosphate. It was shown to have good catalytic activity towards esterification reaction. This approach appears suitable to prepare composites of heteropolyacid for applications which require high stability of heteropolyacid under hydrated conditions.

Keggin type heteropolyacid was prepared *in situ* by wet impregnation of sodium tungstate on zirconium phosphate support. In a typical method, sodium tungstate (15 wt% of W) dissolved in deionized water was added to zirconium phosphate. The pH of the resultant mixture was adjusted to 2 by addition of dilute HCl. It was allowed to sit overnight followed by evaporation at 60° C under vacuum to obtain the final product. The final product, phosphotungstic acid on zirconium phosphate is denoted as HPW/ZrP.

The effect of the inorganic additive on the conductivity of 3M Membrane was evaluated on a recast undoped 3M Membrane and recast 3M Membranes modified with different content of the inorganic additive (Figure 164). With the increase in temperature, proton conductivity values are found to increase for all the doped and 3M control membranes. As the figure illustrates, when the content was increased from 0.5% to 1%, conductivities increased at all temperatures. Above 1% increase in the content gradually decreased the conductivity and 5% doped membrane remained close to the unmodified

3M Membrane. This indicates that above 1% loading, the additional inorganic additive did not facilitate the proton conductivity. Proton conductivity of 1% doped membrane shows good improvement than the undoped control membrane at all the temperatures.

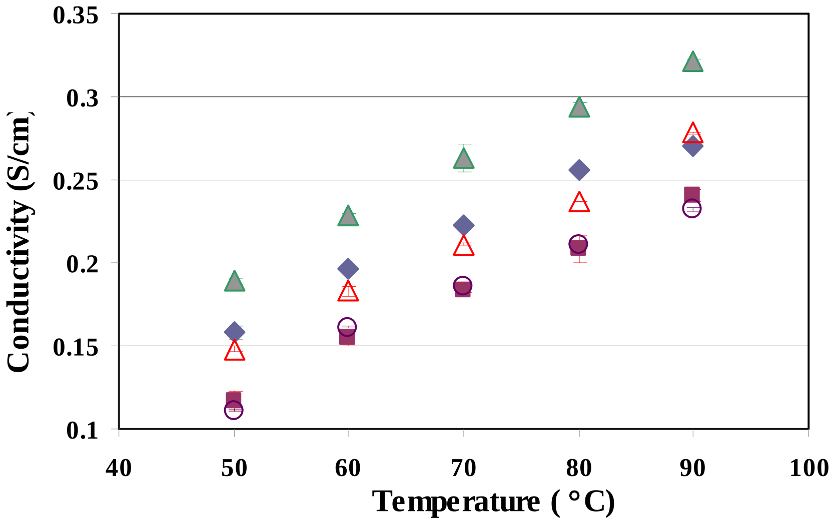

Figure 164. Proton conductivity of the control 3M Membrane (■) and 3M doped with 0.5 % (◆), 1% (▲), 2% (△) and 5% (○) additives at 95 % RH

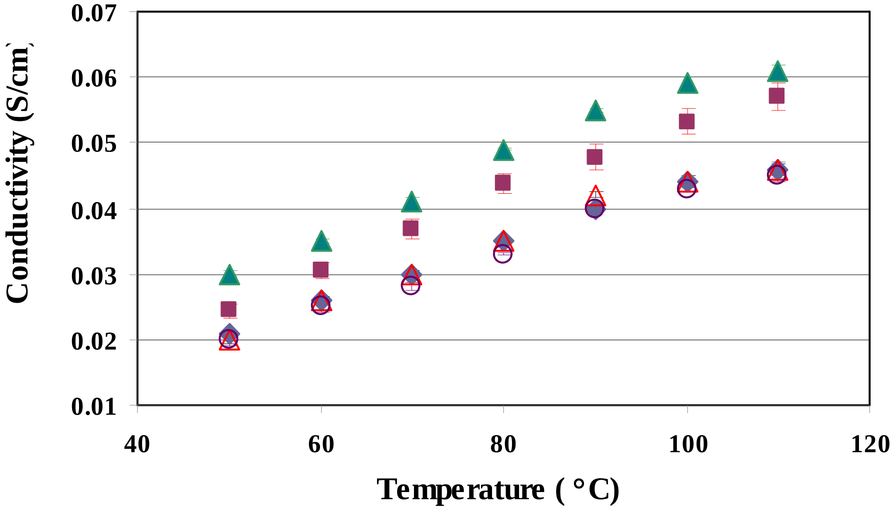

Figure 165. Proton conductivity of the control 3M Membrane (■) and 3M doped with 0.5 % (◆), 1% (▲), 2% (△) and 5% (○) additives at 50% RH

It is obvious that the effect of RH on the conductivity is significant for all the membranes (Figure 165). A decrease in conductivity could be observed for all the membranes from 95 to 50% RH. At 50 %RH only 1% doped membrane performed better than the control membrane. All other membranes exhibited almost similar conductivities at all temperatures and the values are lower than the control membrane. From the proton conductivity data, Arrhenius plots (not shown) were drawn and the activation energies obtained showed that the additive lowered the activation energy for proton conduction.

In attempt to add a metal active for free radical decomposition we loaded $H_xK_{13-x}Ce(SiW_{11}O_{39})_2.xH_2O$ (50 %, by weight) on ZrW_2O_8 nanorods. The required amount of the heteropolyacid was dissolved in 0.1 M HCl. To this solution, 1g of ZrW_2O_8 nanorods was added while stirring. Stirring was continued at 80 °C until it dried completely. It was followed by heating at 120 °C for 12h and 200 °C for 4h. The particles are approximately 50 nm in diameter as shown by SEM.

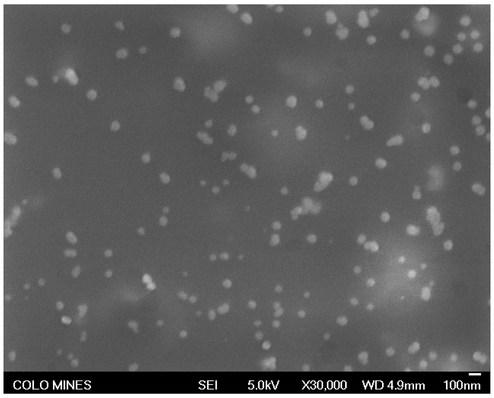

Figure 166. SEM images of 1% additive doped 3M Membrane.

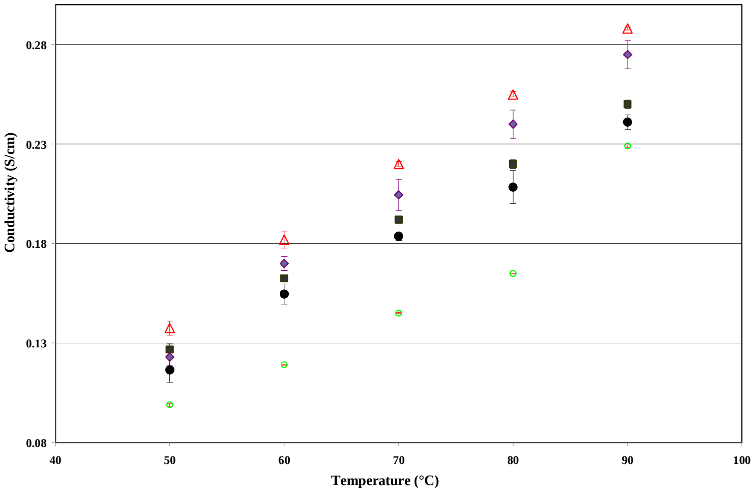

Figure 167. Proton conductivity of 3M(●) and modified 3M Membrane with 0.5% (△), 1%(■), 2%(○) and 5% inorganic content at 95% RH.

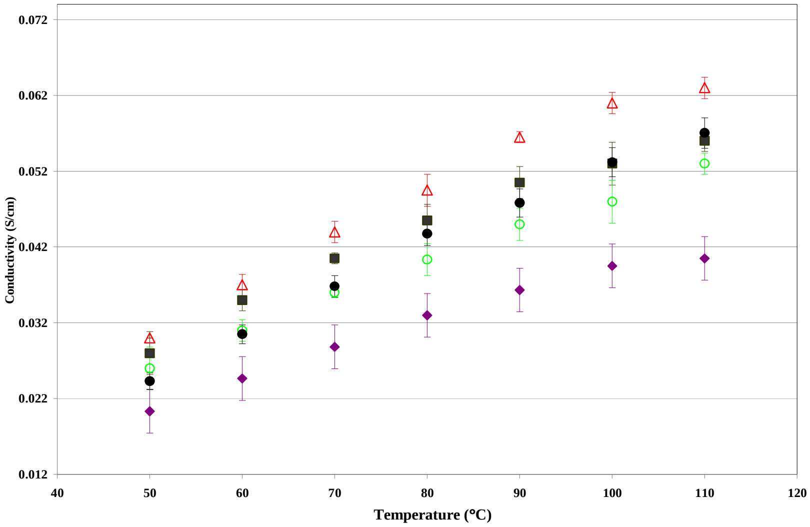

Figure 168. Proton conductivity of 3M(●) and modified 3M Membrane with 0.5% (△), 1%(■), 2%(○) and 5% inorganic content at 50% RH.

Figure 167 shows the effect of inorganic additive incorporation on the proton conductivity of 3M ionomer at 95%RH. As expected, the proton conductivity shows an increasing trend over temperature for all the membranes. Except the 2% additive loaded membrane, all other loadings show enhanced conductivity compared to the undoped control membrane. The best values were obtained from 0.5 % additive doped membrane. At 50% RH, the 5% loaded membrane lost its conductivity considerably and reached closer to the undoped control membrane (Figure 168). Not much enhancement was observed for the 2% and 1% modified membranes compared to the control membrane. At all the three RH conditions, 0.5% doped membrane remained with good conductivity values than the unmodified 3M Membrane.

Appendix 4 - Chemical Degradation Studies of Model – Carried out in Collaboration with Case Western Reserve University

Aromatic, fluorinated and partially fluorinated model compounds (AMCs), representative of hydrocarbon fuel cell membranes were studied under accelerated fuel cell conditions to understand the degradation patterns. Liquid Chromatography-Mass Spectrometry (LC-MS) was used as the major analytical technique to identify degradation fragments. The degradation products observed under the conditions used were mostly due to hydroxylation of the aromatic ring. Some model compounds undergo multi-hydroxylation, dimerization while others broke into smaller fragments. Mass balance data was then obtained to account for amount of AMCs lost during the degradation reaction. The evolved CO_2 due to complete oxidation of AMCs was also quantified, using GC-MS. Fluorinated samples were in addition, analyzed for free fluoride ions after completion of degradation reactions. Degradation rates of AMCs were also compared to previously studied perfluorinated non-aromatic model compounds. The present work examines the mechanism of membrane degradation, using hydroxyl radicals generated *in situ* using Fenton's Reagent, and from photochemical cleavage of hydrogen peroxide. The methodology used, focusing on small molecule model compounds which represent portions of the polymer systems, allows for effective use of organic analytical tools, and follows that used previously to examine degradation in perfluorinated PEMFC systems.[10]

Methods:
The structures of the AMCs used for this study are shown in **Figure 1**. Samples of AMCs 1-10 were commercially available, while AMC11, and AMC12 were synthesized at 3M; all samples were used as received. AMC5 was not used directly for degradation but it was sulfonated to its mono-sulfonic acid, sodium salt (AMC5-S) and then used for the study. AMC2 and AMC4 were also sulfonated and both their sulfonated salts and unsulfonated starting materials were used for the degradation study. AMC2 and AMC5 were sulfonated using 95% H_2SO_4 as the sulfonating agent while HSO_3Cl was used for sulfonating AMC4.

Degradation and Analytical Conditions:
For *Fentons Reagent degradation* experiments, solutions of AMC (100 mM) and ferrous sulfate (1.25 mM) were combined dry nitrogen gas for 5-10 min to remove any dissolved oxygen in the solutions that might quench the radicals. 11 mM of hydrogen peroxide was added every hour for 24 hours to accelerate the degradation test. Fresh ferrous sulfate was again added to the mixture after 7 hours of degradation. Samples were extracted after 1, 3, 5, 7 and 24 hrs for LC-MS analysis of AMC degradation. UV photolysis of hydrogen peroxide was used as a secondary method for the degradation study of model compounds. This method has been used previously for the generation of hydroxyl radicals which are strong oxidants. It also serves as a metal free degradation test for the model compounds. For *UV degradation* experiments, a 170-190W mercury lamp (250-2500 nm) was used as the UV light source for the degradation test. 100 mM solution of AMC placed in quartz cuvette was purged with dry nitrogen gas to remove dissolved oxygen. 100 mM of H_2O_2 was then added to the AMC solution. The covered

solution was placed about 13 cm away from the light source and exposed to UV light for 1hour with constant stirring.

Analysis of degradation products was performed on Thermo Scientific LC-MS, operating in the negative-ion electrospray mode of the range of 50-500 m/z was used. For better separation of the AMCs with sulfone and sulfonic acid groups, an Allure biphenyl column (Restek Allure biphenyl column, 50 × 2.1 mm, 5 µm particle size), utilizing water (Solvent A) and methanol (Solvent B) was used. Water was used as the mobile phase (Solvent A) and Methanol (Solvent B) for majority of the samples.

Results and Discussion

Hydrogen peroxide, alone is a strong oxidant for various organic and inorganic compounds. To improve its oxidation properties transition metal salts, e.g. iron salts, ozone or UV light can be used which activates the peroxide to produce hydroxyl radicals, which are stronger oxidants. The Fenton's Reagent combination of peroxide and ferrous salts has been used effectively to oxidize a variety of organic substances, and is commonly used in fuel cell membrane durability studies. This test was used as the primary method to study the degradation pattern in the model compounds. The combination of hydrogen peroxide and UV light was used as a secondary, metal-free method in this degradation study.

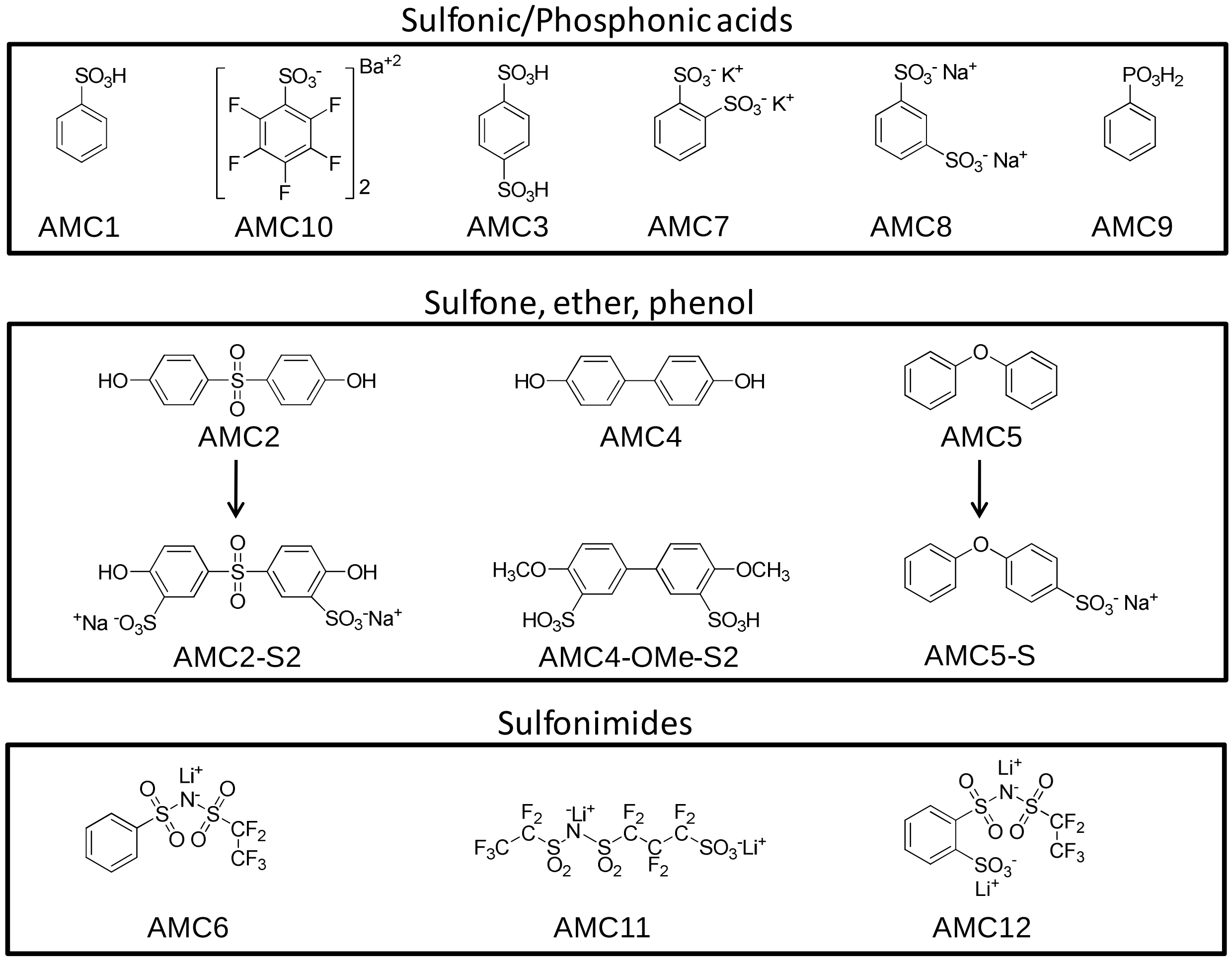

Figure 1. Structures of aromatic model compounds (AMCs) used for the study.

Degradation of AMCs:

The model compounds shown in **Figure 1** were studied in three groupings. The first group contains AMCs with either sulfonic or phosphonic acid groups (e.g.AMC1, AMC7, AMC8, AMC9, and AMC10). The second group is composed of sulfones, ethers and biphenols (e.g.AMC2, AMC4 and AMC5). These AMCs do not contain highly acidic groups hence they were sulfonated and then the sulfonated compounds (e.g.AMC2-S2, AMC5-S and AMC4-OMe-S2) were also studied by the two degradation processes given above (see the chemistry listed in the middle block of **Figure 1)**. The last group of model compounds to be degraded is comprised of sulfonimides such as AMC6, AMC11 and AMC12, and represent a relatively new family of PEM materials of interest within the field.

<u>Degradation of Group 1; Sulfonic/Phosphonic acids</u>**:**

This group of compounds represents the proton conducting groups present on the polymer side-chains of many hydrocarbon PEM membrane polymers. Sulfonate groups are the most commonly utilized acidic groups in PEM materials, and there is interest in potentially functionalizing aromatic rings with more than one sulfonate. To this end, model compounds with one or two sulfonate groups were studied. Treating the compounds with either Fenton's reagent or UV/H_2O_2 exposure showed degradation of the model compounds in this group to various degrees. Figure 2 shows the LC-MS of AMC1 after 24 hrs of exposure to Fenton's degradation test. The chromatogram shows two distinct signals (**a** and **b**); the mass spectra (**a_1** and **b_1**, respectively) of which are shown below. As the mass spectra were collected in negative ion mode, all the MS signals are from negatively charged species; in case of the AMC1 the negatively charged species is formed by the loss of the acidic proton of the sulfonic acid group. Signal **b** in the chromatogram corresponds to the intact AMC1, the corresponding MS (**b_1**) of which shows the parent anion at 157Da. Signal **a** in the chromatogram corresponds to a range of products in the MS (**a_1**) starting from 173Da to 239Da with a difference of 16Da. These MS signals are due to hydroxylation (-OH: 17Da) of the benzene ring of AMC1 in sequential order (net addition of 16Da). Although, the MS shows signals due to various hydroxylated products the major signal is due to di-hydroxylated AMC1 (189Da). From the chromatogram it can also be seen that larger amounts of the starting material has been consumed under the present degradation conditions; although the only degradation products observed under the present MS conditions were hydroxylated anions.

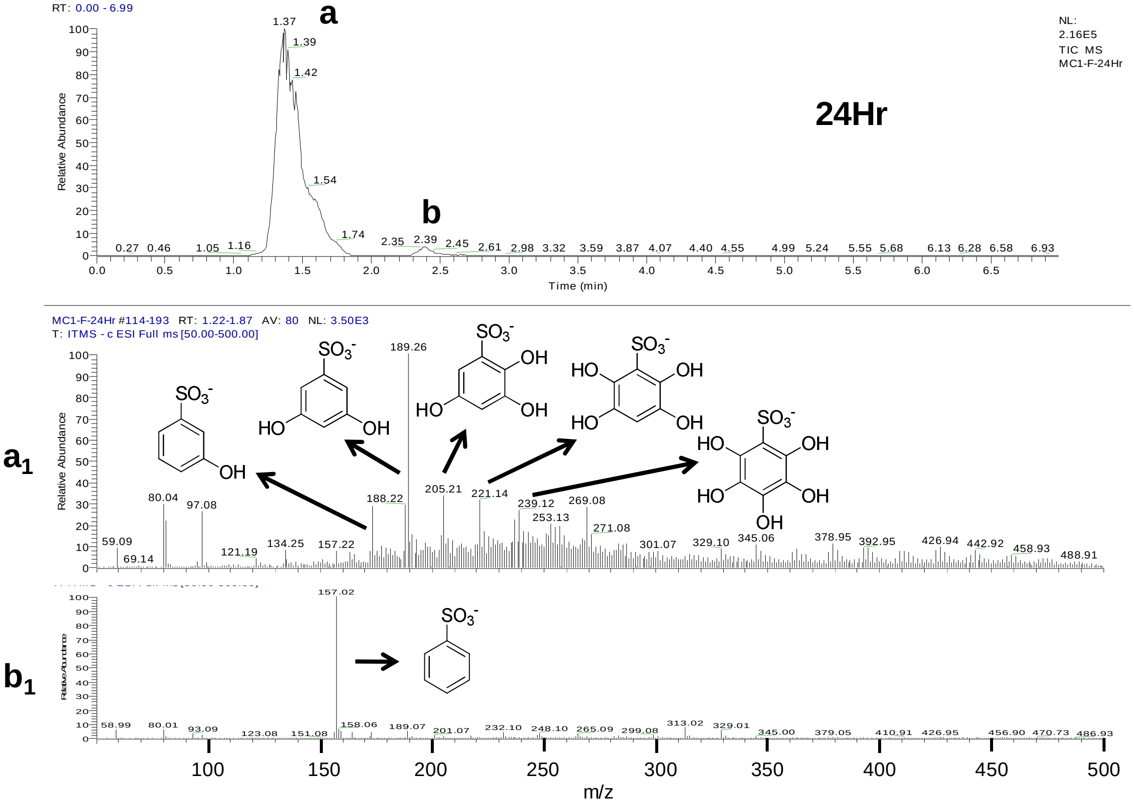

Figure 2. LC-MS spectra of AMC1 after 24hrs of Fenton's degradation test.

Table 1 lists the degradation products observed from both the Fentons and UV degradation methods for the Group 1 AMC compounds. The stability of fluorinated analog of AMC1; AMC10, was also studied under similar degradation conditions. LC-MS analysis (Figures 3, 4**)** of this compound after 24hrs of degradation under the

Fenton's conditions showed formation of very minor amount of mono-hydroxylated products where one of the fluorines was replaced by –OH; the amount of this mono-hydroxylated product increased over a period of two months. Comparing the degradation data of AMC1 and AMC10 after 24hrs of Fenton's degradation test suggests that substitution of hydrogen with fluorine in these aromatic compounds renders them much less susceptible towards radical attack, as one might expect. The phosphonic acid group is another acidic group which is being explored for proton conduction in fuel cell membrane polymers, potentially as a replacement for sulfonates, due to due to its higher conductivity by self-ionization in the absence of water. The effect of hydroxyl radicals on aromatic phosphonic acids was studied using AMC9. This model compound under the Fenton's conditions shows formation of minor amounts of mono-hydroxylated phosphonic acid (m/z 173Da; **Figure 5**). Similar amounts of dihydroxylated product were also observed with UV/H_2O_2 exposure of the aryl phosphonic acid.

The effect of hydroxyl radicals on ortho, metal and para substitute aromatic disulfonates, AMC3, AMC7 and AMC8 were evaluated under the same conditions used for the monoacids. Figures 6a, 6b and 6c show the MS spectra of AMC7, AMC8 and AMC3 after 24 hrs of Fenton's degradation test, respectively. AMC7 shows formation of some mono-hydroxylated and a very low levels of di-hydroxylated anions as the degradation products. Some signals from the formation of benzene sulfonic acid (157Da) and mono-hydroxylated benzene sulfonic acid (173Da) were also detected indicating loss of one of the sulfonic acid groups during the process. AMC8 shows much less degradation products compared to AMC7 while analysis of AMC3 did not reveal any detectable degradation products. The benzene sulfonic acid (m/z 157D) observed in AMC8 is due to the impurity in the compound which was detected during the initial LC-MS analysis of pure compound. Comparing the degradation results of AMC3, AMC7 and AMC8 it can be concluded that ortho-substituted disulfonates are considerably less stable then the analogous meta- and para-substituted aromatics. Owing to its electrophilic nature, the •OH radical shows preference towards the meat position in aromatic rings with deactivating substituent. Thus, AMC3 and AMC8 have fewer sites for the radicals attack than AMC7. EPR studies of sulfonated aromatic model compounds by Roduner suggest that sulfonate substituents are not only useful to increase proton activity but also benefit in reducing the activity of aromatic ring towards hydroxyl radical addition. The low level of degradation products in the case of AMC9 could be due to precipitation of the compound in the solution over the period of 24hrs; this process may occur through formation of a complex with Fe(II)/Fe(III), thus making it unavailable for the reaction. This possibility was confirmed by rapid precipitation on addition of Fe(III) salt to a fresh solution of AMC9. The precipitate formed using an Fe(III) salt and during the Fenton's degradation reaction were both analyzed by elemental analysis and were found to contain Fe, C, O and P.

Degradation of Group 2; sulfones, phenols and ethers:

Polyether sulfones are under consideration as alternative to the poly(tetrafluoroethylene) backbones for PEM membrane polymers. The backbone of such polymers provide toughness and flexibility, with potentially low radical susceptibility compared to other hydrocarbon-based polymers. To study the effect of hydroxyl radical attack on these linkages and end groups, model compounds AMC2, 4 and 5 were selected. These compounds were further sulfonated to either mono- or disulfonic acids to compare the effect of sulfonate groups upon radical attack. The degradation products observed from this group and their sulfonated counter parts are listed in Table 2.

Table 1. Degradation products obtained from UV/H_2O_2 and Fenton's degradation tests of Sulfonic/Phosphonic acids.

AMC	Structures	Degradation Products	
		UV/H_2O_2	Fenton's
AMC1	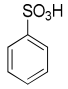	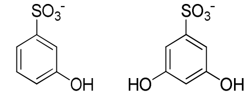	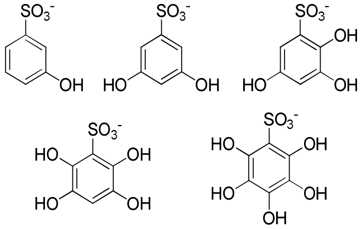
AMC10	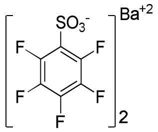		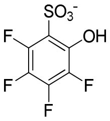
AMC3	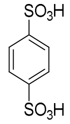	—	—
AMC7	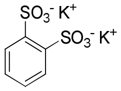	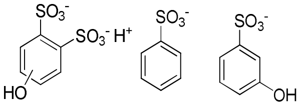	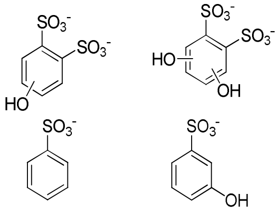
AMC8	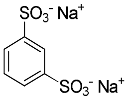	—	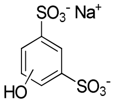
AMC9	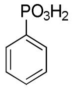	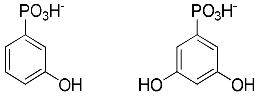	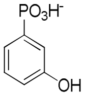

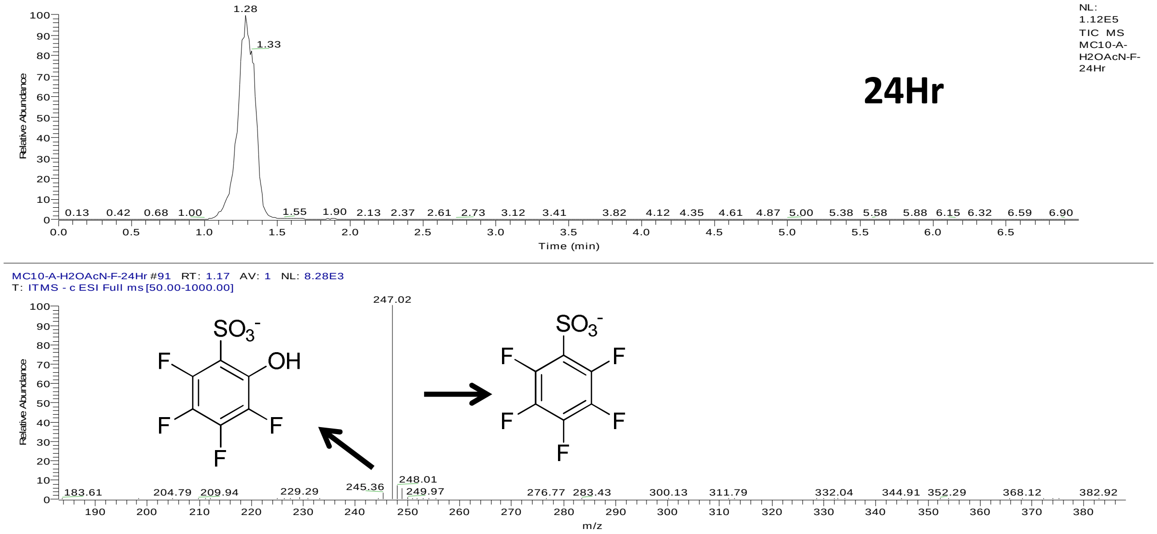

Figure 3. LC-MS spectra of AMC10 after 24hrs of Fenton's degradation.

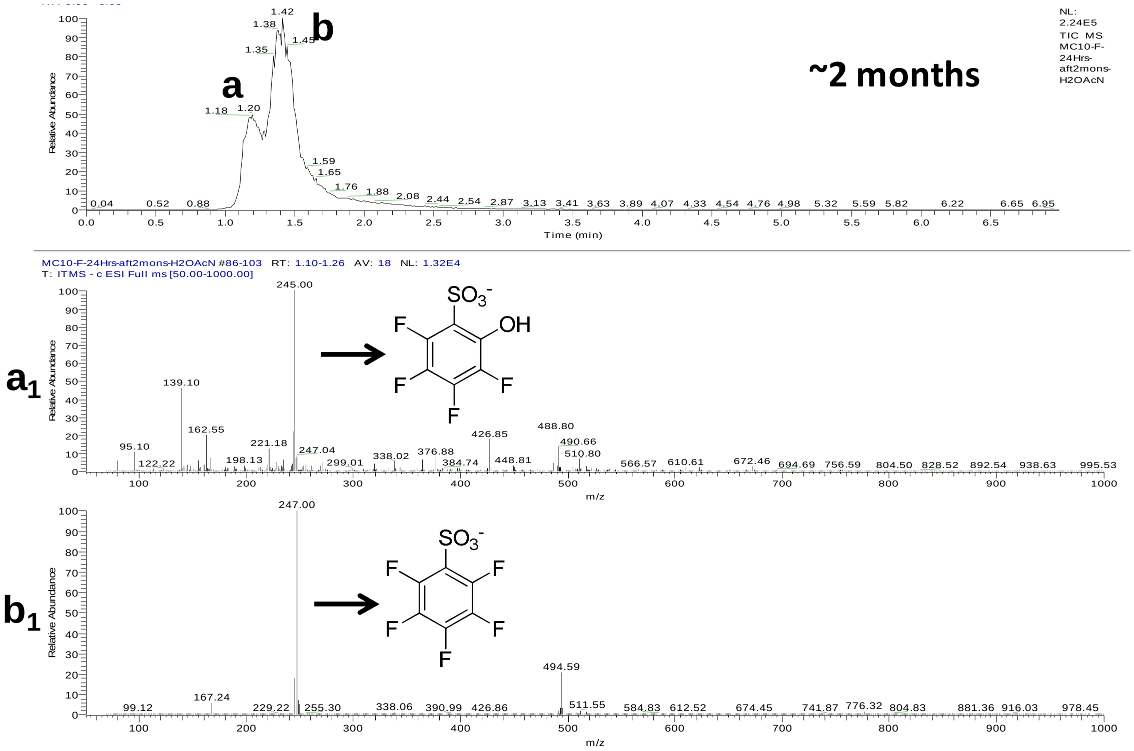

Figure 4. LC-MS Spectra of AMC10 after ~ 2months.

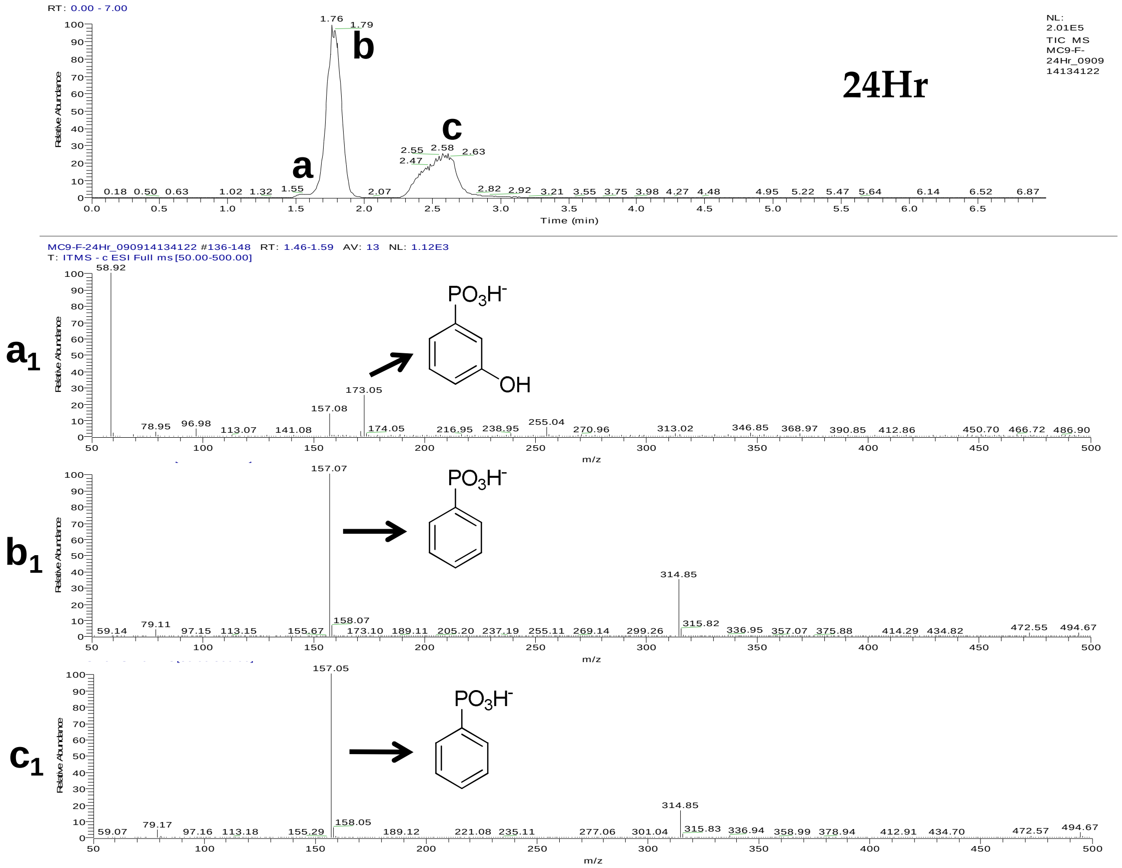

Figure 5. LC-MS spectra of AMC9 after 24hrs of Fenton’s degradation.

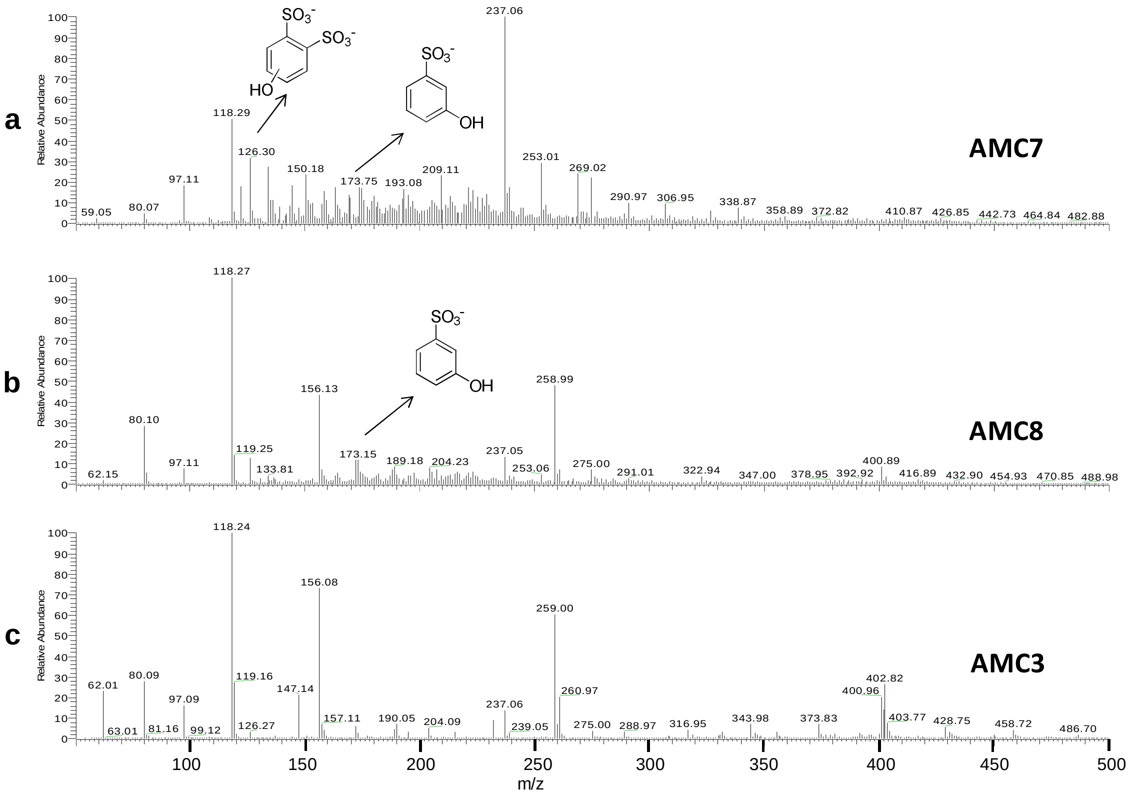

Figure 6. MS spectra after 24 hrs of Fenton's degradation a) AMC7, b) AMC8 and c) AMC3.

Figure 7 shows the LC-MS spectra of the Fenton's degraded AMC2 after 24hrs. The LC trace shows three chromatographic signals **a**, **b**, and **c**. Signal **c** corresponds to the starting material (MS $\mathbf{c_1}$, m/z 249). Some amount of mono-hydroxylation was observed in AMC2 (**b**, $\mathbf{b_1}$, m/z 265). The Fenton's test also results in breaking of AMC2 and the mono-hydroxylated AMC2 at the sulfone link, the negatively charged fragments of which were detected by MS ($\mathbf{a_1}$, fragment **1,** m/z 157, fragment **2,** m/z 173). The UV degradation data also showed breaking of the molecule where fragments **1** and **2** were detected.

Table 2. Degradation products obtained from degradation tests of Sulfones, Phenols and Ether.

AMC	Structures	Degradation Products	
		UV/H_2O_2	Fenton's
AMC2	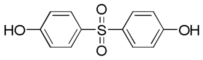	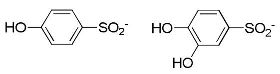	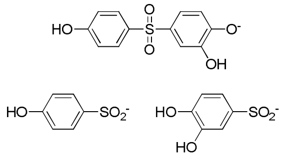
AMC2-S2	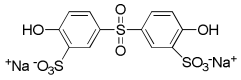	—	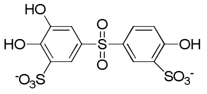
AMC5-S	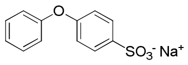	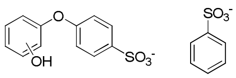	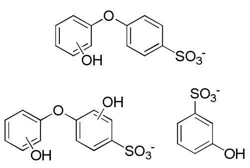
AMC4	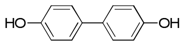	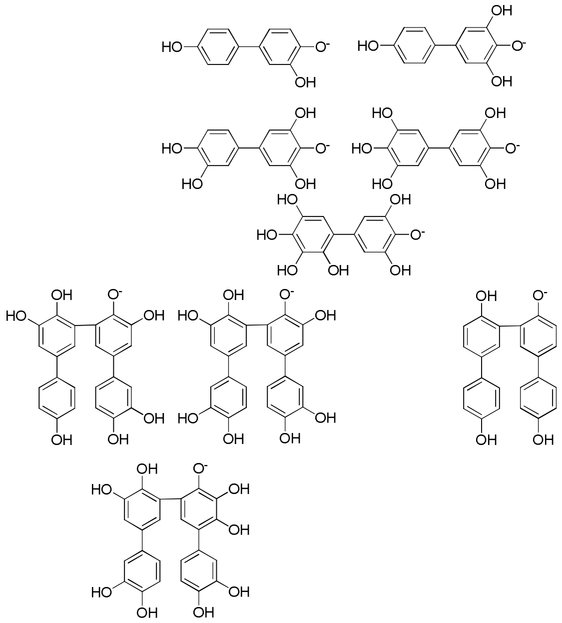	
AMC4-OMe-S2	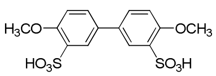	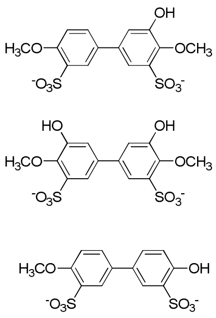	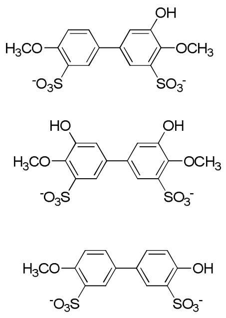

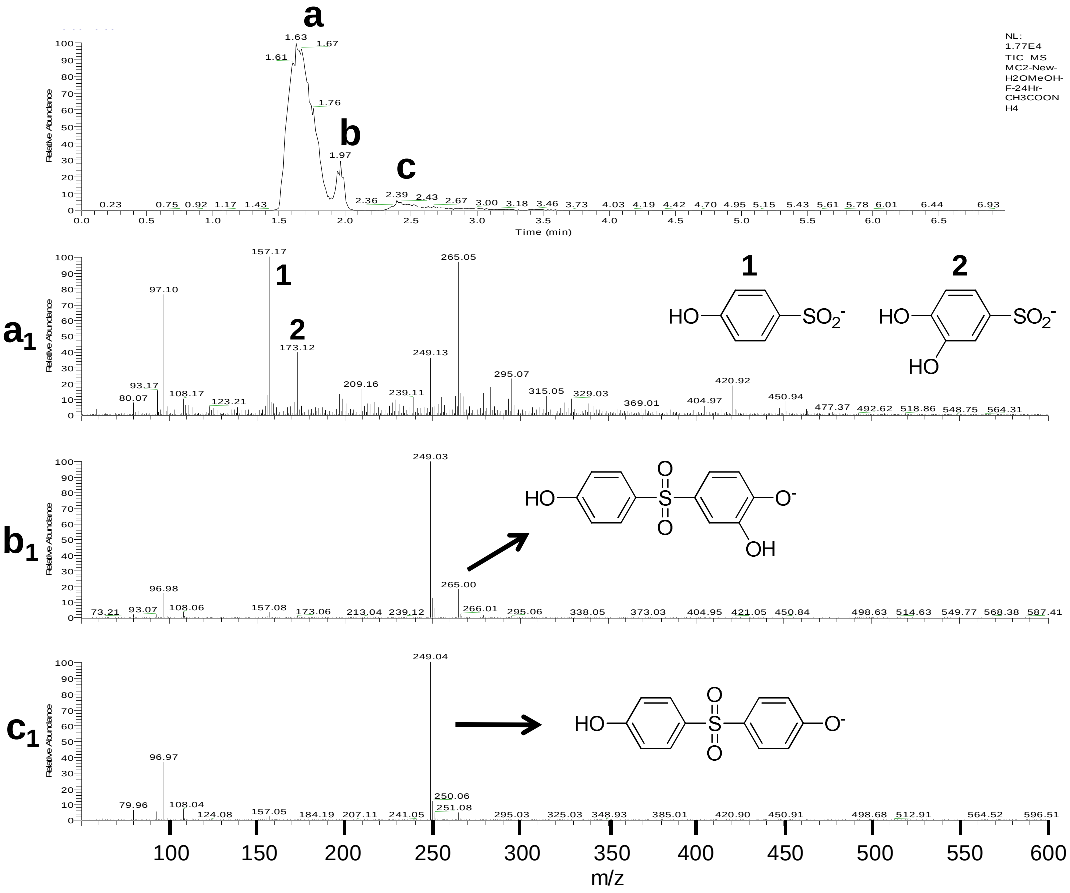

Figure 7. LC-MS spectra of AMC2 after 24hrs of Fenton's degradation test.

Comparing the degradation results of AMC2 to the disulfonated derivative, AMC2-S2; it was observed that the only degradation product obtained was mono-hydroxylated AMC2-S2 (m/2z 212). No signals were detected that suggest fragmentation of the molecule during the degradation reaction, Figure 8. The results suggest that in case of such molecules, sulfonation of the compound inhibits the radical attack, which would otherwise results in backbone cleavage.

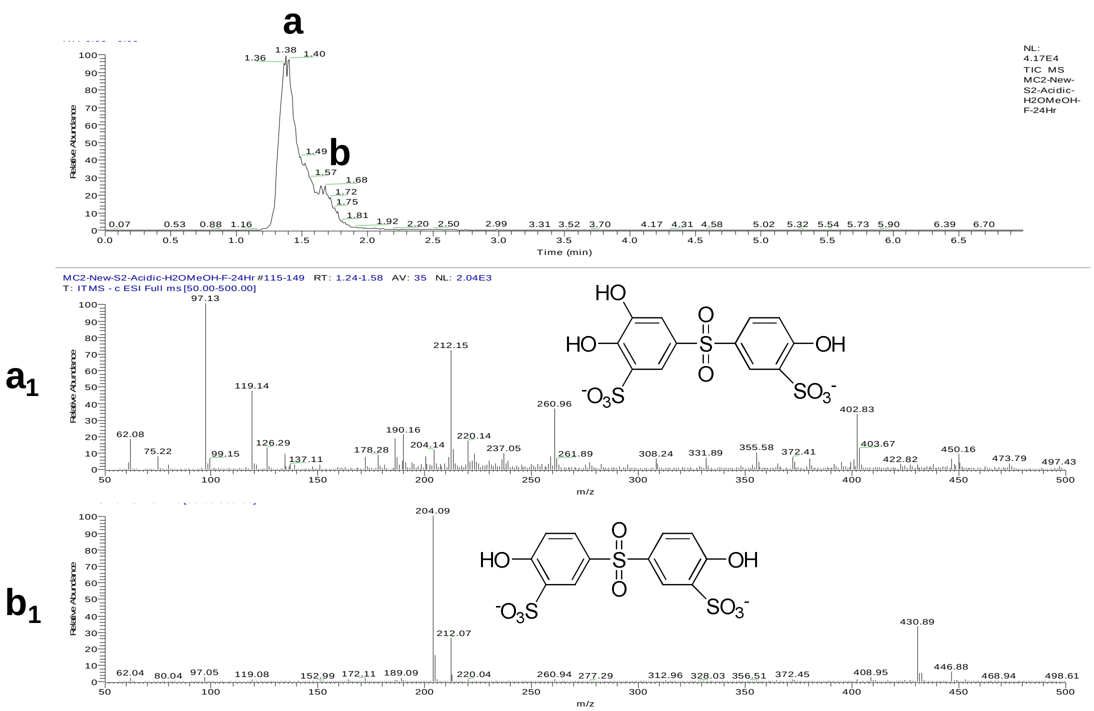

Figure 8. LC-MS spectra of AMC2-S2 after 24 hrs of Fenton’s degradation.

In the case of AMC5, the mono-sulfonated compound (AMC5-S) alone was used for degradation study. Figure 9 shows the results after 24hrs of Fenton’s degradation reaction. LC-MS signal **d**, $\mathbf{d_1}$ is from the intact AMC5-S. From the LC trace it can be seen that a very small amounts of degradation products (**a**, **b**, **c**) were observed.

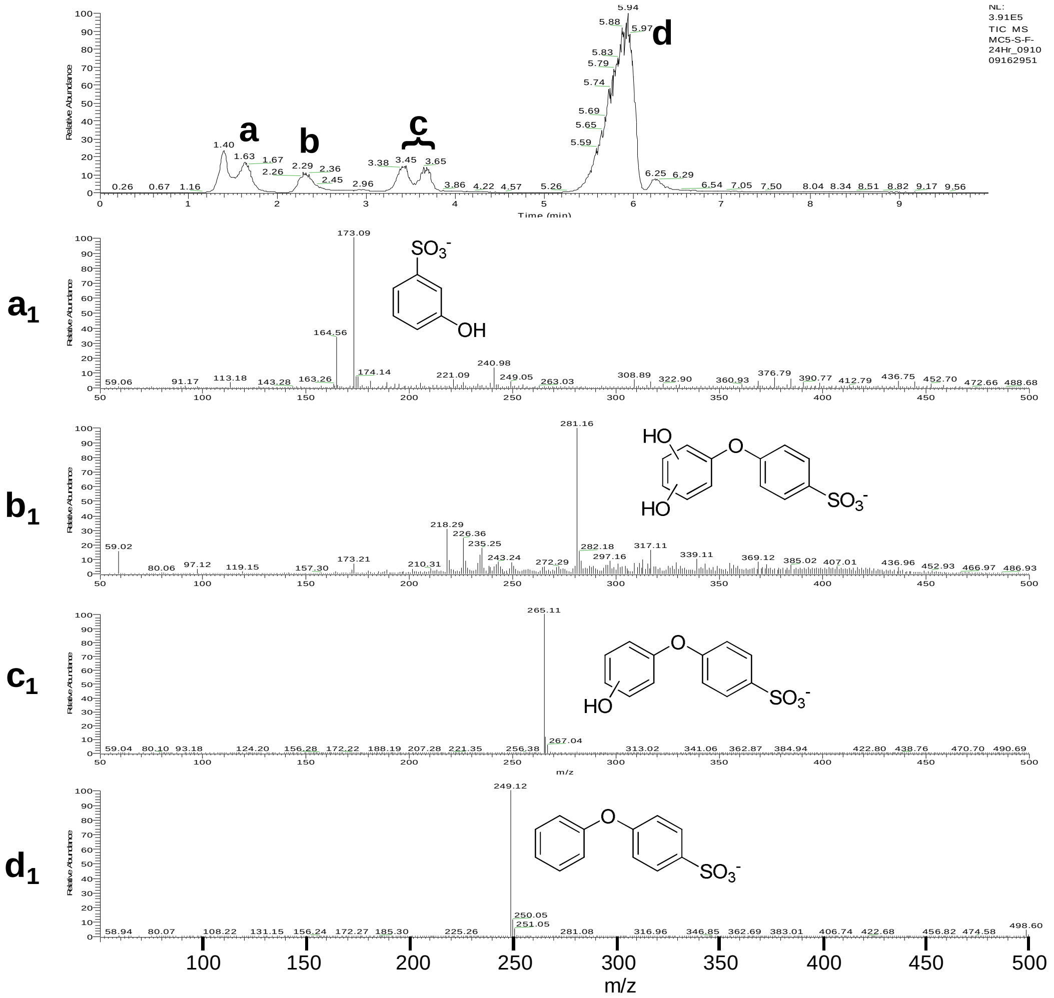

Figure 9. LC-MS spectra of AMC5-S after 24hrs of Fenton's degradation.

The 24hr Fenton's degradation reaction results in formation of mono-(**c**, **c_1**, m/z 265) and di-hydroxylated (**b**, **b_1**, m/z 281) compounds. Some amount of mono-hydroxylated benzenesulfonic acid (**a**, **a_1,** m/z 173) was also observed, which could be formed from either breaking of the hydroxylated compound or breaking of AMC5-S and then hydroxylation of the fragment. Degradation products of AMC5-S suggest that the ether linkages are the weakest bonds in the molecule and are susceptible to radical attack under the degradation conditions. Similar results were also observed in case of perfluorinated ether compounds[10] studied previously, where fragmentation at ether linkages was observed.

Degradation of AMC4 under Fenton's and UV/H_2O_2 conditions showed the most degradation products of all the model compounds. Under both the test conditions it was observed that AMC4 under goes excessive hydroxylation and dimerization (**Table2**). Due to limited solubility of the compound (methanol solvent) addition of $–OCH_3$ groups was also observed among the degradation products (not listed in the table).
The disulfonated dimethoxy substituted AMC4 (AMC4-OMe-S2) however shows very limited hydroxylation and no detectable dimerization compared to AMC4 (**Table 2**). As

seen in the all the other sulfonated model compounds, sulfonation of this compound was helpful to prevent radical attack to a large extent.

Degradation of Group 3; Sulfonimides:

Sulfonimides are another class of functional groups which can be incorporated into proton exchange membranes. As described above, these compounds are considered super acids and may be suitable candidates for acid groups to increase the proton conductivity in PEM. Attack of hydroxyl radicals upon such functional groups had not been previously carried out, so AMC6 and AMC12 were examined in this study. AMC11 was used to study the effect of Fenton's reagent specifically on perfluoroethyl sulfonimide group. The degradation products for the Group 3 model compounds observed after 24hrs of Fenton's test and UV/H_2O_2 analysis are tabulated in **Table 3**.

Table 3. Degradation products obtained from UV/H_2O_2 and Fenton's degradation tests of sulfonimides.

AMC	Structures	Degradation Products	
		UV/H_2O_2	Fenton's
AMC6	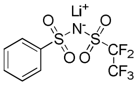	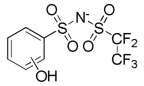 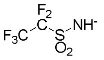	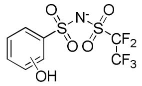 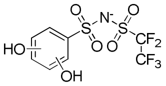 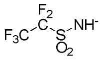
AMC12	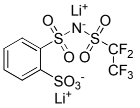	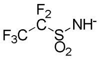	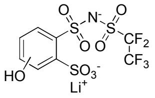 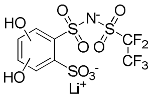 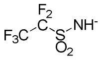
AMC11	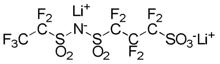	—	—

Three different degradation products were identified in case of AMC6 after 24hrs of Fenton's test. **Figure 10** shows the LC-MS spectra of AMC6. The signal **d**, $\mathbf{d_1}$ (m/z 338) is from intact AMC6. The LC trace shows that large amount of AMC6 has been consumed during the Fenton's degradation. Two minor degradation products obtained were mono- (**c**, $\mathbf{c_1}$, m/z 354) and di-hydroxylated (**b**, $\mathbf{b_1}$, m/z 370) AMC6 while the major degradation product observed is due to the breaking of the S-N bond, which was detected as perfluoroethyl sulfonamide anion (**a**, $\mathbf{a_1}$, m/z 198) in the MS.

Similar results were obtained in the case of AMC12, which is a sulfonated analogue of AMC6. The major product in AMC12 was also perfluoroethyl sulfonamide and minor amounts of mono and di-hydroxylated AMC12. Unlike AMC6, AMC12 does not degrade as much in 24hrs under the present conditions. This could be due to the sulfonate group present in AMC12, thus helping in preventing radical attack.

Loss of the sulfonimide group may lead to drop in conductivity in an actual membrane with AMC6 or AMC12 compounds on side chains. Hence model compound AMC11, a representative of the sulfonamide groups on AMC6 and 12 was also studied under similar degradation conditions. The sample contains perfluoropropane 1,3 disulfonic acid lithium salt as the major impurity which was identified during the initial analysis after the synthesis of AMC11. An increase in the LC peak of this impurity would be an indicative of the breaking of N-S bond in AMC11. During Fenton's degradation, AMC11 was exposed to twice the amount of hydrogen peroxide and fresh Fe(II) solution than AMC6 and 12. However, LC-MS analysis after 24hrs of accelerated conditions did not show any degradation of this compound or any significant increase in the impurity (perfluoropropane 1,3 disulfonic acid lithium salt) suggesting the molecule to be highly resistant to radical attack.

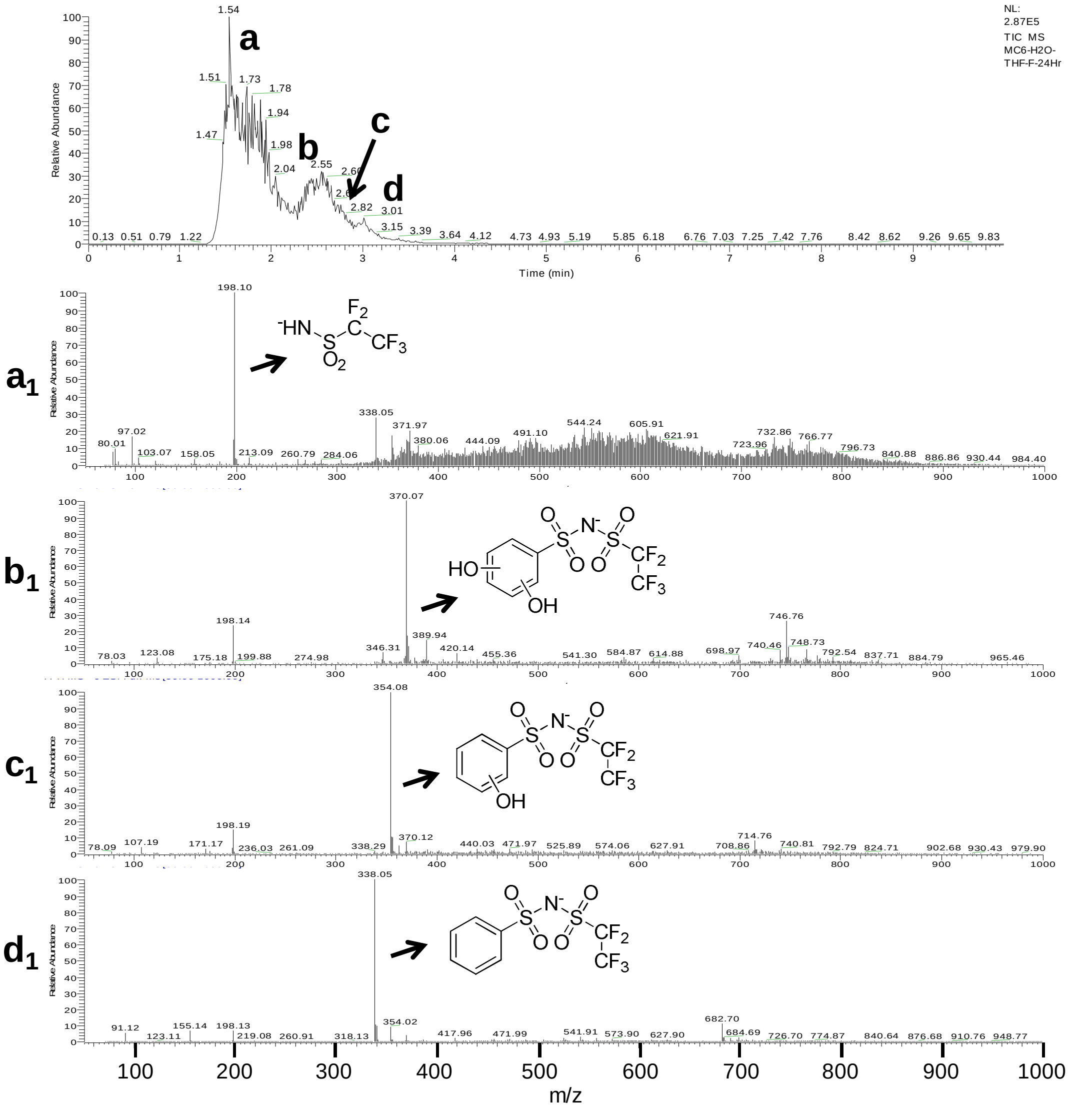

Figure 10. LC-MS spectra of AMC6 after 24hrs of Fenton's degradation test.

Mass Balance:

The degradation reactions used to study the model compounds can also lead to complete oxidation of the molecules, leading to loss of the material in the form of CO_2 or formation of smaller molecules non-detectable under the present MS conditions. To account for the loss of sample undetected by MS, mass balance and amount of CO_2 evolved was calculated. Mass balance experiments were used to calculate the amount of sample not detected by the MS or lost in the form of CO_2 due to complete oxidation of model compounds. Thus the data also gives more in-depth information on the stability of the model compounds studied. Comparing the percentage of model compound lost in AMC1 and its fluorinated version, AMC10, for example, shows that fluorinating the aromatic ring does increase the stability of the ring. **Table 4** shows the mass balance results of the all model compounds analyzed for mass lost during 24 hours of Fenton's degradation testing.

Table 4. Mass balance data: percentage of AMCs lost after 24hrs of Fenton's degradation test.

AMCs	% Lost
Sulfonic/Phosphonic acid	
AMC1	60
AMC10	42
AMC3	70
AMC7	52
AMC9	75
Sulfones, Biphenols and Ether	
AMC2	13
AMC2-S2	75
AMC5-S	58
Sulfonimides	
AMC11	40
*AMC12	6.7
*AMC6	75

*non-acidic samples

This analysis was also useful in determining the stability of the analogous disulfonates AMC3, AMC7 and AMC8. The LC-MS study demonstrated that AMC3 was the most stable as there were no detectable degradation products observed. The mass balance analysis of the compound actually determined that AMC3 is lost about 18% more than AMC7, while no measurable loss was observed in case of AMC8. The results suggest that AMC8 which is a meta-disubstituted compound is the most stable among the three analogs and resist the radical attack under the present degradation conditions. As mentioned earlier this stability could be due to the meta substitution of sulfonate groups on the aryl ring presenting fewer meta positions for the •OH attack.

The stability of sulfonated versus non-sulfonated model compounds was also evaluated by mass balance of the two kind of sample. AMC2-S2 which is the disulfonated version of AMC2 shows fewer degradation products although the mass balance experiment shows that there is 62% more of AMC2-S2 lost during degradation than the non-sulfonated compound. In this particular case it was observed that although fewer degradation products (hydroxylation) were observed, and no C-C bond breaking was detected in the LC-MS analysis, the sulfonated compound (AMC2-S2) may in fact either breaks into much smaller non-detectable compounds or completely oxidizes to CO_2. Thus in case of AMC2, sulfonation was not able to successfully prevent radical attack. Mass balance analysis of the sulfonamide model compounds, however shows that sulfonated AMC12 has much less loss of compound compared to non-sulfonated AMC6 after the Fenton’s test. In this instance sulfonation decreases the amount of degradation of the molecule under the present degradation conditions. AMC11 on the other hand degrades to a greater extent, despite the presence of detectable degradation products using LC-MS. ***A very important lesson here is that the presence or absence of detectable degradation products by LCMS is only one indicator of model compound degradation. It is possible to detect several degradation products, but have this produced in low yields. It is also possible to not detect degradation products, while losing a significant portion of starting model compounds to undetectable degradation products.***

Table 5. Percentage of CO_2(g) evolved after 1hr and 24hrs of Fenton’s degradation test.

Sample	% CO_2 (g) evolved	
	1Hr	24Hr
Sulfonic/Phosphonic acids		
AMC1	0.001	0.515
AMC10	0.004	0.023
AMC3	0.005	0.015
AMC7	0.008	0.33
AMC8	0.004	0.254
*AMC9	0.001	0.004
Sulfones, Biphenols and Ether		
AMC2	0.001	0.019
AMC2-S2	0.007	0.052
AMC4	0.001	0.007
AMC4-OMe-S2	0.002	0.002
AMC5-S	0.002	0.004
Sulfonimides		
AMC6	0.002	0.184
AMC11	0.011	0.028
AMC12	0.017	0.028

* % CO_2(g) evolution in AMC9 biased due to precipitation during Fenton's degradation test.

To better understand the fate of model compounds during radical degradation, CO_2 gas generated during Fenton's test of the AMCs was quantified GC-MS after 1 and 24hrs of Fenton's degradation. The calculated values were compared to percentage of CO_2 in air (0.039%) which gives an estimate on amount of complete oxidation of the AMCs under the present degradation conditions, are given in **Table 5**.

The CO_2 analysis shows that fluorinated AMC10 is more stable towards the degradation conditions than AMC, due to the fluorination of the compound. Among the analogous di-substituted compounds, AMC3, AMC7 and AMC8, AMC7 undergo the greatest degree of oxidation to produce CO_2 while AMC3 produces the least CO_2 in 24hrs. The mass balance study of the three compounds has revealed AMC3 to undergo the most degradation, while the CO_2 analysis shows that this degradation does not result into complete oxidation of the compound. AMC9 produced the least amount of CO_2 , but this result probably results precipitation of model compound, rather than accurate reactivity, during the Fenton's degradation. The sulfones, biphenols, ether and their sulfonated forms (AMC2, AMC2-S2, AMC4, AMC4-OMe-S2, and AMC5-S) in general produce less CO_2 after 24hrs of Fenton's degradation, i.e. they oxidize less compared to the sulfonic acids (AMC1, AMC10, AMC3, AMC7 and AMC8). Among the group AMC2-S2 oxidizes much more than AMC2 in spite of sulfonation, while, sulfonated methoxy derivative AMC4-OMe-S2 shows less oxidation. The CO_2 results obtained in the case of AMC2 and AMC2-S2 corroborates the mass-balance results and suggests that AMC2-S2 degraded to much higher degree than AMC2, also the degradation reaction results in complete oxidation of the molecule to for CO_2 gas. Sulfonimides also produce less CO_2 after 24hrs of degradation compared to sulfonic acids. Comparing the CO_2 evolution of AMC6 and AMC12 it can be seen that AMC12 oxidizes much less than AMC6, perhaps due to the sulfonation. AMC11, which is structurally similar to the sulfonimide groups on AMC6 and 12 also show comparable levels oxidation to them. These CO_2 evolution results are concurrent with their mass balance analysis and suggest that the in general sulfonic/phosphonic acids are much susceptible to radical attack and undergo complete oxidation than sulfones, biphenols, ether and sulfonimides.

Comparing mass balance and CO_2 evolution results of AMC11 suggests that in addition to CO_2 evolution there may also be production of fluoride ions during the degradation reaction. To test this, AMC6, AMC11, AMC12 and AMC10 were degraded for 24hrs in Fenton's Reagent, and the resultant solutions were analyzed for free fluoride ions using a fluoride ions selective electrode, **Table 6**.

Table 6. Fluoride ions (in ppm) evolved after 24hrs of Fenton's degradation test.

Sample	avg(mV)	ppm of F ions evolved
AMC6	52.8	0.5
AMC11	-26.0	24
AMC12	27.7	1.6
*AMC10	-59.4	91
†AMC10	-77.9	256.5
* after 24hrs †after 2months		

From the fluoride analysis it was found that AMC12 produces higher amounts of fluoride ions during degradation compared to AMC6 although it degrades to less degree. While AMC11, which is representative of the side chains of AMC6 and 11 shows much higher production of free fluoride ions. This result supports the higher percentage of sample lost in mass balance analysis and lower CO_2 production. AMC10 produces the highest amount of free fluoride ions after 24hrs of Fenton's degradation which increases over a period of 2months. This fluoride generation is likely due to replacement of one of the fluorine atoms with a hydroxyl group.

<u>Competitive Degradation</u>**:**

Competitive degradation experiments were used to determine the rate of degradation of AMCs compared to previously studied MC7/MC8 (the model compound analogs of Nafion™ and the 3M perfluorinated ionomer, respectively. Calculated reactivity ratios of AMCs to MC7/MC8 are presented in **Table 7**. *The AMCs were found to be generally more susceptible to degradation than the perfluorinated non-aromatic MC7/MC8*. AMC1 and AMC10 both showed comparable degradation rates to MC7/MC8 while AMC9 degrades two times faster than both MC7 and MC8. The reactivity ratios for AMC9 could be affected due to precipitation of AMC9 during Fenton's test. Comparing the reactivity ratios of the disulfonates it was found that AMC3 and AMC8 also have comparable degradation rates to MC7/MC8 where as AMC7 degrades much faster. The high reactivity of AMC7 may be due to rapid oxidation of that model compound to smaller molecules which could not be detected by MS (mass balance results) and to complete oxidation to CO_2. Sulfones and sulfonated sulfones also showed comparable reactivity to MC7/MC8 except for sulfonated ether, AMC5-S, which degraded about six times faster than MC7/MC8, perhaps due to its relatively labile ether linkages. From the reactivity ratios of AMC5-S it can also be concluded that the ether linkages in aromatic compounds are more susceptible to radical attack than the those in the perfluorinated non-aromatic model compounds such as MC7/MC8. The sulfonimides, AMC6, 11 and 12 so far had the most comparable degradation rates to MC7/MC8.

Table 7. Competitive degradation test: Reactivity ratios of AMCs compared to MC7 and MC8.

Sample	Reactivity Ratios	
	MC7	MC8
Sulfonic/Phosphnic acid		
AMC1	1:01	0.5:1
AMC10	0.8:1	0.7:1
AMC3	1:01	0.1:1
AMC7	23:01	9:01
AMC8	1.1:1	0.7:1
AMC9	2:01	2:01
Sulfones, Biphenols and Ethers		
AMC2-S2	0.8:1	1.2:1
AMC4-OMe-S2	1.5:1	0.9:1
AMC5-S	7:01	6:01
Sulfonimides		
AMC6	0.6:1	1:01
AMC11	1:01	1.2:1
AMC12	1.1:1	1.1:1

5- Conclusions

A series of 15 model compounds were subjected to Fenton's Reagent and UV/hydrogen peroxide radical degradation, followed by product analysis, mass balance, and carbon dioxide quantification. Tested singly, and in pair-wise competitive reactions with perfluorinated compounds which model the current state-of-the-art, membrane polymers, these model studies allow us to better understand degradation in the alternative, aromatic hydrocarbon membrane systems. Key conclusions are as follow:

- *Ortho*-disulfonation of aromatic rings results in unstable structures which degrade an order of magnitude faster than *meta*- or *para-substituted* systems, and an order of magnitude faster than the PFSA models. Both loss of one sulfonate, and ring hydroxylation are observed to occur.
- From a chemical stability standpoint, Aryl phosphonates appear to be credible alternatives to aryl sulfonates, showing only modest ring hydroxylation when compared to the sulfonates, and exhibiting overall low comparative degradation rates
- Sulfonated aryl ethers degrade an order of magnitude faster than aryl sulfones or the PFSA models. The aryl ether shows degradation through loss of sulfonate,

ring hydroxylation, and cleavage of the ether link, with little carbon dioxide generation. The aryl sulfones were prone to ring hydroxylation to a significant degree

- Perfluorinated aryl sulfonates are highly prone to loss of fluoride under radical conditions
- Comparing perfluorethyl, phenyl sulfonimide with its aryl-sulfonated analog, and an aliphatic perfluoroalkyl sulfonimide, the aliphatic system loses fluoride at a rate an order of magnitude greater than the two aromatic models; overall degradation rates for the three sulfonimides were comparable to those of the PFSA model compounds. Despite the higher fluoride loss in the aliphatic system, no LCMS detectable products were observed during degradation of this model, whereas the aromatic models showed ring hydroxylation, N-S bond cleavage, and in the case of the sulfonated aryl model compound, desulfonation. All three of these sulfonimides exhibited moderate rates of carbon dioxide generation during radical degradation. Summing these results together, it appears that the sulfonimides can be sufficiently stable proton transport groups in PEM systems, with loss of fluorine characterizing degradation in the aliphatic system, and attack on the aryl ring dominating degradation of the aryl sulfonimides.

References:

1. Steele, B. C. H., Heinzel, A. *Nature* (London, UK), **414**, 345, 2001.
2. Kreuer, K. D. *J Membr Sci*, **185**, 29, 2001.
3. Lashway, R. W. *MRS Bull*, **30**, 581, 2005.
4. de Bruijn, F. *Green Chem*., **7**, 132, 2005.
5. Berlastsky, S., Cipollini, N., Condit, D., Madden, T., Aliev, M. A., Atrazhev, V. V., Kuzminyh, N. Yu., E. N. Timohina, E. N. *208th Electrochemical Society National Meeting,* October **2005**, Los Angeles CA, paper 1189.
6. Schiraldi, D. A.; *Polym. Rev., 46(3)*, 315, 2006.
7. Zhou, C., Savant, D., Ghassemi, H., Schiraldi, D. A., Zawodzinski Jr., T. A., "PEMFC membrane – life-limiting considerations", in *Encyclopedia of Electrochemical Power Sources,* Scrosati, B., Ogumi, Z., Rand, D., Moseley, P., Dyer, C., Garche, J., eds., 2009, Elsevier, Amsterdam, 755-64.
8. Mauritz, K.A., Moore, R. B.; *Chem. Rev.,* **104(10)**, 4535, 2004.
9. Curtin, D. E.; Lousenberg, R. D.; Henry, T. J.; Tangeman, P. C.; Tisack, M. E. *J. Power Sources,* **131**, 41, 2004.
10. Zhou, C., Zawodzinski Jr., T. A., Schiraldi, D. A., *Macromolecules,* **40**, 8695-8707, 2007.
11. Ghassemi, H., McGrath, J.E., *Polymer*, **45(17),** 5847, 2004.
12. Ghassemi, H., Ndip, G., McGrath, J.E., *Polymer,* **45(17),** 5855, 2004.
13. Schiraldi, D. A., Savant, D., "Chemical Durability Studies of PFSA and Nonfluorinated PEM Materials" in *Fuel Cell Chemistry and Operation*, Herring, A., Zawodzinski, T., Hamrock, S., eds., ACS Symposium Series, 2010, Washington D.C., American Chemical Society, Ch. 9, 125-36.
14. Asano, N., Aoki, M., Suzuki, S., Miyatake, K., Uchida, H., Watanabe, M., *J. Am. Chem. Soc.,* **128**, 1762-9, 2006.